

Top Quark Mass Effects in Higgs and Z Boson Pair Production and Higgs Boson Decays

Zur Erlangung des akademischen Grades eines

**DOKTORS DER NATURWISSENSCHAFTEN
(Dr. rer. nat.)**

von der KIT-Fakultät für Physik
des Karlsruher Instituts für Technologie (KIT)
angenommene

DISSERTATION

von

M.Sc. David Wellmann

aus Leipzig

Tag der mündlichen Prüfung: 31. Januar 2020

Referent: Prof. Dr. Matthias Steinhauser

Korreferent: Prof. Dr. Kirill Melnikov



This document is licensed under a Creative Commons Attribution-ShareAlike 4.0 International License (CC BY-SA 4.0):

<https://creativecommons.org/licenses/by-sa/4.0/deed.en>

Contents

1. Introduction	1
2. Z-Boson Pair Production	5
2.1. Introduction	6
2.2. $gg \rightarrow ZZ$	7
2.2.1. The Process $gg \rightarrow ZZ$	7
2.2.2. The Tensor Structure	8
2.2.3. The Projectors	11
2.2.4. Orthogonal Basis	12
2.3. Amplitude	15
2.3.1. General Layout of the Calculation	15
2.3.2. Feynman Graph Generation	17
2.3.3. Asymptotic Expansion	18
2.3.4. Reduction to Master Integrals	20
2.3.5. Calculation of the Master Integrals	24
2.3.6. Renormalization	28
2.4. Form Factors	30
2.4.1. Definitions, Prefactors & Numerical Values	30
2.4.2. Exact Leading Order Result	32
2.4.3. Large Top Mass Expansion	35
2.4.4. High Energy Expansion	39
2.4.5. Comparing LO Exact vs. Expansions	42
2.4.6. Importance of Finite M_Z Corrections	47
2.4.7. Radius of Convergence	49
2.4.8. Padé Approximation	50
2.5. NLO Results	56
2.5.1. NLO Form Factors	56
2.5.2. NLO Virtual Finite XS	60
2.6. Conclusion and Outlook	65
3. Higgs-Boson Pair Production	67
3.1. Introduction	68
3.2. $gg \rightarrow HH$	71
3.2.1. The Process $gg \rightarrow HH$	71
3.2.2. Calculation of the Form Factors	76
3.3. Form Factors: Analytical and Numerical Results	78
3.3.1. Leading Order Results	78
3.3.2. Finite Higgs Boson Mass Effects	81

3.3.3.	Next-to-Leading Order Results	82
3.3.4.	Dependence on the Scattering Angle	87
3.4.	NLO Virtual Finite	91
3.4.1.	Definition: \mathcal{V}_{fin}	91
3.4.2.	\mathcal{V}_{fin} : Comparison against Literature Results	92
3.4.3.	Padé-improved \mathcal{V}_{fin} : Comparison against Literature Results	94
3.4.4.	Application of the NLO Results	98
3.5.	Hadronic Cross Section	101
3.6.	Conclusion and Outlook	103
4.	Hadronic Higgs Decay	105
4.1.	Introduction	106
4.2.	The Process $H \rightarrow$ Hadrons	107
4.3.	Calculation of the Correlator Functions	109
4.4.	Results	111
4.4.1.	Δ_{11}	111
4.4.2.	Δ_{12}	111
4.4.3.	Δ_{22}	111
4.4.4.	Numerical Results	112
4.5.	Conclusion	115
5.	Conclusion and Outlook	117
A.	Appendix $gg \rightarrow ZZ$	119
A.1.	Explicit tensor structures $\mathcal{T}^{\mu\nu\rho\sigma}$	120
A.2.	Basis Change $T^{\mu\nu\rho\sigma} \rightarrow \mathcal{T}^{\mu\nu\rho\sigma}$	121
A.3.	Integral Families and Master Integrals	124
A.4.	Change of Variables	129
B.	Appendix $gg \rightarrow HH$	131
B.1.	Projectors	131
B.2.	Additional Plots	132
C.	Appendix $gg \rightarrow \gamma\gamma$	137
C.1.	Tensor Structure	137
D.	Appendix $gg \rightarrow Z\gamma$	139
D.1.	Tensor Structure	139
E.	Appendix $H \rightarrow$ Hadrons	141
E.1.	Effective Couplings	141
	Bibliography	145

1. Introduction

Physics is a curiosity driven science, asking questions of what is the universe made of, and why it behaves in the way in which we observe. In the field of Particle Physics, the focus narrows down to scales far below that which can be seen by eye, trying to break down matter into its smallest building blocks and searching for clues that allow the formulation of a theory which explains how nature works at its most fundamental level. The framework of Quantum Field Theory (QFT), whose development started more than 100 years ago, provides the mathematical and physical ground for the description of phenomena that appear in this context. On this foundation, the Standard Model of particle physics (SM) was built and its studies and attempts to go beyond it defined Particle Physics during the last 50 years. At the core of this model is a gauge theory and the mechanism of symmetry breaking realized through the scalar Higgs field with its quartic potential which provides, in a consistent way, masses to all observed particles. The associated Higgs boson is one of the many predictions of the SM. With its discovery in 2012 [1, 2], every elementary particle present in the SM has by now been experimentally observed, making the SM an extremely successful theory.

The interest of this thesis lies with the three heaviest elementary particles in the SM; the Z boson with a mass of 91.1876 ± 0.0021 GeV [3] discovered at CERN in 1983, the top quark with a mass of 172.9 ± 0.4 GeV [3] discovered at Fermilab in 1995 and the Higgs boson with a mass of 125.10 ± 0.14 GeV [3] discovered in 2012 at CERN.

Although all free parameters necessary to describe the SM have been measured and the shape of the potential of the Higgs field is completely determined by the rest of the theory, to date it has not been measured by experiments to any reasonable precision. The most stringent constraint for the relevant parameter κ_λ (which characterizes the coupling strength of Higgs bosons to themselves and should, if the SM proves to be correct, be equal to one) is given by the CMS and ATLAS experiments as $-11.8 < \kappa_\lambda < 18.8$ [4] and as $-5.0 < \kappa_\lambda < 12.0$ [5], respectively.

One process considered in this thesis, which directly depends on the self-coupling between Higgs bosons, is the production of a pair of Higgs bosons. ATLAS and CMS experiments study this process at the Large Hadron Collider (LHC) and it is therefore useful to consider the production of Higgs boson pairs via gluon fusion since the rate of this process is, compared to the other channels, greatly enhanced by the large gluon luminosity at the LHC. The calculation of theoretical predictions at the second order in perturbative Quantum Chromodynamics (QCD) for this process will be the topic of chapter 3. A second process, which is of great importance for measurements constraining the properties of the Higgs boson, such as its width and quantum numbers, which also allows for high precision tests of the electroweak sector of the SM is the pair production of two Z bosons in gluon fusion which will be presented in chapter 2. The last topic, investigated in chapter 4, treats the dominant hadronic decay mode of the Higgs boson, where the direct decay into bottom

quarks together with the decay to gluons make up about 70% of the total hadronic decay. The computation of top quark induced four loop corrections to the hadronic decay width of the Higgs boson will be the topic in that chapter of the thesis.

What started as an ‘observation of a new particle’ in 2012 has, with the end of LHC Run 2, begun to turn into precision studies of the Higgs boson properties and the SM in general. Precise experimental results require precise predictions on the theory side. In the framework of QFT, providing such predictions requires the calculation of scattering amplitudes whose complexity rises rapidly with the number of closed loops, external particles and internal mass scales.

Any N -loop Feynman diagram is given by a N -fold $d = 4 - 2\epsilon$ dimensional Feynman integral which, at one-loop order are mostly still ‘easy enough’ to be solved, such that an analytic result can be derived for them. At two loops, they become both more numerous and more difficult to compute analytically. Exact results are only available for a rather small fraction of all possible Feynman integrals where the number of external particles and internal scales is small. By considering these integrals in a limit where particles are considered to be massless, many exact results can be obtained. However, in all of the processes mentioned above, the top quark plays an important role since the coupling of the Higgs boson is proportional to the masses of the interacting particles, of which the top quark is the heaviest. The massless limit is therefore a very crude approximation.

Finding an exact, analytic solution for these problems is very difficult and it is not clear if it can even be done with the set of mathematical tools that are currently used in theoretical particle physics. There are, however, two other possible ways to approach this problem which lead to physical results.

First, numerical evaluation of Feynman integrals including the complete dependence on all scales, which is difficult but possible. Once properly implemented, one can evaluate every integral for any desired phase space point to obtain a result which should correspond to the exact result within the bounds of uncertainty from the numerical integration. This method is usually very flexible when it comes to considering similar but different processes. Drawbacks are that the ‘hard part’ of calculating the integral has to be repeated for every single evaluation and that any result is only valid for exactly one combination of input parameters and cannot be recycled if they change. Furthermore, requiring high numerical precision makes the integration slow and CPU-time intensive.

Second, the exact result can be approximated by expansions in small scales or ratios of scales of the problem. In the case of the top quark loop-induced processes discussed in this thesis, this means to consider finite top quark mass corrections as a power series in ratios of m_t and the energy scale \sqrt{s} of the process that are small in the region considered. Therefore, at low energies one recovers the top quark mass dependence by including corrections in s/m_t^2 while at high energies the exact result can be approximated by a series in m_t^2/s . The advantage of this approach is, that the ‘hard part’ of the calculation, evaluating the series coefficients, has to be done only once. The resulting expressions are usually given in terms of well-known functions and allow for a fast evaluation. A drawback is, that such expansions are only valid in certain parts of the phase space (e.g. the high energy expansion requires $m_t^2 \ll s$ and can therefore not yield valid results at $s \leq m_t^2$).

In this thesis, techniques to derive such low-energy and high-energy expansions are exploited to obtain expansions in ratios of scales involving m_t , m_H and m_Z . It should be clear that there is a finite radius of convergence associated with any such truncated low- or high-energy expansion, outside of which the expansions diverge. The question of finite radius of convergence of a power series and ways to go beyond it is widely studied in mathematics. One promising approach that emerged in this context is the application of Padé approximants, which rewrite a power series as a rational polynomial that, if series expanded, reproduces up to higher orders exactly the same power series representation but will usually not diverge if evaluated outside the radius of convergence of the underlying power series. Based on such Padé approximants, a systematic approach is developed which allows one to obtain a stable and reliable prediction for a much larger part of the phase space than the initial power series is able to describe.

In chapter 2, the on-shell process $gg \rightarrow ZZ$ is considered as a perturbative expansion at leading order in the electroweak coupling α and next-to-leading order in the strong coupling α_s . Both the high-energy expansion up to order m_t^{32} and the low-energy expansion up to order $1/m_t^{12}$ are calculated at one and two loops (LO and NLO, respectively). For the high-energy expansion, finite Z boson mass effects are taken into account by means of a Taylor expansion around $m_Z = 0$, including correction terms up to m_Z^4 . A method based on Padé approximants is developed that makes use of the many higher order terms in the high energy expansion in order to extend its predictive power to a larger part of the phase space. The low- and high-energy expansions, as well as the Padé approximation method, are verified at LO against the exact result. Using the same methods at NLO, predictions are made for the 20 NLO form factors and the finite contribution of the virtual NLO correction to the partonic cross section.

Chapter 3 treats the on-shell process $gg \rightarrow HH$ in a similar manner to chapter 2 at $\mathcal{O}(\alpha, \alpha_s^2, m_t^{32}, m_H^2)$. NLO predictions for the form factors and the virtual correction to the partonic cross section, \mathcal{V}_{fin} , are made and the latter is compared against existing numerical exact results.

Chapter 4 treats the process $H \rightarrow$ hadrons at four loops in an effective field theory where the top quark has been integrated out. The top quark induced results at α_s^4 are compared against known massless contributions from the literature.

Chapter 5 gives a short summary of the thesis.

2. Z-Boson Pair Production

2.1. Introduction

In this chapter, the process of Z pair production via gluon fusion is considered for both the direct production of two Z bosons and the Higgs mediated Z pair production, $gg \rightarrow H \rightarrow ZZ$. This process is important since it was one of the channels used in the discovery of the Higgs boson in 2012. By now, many properties of the Higgs boson have been studied at the LHC. Yet, with an energy resolution that is three order of magnitude larger than the value for the width of the Higgs boson predicted by the SM of $\Gamma_H = 4.10 \text{ MeV} \pm 1.4\%$ [6], no direct measurement of Γ_H is possible at the LHC [7]. It has however been proposed to compare rates for on-shell and off-shell Higgs boson production in the process $gg \rightarrow H \rightarrow ZZ$ (with a subsequent decay into two lepton pairs) to indirectly determine the width of the Higgs boson [8–10].

The exact calculation of $gg \rightarrow ZZ$ at LO has been performed in Ref. [11]. LO and Leptonic decays were considered in Refs. [12–14]. Two-loop results for massless quarks have been presented in Refs. [15–17] and large top mass expansions at two-loops were studied in [18–20]. Recently, also an expansion around the top pair production threshold became available in Ref. [21] which has been combined with the large mass expansion on the basis of conformal mapping and Padé approximants [22–25] in Ref. [21] (see also Ref. [26]).

In this thesis, the top quark induced corrections to the process $gg \rightarrow ZZ$ are considered at LO in the electroweak coupling and NLO in the strong coupling. Note, that although the contributions of light quarks are large, they are not considered in this thesis as the focus lies on corrections induced by massive top quarks. This process starts at one loop, which in the following is referred to as LO. In what follows, the LO contribution can be calculated exactly, and also in the high energy approximation and the large top mass approximation. At NLO or two-loop order, the process is calculated in both the large top mass expansion and the high energy expansion. For the large top mass expansion, finite top mass terms are included up to m_t^{-12} at LO and NLO, whereas for the high energy expansion, a double series in both the Z boson mass and the top quark mass is considered with terms up to m_t^{32} and m_Z^4 both at LO and NLO.

At LO, both the high-energy expansion and the large-mass expansion agree very well with the exact result within their region of convergence. A method based on Padé approximants is developed to extend the range of validity of the expansions beyond their radius of convergence. It is shown that this method provides good predictions and reliable uncertainty estimates when compared against the exact LO result. Therefore, it is applied also at NLO in order to provide predictions for the real and imaginary parts of all 20 form factors in a large part of the phase space. Also predictions for the final contribution of the virtual NLO calculation to the partonic cross section are presented.

The chapter starts in section 2.2 with the general discussion of the process and its tensor structure. In section 2.3 the computational details are explained. Section 2.4 shows the results for the form factors, discusses the importance of the quartic term in the Z mass expansion and introduces the Padé approximation procedure. Section 2.5 show the NLO results for the form factors and the differential partonic cross section. Section 2.6 finishes with a conclusion and outlook.

2.2. $gg \rightarrow ZZ$

This section provides an overview of the general structure of the process under consideration before the more technical details of its calculation are discussed in the following sections.

2.2.1. The Process $gg \rightarrow ZZ$

The process of gluon fusion into a pair of Z bosons, denoted by $g(p_1)g(p_2) \rightarrow Z(-p_3)Z(-p_4)$, is a $2 \rightarrow 2$ process with two incoming gluons of momenta p_1 and p_2 and two outgoing Z bosons of momenta $-p_3$ and $-p_4$ as depicted in Fig. 2.1.

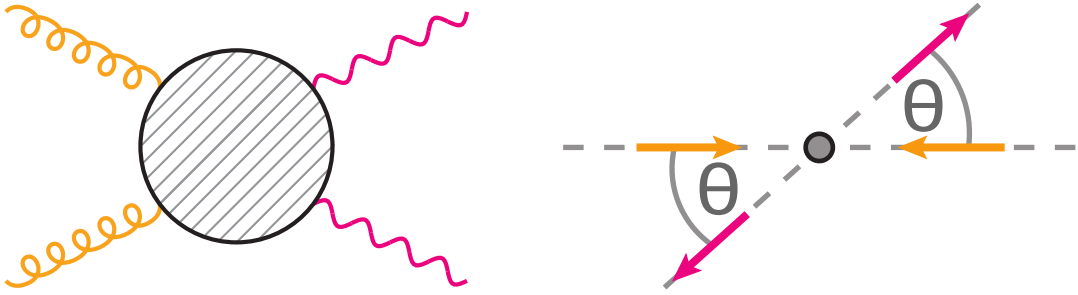


Figure 2.1.: Left: Schematic graph for the process $g(p_1)g(p_2) \rightarrow Z(-p_3)Z(-p_4)$. Curly lines indicate gluons, wavy lines Z bosons. The shaded area in the centre of the diagram represents one- and two-loop QCD or EW insertions. Right: Schematic picture of the centre-of-mass frame of the incoming gluon momenta p_1 and p_2 along the beam line and the outgoing Z bosons with momenta $-p_3$ and $-p_4$, scattered at an angle θ with respect to the beam line.

Each of the four external particles is a vector boson that comes with its own polarization vector \mathcal{E} . This means that, the amplitude for the process can be described by

$$\mathcal{A}_{ggZZ} = \sum_{\lambda_1, \lambda_2, \lambda_3, \lambda_4} \mathcal{E}_\mu^{\lambda_1} \mathcal{E}_\nu^{\lambda_2} \mathcal{E}_\rho^{\lambda_3} \mathcal{E}_\sigma^{\lambda_4} \mathcal{A}_{ggZZ}^{\mu\nu\rho\sigma}, \quad (2.1)$$

where the notation $\mathcal{E}_\mu^{\lambda_1}$ is a short hand notation for the polarization vector $\mathcal{E}_\mu(\lambda_1, p_1)$ with polarization λ_1 and momentum p_1 . Using the centre-of-mass frame shown in the right panel of Fig. 2.1, with a partonic centre-of-mass energy \sqrt{s} , the gluon and Z boson momenta can be written as

$$p_1 = \begin{pmatrix} \sqrt{s}/2 \\ \sqrt{s}/2 \\ 0 \\ 0 \end{pmatrix}, \quad p_2 = \begin{pmatrix} \sqrt{s}/2 \\ -\sqrt{s}/2 \\ 0 \\ 0 \end{pmatrix}, \quad p_3 = \begin{pmatrix} \sqrt{q^2 + m_Z^2} \\ q \cos(\theta) \\ q \sin(\theta) \\ 0 \end{pmatrix}, \quad p_4 = \begin{pmatrix} \sqrt{q^2 + m_Z^2} \\ -q \cos(\theta) \\ -q \sin(\theta) \\ 0 \end{pmatrix}. \quad (2.2)$$

The choice of setting the momenta of the external particles of the process on their mass shell yields the conditions

$$p_1^2 = p_2^2 = 0 \quad \text{and} \quad p_3^2 = p_4^2 = m_Z^2. \quad (2.3)$$

Furthermore, energy-momentum conservation yields $q^2 = s/4 - m_Z^2$ and therefore

$$s = (p_1 + p_2)^2 = s, \quad (2.4)$$

$$t = (p_1 + p_3)^2 = -\frac{s}{2} \left(1 - 2 \frac{m_Z^2}{s} - \cos(\theta) \sqrt{1 - 4 \frac{m_Z^2}{s}} \right), \quad (2.5)$$

$$u = (p_2 + p_3)^2 = -\frac{s}{2} \left(1 - 2 \frac{m_Z^2}{s} + \cos(\theta) \sqrt{1 - 4 \frac{m_Z^2}{s}} \right), \quad (2.6)$$

with s , t and u being the Mandelstam variables obeying the relation

$$s + t + u = 2m_Z^2. \quad (2.7)$$

Before starting to look into the calculation of the diagrams contributing to the process, it is advantageous to know more about the structure of $\mathcal{A}_{ggZZ}^{\mu\nu\rho\sigma}$ itself which will be the topic of the next paragraph.

2.2.2. The Tensor Structure

The amplitude on the l.h.s of Eq. 2.1 is a Lorentz scalar. It is obtained from the contraction of an a priori general Lorentz tensor of rank four with the four polarization vectors of the external gluons and Z bosons. The idea of the following paragraph is to deduce a decomposition of this general Lorentz tensor into an explicit linear combination of simpler rank-four Lorentz covariants.

Starting very generally, the scattering amplitude needs to describe the interaction of a pair of gluons and a pair of Z bosons, all being vector particles carrying different momenta and polarization vectors with different Lorentz indices. It is therefore clear, that the amplitude carries four open Lorentz indices, and can be built from a basis of rank four Lorentz covariants. Since the Z boson does not only come with a vector coupling but also an axial vector coupling, this implies the existence of γ_5 and therefore Levi-Civita ϵ tensors in the amplitude. However, due to charge-parity conservation, γ_5 will either always cancel directly or appear in pairs with both external Z bosons coupling to the same fermion line¹. Fermion traces in the latter case contain then two γ_5 which can be eliminated using the usual anti-commutation relations. As a consequence, the amplitude can be written in terms of rank four tensors built from metric tensors and external momenta only.

To keep track of all possible permutations and combinations of different indices involved it is useful to define the following sets and operations on them:

$$\Theta = \{\mu, \nu, \rho, \sigma\} \quad (2.8)$$

Θ is a set of four different Lorentz indices. With the size operator² $|S|$, denoting the number of elements contained in an arbitrary set S , define

$$S^{[k]} = \{ s \subseteq S \mid |s| = k \}, \quad (2.9)$$

¹At LO and NLO, the external Z bosons couple to distinct fermion lines only for the case of double triangle diagrams. However, these are not considered here since they are products of the one-loop $gg \rightarrow Z$ form factor which is known exactly in m_t [27, 28]. See also section 3.4.2 in [20] for further reading.

²Consider the set $\Theta = \{\mu, \nu, \rho, \sigma\}$. Then $|\Theta| = 4$.

where $S^{[k]}$ is the k -subset of S , building the set of all subsets of length k of S . Consider for example the 2-subset of Θ

$$\Theta^{[2]} = \{ \{ \mu, \nu \}, \{ \mu, \rho \}, \{ \mu, \sigma \}, \{ \nu, \rho \}, \{ \nu, \sigma \}, \{ \rho, \sigma \} \}. \quad (2.10)$$

Using eq. (2.10) one can define the set Ω of permutations of Lorentz indices for one metric tensor and two external momenta

$$\Omega = \left\{ \{ \omega_1, \omega_2, \omega_3, \omega_4 \} \mid \{ \omega_1, \omega_2 \} \in \Theta^{[2]}, \{ \omega_3, \omega_4 \} = \Theta \setminus \{ \omega_1, \omega_2 \} \right\}, \quad (2.11)$$

with $|\Omega| = 6$. The complement operator³ in $\Theta \setminus \{ \omega_1, \omega_2 \}$ denotes the removal of the elements ω_1 and ω_2 from the set Θ . Furthermore define the set Φ of permutations of Lorentz indices for two metric tensors

$$\Phi = \left\{ \{ \{ \phi_1, \phi_2 \}, \{ \phi_3, \phi_4 \} \} \in \left(\Theta^{[2]} \right)^{[2]} \mid \{ \phi_1, \phi_2 \} \cap \{ \phi_3, \phi_4 \} = \{ \} \right\}, \quad (2.12)$$

with $|\Phi| = 3$. Considering all possible permutations of the four Lorentz indices in Θ with either two metric tensors or one metric tensor and two external momenta or four external momenta together with all possible combinations of the four momentum indices of the external particles leads to a most general linear combination of $3 + 6 \cdot 4^2 + 4^4 = 355$ terms

$$\mathcal{A}_{ggZZ}^{\mu\nu\rho\sigma} = \sum_{\phi \in \Phi} c_\phi g^{\phi_1\phi_2} g^{\phi_3\phi_4} + \sum_{\omega \in \Omega} \sum_{i,j=1}^4 c_{\omega ij} g^{\omega_1\omega_2} p_i^{\omega_3} p_j^{\omega_4} + \sum_{i,j,k,l=1}^4 c_{ijkl} p_i^\mu p_j^\nu p_k^\rho p_l^\sigma. \quad (2.13)$$

However, due to momentum conservation, one of the external momenta is redundant and can be expressed in terms of the other three. Choosing to replace p_4 , all tensors from Eq. (2.13) containing p_4 split up according to

$$p_4 = -p_1 - p_2 - p_3, \quad (2.14)$$

lowering the number of Lorentz structures by 217 to a count of $3 + 6 \cdot 3^2 + 3^4 = 138$ terms. The structure remains the same as in eq. (2.13) with the modification that the sum over the momentum indices runs from 1 to 3 instead of 4. Relabeling for convenience the new coefficients to a_k and changing to a simpler notation gives:

$$\mathcal{A}_{ggZZ}^{\mu\nu\rho\sigma} = \sum_{k=1}^{138} a_k \mathcal{T}_k^{\mu\nu\rho\sigma}. \quad (2.15)$$

In principle, any of these 138 tensor structures $\mathcal{T}_k^{\mu\nu\rho\sigma}$ ⁴ can have a non-zero coefficient a_k contributing to the amplitude. Nevertheless, only a small number of these will also contribute to the cross section. The reason for this is that after the contraction of the amplitude with the four polarization vectors of the external gluons and Z bosons as given in eq. (2.1) a large number of terms simply drop out.

³Consider the two sets $\Theta = \{ \mu, \nu, \rho, \sigma \}$ and $\Sigma = \{ \nu, \sigma \}$. Then $\Theta \setminus \Sigma = \{ \mu, \rho \}$.

⁴A complete list of all 138 tensor from eq. (2.15) is given in eq. (A.1) of appendix A.1.

One can enforce the cancellation of 62 terms by imposing a smart gauge choice for the external gluons. Applying the lightcone gauge⁵ for the gluon with the momentum p_1 while using the other gluon momentum as reference vector $r = p_2$ and treating the second gluon similarly yields the conditions:

$$\mathcal{E}_\mu^{\lambda_1} p_2^\mu = 0, \quad (2.16)$$

$$\mathcal{E}_\nu^{\lambda_2} p_1^\nu = 0. \quad (2.17)$$

Conditions (2.16) and (2.17) imply, that after contraction with the polarization vectors, all contributions from tensors $\mathcal{T}_k^{\mu\nu\rho\sigma}$ containing either p_2^μ or p_1^ν are set to zero. Thus, the number of relevant tensor structures shrinks to $3+37+36 = 76$. However, as a consequence of the gauge fixing, the polarization sums for both gluons become more involved:

$$\sum_{\lambda_1} \mathcal{E}_\mu(\lambda_1, p_1) \mathcal{E}_{\mu'}^*(\lambda_1, p_1) = -g_{\mu\mu'} + \frac{p_1^\mu p_2^{\mu'} + p_2^\mu p_1^{\mu'}}{p_1 \cdot p_2}, \quad (2.18)$$

$$\sum_{\lambda_2} \mathcal{E}_\nu(\lambda_2, p_2) \mathcal{E}_{\nu'}^*(\lambda_2, p_2) = -g_{\nu\nu'} + \frac{p_2^\nu p_1^{\nu'} + p_1^\nu p_2^{\nu'}}{p_1 \cdot p_2}. \quad (2.19)$$

The reduction to a smaller set of tensor structures further benefits from the transversality of polarization vectors with respect to the momentum of their particle. This means, that for each of the four external particles, the contraction of their polarization vector with the momentum carried by that particle yields zero. Hence, this adds another three conditions similar to eq. (2.18) and (2.19)

$$\mathcal{E}_\mu^{\lambda_1} p_1^\mu = 0, \quad (2.20)$$

$$\mathcal{E}_\nu^{\lambda_2} p_2^\nu = 0, \quad (2.21)$$

$$\mathcal{E}_\rho^{\lambda_3} p_3^\rho = 0, \quad (2.22)$$

plus a fourth condition

$$\mathcal{E}_\sigma^{\lambda_4} p_4^\sigma = \mathcal{E}_\sigma^{\lambda_4} (-p_1^\sigma - p_2^\sigma - p_3^\sigma) = 0, \quad (2.23)$$

which means that one of the scalar products in Eq. (2.23) is redundant. Applying equations (2.20) to (2.22) removes an additional 50 tensor structures and only $3 + 17 + 6 = 26$ terms remain. Using the redundancy of one of the three scalar products on the right hand side of the last equation (2.23), one can express for example $\mathcal{E}_\sigma^{\lambda_4} p_3^\sigma$ by the sum of the other two scalar products $-\mathcal{E}_\sigma^{\lambda_4} p_1^\sigma - \mathcal{E}_\sigma^{\lambda_4} p_2^\sigma$ and write thereby the amplitude in terms of $3 + 13 + 4 = 20$

⁵Gluon prop. in lightcone gauge: $i\Pi_{ab}^{\mu\nu} = \frac{1}{p^2+i\epsilon} \left[-g^{\mu\nu} + \frac{p^\mu r^\nu + r^\mu p^\nu}{r \cdot p} \right] \delta_{ab}$ with light-like reference vector r^μ .

structures⁶.

$$\begin{aligned}
 \mathcal{A}_{ggZZ} = & \sum_{\lambda_1, \lambda_2, \lambda_3, \lambda_4} \mathcal{E}_\mu^{\lambda_1} \mathcal{E}_\nu^{\lambda_2} \mathcal{E}_\rho^{\lambda_3} \mathcal{E}_\sigma^{\lambda_4} \left(a_1 g^{\mu\nu} g^{\rho\sigma} + a_2 g^{\mu\rho} g^{\nu\sigma} + a_3 g^{\mu\sigma} g^{\nu\rho} \right. \\
 & + a_4 g^{\mu\sigma} p_1^\rho p_3^\nu + a_5 g^{\mu\sigma} p_2^\rho p_3^\nu + a_6 g^{\nu\sigma} p_1^\rho p_3^\mu + a_7 g^{\nu\sigma} p_2^\rho p_3^\mu + a_8 g^{\rho\sigma} p_3^\mu p_3^\nu \\
 & + (a_9 - a_{21}) g^{\mu\nu} p_1^\rho p_1^\sigma + (a_{10} - a_{21}) g^{\mu\nu} p_1^\rho p_2^\sigma + (a_{11} - a_{22}) g^{\mu\nu} p_2^\rho p_1^\sigma \\
 & + (a_{12} - a_{22}) g^{\mu\nu} p_2^\rho p_2^\sigma + (a_{13} - a_{23}) g^{\mu\rho} p_1^\sigma p_3^\nu + (a_{14} - a_{23}) g^{\mu\rho} p_2^\sigma p_3^\nu \\
 & + (a_{15} - a_{24}) g^{\nu\rho} p_1^\sigma p_3^\mu + (a_{16} - a_{24}) g^{\nu\rho} p_2^\sigma p_3^\mu + (a_{17} - a_{25}) p_1^\rho p_1^\sigma p_3^\mu p_3^\nu \\
 & \left. + (a_{18} - a_{25}) p_1^\rho p_2^\sigma p_3^\mu p_3^\nu + (a_{19} - a_{26}) p_2^\rho p_1^\sigma p_3^\mu p_3^\nu + (a_{20} - a_{26}) p_2^\rho p_2^\sigma p_3^\mu p_3^\nu \right), \quad (2.24)
 \end{aligned}$$

where the coefficients of the tensors $\mathcal{T}_k^{\mu\nu\rho\sigma}$ in terms of a_k can be relabeled into α_k :

$$\mathcal{A}_{ggZZ} = \sum_{\lambda_1, \lambda_2, \lambda_3, \lambda_4} \mathcal{E}_\mu^{\lambda_1} \mathcal{E}_\nu^{\lambda_2} \mathcal{E}_\rho^{\lambda_3} \mathcal{E}_\sigma^{\lambda_4} \sum_{k=1}^{20} \alpha_k \mathcal{T}_k^{\mu\nu\rho\sigma}. \quad (2.25)$$

Eq. (2.25) shows that the process $gg \rightarrow ZZ$ can, to all orders, be expressed through 20 tensor structures only. These structures agree with those found in [15]. The next step is to derive projectors that allow direct access to the 26 coefficients a_k in (2.24) that translate to the 20 coefficients α_k in equation (2.25).

2.2.3. The Projectors

Performing the loop integration or also the reduction to master integrals with open Lorentz indices is cumbersome. It is therefore convenient to introduce projectors $\Pi_{i, \mu\nu\rho\sigma}$, serving two purposes. First, multiplying $\Pi_{i, \mu\nu\rho\sigma}$ with the amplitude in Eq. (2.15) saturates the open indices from contributing Feynman diagrams. One is left with a scalar amplitude and scalar integrals that are much easier to handle. Second, by choosing a linear combination

$$\Pi_{i, \mu\nu\rho\sigma} = \sum_{j=1}^{138} \pi_{ij} \mathcal{T}_{j, \mu\nu\rho\sigma}, \quad (2.26)$$

with properly chosen coefficients π_{ij} , one can construct the projectors such that they project out single coefficients a_k from Eq. (2.15), therefore earning the name projectors. Requiring $\Pi_{\mu\nu\rho\sigma} = \mathcal{T}_{\mu\nu\rho\sigma}^{-1}$ leads to a system of equations that can be solved for the coefficients π_{ij} ⁷:

$$\Pi_{i, \mu\nu\rho\sigma} \mathcal{T}_k^{\mu\nu\rho\sigma} = \sum_{j=1}^{138} \pi_{ij} \mathcal{T}_{j, \mu\nu\rho\sigma} \mathcal{T}_k^{\mu\nu\rho\sigma} \stackrel{!}{=} \delta_{ik}. \quad (2.27)$$

⁶See eq. (A.1) of appendix A.1 for the complete set of all tensors $\mathcal{T}_i^{\mu\nu\rho\sigma}$ with $i \in \{1, \dots, 138\}$.

⁷There are 138 independent systems of 138 equations each, that can be solved in parallel. In this thesis, only the first 26 systems need to be solved, providing the coefficients for the projectors $\Pi_{1, \mu\nu\rho\sigma}, \dots, \Pi_{26, \mu\nu\rho\sigma}$.

The coefficients π_{ij} are functions of the space-time dimension d and scalar products of the external momenta that originate from the contraction of the tensors in Eq. (2.27). Applying projector $\Pi_{i,\mu\nu\rho\sigma}$ to the amplitude $\mathcal{A}^{\mu\nu\rho\sigma}$ returns the coefficient (or form factor) a_i :

$$\Pi_{i,\mu\nu\rho\sigma}\mathcal{A}_{\text{ggZZ}}^{\mu\nu\rho\sigma} = \sum_{k=1}^{138} a_k \Pi_{i,\mu\nu\rho\sigma} \mathcal{T}_k^{\mu\nu\rho\sigma} = \sum_{k=1}^{138} a_k \delta_{ik} = a_i. \quad (2.28)$$

It is again important to stress, that in this thesis all 26 projectors were calculated to allow access to the first 26 form factors of (2.15) that contribute to the amplitude in Eq. (2.24) with 20 different tensor structures.

2.2.4. Orthogonal Basis

In principle, the knowledge of the tensor structures $\mathcal{T}_k^{\mu\nu\rho\sigma}$ is sufficient to determine the projectors from section 2.2.3 and the corresponding form factors α_k . However, upon squaring the amplitude for the calculation of the cross section of the process, one is forced to compute a large number of all $20 \times 20 = 400$ cross terms which makes it very difficult to investigate the impact of individual form factors a_k . The goal of this subsection is to derive a set of new, orthogonal tensors $T^{\mu\nu\rho\sigma}$ whose associated coefficients or form factors only contribute to the cross section by their absolute square and that do not ‘talk’ to form factors of other tensor structures.

$$\mathcal{A}_{\text{ggZZ}}^{\mu\nu\rho\sigma} = \sum_{k=1}^{20} \alpha_k \mathcal{T}_k^{\mu\nu\rho\sigma} = \sum_{l=1}^{20} \beta_l T_l^{\mu\nu\rho\sigma} \quad \text{with} \quad T_l = \sum_{m=1}^{20} \gamma_{lm} \mathcal{T}_m^{\mu\nu\rho\sigma} \quad (2.29)$$

Since calculating the cross section involves the summation over the polarizations of the external gluons and Z-bosons, it is important to take their corresponding summation rules into account in the orthogonality relation that the tensors in the new basis should fulfill:

$$\sum_{\lambda_1, \lambda_2, \lambda_3, \lambda_4} \mathcal{E}_\mu^{\lambda_1} \mathcal{E}_\nu^{\lambda_2} \mathcal{E}_\rho^{\lambda_3} \mathcal{E}_\sigma^{\lambda_4} T_a^{\mu\nu\rho\sigma} \mathcal{E}_{\mu'}^{\lambda_1*} \mathcal{E}_{\nu'}^{\lambda_2*} \mathcal{E}_{\rho'}^{\lambda_3*} \mathcal{E}_{\sigma'}^{\lambda_4*} T_b^{*\mu'\nu'\rho'\sigma'} = c_a \delta_{ab} \quad (2.30)$$

The right hand side of equation (2.30) contains coefficients c_a that need not be one, since the new tensor basis is required to be orthogonal but not orthonormal. This choice was made in order to avoid the introduction of square roots of scalar products between the external momenta.

The gauge choice for the external particles that allows one to write down the amplitude in the simple form derived in section 2.2.2 dictates the polarization sums. For the gluons, they are given in Eqs. (2.18) and (2.19). The corresponding polarization sums for the Z bosons are given by

$$\sum_{\lambda_3} \mathcal{E}_\rho(\lambda_3, p_3) \mathcal{E}_{\rho'}^*(\lambda_3, p_3) = -g_{\rho\rho'} + \frac{p_{3,\rho} p_{3,\rho'}}{p_3 \cdot p_3}, \quad (2.31)$$

$$\sum_{\lambda_4} \mathcal{E}_\sigma(\lambda_4, p_4) \mathcal{E}_{\sigma'}^*(\lambda_4, p_4) = -g_{\sigma\sigma'} + \frac{p_{4,\sigma} p_{4,\sigma'}}{p_4 \cdot p_4}, \quad (2.32)$$

where the momenta p_3 and p_4 are on the mass shell and hence, $p_3 \cdot p_3 = p_4 \cdot p_4 = m_Z^2$ evaluates to the squared mass of the Z boson. Again, the momentum p_4 has to be expressed in terms of the other momenta according to Eq. (2.18).

The first element of the set of new orthogonal tensors $\tilde{T}_i = N_i T_i$, with normalization factors N_i , can be any one of the initial set of tensors \mathcal{T} . All subsequent additions are appended one by one with the algorithmic procedure known as the Gram-Schmidt orthogonalization:

$$\tilde{T}_i^{\mu\nu\rho\sigma} = \mathcal{T}_i^{\mu\nu\rho\sigma} - \sum_{j=1}^{i-1} \frac{\sum_{\lambda_1, \dots, \lambda_4} \mathcal{E}_\mu^{\lambda_1} \dots \mathcal{E}_\sigma^{\lambda_4} \tilde{T}_j^{\mu\nu\rho\sigma} \mathcal{E}_{\mu'}^{\lambda_1*} \dots \mathcal{E}_{\sigma'}^{\lambda_4*} \tilde{T}_i^{*\mu'\nu'\rho'\sigma'}}{\sum_{\lambda_1, \dots, \lambda_4} \mathcal{E}_\mu^{\lambda_1} \dots \mathcal{E}_\sigma^{\lambda_4} \tilde{T}_j^{\mu\nu\rho\sigma} \mathcal{E}_{\mu'}^{\lambda_1*} \dots \mathcal{E}_{\sigma'}^{\lambda_4*} \tilde{T}_j^{*\mu'\nu'\rho'\sigma'}} \tilde{T}_j^{\mu\nu\rho\sigma}. \quad (2.33)$$

Equation (2.33) ensures the requested orthogonality from Eq. (2.30) but not necessarily an optimal normalization for the new tensors $\tilde{T}_i^{\mu\nu\rho\sigma}$, which is why the normalization factors N_i were introduced. Already the arbitrariness in the choice for the starting tensor makes it clear that the resulting set of orthogonal tensors is not unique. The outcome depends directly on the order in which the old tensors are added to the new set. That means, there are $20! \approx 2 \cdot 10^{18}$ orthogonalization approaches and many of them lead to undesirably awkward and lengthy solutions. Here a lot of handwork is needed to find a good solution for the set

$$\tilde{T}_l^{\mu\nu\rho\sigma} = \sum_{m=1}^{20} \tilde{\gamma}_{lm} \mathcal{T}_m^{\mu\nu\rho\sigma} \quad (2.34)$$

with

$$\sum_{\lambda_1, \dots, \lambda_4} \mathcal{E}_\mu^{\lambda_1} \dots \mathcal{E}_\sigma^{\lambda_4} \tilde{T}_a^{\mu\nu\rho\sigma} \mathcal{E}_{\mu'}^{\lambda_1*} \dots \mathcal{E}_{\sigma'}^{\lambda_4*} \tilde{T}_b^{*\mu'\nu'\rho'\sigma'} = \tilde{c}_a \delta_{ab} + \mathcal{O}(\epsilon), \quad (2.35)$$

Where the $\mathcal{O}(\epsilon)$ term contains non-diagonal entries that vanish in the limit $\epsilon \rightarrow 0$. Some ‘goodness’ criteria that were used as guiding principles for finding the optimal order of the initial set and successfully orthogonalizing it to a useful new set were:

- Small size of the coefficients $\tilde{\gamma}_{lm}$
- Independence of $\tilde{\gamma}_{lm}$ of the dimension d
- Small number of prime factors in the set \tilde{c}_a

The first point is self explanatory. The second point is quite important since a tensor basis change that depends on $d = 4 - 2\epsilon$ can only be performed without loss of information if the amplitude is exact in d (or expanded sufficiently high in ϵ). Usually this is not the case and the amplitude is derived in an expansion in the dimensional regularization parameter ϵ . Therefore, a basis change that is independent of d or ϵ can be done at any stage of the calculation without requiring a higher expansion depth in ϵ . The last point has more aesthetic reasons and goes hand in hand with point one: For bad choices of the initial order of set $\mathcal{T}_i^{\mu\nu\rho\sigma}$ the coefficients $\tilde{\gamma}_{lm}$ can contain multiples of different prime numbers which

will result in possibly large factors in \tilde{c}_a that are just artifacts of the orthogonalization procedure and should be avoided.

Once a good candidate for an initial order that leads to a basis change that fulfills the ‘goodness’ criteria from above is found⁸ the basis change coefficients $\tilde{\gamma}_{lm} = N_l \gamma_{lm}$ from equation (2.35) are rescaled by the factors N_l such that the terms $c_l = \tilde{c}_l / N_l^2$ from Eq. (2.30) become as simple as possible:

$$c_1 = c_2 = 1 \quad \xrightarrow{d=4} \quad 1 \quad (2.36)$$

$$c_3 = c_4 = \dots = c_9 = d - 3 \quad \xrightarrow{d=4} \quad 1 \quad (2.37)$$

$$c_{10} = (d - 3)^2 \quad \xrightarrow{d=4} \quad 1 \quad (2.38)$$

$$c_{11} = c_{12} = p_T^2 m_Z^2 \quad \xrightarrow{d=4} \quad p_T^2 m_Z^2 \quad (2.39)$$

$$c_{13} = c_{14} = \dots = c_{18} = p_T^2 m_Z^2 (d - 3) \quad \xrightarrow{d=4} \quad p_T^2 m_Z^2 \quad (2.40)$$

$$c_{19} = c_{20} = 2(d - 3)(d - 4) \quad \xrightarrow{d=4} \quad 0 \quad (2.41)$$

Finally, using this new basis from Eq. (2.29) that already fulfills the orthogonality condition from Eq. (2.30) and is given explicitly in eqs. (A.2) to (A.21) in appendix A.2 allows for a very simple computation of the absolute square of the amplitude:

$$\sum_{\lambda_1, \dots, \lambda_4} |\mathcal{A}_{\text{ggZZ}}|^2 = \sum_{\lambda_1, \dots, \lambda_4} \mathcal{E}_\mu^{\lambda_1} \dots \mathcal{E}_\sigma^{\lambda_4} \mathcal{A}_{\text{ggZZ}}^{\mu\nu\rho\sigma} \mathcal{E}_{\mu'}^{\lambda_1*} \dots \mathcal{E}_{\sigma'}^{\lambda_4*} \mathcal{A}_{\text{ggZZ}}^{*\mu'\nu'\rho'\sigma'} = \sum_{l=1}^{20} c_l |\beta_l|^2 \quad . \quad (2.42)$$

It is interesting to note that in the limit of $d \rightarrow 4$, the contributions of the finite part of the form factors b_{19} and b_{20} to the cross section vanish according to Eq. (2.41). It is furthermore important to note that in principle, the coefficients c_i are $\epsilon = (4-d)/2$ dependent. However, after renormalization, the form factors α_k from Eq. (2.25) are finite (see section 2.3.6) and the coefficients c_i can be evaluated at $d = 4$. This means, that the non-diagonal terms from Eq. (2.35) vanish and Eq. (2.42) can safely be applied.

The tensor decomposition and their corresponding projectors derived in this section will be used in the next section where the computation of the amplitude, starting from the generation of Feynman diagrams, will be discussed in detail.

⁸The order used in this thesis is $i \in \{17, 18, 19, 20, 4, 5, 6, 7, 10, 11, 12, 13, 14, 15, 8, 9, 1, 2, 16, 3\}$ where the numbers i refer to the tensor in Eq. (2.25) accompanied by the coefficients α_i .

2.3. Amplitude

In this thesis, the process of Z boson pair production via gluon fusion will be considered in a perturbative expansion up to the second order in the strong coupling constant α_s and the first order in the electroweak coupling constant α . Since in the Standard Model the Z boson does not couple directly to gluons, there are no tree diagrams contributing to the process. Consequently the leading order, denoted throughout this thesis as LO, is proportional to $\alpha_s\alpha$ and starts already with a loop integral as shown in Fig. 2.2. Analogously, the next-to-leading order is proportional to $\alpha\alpha_s^2$ and will be referred to as NLO.

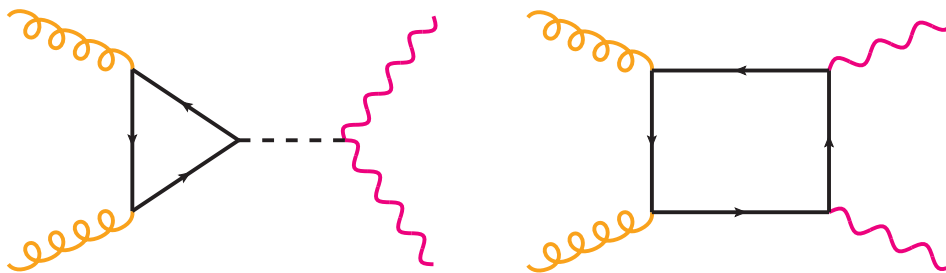


Figure 2.2.: Two of the eight Feynman diagrams that contribute at leading order to the process $gg \rightarrow ZZ$. Curly lines denote gluons, wavy lines Z bosons, dashed lines Higgs bosons and solid lines quarks. Throughout this thesis, only top quarks are considered. The diagrams of the left and right hand side are referred to as 'triangle' and 'box' type diagrams, respectively.

As already pointed out in the Introduction 2.1, calculating the $gg \rightarrow ZZ$ amplitude analytically at NLO with exact top quark mass dependence is currently not possible. Instead, the exact dependence on the top quark mass will be approximated in this work from two sides. First, in an asymptotic expansion in the limit that all scales are much smaller than the top quark mass, which is valid for small energies (denoted by LT as in "large top quark mass expansion") and, second, in an asymptotic expansion for high energies, where the top quark mass is small (denoted by ST as in "small top quark mass expansion"). As the explicit calculation follows a similar structure in both cases, it will be explained only once in this section. However, if there are differences they will be pointed out and highlighted for the two different limits.

2.3.1. General Layout of the Calculation

This subsection provides a quick overview of the steps that are needed to arrive at an analytic expression for the amplitude. It is the goal of this calculation to find the 20 form factors β_l in Eq. (2.29) analytically. Knowing these, they can be used together with the cross section coefficients c_l from eqs (2.36)-(2.41) to compute the squared amplitude from Eq. (2.42). Since the computation is quite demanding and requires a lot of computing power, it is advisable to split it into small parts that can be treated in parallel.

Starting from Feynman graphs whose generation will be discussed in section 2.3.2, generate 138 copies of each diagram $D_k^{\mu\nu\rho\sigma}$ where every copy is tagged by a symbol t_j and contracted

with one of the 138 simple tensors $\mathcal{T}_{j,\mu\nu\rho\sigma}$ given in appendix A.1. In this way, the open indices of the diagram D_k are contracted and all following quantities are scalar expressions. Replacing the symbol t_j by the j^{th} coefficient π_{ij} of the i^{th} projector $\Pi_{i,\mu\nu\rho\sigma}$

$$t_j = \pi_{ij} \quad (2.43)$$

and summing both over all contributing diagrams and the 138 simple tensors $\mathcal{T}_{j,\mu\nu\rho\sigma}$ the form factor a_i from Eq. (2.28) can be assembled at any point in the calculation:

$$a_i^{(n)} = \sum_{k=1}^{N_{\text{dia}}^{(n)}} \sum_{j=1}^{138} \pi_{ij} \mathcal{T}_{j,\mu\nu\rho\sigma} D_k^{(n),\mu\nu\rho\sigma} = \sum_{k=1}^{N_{\text{dia}}^{(n)}} \Pi_{i,\mu\nu\rho\sigma} D_k^{(n),\mu\nu\rho\sigma} . \quad (2.44)$$

Here, n is the loop order and $N_{\text{dia}}^{(n)}$ is the number of diagrams contributing to $gg \rightarrow ZZ$ at the order n . This approach of applying the projectors has several advantages: Instead of multiplying each diagram by a sum of 26 projectors with 138 tensors and their associated projector coefficients and thereby unnecessarily inflating the number of terms that have to be carried through every step of the calculation, the problem is split into $N_{\text{dia}}^{(n)} \times 138$ sub-problems. These sub-problems can be organized very easily and treated in parallel.

The calculation of the amplitude is performed for the most part with the help of FORM[29]. It is a computer algebra system that was designed especially for the kind of large-scale symbolic manipulations of expressions that appear in particle physics when calculating amplitudes. FORM can natively perform traces over gamma matrices and is in general much faster in processing huge expressions than other computer algebra systems like Mathematica or Maple but does only offer a comparably narrow range of functionalities. In this thesis, the multicore version TFORM-4.2[30]⁹ was used that allows to exploit the full potential of the computer cluster hosted at and maintained by the Institute for Theoretical Particle Physics (TTP) at the Karlsruhe Institute of Technology (KIT).

After generating the Feynman diagrams, they are translated into FORM-code and supplemented with the Dirac and color structure given by their corresponding Feynman rules. The color algebra is taken care of by the FORM package color[33], the Dirac algebra and traces over gamma matrices as well as simplifications of the rational functions in the variables appearing in intermediate results are performed directly in FORM.

Next, in the case of the large top quark mass expansion (LT), the asymptotic expansion is described in section 2.3.3. Then, both the LT and the ST result are obtained as a linear

⁹Many of the calculations performed in this thesis depend on the PolyRatFun implementation of TFORM that has major bugs in version 4.2, preventing the successful treatment of large rational functions [31]. To be more explicit, spurious division by zero appeared at random in a small fraction of the computations such that no reliable and reproducible result could be obtained. Therefore it was necessary to switch to an old commit of TFORM using the git version tool command `git reset --hard f766b04` after which this bug was presumably introduced.

It seems like the bug is related to a wrong ordering of the terms in a polynomial [32]. The PolyRatFun routines rely on this ordering when performing multiplications. If for whatever reason one of the polynomials is not ordered in the right way, the multiplication will give a wrong result which can also include division by zero - and goes unnoticed otherwise!

This can most likely be fixed by using the option `on_highfirst` which forces an ordering for all terms in every step and would allow to use the latest version of FORM.

combination of a large number of scalar integrals. These are reduced to a set of so-called master integrals in section 2.3.4 and solved in section 2.3.5 where, in the (LT) case all integrals are known and in the high energy case (ST), an asymptotic ansatz is employed. Finally, after inserting the solutions for the master integrals, the amplitude is renormalized in section 2.3.6 and the 26 finite form factors a_i from Eq. (2.24) can be extracted according to Eq. (2.44). The last step combines the 26 form factors a_i into the 20 form factors α_i from Eq. (2.25) which can then be rewritten in terms of the form factors β_i in the orthogonal basis following Eq. (2.29), where the basis change relations are given in appendix A.2.

2.3.2. Feynman Graph Generation

The number of Feynman diagrams needed for the process $gg \rightarrow ZZ$ at the first two orders in the perturbation series is still $\mathcal{O}(100)$. It is however still profitable to generate them in a systematic and automated way in order to minimize manual interaction, avoiding additional sources for errors due to forgotten symmetry factors etc. There are several tools available for this step and one of the most commonly used is QGRAF [34].

This FORTRAN program takes as an input a Lagrangian which is given in form of a list of allowed propagators and vertices together with a list of incoming and outgoing particles as shown in figure 2.3 and returns a list of Feynman diagrams in a computer readable format suited for further treatment. Throughout this thesis all Feynman diagrams contributing to any amplitude were generated automatically with QGRAF3.3.

QGRAF-1: Input Lagrangian 'lag'

```

1 * propagators
2 [ftq,ftq,-]
3 [h,h,+]
4 [z,z,+]
5 [g,g+,notadpole]
6 [c,C,-]
7 [sigma,sigma+,notadpole]
8 * vertices
9 [fTq,ftq,g; tag = '0']
10 [g,g,sigma; tag = '0']
11 [fTq,ftq,h; tag = '1']
12 [fTq,ftq,z; tag = '1']
13 [g,g,g; tag = '0']
14 [C,c,g; tag = '0']
15 [z,z,h; tag = '1']

```

QGRAF-2: Config File

```

1 output = 'diagrams.out' ;
2 style = 'q2e.sty' ;
3 model = 'lag' ;
4 in = g,g ;
5 out = z,z ;
6 loops = 2 ;
7 loop_momentum = k ;
8 options = onshell ;
9 true = bridge[g,0,0] ;
10 true = bridge[sigma,0,0] ;
11 true = iprop[h,0,1] ;
12 true = iprop[z,0,0] ;
13 true = vsum[tag,2,2] ;

```

Figure 2.3.: QGRAF input and config files for the process $gg \rightarrow ZZ$. Please refer to the QGRAF documentation [34] for syntax details.

Figure 2.3 shows the QGRAF input files used to generate the Feynman diagrams for $gg \rightarrow ZZ$. The program essentially computes the combinatorics of generating all possible ways two gluons can generate two Z bosons the provided propagators and vertices allow, and

supplements them with symmetry factors and the correct signs due to commutation relations.

However, in order not to produce diagrams that contribute at lower or higher order in the electroweak coupling constant α than what is considered here, it is necessary to ‘tag’ the corresponding electroweak vertices and require in the QGRAF config file that every diagram that is produced must contain exactly such vertices (see the highlighted parts in lines 9-15 of QGRAF-1 and line 13 of QGRAF-2 in fig. 2.3). Line 9 of the config file in fig. 2.3 prevents the generation of double triangle diagrams at two loops. These diagrams are in some sense no true two loop diagrams, since they can be decomposed into products of the one-loop $gg \rightarrow Z$ form factor which is known exactly in m_t [27, 28] and therefore not considered in this thesis.

Running QGRAF with the settings above for $gg \rightarrow ZZ$ generates 8 Feynman diagrams at LO, of which a sample of two diagrams is shown in fig 2.2. At NLO, there are 118 Feynman diagrams. Also for these, some representative example diagrams are collected in fig. 2.4.

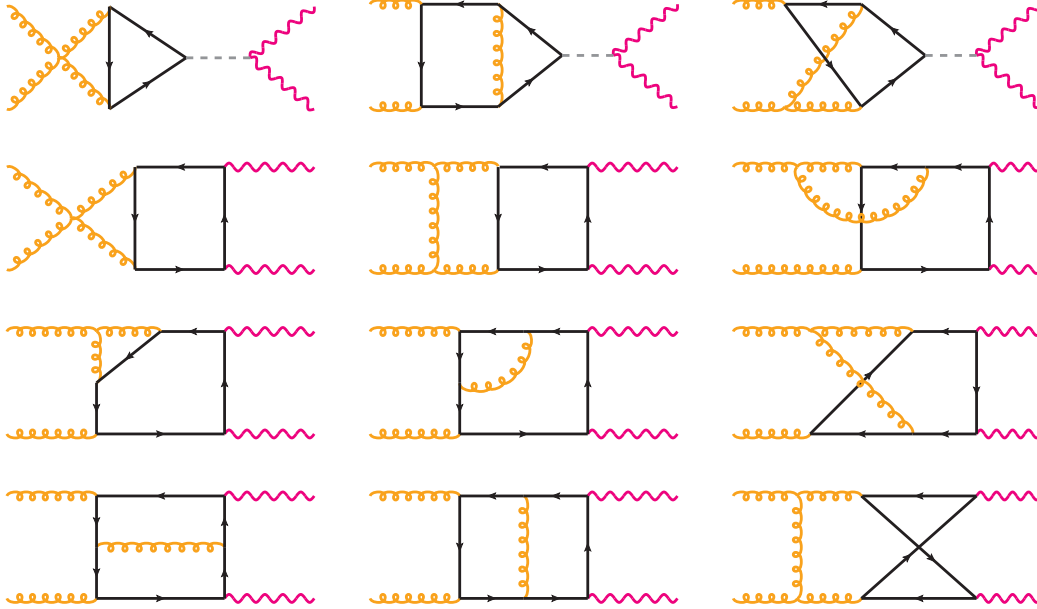


Figure 2.4.: Some representative diagrams that contribute at NLO to the process $gg \rightarrow ZZ$.

2.3.3. Asymptotic Expansion

Calculating Feynman diagrams that contribute to $gg \rightarrow ZZ$ means solving many $d = 4 - 2\epsilon$ -dimensional integrals that depend on the momenta of the external particles, their masses and the masses of the propagating internal particles. In case of $gg \rightarrow ZZ$, with all external particles on-shell, the corresponding set of variables is given by the space-time dimension d , the Mandelstam variables¹⁰ s and t , the Z boson mass m_Z and the top quark mass m_t . Here, the Higgs boson mass m_H is not listed since it appears only in diagrams of the triangle type shown on the left hand side of Fig. 2.2 as a factorized propagator $1/(s - m_H^2)$

¹⁰See eqs. (2.3)-(2.7).

and it is never involved in any loop integration. Calculating such integrals analytically keeping dependence on all scales is very hard.

However, one can approach the problem from the perspective of very high or low energies; in the limit of small centre-of-mass energies \sqrt{s} (LT-case) the mass of the top quark is much larger than any other energy scale and the integrals can be solved in an expansion in the small ratio

$$\frac{s}{4m_t^2} \ll 1, \quad (2.45)$$

whereas in contrast in the limit of large centre-of-mass energies \sqrt{s} (ST-case) the inverse ratio becomes small and can be used as an expansion parameter

$$\frac{4m_t^2}{s} \ll 1. \quad (2.46)$$

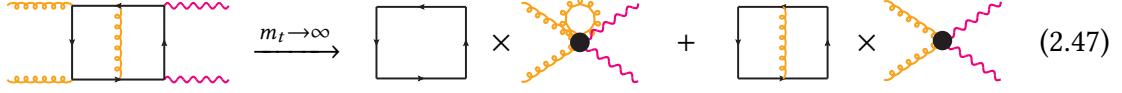
The theoretical framework for consistently expanding Feynman integrals in these limits is called asymptotic expansion [35–37]. Whereas for the (ST) case of high energies the opportunity to apply these expansions presents itself at a much later stage in the calculation by means of a certain ansatz in solving the differential equations for the master integrals (see section 2.3.5), this is different for the low energy (LT) case. Here, the advantage of the asymptotic large top mass expansion procedure is that it can be applied very early and prior to integration, directly manipulating the integrands. The general idea is algorithmic and works on a diagrammatic level:

1. Identify for each diagram all possible subgraphs that include all ‘hard’ lines (meaning in this case all top quark propagators) and that are also one-particle-irreducible with respect to cutting light lines (meaning in this case gluon propagators). The graph that remains after contracting all lines of the subgraph to a point is called the co-subgraph. Replace the initial Feynman diagram by a sum over the pairs of subgraphs and associated co-subgraphs.
2. Expand the subgraphs in the small quantities, i.e. in the ratios of the external momenta to the top quark mass and evaluate the resulting integrals. Insert the result of the integration as an effective vertex into the corresponding co-subgraph.

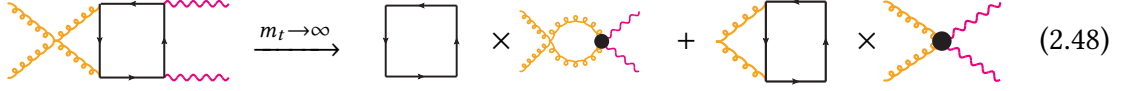
The procedure described above is implemented in FORM in the programs q2e and exp [38, 39]. First, q2e maps the Feynman diagrams produced by QGRAF to integral families in notation which exp can process and exp performs the asymptotic expansion in the large top quark mass. The resulting expressions are then supplemented with the color factors and gamma matrices given by the Feynman rules and treated in TFORM.

Subsequently, all emerging subgraph integrals from step 2 are mapped to massive one- and two-loop tadpole integrals. This type of integral can be integrated by means of the FORM program MATAD[40]. The remaining integrals in the amplitude are now much simpler since they do not depend on the top quark mass anymore. Considering that in this thesis the process $gg \rightarrow ZZ$ is calculated only up to order $\alpha\alpha_s^2$ implies that the propagators in the remaining integrals have to be gluon propagators. Therefore, in the LT case, the only

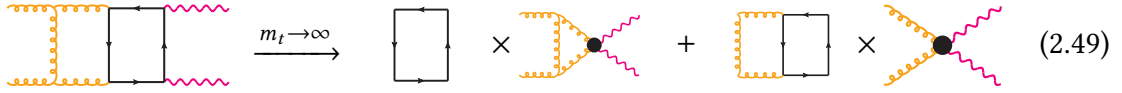
types of integrals that are left over after the application of the asymptotic expansion in the large top quark mass are one-loop massless propagator and triangle type integrals.



$$(2.47)$$



$$(2.48)$$



$$(2.49)$$

Figures 2.47-2.49 demonstrate how the procedure works. Each of the three two loop diagrams splits into a sum of two subgraphs and their associated co-subgraphs. The subgraphs can be mapped to one- and two-loop tadpole integrals. The co-subgraphs that come together with a one-loop tadpole are either scaleless tadpoles that evaluate to zero like in Eq. (2.47), massless propagator type integrals as in Eq. (2.48) or massless triangle type integrals, shown in Eq. (2.49). The reduction of such remaining integrals to a small set of master integrals is the topic of the next subsection.

2.3.4. Reduction to Master Integrals

Reduction of the scalar integrals

In the high energy case (ST), every product $D_{jk}^{(n)} = \mathcal{T}_{j,\mu\nu\rho\sigma} D_k^{(n),\mu\nu\rho\sigma}$ of one of the simple tensors from appendix A.1 with a n -loop Feynman diagram contributing to the amplitude $\mathcal{A}_{ggZZ}^{\mu\nu\rho\sigma}$ (see section 2.3.1) can, after contracting indices, applying Dirac algebra and taking traces, be written as a sum over scalar, multidimensional integrals $\mathcal{I}^{(n)}$

$$D_{jk}^{(1)} = \mathcal{T}_{j,\mu\nu\rho\sigma} D_k^{(1),\mu\nu\rho\sigma} = \sum_{l=1}^{210} D_{jkl}^{(1)}(d, s, t, m_t, m_h, m_Z) \mathcal{I}_l^{(1)}(d, s, t, m_t, m_Z) \quad (2.50)$$

$$D_{jk}^{(2)} = \mathcal{T}_{j,\mu\nu\rho\sigma} D_k^{(2),\mu\nu\rho\sigma} = \sum_{l=1}^{37779} D_{jkl}^{(2)}(d, s, t, m_t, m_h, m_Z) \mathcal{I}_l^{(2)}(d, s, t, m_t, m_Z) , \quad (2.51)$$

where every integral $\mathcal{I}_l^{(n)}$ can be mapped to one of 3 one-loop and 34 two-loop integral families given in the appendices A of [41] and [42]. The large number of $\mathcal{O}(40,000)$ integrals to perform presents a problem. Furthermore, many of the integrals $\mathcal{I}_l^{(n)}$ contain denominators or numerators that are raised to high powers which makes their computation complicated. On the other hand, the set of integrals is not linearly independent. Thus, it is possible to find a basis of only a few integrals, so-called ‘master integrals’. One can then write any of the integrals $\mathcal{I}_l^{(n)}$ as a linear combination of these so-called master integrals.

The task of computing a large number of integrals is thereby reduced to finding a solution to only a few master integrals.

There exists an algorithmic procedure to find this decomposition into master integrals called the Laporta algorithm [43]. It makes use of the technique of integration by parts [44, 45] to derive relations between the individual integrals and subsequently solves the generated system of equations in a way, that reduces the powers of the propagators and numerators that appear in the integrals.

For the process $gg \rightarrow ZZ$ this is quite cumbersome since there are many scales involved as every integral depends on d, s, t, m_t and m_Z . In order to make the whole calculation feasible, the integrals and their coefficients are expanded in the small quantity $m_Z^2/m_t^2 \approx 0.277$

$$D_{jk}^{(1)} = \sum_{l_0=1}^{210} \tilde{D}_{jkl_0}^{(1)} \tilde{I}_{l_0}^{(1)} + \left(\frac{m_Z^2}{m_t^2}\right)^1 \sum_{l_2=1}^{392} \tilde{D}_{jkl_2}^{(1)} \tilde{I}_{l_2}^{(1)} + \left(\frac{m_Z^2}{m_t^2}\right)^2 \sum_{l_4=1}^{728} \tilde{D}_{jkl_4}^{(1)} \tilde{I}_{l_4}^{(1)} + \mathcal{O}\left(\frac{m_Z^2}{m_t^2}\right)^3 \quad (2.52)$$

$$D_{jk}^{(2)} = \sum_{l_0=1}^{37779} \tilde{D}_{jkl_0}^{(2)} \tilde{I}_{l_0}^{(2)} + \left(\frac{m_Z^2}{m_t^2}\right)^1 \sum_{l_2=1}^{169748} \tilde{D}_{jkl_2}^{(2)} \tilde{I}_{l_2}^{(2)} + \left(\frac{m_Z^2}{m_t^2}\right)^2 \sum_{l_4=1}^{572063} \tilde{D}_{jkl_4}^{(2)} \tilde{I}_{l_4}^{(2)} + \mathcal{O}\left(\frac{m_Z^2}{m_t^2}\right)^3, \quad (2.53)$$

where the m_Z dependence is factored out explicitly and the integrals $\tilde{I}_l^{(n)}$ ¹¹ and their coefficients $\tilde{D}_{jkl}^{(n)}$ depend only on d, s, t and m_t ¹². Computing the reduction of the integrals is now much easier. However there is a trade off since the number of integrals to be reduced is also significantly higher. In this thesis, the expansion in the Z boson mass was performed in the computer algebra system Mathematica12 [46] using the package LiteRed [47, 48]. Including the first three terms in the expansion in the Z boson mass increases the total number of scalar integrals at LO and NLO to more than 780.000.

The reduction itself was performed on family-by-family basis using the latest development version FIRE6.3.dev[49] of the C++ program FIRE [50] which is a fast implementation of the Laporta algorithm mentioned above. Using additional information on symmetries of the problem that can be generated with the help of LiteRed, the FIRE reduction gets a considerable speedup [51, 52]. Moreover, the newest version of FIRE makes use of parallelization on various levels such that the reduction to master integrals of the most difficult family took less than 5 days and used less than 200 GB of RAM on one of the high performance servers of the TTP computer cluster with two Intel[®] Xeon[®] Gold 6144 CPUs providing 32 threads at a maximum frequency of 4.2 GHz. Fig. 2.5 shows the configuration file used for the reduction of the family mentioned above. Note the usage of the `lbases` and `sbases` from LiteRed.

The Laporta algorithm implemented in FIRE reduces the number of integrals to a small set of supposed master integrals which is, however, unfortunately not minimal. In this thesis, the FIRE reduction mapped the 780920 input integrals $\tilde{I}_l^{(n)}$ to 1244 ‘pseudo master integrals’ which is a gain factor of more than 600.

¹¹Note, that for the new integrals Eq. (2.7) changes to $s + t + u = 0$.

¹²Note, that up to now, the amplitude is still exact in m_t .

```

FIRE6.3.dev-1: 91.config
1 #fermat      FIRE6/extra/ferl64/fer64
2 #threads    32
3 #fthreads   s128
4 #lthreads   32
5 #variables  d,s,t,mts
6 #pos_pref   -1
7 #database   /nvme01
8 #bucket     30
9 #start
10 #problem    91 litered/v91.sbases
11 #lbases    litered/v91.lbases
12 #preferred  91.preferred
13 #integrals  91.intlist
14 #output     91.tables.m

```

Figure 2.5.: Exemplary FIRE config file for the process $gg \rightarrow ZZ$ of family number 91. Please refer to the FIRE documentation [49] for syntax details.

Minimalizing the set of master integrals

The resulting set of more than a thousand 'pseudo master integrals' is however not a minimal set as there are for example many pseudo master integrals that appear under different notation in different integral families but that are actually the same integral:

$$G_6(1, 1, 2, 1, 1, 1, 1) \equiv G_6(1, 1, 1, 1, 1, 2, 1) \quad \text{or} \quad G_{11}(0, 1, 1, 0, 1, 1, 2, 0, 0) \equiv G_{91}(1, 0, 2, 0, 1, 1, 1, 0, 0)$$

The first step on the way to a minimal set of true master integrals is to find these equivalent pseudo master integrals, choose one of them as a master integral and replace the other, differently named occurrences by it. This can be done using the FIRE command `FindRules[]` which re-expresses integrals in the notation independent, unique form of the so called alpha representation. This allows then to easily identify equivalent integrals and reduce the number of pseudo master integrals by roughly a factor five to 241 of which 10 are LO integrals and 231 are NLO integrals.

In a second step, one can apply the `FindRules[]` command already on the initial set of scalar integrals¹³, apply subsequently the reduction and finally `FindRules[]` again. Since `FindRules[]` maps only equivalent integrals from within the given set of integrals, only a subset of the full reduction rules is needed. One can then compare the resulting sets of

¹³Actually, the initial set was systematically extended by additional integrals with contracted lines and a different 'dot-distribution'. Then all integrals with a sum of their propagator powers larger than 8 were discarded. See Ref. [41] for more details.

reduced integrals from step one and step two which should – in case of an ideal reduction procedure – be equivalent. If subtracting both results gives a nonzero expression, the set of pseudo master integrals is not minimal and one can use these additional relations to eliminate further pseudo master integrals. In this way, 70 additional remappings could be identified and all integrals were mapped to the minimal set of 171 = 10 at LO + 161 at NLO master integrals from Ref [42] which represents a gain factor of more than 4500 compared to the $O(780,000)$ integrals at the beginning. Thus, Eqs. (2.52) and (2.53) can be written as

$$D_{jk}^{(1)} = \sum_{l=1}^{10} \left(\widehat{D}_{jkl}^{(1)} + \left(\frac{m_Z^2}{m_t^2} \right)^1 \widehat{D}_{jkl}^{(1)} + \left(\frac{m_Z^2}{m_t^2} \right)^2 \widehat{D}_{jkl}^{(1)} + \mathcal{O} \left(\frac{m_Z^2}{m_t^2} \right)^3 \right) M_l^{(1)} \quad (2.54)$$

$$D_{jk}^{(2)} = \sum_{l=1}^{161} \left(\widehat{D}_{jkl}^{(2)} + \left(\frac{m_Z^2}{m_t^2} \right)^1 \widehat{D}_{jkl}^{(2)} + \left(\frac{m_Z^2}{m_t^2} \right)^2 \widehat{D}_{jkl}^{(2)} + \mathcal{O} \left(\frac{m_Z^2}{m_t^2} \right)^3 \right) M_l^{(2)}. \quad (2.55)$$

Insertion of the reduction tables

In order to realize these mappings, all lookup tables from the FIRE output have to be processed which is nearly as computationally expensive as computing them in the first place. The combined size of all 37 families amounts to slightly less than 50 GB. The existing Mathematica routines are not able to handle these files since Mathematica was never designed to do algebraic manipulations to the enormous extent that appears in those expressions. For this purpose, a new Mathematica routine was written that divides and parallelizes the tasks on several levels and manages to process the hardest family in less than a day. The resulting reduction table entries of the form

$$\widehat{I}_k^{(1)} = \sum_{l=1}^{10} m_l M_l^{(1)} \quad \text{and} \quad \widehat{I}_k^{(2)} = \sum_{l=1}^{161} m_l M_l^{(2)}, \quad (2.56)$$

where the m_l are rational polynomials in s , t , m_t and ϵ , have to be transformed to FORM readable id statements in order to apply them to the diagrams $D_{jk}^{(n)}$ and thereby to the amplitude, respectively. However, applying just a normal list of replacements would mean, that in average nearly 400,000 integral comparisons would have to happen until the right replacement is found. Since the amplitude itself, after the expansion in m_Z at NLO, is a file of more than 100 GB composed of more than $1.3 \cdot 10^9$ terms, this would be a major bottleneck in the calculation. Instead, the reduction relations (2.56) are compiled into a so-called tablebase which allows for a much faster lookup and insertion [53]¹⁴.

In the LT case, the massless one-loop triangle, propagator and tadpole integrals were mapped to the topD0111 topology from chapter 3.5.1 in [54] such that the existing reduction tables (taken from [54]) could be reused to perform the reduction to masters.

¹⁴Putting /formswap directly in RAM (/dev/shm) highly reduces the creation time for large tablebases.

2.3.5. Calculation of the Master Integrals

Starting with the LT case, there are two types of integrals in the problem; massless form factor integrals and massive one- and two-loop tadpole integrals (see the discussion in section 2.3.3). The former could all be reduced to the massless one-loop two-point function which is e.g. given in appendix A.7 of [55]. The latter were treated with the FORM program MATAD[40] which has solutions for all massive tadpole integrals up to three loops implemented in terms of Gamma functions and their associated ϵ -expansion.

For the ST case, all integrals could be mapped to the 10 LO and 161 NLO master integrals that were calculated in Refs. [41, 42, 56]. For completeness, this subsection is intended to sketch in short the computation of these 171 integrals in the high energy expansion.

Computing the master integrals

The final set of master integrals $M_l^{(n)}$ from Eq. (2.56) consists of 10 integrals at LO and 161 integrals at NLO, of which 131 are planar and 30 are non-planar. Their explicit form is given in appendix A.3. The master integrals are functions of the dimensional regularization parameter ϵ , the top quark mass m_t and the Mandelstam variables s and t . The exact calculation of such massive two-loop four point functions is difficult and continues to be a topic of ongoing research.¹⁵ However, since the goal is to obtain a high-energy expansion of these master integral, it is not necessary to compute them with the exact dependence on all scales. Instead, one can make use of the high energy requirement

$$m_t^2 \ll s, |t| \quad (2.57)$$

and use the ansatz¹⁶

$$M_l^{(n)}(s, t, m_t, \epsilon) = \sum_{ijk} C_{l,ijk}^{(n)}(s, t) \epsilon^i (m_t)^j \log^k(m_t^2) \quad , \quad n \in \{\text{LO, NLO}\} \quad (2.58)$$

where the dependence on both the top quark mass m_t and the dimensional regularization parameter ϵ is made explicit such that the coefficients $C_{l,ijk}$ depend only on s and t . Furthermore one can set, for example, $s = 1$ and reconstruct the s dependence later from dimensional analysis which means that the coefficients $C_{l,ijk}^{(n)}$ essentially depend only on one variable. Note, that this ansatz allows also odd powers in m_t .

The master integrals are solved using the method of differential equations [62, 63], where the vector of master integrals \vec{M} is differentiated with respect to one of the three kinematic variables s , t and m_t using the Mathematica program LiteRed. The resulting expression is again reduced to the same master integrals such that one obtains three coupled systems of first order differential equations

$$\frac{d}{dx} \vec{M} = D(s, t, m_t, \epsilon) \vec{M} \quad \text{with} \quad x \in \{s, t, m_t\} \quad . \quad (2.59)$$

¹⁵See for example ref. [57–60].

¹⁶For further reading, the ansatz from Eq. (2.57) is discussed in Ref. [56] where it is shown, that by using the method of expansion by regions [37, 61], all integrals can be derived from a few template integrals that show a direct dependence on the top quark mass to some power including the dimensional regularization parameter ϵ . Hence, all further derivatives of these 'template' integrals can therefore be written in terms of powers and logarithms of m_t .

Since the ansatz in Eq. (2.58) provides all m_t dependence in an explicit way, the differential equation in m_t transforms actually to a simple system of linear equations. This means, that once the coefficients $C_{l,ij_0k}^{(n)}$ that come with the leading order j_0 in m_t are known, one can in principle compute as many further terms in m_t with $j > j_0$ as desired or computationally manageable just by solving the system of linear equations in m_t , order by order.

Any solution found for the master integrals has then to satisfy the up-to-then unused differential equation in s , which serves in that way as a cross check.

There are several possible ways how to compute the boundary conditions in form of the t -dependent coefficients $C_{l,ij_0k}^{(n)}$. One could for example solve the master integrals for a simple choice of s and t (e.g. $s = 1, t = 1$) and use the result as a boundary condition for solving the differential equation in t . Doing this, one obtains results in terms of polylogarithms that can be rewritten in terms of harmonic polylogarithms [64].

Instead, the method of expansion by regions [61, 65] was used in Ref. [56] to derive the boundary conditions: When integrating over loop momenta of Feynman diagrams with multiple lines, there are momentum configurations, where one propagator carries much more momentum than all other propagators in the diagram and is therefore referred as 'hard', whereas in comparison, the momenta of the other propagators are small and called 'soft'. One can make use of this configuration and expand the integrand in ratios, that are small in this special momentum configuration region. The resulting integral is then less complex and can be solved more easily.

The method of expansion by regions identifies all possible momentum configuration regions and allows to rewrite an integral as a sum of as many copies of the same integral as there are different regions where however each integrand is expanded in the quantities that are small in their corresponding region, including m_t , which – due to Eq. 2.57 is always considered 'soft'. It was applied to the master integrals using the Mathematica program `asy.m`. The resulting integrals are given in the limit $m_t \rightarrow 0$ and can be expressed as multifold Mellin-Barnes (MB) integrals (see for example Ref. [55] for an introduction) that still contain the exact t dependence. Here, the Mathematica packages `MB.m` [66] and `MBresolve.m` [67] can be used together for both analytic manipulation of the integrals and their numerical solution. Note that, together with recently developed MB integration techniques from Ref. [56], they were key ingredients for solving the master integrals.

As one is interested in the coefficient $C_{l,ij_0k}^{(n)}$ only, it is sufficient to compute the coefficients of the leading terms in m_t ¹⁷. Furthermore, since the solutions of the integrals are known to be expressible in terms of harmonic polylogarithms, one can Taylor expand the integrand around $t = 0$ by taking a series of residues and compare coefficients with the same Taylor expansion of a general linear combination of harmonic polylogarithms including up to weight 6. Intermediate integrals that are t independent can be evaluated numerically with high precision and their analytic form be reconstructed with the help of the PSLQ algorithm [68] on the basis of up to weight 6 products from the elements of

$$\{1, \log(2), \pi^2, \zeta_3, \pi^4, \text{Li}_4(1/2), \zeta_5, \text{Li}_5(1/2), \pi^6, \text{Li}_6(1/2), S_{3,3}(-1)\} .$$

¹⁷For 9 integrals, also the next-to-leading terms in the m_t series were needed as boundary condition for the linear system of equations in m_t .

Analytic continuation

For computing the master integrals above it is in some cases beneficial to assume for the involved variables certain kinematical configurations. Some of these might be unphysical like the choice $s < 0$, yet they can, for example, render an integrand real-valued and reduce thereby calculational complexity in intermediate steps. On the other hand it is very cumbersome to work with results containing functions that exhibit branch cuts and need small imaginary additions in their variables that are of the form $-i0^+$ or similar.

In order to avoid this, all results have been analytically continued to the physical region

$$s > 0 \quad , \quad t < 0 \quad , \quad u < 0 \quad (2.60)$$

and all logarithms and harmonic logarithms have been written as functions of dimensionless combinations of variables that yield for all physically allowed phase space points only real values. As a consequence, all results in this thesis have an explicit imaginary part and can at any point be evaluated to arbitrary precision without ever possibly running into numerical instabilities due to '0+' problems.

Furthermore, all harmonic polylogarithms (HPLs) have been rewritten such, that they have only positive indices. This reduced the number of different functions in the expressions for the master integrals from 93 to 15. After the insertion of the master integrals into the amplitude, only six weight four HPLs

$$H_2\left(-\frac{t}{s}\right) \quad , \quad H_3\left(-\frac{t}{s}\right) \quad , \quad H_4\left(-\frac{t}{s}\right) \quad , \quad H_{22}\left(-\frac{t}{s}\right) \quad , \quad H_{21}\left(-\frac{t}{s}\right) \quad , \quad H_{211}\left(-\frac{t}{s}\right) \quad , \quad (2.61)$$

which can be expressed in terms of polylogarithms (see appendix A.3) and three logarithmic functions remain

$$\log\left(-\frac{t}{s}\right) \quad , \quad \log\left(\frac{s+t}{s}\right) \quad , \quad \log\left(\frac{m_t^2}{s}\right) \quad . \quad (2.62)$$

Both the numerical evaluations of the HPLs and the analytic transformations in this thesis were done with the help of the Mathematica package HPL [69, 70].

Master integral cross checks

Using the methods outlined above, all 10 LO and 161 NLO master integrals could be computed up to and including $\mathcal{O}(m_t^{32})$ ¹⁸. They are available from Ref. [42]. One important check of the results is provided by the master integrals that were computed for the process $gg \rightarrow Hg$ in Ref. [71] up to $\mathcal{O}(m_t^2)$. In the mutual overlap of the two different bases of master integrals, both sets are in full agreement up to the given order in ϵ and m_t . Furthermore, every integral has been cross checked numerically using two different programs, FIESTA [72] and pySecDec [73]. Also here full agreement was found in the region, where the high energy expansion converges.

The upper panel of Fig. 2.6 shows the imaginary part of of the ϵ^0 contribution one of the 30 non-planar 2-loop master integrals at a scattering angle of $\theta = \pi/2$, rescaled by

¹⁸The actual expansion depth in m_t depends on the amplitude, such that for integrals that are accompanied by a m_t^{-2} pole from the amplitude have to be computed up to m_t^{34} etc.

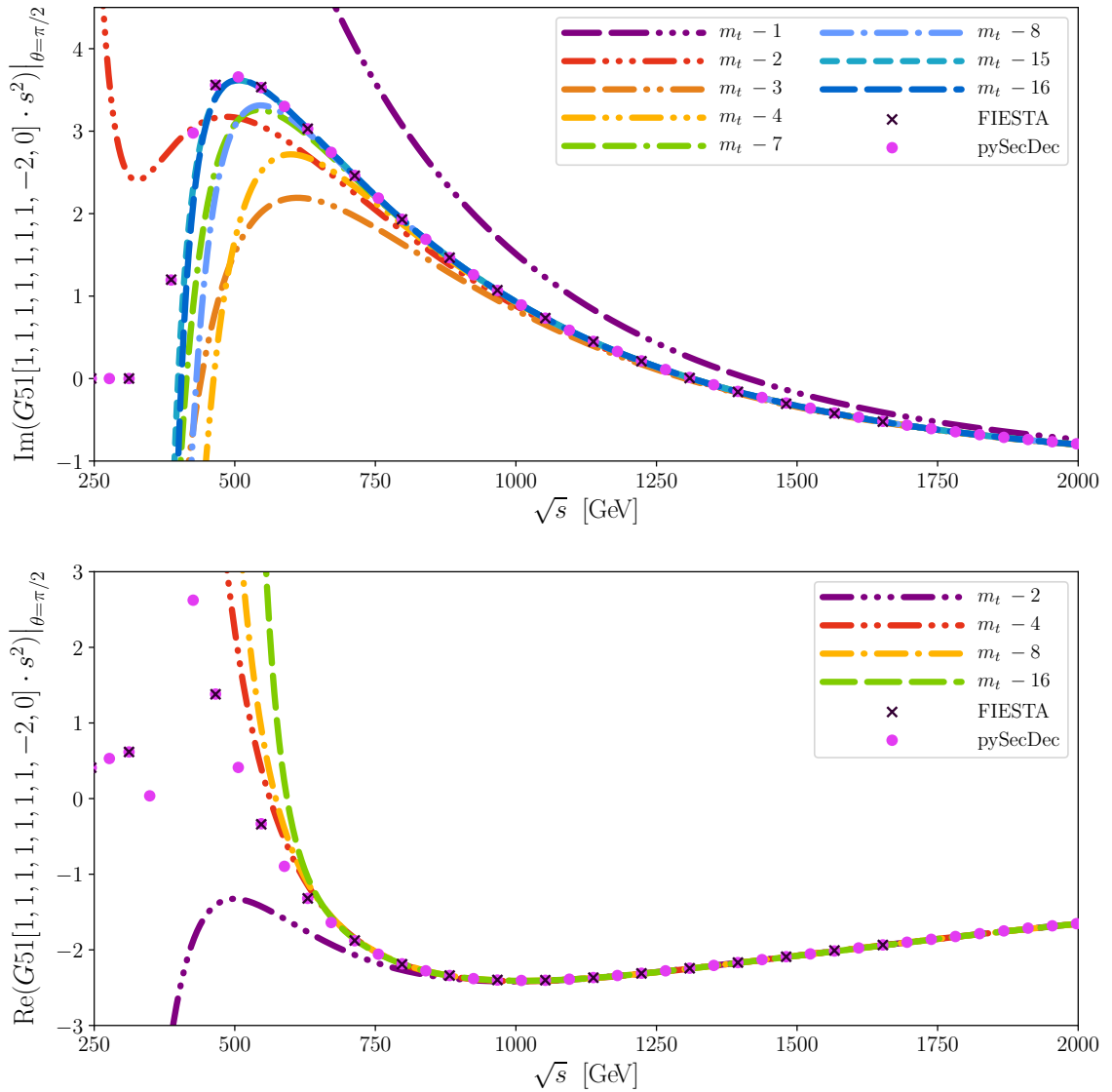


Figure 2.6.: Upper panel: Imaginary part of the ϵ^0 contribution of the non-planar master integral $G_{51}(1, 1, 1, 1, 1, 1, 1, -2, 0)$, rescaled with s^2 . High energy expansions are shown as dash-dotted lines, exact numerical evaluations of FIESTA and pySecDec as crosses and dots. Lower panel: Real part of the ϵ^0 contribution of the non-planar master integral $G_{51}(1, 1, 1, 1, 1, 1, 1, -2, 0)$, rescaled with s^2 . High energy expansions are shown as dash-dotted lines, exact numerical evaluations of FIESTA and pySecDec as crosses and dots.

a factor s^2 . One needs to stress here, that only the non-planar 2-loop integrals exhibit odd powers in m_t and that they come only in the imaginary part of the masters. The numerical impact of these terms is non-negligible as can be seen from different expansion depths in m_t . Only once these odd contribution are included one finds agreement with the numerical calculation of both pySecDec and FIESTA. It is interesting to note, that the odd power contributions first worsen the reproduction of the exact result and only

their combination with the following even power gives a good description of the exact result. This suggests, that one should always combine an even m_t^{2n} contribution with the corresponding m_t^{2n-1} odd contribution. This observation will be used later, for the construction of Padé approximants. For completeness, the Figure 2.6 shows in its lower panel also the corresponding real part of the same integral. Here, no odd terms contribute and one observes good agreement between the numerical calculations of FIESTA and pySecDec with the high energy expansion down to $\sqrt{s} \approx 700$ GeV.

2.3.6. Renormalization

In this thesis, both infrared (IR) and ultraviolet (UV) divergences are regularized in dimensional regularization with the shifted dimension

$$d = 4 - 2\epsilon . \quad (2.63)$$

Therefore, all integrals are carried out in d dimensions or, to be more explicit, in an expansion in the small regularization parameter ϵ around zero. The term ‘finite result’ refers in the following to results that do not diverge when the physical number of dimensions 4 is recovered by performing the limit

$$d \xrightarrow{\epsilon \rightarrow 0} 4 . \quad (2.64)$$

For the process $gg \rightarrow ZZ$, the amplitude is finite at LO and both UV- and IR-poles appear first starting from NLO. The UV-poles are treated by renormalizing¹⁹ the strong coupling constant α_s in the $\overline{\text{MS}}$ scheme via the multiplicative renormalization constant $Z_{\alpha_s}^{\overline{\text{MS}}}$

$$\alpha_s^{\text{bare}} = Z_{\alpha_s}^{\overline{\text{MS}}} \alpha_s \quad \text{with} \quad Z_{\alpha_s}^{\overline{\text{MS}}} = 1 - \left(\frac{\alpha_s}{\pi} \right) \frac{\beta_0}{\epsilon} + \mathcal{O}(\alpha_s^2) , \quad (2.65)$$

where $\beta_0 = \frac{11}{12}C_A - \frac{1}{3}T_R n_f$ is the coefficient of the beta function with $T_R = \frac{1}{2}$, the number of fermions n_f and the color factor $C_A = 3$. The second source of UV-divergences is treated by the top quark mass renormalization in the on-shell scheme with the multiplicative renormalization constant $Z_{m_t}^{\text{OS}}$

$$m_t^{\text{bare}} = Z_{m_t}^{\text{OS}} m_t \quad \text{with} \quad Z_{m_t}^{\text{OS}} = 1 - \left(\frac{\alpha_s}{\pi} \right) C_F \left(\frac{\mu^2}{m_t^2} \right)^\epsilon \left(\frac{3}{4\epsilon} + 1 \right) + \mathcal{O}(\alpha_s^2, \epsilon) , \quad (2.66)$$

where μ is the renormalization scale.

The remaining ϵ -poles cancel against the IR-divergent contributions of the real corrections to the process. Since in this thesis only virtual corrections are considered these poles need to be subtracted differently. In ref. [75] the general pole structure of QCD on-shell amplitudes is predicted such that, without computing the real corrections, one can still produce an IR-finite virtual amplitude as

$$\mathcal{A}_{\text{ggzz}}^{\text{NLO}, \text{Vfin}} = \mathcal{A}_{\text{ggzz}}^{\text{NLO}}|_{\text{UV-finite}} + C_{gg} \mathcal{A}_{\text{ggzz}}^{\text{LO}} . \quad (2.67)$$

¹⁹A thorough introduction to the topic of renormalization is given for example in [74].

where in this thesis C_{gg} will be called the Catani operator given by [75, 76]

$$C_{gg} = \left(\frac{\alpha_s}{\pi}\right) \frac{e^{\epsilon\gamma_E}}{\Gamma(1-\epsilon)} \left(\frac{\mu^2}{-s - I\delta}\right)^\epsilon \left[\frac{C_A}{2\epsilon^2} + \frac{\beta_0}{\epsilon}\right], \quad (2.68)$$

with the Euler-Mascheroni constant γ_E , the renormalization scale μ and β_0 as given above.²⁰ The quantity on the left hand side of Eq. (2.67) is called the virtual finite part of the NLO Amplitude of the process $gg \rightarrow ZZ$ and is finite in the limit of (2.64). Eq. (2.67) holds also separately for each form factor that contributes to \mathcal{A}_{ggzz} . The explicit form of these form factors will be the topic of the next section.

²⁰Note that the Catani operator of Eq. (2.68) has a second order pole in ϵ . It is therefore necessary to compute the LO part of the amplitude $\mathcal{A}_{ggzz}^{\text{LO}}$ up to and including the second order in ϵ .

2.4. Form Factors

In section 2.2.2 it was shown that the amplitude \mathcal{A}_{ggZZ} can be decomposed into 20 contributions, the form factors α_k (see Eq. (2.25)). Moreover, a basis change was presented in section 2.2.4 that builds new form factors β allowing for a very simple evaluation of the polarization sums when squaring the amplitude (see Eq. (2.42)). The calculation of these form factors was one of main goals of this thesis and the following subsections discuss both exact results and approximations in the LT and ST limit.

2.4.1. Definitions, Prefactors & Numerical Values

In the previous sections, it was convenient for the derivation and discussion of the general structure of the amplitude to simply call the coefficients α_k ²¹ of the tensors $\mathcal{T}_k^{\mu\nu\rho\sigma}$ or later the coefficients β_i of the orthogonal tensors $T_i^{\mu\nu\rho\sigma}$, the form factors of the process. More explicitly, the β_i are, according to section 2.3.6, the UV renormalized and IR subtracted form factors which are computed in a power series in the strong coupling constant α_s at 1-loop (LO) and 2-loop (NLO). To make this visible, it is helpful to rewrite them as

$$\beta_i = \alpha_s m_Z^2 \delta_{ab} \frac{G_F \sqrt{2}}{\pi} \left[\mathcal{B}_i^{\text{LO}} + \frac{\alpha_s}{\pi} \mathcal{B}_i^{\text{NLO}} + \mathcal{O}\left(\frac{\alpha_s}{\pi}\right)^2 \right]. \quad (2.69)$$

Since there is no direct gluon to Z boson coupling in the Standard Model of particle physics, the process starts already at leading order with a top quark loop. Therefore, every Feynman diagram that contributes to the process $gg \rightarrow ZZ$ has at least two QCD couplings of a gluon to top quarks and two electroweak couplings. Hence, all form factors share a common prefactor that is proportional to both α and α_s . Rewriting the electroweak coupling α as

$$\alpha = \frac{e^2}{4\pi} = \frac{G_F \sqrt{2}}{\pi} m_Z^2 \cos^2(\theta_W), \quad (2.70)$$

with the Fermi constant G_F , and the weak mixing angle θ_W leads to the prefactor that in Eq. (2.69) is pulled out from both the leading order form factors $\mathcal{B}_i^{\text{LO}}$ and the next-to-leading order form factors $\mathcal{B}_i^{\text{NLO}}$. The factor δ_{ab} contains the color indices of the incoming gluons and evaluates after squaring the amplitude in the color trace to

$$N_A = N_c^2 - 1 = 8. \quad (2.71)$$

Note that the factor m_Z^2 in Eq. (2.69) is *not* taken into account when the m_Z expansion is discussed. In order to separate the Higgs boson mediated 'triangle' contributions (see left panel of fig. 2.2) from the rest, every form factor \mathcal{B}_i is furthermore split into a 'triangle' and a 'box' part

$$\mathcal{B}_i = \mathcal{B}_{i,\Delta} + \mathcal{B}_{i,\square}. \quad (2.72)$$

²¹See the end of section 2.2.2 where the linear combinations of the coefficients $a_1 \cdots a_{26}$ from equation (2.24) are relabeled $\alpha_1 \cdots \alpha_{20}$ to form the final decomposition of the amplitude into naïve form factors in equation (2.25). From now on however, only the β_k of the orthogonal tensors will be considered.

The form factors \mathcal{B}_i , which will be discussed in detail in this section, will eventually contribute to the partonic cross section σ_{part} which is defined as the integral

$$\sigma_{\text{part}}(s_{\text{part}}) = \int_{t(\theta_{\min})}^{t(\theta_{\max})} \frac{d\sigma}{dt} dt = \int_{-1}^1 \frac{d\sigma}{dt} \frac{dt}{d\cos(\theta)} d\cos(\theta), \quad (2.73)$$

where the integration limits $t(\theta_{\min})$ and $t(\theta_{\max})$ can be written using Eq. (2.5) at the extreme values of the scattering angle θ as

$$t(\theta_{\min} = 0) = -\frac{s}{2} \left(1 - \frac{2m_Z^2}{s} - \sqrt{1 - \frac{4m_Z^2}{s}} \right) \quad (2.74)$$

$$t(\theta_{\max} = \pi) = -\frac{s}{2} \left(1 - \frac{2m_Z^2}{s} + \sqrt{1 - \frac{4m_Z^2}{s}} \right). \quad (2.75)$$

They translate after the change of variables to $\cos(\theta) \in [-1, 1]$, respecting the Jacobian

$$\frac{dt}{d\cos(\theta)} = \frac{s}{2} \sqrt{1 - \frac{4m_Z^2}{s}}. \quad (2.76)$$

The differential partonic cross section $d\sigma/dt$ is obtained by averaging the absolute square of the amplitude over all possible color and polarization states of the incoming gluons and summing over the polarizations of the outgoing Z bosons:

$$\frac{d\sigma}{dt} = \frac{1}{16\pi s^2} \frac{1}{8} \sum_a \frac{1}{8} \sum_b \frac{1}{2} \sum_{\lambda_1} \frac{1}{2} \sum_{\lambda_2} \sum_{\lambda_3} \sum_{\lambda_4} |\mathcal{A}_{\text{ggZZ}}|^2, \quad (2.77)$$

with the kinematic factor $1/(16\pi s^2)$ for the $2 \rightarrow 2$ decay. Using Eq. (2.42) together with Eq. (2.69) allows to express the differential partonic cross section in terms of the form factors $\mathcal{B}_i^{\text{LO}}$ and $\mathcal{B}_i^{\text{NLO}}$ through

$$\begin{aligned} \frac{d\sigma}{dt} &= \frac{1}{16\pi s^2} \frac{1}{8} \frac{1}{8} \frac{1}{2} \frac{1}{2} \sum_a \sum_b \sum_{i=1}^{20} c_i |\beta_i|^2 \\ &= \frac{1}{16\pi s^2} \frac{1}{256} \frac{\alpha_s^2}{\pi^2} m_Z^4 G_F^2 \sum_a \delta_{aa} \sum_{i=1}^{20} c_i \left| \mathcal{B}_i^{\text{LO}} + \frac{\alpha_s}{\pi} \mathcal{B}_i^{\text{NLO}} + \mathcal{O}\left(\frac{\alpha_s}{\pi}\right)^2 \right|^2 \\ &= \frac{m_Z^4 G_F^2 \alpha_s^2}{256\pi s^2 \pi^2} \sum_{i=1}^{20} c_i \left(|\mathcal{B}_i^{\text{LO}}|^2 + \frac{\alpha_s}{\pi} \left[\mathcal{B}_i^{\text{LO}} (\mathcal{B}_i^{\text{NLO}})^* + (\mathcal{B}_i^{\text{LO}})^* \mathcal{B}_i^{\text{NLO}} \right] \right) + \mathcal{O}\left(\frac{\alpha_s}{\pi}\right)^2. \end{aligned} \quad (2.78)$$

The c_i are given in eqs. (2.36) to (2.41). After the renormalization of the form factors, the regularization parameter ϵ can be set to zero and the c_i simplify to (see section 2.2.4)

$$c_1 = c_2 = \dots = c_{10} = 1, \quad c_{11} = c_{12} = \dots = c_{18} = p_T^2 m_Z^2, \quad c_{19} = c_{20} = 0, \quad (2.79)$$

with the transverse momentum p_T which can be expressed via the Mandelstam variables from eqs. (2.4) to (2.6) and is given by

$$p_T^2 = \frac{tu - m_Z^4}{s} . \quad (2.80)$$

For the numerical evaluation it is necessary to choose appropriate values for the physical constants. Since all results are obtained in an analytic form, it is very easy to switch to an other set of input values. In this thesis, the most recent values from the Particle Data Group [3] are used which are listed in the following:

$$m_Z = 91.1876 \pm 0.0021 \text{ GeV} , \quad (2.81)$$

$$m_H = 125.10 \pm 0.14 \text{ GeV} , \quad (2.82)$$

$$m_t = 172.9 \pm 0.4 \text{ GeV} . \quad (2.83)$$

Additionally, the other Standard Model parameters that appear in the process $gg \rightarrow ZZ$ are chosen as

$$G_F = 1.1663787 \times 10^{-5} \text{ GeV}^{-2} , \quad (2.84)$$

$$\sin^2(\theta_W) = 0.23122 \pm 0.00004 , \quad (2.85)$$

$$\alpha_s \equiv \alpha_s(m_Z) = 0.1181 \pm 0.0011 . \quad (2.86)$$

The next sections will discuss first the LO exact results and subsequently the corresponding LT and ST approximations.

2.4.2. Exact Leading Order Result

The process of double Z boson production via gluon fusion has already been calculated with full top quark mass dependence at the leading order in the strong coupling constant more than thirty years ago in ref. [11]. It is however instructive to redo such calculations with modern tools. In this thesis, the LO exact result was computed using the tool chain of `FeynCalc`[77, 78] and `FormCalc`[79, 80] that semi-automatically computes the finite part of one-loop amplitudes. Manipulating intermediate expressions allows one to recover the tensor structure of the process and extract the corresponding form factors. These are expressed in terms of the usual B_0 , C_0 and D_0 functions which can for example be evaluated numerically with the `Mathematica` package `LoopTools`[79, 81].

Unfortunately, there are drawbacks to using `LoopTools`: First of all, `LoopTools` provides only results to an accuracy of $\mathcal{O}(10)$ digits which under normal circumstances suffices to produce plots. Yet, in section 2.5, the exact LO result will be used as part of an analytic expression that needs to be evaluated to high precision in order to avoid numerical artifacts when calculating Padé approximations. Secondly, the package `LoopTools` introduces small imaginary offsets to ensure the usage of the right branches of the Passarino-Veltman functions. Assigning fixed numerical values to them can cause severe numerical instabilities in some limits, e.g. for vanishing transverse momentum.

Instead, in this thesis, the Passarino-Veltman functions B_0 , C_0 and D_0 from `FormCalc` were converted to the notation of the `Mathematica` program `Package-X`[82, 83] which was

designed to rewrite those functions in terms of their own implementation of polylogarithms and other elementary functions that respect the right branch cuts without having to resort to infinitesimal numerical parameters. Since all functions are constructed from built-in Mathematica functions, they can also be evaluated to arbitrary precision.

Defining in analogy to Eq. (2.69) the naïve form factors α_i in terms of the 1- and 2-loop contributions $\mathfrak{A}_i^{\text{LO}}$ and $\mathfrak{A}_i^{\text{NLO}}$ as

$$\alpha_i = \alpha_s m_Z^2 \delta_{ab} \frac{G_F \sqrt{2}}{\pi} \left[\mathfrak{A}_i^{\text{LO}} + \frac{\alpha_s}{\pi} \mathfrak{A}_i^{\text{NLO}} + \mathcal{O}\left(\frac{\alpha_s}{\pi}\right)^2 \right], \quad (2.87)$$

where the transition between the \mathfrak{A}_i and \mathcal{B}_i can be performed via the basis change given in Eq. (2.29), the triangle part of the exact LO form factors is given by:

$$\mathfrak{A}_{1,\Delta}^{\text{LO,exact}} = \frac{m_t^2}{s - m_H^2} (2B_{0,2} - 8C_{0,5} + sC_{0,2}) \quad , \quad \mathfrak{A}_{2,\Delta}^{\text{LO,exact}} = \dots = \mathfrak{A}_{20,\Delta}^{\text{LO,exact}} = 0, \quad (2.88)$$

where $B_{0,\dots}$, $C_{0,\dots}$ and $D_{0,\dots}$ are abbreviations for two-, three and four-point one-loop integrals depending on the kinematic variables s , t and m_t . They are defined in [84]. As can be seen above, one can benefit in the case of the triangle form factors from the fact that they only contribute to the simple tensor $\mathcal{T}_1^{\mu\nu\rho\sigma} = g^{\mu\nu}g^{\rho\sigma}$. The \mathfrak{A} form factors are, by the size of the expressions, in general smaller than the \mathcal{B} form factors. For their numerical evaluation it is therefore advantageous to start from the analytic form of the \mathfrak{A} form factors, evaluate them numerically and perform only afterwards the basis change to the \mathcal{B} form factors. This is also the reason why in the ancillary file to this thesis [84] the \mathfrak{A} form factors are given together with the basis change to the \mathcal{B} form factors.

The remaining box contribution can be split into a vector and an axial-vector part²². The vector part

$$\begin{aligned} \mathfrak{A}_{1,\square,\text{ve}}^{\text{LO,exact}} = & 2 \left(\frac{1}{4} - Q_t \sin^2(\theta_W) \right)^2 \left(2B_{0,1} + 2C_{0,12}m_Z^2 - 2C_{0,12}t + s(4C_{0,13} + 3C_{0,3} + C_{0,7}) \right. \\ & + C_{0,1}(m_Z^2 + s - t) - 16C_{0,6} + 4C_{0,8}m_Z^2 + C_{0,8}s + 4D_{0,10}m_Z^2 - 4D_{0,10}t - u(4D_{0,11} \\ & + m_t^2(D_{0,1} + 8D_{0,23} + 4D_{0,32} + D_{0,37}m_Z^2 - 2D_{0,4} + D_{0,52}s + t(-D_{0,53} + D_{0,71} + D_{0,72} \\ & + D_{0,2}) - D_{0,94}) + 3D_{0,53}m_Z^2 + 2D_{0,5} - 4D_{0,6} + D_{0,73}m_Z^2 - D_{0,73}s + 2D_{0,75}m_Z^2 \\ & + D_{0,93}s + D_{0,94}m_Z^2) + 4D_{0,11}m_Z^2 + 2D_{0,1}m_t^2m_Z^2 - D_{0,1}m_t^2s - D_{0,1}m_t^2t - 8D_{0,22}t \\ & + 2D_{0,2}m_t^2m_Z^2 - D_{0,2}m_t^2s - D_{0,2}m_t^2t + 4D_{0,31}m_Z^2 - 4D_{0,31}t + 4D_{0,32}m_Z^2 + D_{0,37}m_Z^4 \\ & - 2D_{0,38}m_Z^4 + 2D_{0,38}m_Z^2t - 4D_{0,4}s - 2D_{0,4}t + D_{0,51}m_Z^2s - D_{0,51}st + D_{0,52}m_Z^2s \\ & + D_{0,53}m_Z^4 + D_{0,53}m_Z^2t - 4D_{0,5}s + 2D_{0,5}t + D_{0,67}s^2 + D_{0,68}s^2 - D_{0,69}m_Z^4 + 2D_{0,69}m_Z^2t \\ & - D_{0,69}t^2 - 6D_{0,6}m_Z^2 + 6D_{0,6}t + D_{0,71}m_Z^4 + D_{0,72}m_Z^4 + D_{0,73}m_Z^4 + D_{0,74}m_Z^4 - 2D_{0,74}m_Z^2t \\ & + D_{0,74}t^2 + u^2(D_{0,75} - D_{0,76}) + D_{0,75}m_Z^4 + D_{0,76}m_Z^4 + 16D_{0,7} + 16D_{0,8} + D_{0,92}m_Z^2s \\ & \left. - D_{0,92}st + D_{0,93}m_Z^2s + D_{0,94}m_Z^4 - D_{0,94}m_Z^2t + 16D_{0,9} \right), \quad (2.89) \end{aligned}$$

²²Note, that there are no mixed vector-axial-vector contributions as discussed in section 2.2.2.

2. Z-Boson Pair Production

has contributions from two vector couplings with $g_{\text{vec}} = \frac{1}{4} - Q_t \sin^2(\theta_W)$ where $Q_t = \frac{2}{3}$ is the charge of the top quark. The corresponding axial-vector part

$$\begin{aligned} \mathfrak{A}_{1,\square,\text{ax}}^{\text{LO,exact}} = 2 \left(\frac{1}{4} \right)^2 & \left(2B_{0,1} + 2C_{0,12} (m_Z^2 - t) + 4 \left(C_{0,13}s + C_{0,8}m_Z^2 + D_{0,10} (m_Z^2 - t) - u(D_{0,11} \right. \right. \\ & + 2D_{0,23} + D_{0,32}) + D_{0,11}m_Z^2 - 2D_{0,22}t + D_{0,31}m_Z^2 - D_{0,31}t + D_{0,32}m_Z^2) + C_{0,1} (m_Z^2 \\ & + s - t) + C_{0,3} (8m_t^2 + 3s) - 16C_{0,6} + s(C_{0,7} + C_{0,8}) - u(m_t^2(D_{0,1} + D_{0,2}) + D_{0,37}m_Z^2 \\ & + D_{0,52}s + t(-D_{0,53} + D_{0,71} + D_{0,72} - D_{0,94}) + 3D_{0,53}m_Z^2 + 2D_{0,5} - 4D_{0,6} + D_{0,73}m_Z^2 \\ & - D_{0,73}s + 2D_{0,75}m_Z^2 + D_{0,93}s + D_{0,94}m_Z^2) + 2D_{0,1}m_t^2m_Z^2 + D_{0,1}m_t^2s - D_{0,1}m_t^2t \\ & + 2D_{0,2}m_t^2m_Z^2 + D_{0,2}m_t^2s - D_{0,2}m_t^2t + D_{0,37}m_Z^4 - 2D_{0,38}m_Z^4 + 2D_{0,38}m_Z^2t + 2D_{0,3}m_t^2s \\ & - 2D_{0,4}(8m_t^2 + 2s + t - u) + D_{0,51}m_Z^2s - D_{0,51}st + D_{0,52}m_Z^2s + D_{0,53}m_Z^4 + D_{0,53}m_Z^2t \\ & - 16D_{0,5}m_t^2 - 4D_{0,5}s + 2D_{0,5}t + D_{0,67}s^2 + D_{0,68}s^2 - D_{0,69}m_Z^4 + 2D_{0,69}m_Z^2t - D_{0,69}t^2 \\ & - 16D_{0,6}m_t^2 - 6D_{0,6}m_Z^2 + 6D_{0,6}t + D_{0,71}m_Z^4 + D_{0,72}m_Z^4 + D_{0,73}m_Z^4 + D_{0,74}m_Z^4 \\ & - 2D_{0,74}m_Z^2t + D_{0,74}t^2 + u^2(D_{0,75} - D_{0,76}) + D_{0,75}m_Z^4 + D_{0,76}m_Z^4 + 16D_{0,7} + 16D_{0,8} \\ & \left. \left. + D_{0,92}m_Z^2s - D_{0,92}st + D_{0,93}m_Z^2s + D_{0,94}m_Z^4 - D_{0,94}m_Z^2t + 16D_{0,9} \right) \right), \end{aligned} \quad (2.90)$$

is then analogously proportional to the square of the axial-vector coupling $g_{\text{ax}} = \frac{1}{4}$. The remaining form factors $\mathfrak{A}_{2,\square,\text{ve}}^{\text{LO,exact}} \dots \mathfrak{A}_{20,\square,\text{ve}}^{\text{LO,exact}}$ as well as $\mathfrak{A}_{2,\square,\text{ax}}^{\text{LO,exact}} \dots \mathfrak{A}_{20,\square,\text{ax}}^{\text{LO,exact}}$ are given in the ancillary file [84] to this thesis together with the definitions of the functions $B_{0,i}$, $C_{0,i}$ and $D_{0,i}$ and the basis change to obtain the orthogonal \mathcal{B} representations. Using these, one can compute the LO part of the partonic differential cross-section $d\sigma/dt$ according to Eq. (2.78), tag the 'triangle' part and plot the individual contributions.

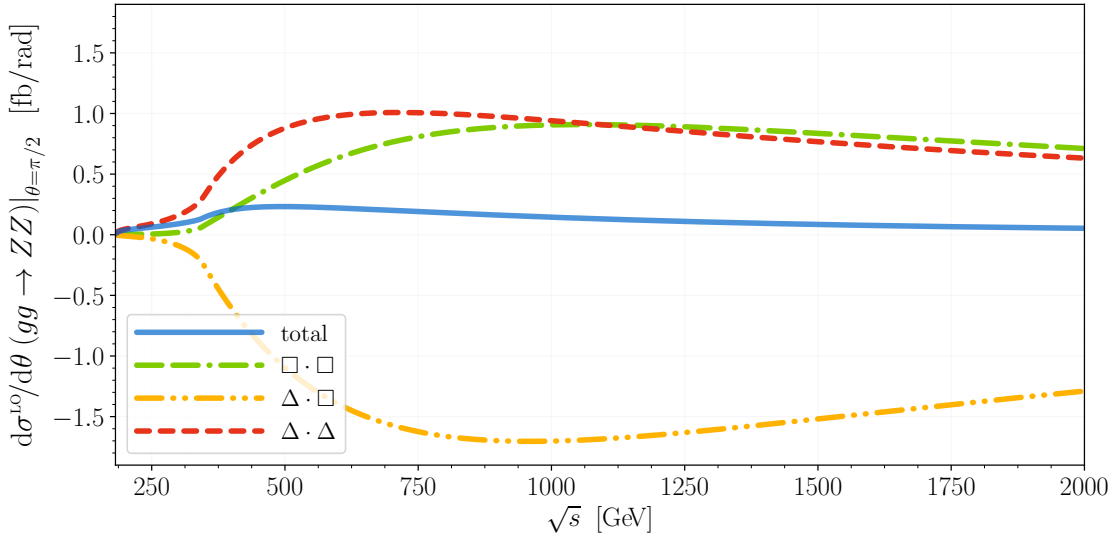


Figure 2.7.: Exact leading order contributions to the partonic partial differential cross section for a fixed scattering angle of $\theta = \pi/2$. The dashed red line shows purely Higgs mediated contributions ($\Delta \cdot \Delta$) while the green line with the dash-dash-dot pattern shows contributions from box diagrams only ($\square \cdot \square$). The yellow dash-dot-dot patterned curve gives the interference term ($\Delta \cdot \square$). The solid blue line is the sum of all contributions.

One observes in figure 2.7 very strong cancellations between the individual parts that are either purely mediated by the Higgs boson ($\Delta \cdot \Delta$) or without it ($\square \cdot \square$) against the mixed interference term ($\Delta \cdot \square$). Whereas for partonic centre-of-mass energies below $\sqrt{s} \approx 500$ GeV the Higgs boson mediated parts dominate the cross section this is not true for high energies. Starting from around 1 TeV, the green line showing the Higgs-independent contribution has roughly the same size as the red curve showing the pure Higgs boson mediated production. It becomes clear, that for a valid description of the process $gg \rightarrow ZZ$ at partonic centre-of-mass energies above $\sqrt{s} \approx 500$ GeV all three parts are equally important and need to be taken into account in order to achieve the cancellation that leads to the cross section shown as the solid blue line.

2.4.3. Large Top Mass Expansion

The contribution from top quarks to di-Z production via gluon fusion in the framework of a large mass expansion has already, to some extent, been considered in the literature. In Ref. [18], the full amplitude has been calculated at LO and NLO up to the first non-vanishing term in the m_t expansion. The authors give explicit results for the LO and the renormalized NLO axial part of the amplitude which could successfully be cross checked and agrees with the results for the LT expansion derived in this thesis²³. Furthermore, in Ref. [20] the interference part between the Higgs boson mediated parts (Δ) and the rest (\square) has been calculated in the large top mass expansion. Since the authors present both the axial and the vector part of the interference part of the amplitude up to $1/m_t^{12}$ in the large top mass expansion this constitutes a second, complimentary possibility for cross checks of the LT result derived in this thesis. By projecting out the corresponding interference term, full agreement at both LO and NLO was found to all given orders in the m_t expansion. Defining the ratios:

$$r_s = \frac{s}{m_t^2}, \quad r_t = \frac{t}{m_t^2}, \quad r_z = \frac{m_z^2}{m_t^2}, \quad (2.91)$$

the LO result for the first, naïve form factor $\mathfrak{A}_1^{\text{LO,LT}}$ is given by

$$\mathfrak{A}_{1,\Delta}^{\text{LO,LT}} = \frac{m_t^2}{s - m_H^2} \left(\frac{r_s}{3} + \frac{7r_s^2}{360} + \frac{r_s^3}{504} + \frac{13r_s^4}{50400} + \frac{2r_s^5}{51975} + \frac{19r_s^6}{3027024} + \frac{r_s^7}{917280} \right) + O(m_t^{-14}), \quad (2.92)$$

where the box contribution can again be split into a vector part

$$\begin{aligned} \mathfrak{A}_{1,\square,\text{ve}}^{\text{LO,LT}} = & \left(\frac{1}{4} - Q_t \sin^2(\theta_W) \right)^2 \left(\frac{r_s^2}{30} - \frac{7r_s r_t}{45} - \frac{7r_t^2}{45} + r_z \left(\frac{14r_t}{45} - \frac{r_s}{15} \right) - \frac{7r_z^2}{45} - \frac{2r_s^3}{315} - \frac{13r_s^2 r_t}{1890} \right. \\ & - \frac{13r_s r_t^2}{1890} + r_z \left(\frac{r_s^2}{30} - \frac{8r_s r_t}{135} - \frac{23r_t^2}{315} \right) + r_z^2 \left(\frac{46r_t}{315} - \frac{43r_s}{1890} \right) - \frac{23r_z^3}{315} + \frac{r_s^4}{945} + \frac{23r_s^3 r_t}{37800} - \frac{r_s^2 r_t^2}{350} \\ & \left. - \frac{131r_s r_t^3}{18900} - \frac{131r_t^4}{37800} + r_z \left(-\frac{31r_s^3}{3780} - \frac{103r_s^2 r_t}{37800} + \frac{467r_s r_t^2}{37800} + \frac{131r_t^3}{9450} \right) + r_z^2 \left(\frac{733r_s^2}{37800} - \frac{146r_s r_t}{4725} \right) \right) \end{aligned}$$

²³There are two minor and obvious typos in both formula (5) and formula (7). The term $f_{\mu\rho}^1 f_\beta^{2,\mu}$ in Eq. (5) should come with a minus sign and in the last line of Eq. (7), p_1^μ and p_2^ν should be swapped for p_2^μ and p_1^ν , respectively. Otherwise, the term is trivially zero.

$$\begin{aligned}
 & -\frac{43r_t^2}{900} + r_z^3 \left(\frac{641r_t}{9450} - \frac{13r_s}{4200} \right) - \frac{1151r_z^4}{37800} - \frac{4r_s^5}{17325} - \frac{139r_s^4r_t}{207900} - \frac{47r_s^3r_t^2}{207900} + \frac{46r_s^2r_t^3}{51975} + \frac{23r_sr_t^4}{51975} \\
 & + r_z \left(\frac{2r_s^4}{945} + \frac{46r_s^3r_t}{17325} - \frac{389r_s^2r_t^2}{103950} - \frac{62r_sr_t^3}{7425} - \frac{19r_t^4}{5775} \right) + r_z^2 \left(-\frac{1501r_s^3}{207900} - \frac{193r_s^2r_t}{207900} + \frac{1153r_sr_t^2}{69300} \right. \\
 & + \frac{76r_t^3}{5775} \left. \right) + r_z^3 \left(\frac{283r_s^2}{29700} - \frac{1979r_sr_t}{103950} - \frac{136r_t^2}{4725} \right) + r_z^4 \left(\frac{383r_s}{207900} + \frac{232r_t}{7425} \right) - \frac{641r_z^5}{51975} + \frac{r_s^6}{24024} \\
 & + \frac{523r_s^5r_t}{3783780} + \frac{227r_s^4r_t^2}{1940400} - \frac{3041r_s^3r_t^3}{18918900} - \frac{199r_s^2r_t^4}{529200} - \frac{179r_sr_t^5}{504504} - \frac{179r_t^6}{1513512} + r_z \left(-\frac{5r_s^5}{9828} \right. \\
 & - \frac{155r_s^4r_t}{116424} - \frac{1217r_s^3r_t^2}{4729725} + \frac{13999r_s^2r_t^3}{6306300} + \frac{1241r_sr_t^4}{582120} + \frac{179r_t^5}{252252} \left. \right) + r_z^2 \left(\frac{1979r_s^4}{840840} + \frac{16909r_s^3r_t}{5405400} \right. \\
 & - \frac{1832r_s^2r_t^2}{429975} - \frac{79r_sr_t^3}{8820} - \frac{5695r_t^4}{1513512} \left. \right) + r_z^3 \left(-\frac{2551r_s^3}{504504} + \frac{22241r_s^2r_t}{56756700} + \frac{41584r_sr_t^2}{2837835} + \frac{355r_t^3}{34398} \right) \\
 & + r_z^4 \left(\frac{44699r_s^2}{10810800} - \frac{273727r_sr_t}{22702680} - \frac{25085r_t^2}{1513512} \right) + r_z^5 \left(\frac{49457r_s}{22702680} + \frac{10897r_t}{756756} \right) - \frac{7529r_z^6}{1513512} \\
 & + \mathcal{O}(m_t^{-14}) , \tag{2.93}
 \end{aligned}$$

and an axial part,

$$\begin{aligned}
 \mathfrak{R}_{1,\square,\text{ax}}^{\text{LO,LT}} &= \left(\frac{1}{4} \right)^2 \left(\frac{4r_s}{3} - \frac{r_s^2}{90} - \frac{r_sr_t}{9} - \frac{r_t^2}{9} + r_z \left(\frac{r_s}{3} + \frac{2r_t}{9} \right) - \frac{r_z^2}{9} + \frac{4r_s^3}{315} + \frac{r_s^2r_t}{54} + \frac{r_sr_t^2}{54} + r_z \left(-\frac{r_s^2}{30} \right. \right. \\
 & - \frac{11r_sr_t}{135} - \frac{2r_t^2}{45} \left. \right) + r_z^2 \left(\frac{29r_s}{270} + \frac{4r_t}{45} \right) - \frac{2r_z^3}{45} - \frac{r_s^4}{1575} - \frac{71r_s^3r_t}{12600} - \frac{13r_s^2r_t^2}{1575} - \frac{11r_sr_t^3}{2100} - \frac{11r_t^4}{4200} \\
 & + r_z \left(\frac{r_s^3}{84} + \frac{53r_s^2r_t}{1800} + \frac{361r_sr_t^2}{12600} + \frac{11r_t^3}{1050} \right) + r_z^2 \left(-\frac{341r_s^2}{12600} - \frac{88r_sr_t}{1575} - \frac{3r_t^2}{100} \right) + r_z^3 \left(\frac{529r_s}{12600} \right. \\
 & + \frac{41r_t}{1050} \left. \right) - \frac{71r_z^4}{4200} + \frac{2r_s^5}{5775} + \frac{r_s^4r_t}{900} + \frac{43r_s^3r_t^2}{18900} + \frac{11r_s^2r_t^3}{4725} + \frac{11r_sr_t^4}{9450} + r_z \left(-\frac{2r_s^4}{945} - \frac{89r_s^3r_t}{9450} \right. \\
 & - \frac{67r_s^2r_t^2}{4725} - \frac{44r_sr_t^3}{4725} - \frac{11r_t^4}{4725} \left. \right) + r_z^2 \left(\frac{46r_s^3}{4725} + \frac{517r_s^2r_t}{18900} + \frac{509r_sr_t^2}{18900} + \frac{44r_t^3}{4725} \right) + r_z^3 \left(-\frac{47r_s^2}{2700} \right. \\
 & - \frac{47r_sr_t}{1350} - \frac{86r_t^2}{4725} \left. \right) + r_z^4 \left(\frac{49r_s}{2700} + \frac{4r_t}{225} \right) - \frac{31r_z^5}{4725} - \frac{5r_s^6}{168168} - \frac{43r_s^5r_t}{145530} - \frac{463r_s^4r_t^2}{646800} - \frac{1361r_s^3r_t^3}{1455300} \\
 & - \frac{4097r_s^2r_t^4}{5821200} - \frac{r_sr_t^5}{3528} - \frac{r_t^6}{10584} + r_z \left(\frac{5r_s^5}{8316} + \frac{1601r_s^4r_t}{582120} + \frac{361r_s^3r_t^2}{66150} + \frac{2659r_s^2r_t^3}{485100} + \frac{1601r_sr_t^4}{582120} \right. \\
 & + \frac{r_t^5}{1764} \left. \right) + r_z^2 \left(-\frac{47r_s^4}{17640} - \frac{4511r_s^3r_t}{415800} - \frac{11849r_s^2r_t^2}{727650} - \frac{1049r_sr_t^3}{97020} - \frac{29r_t^4}{10584} \right) + r_z^3 \left(\frac{157r_s^3}{21560} \right. \\
 & + \frac{92801r_s^2r_t}{4365900} + \frac{4603r_sr_t^2}{218295} + \frac{19r_t^3}{2646} \left. \right) + r_z^4 \left(-\frac{8581r_s^2}{831600} - \frac{35839r_sr_t}{1746360} - \frac{1229r_t^2}{116424} \right) + r_z^5 \left(\frac{14429r_s}{1746360} \right. \\
 & + \frac{481r_t}{58212} - \frac{305r_z^6}{116424} \left. \right) + \mathcal{O}(m_t^{-14}) . \tag{2.94}
 \end{aligned}$$

The remaining form factors are given in the ancillary file [84] to this thesis. Using the basis change given in Eq. (2.29), the set of orthogonal form factors can be computed. Figures 2.8 and 2.9 demonstrate the convergence behaviour of the series in inverse powers of m_t for \mathcal{B}_1 and \mathcal{B}_2 . The curves coming in various different dash-patterns show different expansion depths, starting from m_t^0 (dark blue, double-dashed, triple dotted) up to m_t^{-12}

(red, short-dashed). One can observe a clear tendency that the more terms in the expansion are used, the closer it gets to the exact result shown in solid purple. Including the deepest expansion term (m_t^{-12}) yields a nearly perfect description of the exact result up to the top quark production threshold at a centre-of-mass energy of $\sqrt{s} = 346$ GeV.

Furthermore, one can already conclude from those two examples, that the quality of the approximation improves visibly by incorporating additional terms beyond the leading one.

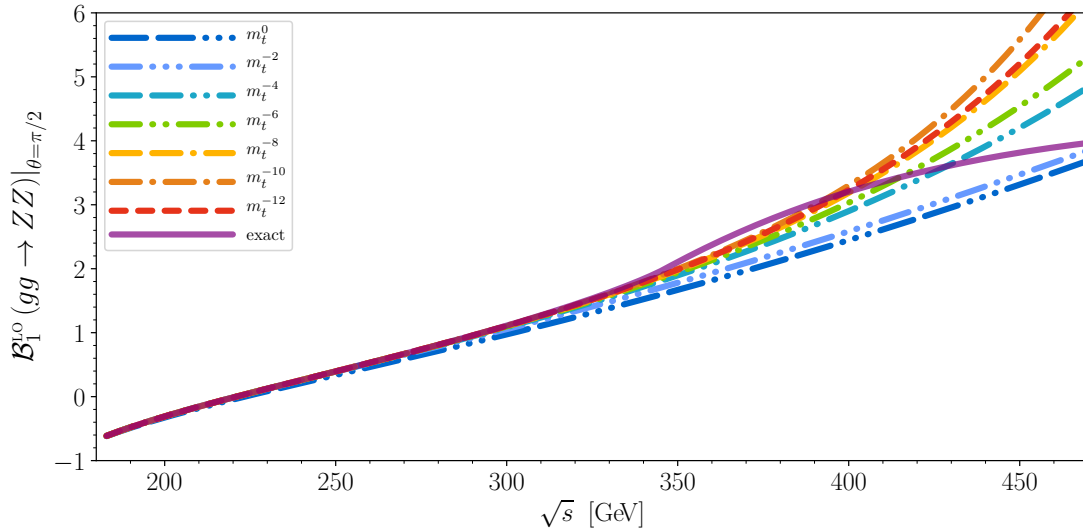


Figure 2.8.: Real part of \mathcal{B}_1 at LO at a scattering angle of $\theta = \frac{\pi}{2}$ as a function of the centre-of-mass energy \sqrt{s} . Dashed and dash-dotted lines show various expansion depths in the LT approximation. The solid purple line shows the exact result.

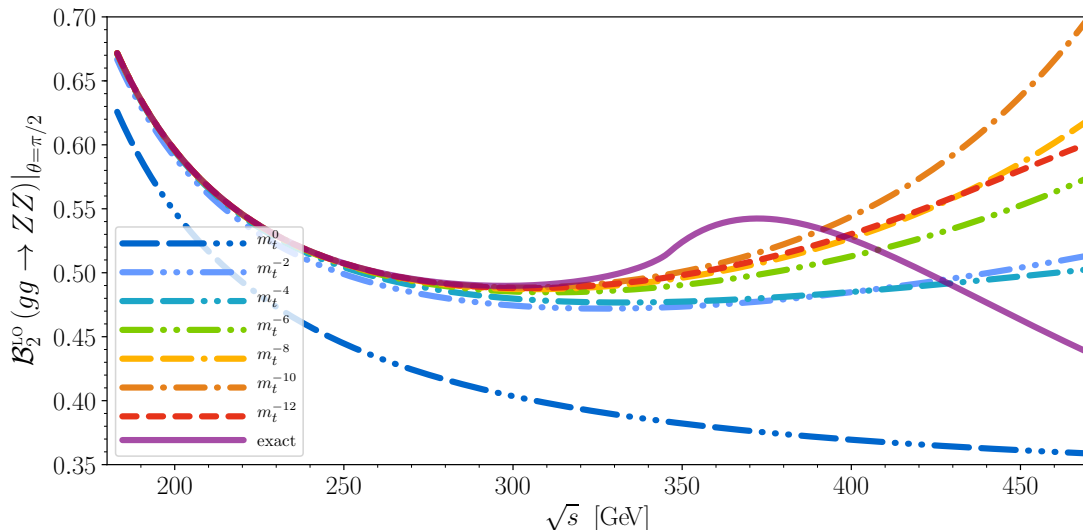


Figure 2.9.: Real part of \mathcal{B}_2 at LO at a scattering angle of $\theta = \frac{\pi}{2}$ as a function of the centre-of-mass energy \sqrt{s} . Dashed and dash-dotted lines show various expansion depths in the LT approximation. The solid purple line shows the exact result.

The kinks the exact results show in figs. 2.8 and 2.9 that are followed by an abrupt change in the shape of the curves are due to the fact that the amplitude develops an imaginary part once the energy threshold for the production of a top quark pair is reached, which is at $\sqrt{s} = 2m_t = 346$ GeV. This feature is absent in the LT approximation which cannot produce an imaginary part and therefore fails, as expected, to describe the exact result for energies above the top quark threshold. There, the assumption $s \ll m_t^2$ from Eq. (2.45) of small energy scales in comparison to the top quark mass is clearly violated and the approximation is not valid anymore. This fact can also be seen in fig. 2.10, where the differential partonic cross section is plotted for a fixed scattering angle $\theta = \frac{\pi}{2}$ against the partonic centre-of-mass energy \sqrt{s} :

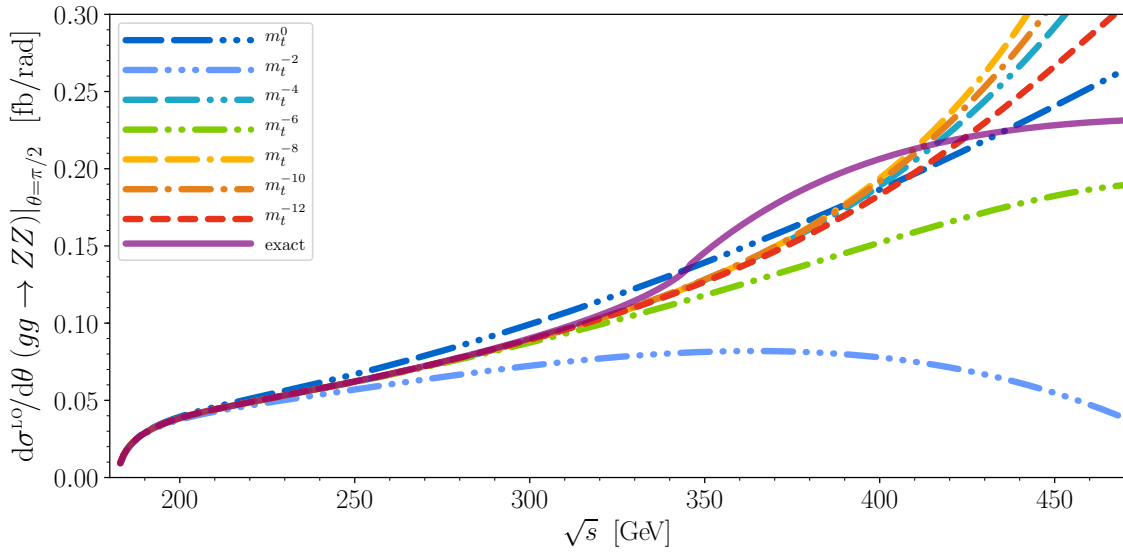


Figure 2.10.: LO differential partonic cross section for $gg \rightarrow ZZ$ for a fixed scattering angle $\theta = \frac{\pi}{2}$. The exact result is shown as solid purple line, the LT approximation is drawn for different expansion depths, ranging from m_t^0 (double-dashed and triple-dotted, dark blue) to m_t^{-12} (short-dashed, red).

One can observe from fig. 2.10, that for the scattering angle $\theta = \pi/2$, the first two terms in the LT expansion (m_t^0 and m_t^{-2}) can only be used as a rough estimate for the actual value of the cross section. Both of them remain within 5% of the exact result for energies below $\sqrt{s} \approx 225$ GeV above which their description of the exact result deteriorates quickly and higher terms need to be taken into account to obtain a good description up to the top quark threshold. In contrast, including up to $1/m_t^8$ in the expansion yields the yellow double-dashed, single-dotted curve that stays within 1% of the exact result up to $\sqrt{s} \approx 300$ GeV. Finally, the red, short-dashed curve shows the LT expansion using all available terms, including m_t^{-12} . It extends the 1% mark to slightly below $\sqrt{s} \approx 320$ GeV and describes the exact result within 4% at $\sqrt{s} \approx 340$ GeV and 8% at the production threshold $\sqrt{s} = 2m_t = 346$ GeV. For higher energies, the LT approximation clearly fails to describe the exact result, shown as solid purple line, and one needs to resort to a different method, the high energy expansion which is the topic of the next section.

2.4.4. High Energy Expansion

So far, the process $gg \rightarrow ZZ$ has not been treated in the literature in the limit of high energies for a non-vanishing top quark mass, except for a brief discussion of the high energy behavior of the LO exact result in [11]. In this section, the results for the high energy expansion ST of this process, one of the main results of this thesis, are presented and discussed first at LO and afterwards in section 2.5.1 also at NLO. To write down an explicit expression for the first terms in both the expansion in the top quark mass and in the Z boson mass, one can make reuse of the ratios given in Eq. (2.91) as in

$$r_{is} = r_s^{-1} = \frac{m_t^2}{s} \quad , \quad r_z = \frac{m_Z^2}{m_t^2} \quad , \quad (2.95)$$

In addition for the sake of brevity, it is convenient to pull explicit $i\pi$ terms into the appearing logarithms and define:

$$l_m = \log\left(\frac{m_t^2}{s}\right) + i\pi \quad , \quad l_t = \log\left(-\frac{t}{s}\right) + i\pi \quad , \quad l_{st} = \log\left(\frac{s+t}{s}\right) + i\pi \quad . \quad (2.96)$$

Note that the arguments of the logarithms in Eq. (2.96) are always positive since $t < 0$ and $|t| < s/2$ and all imaginary parts are made explicit. In analogy to the exact result and the LT approximation, the naïve LO form factor $\mathfrak{A}_{1,\Delta}^{\text{LO,ST}}$ can again be split into the triangle part

$$\mathfrak{A}_{1,\Delta}^{\text{LO,ST}} = \frac{s}{s - m_H^2} \frac{1}{2} \left((4 - l_m^2) r_{is} + (4l_m^2 - 4l_m) r_{is}^2 \right) + \mathcal{O}(r_{is}^3) \quad , \quad (2.97)$$

the vector part

$$\begin{aligned} \mathfrak{A}_{1,\square,\text{ve}}^{\text{LO,ST}} = & \frac{1}{3s^2t^3(s+t)^4} \left(\frac{1}{4} - Q_t \sin^2(\theta_W) \right)^2 \left(2l_{st}^2 t(s+t)^5 (s^3 + 3s^2t + t^3) + l_{st} (-2l_t t^3 (3s^2 \right. \\ & + 2st + 2t^2)(s+t)^4 - 4st^2(s+t)^6) + 2l_t^2 t^4 (s+t)^2 (3s^3 + 6s^2t + 3st^2 + t^3) + 4l_t st^5 (s+t)^3 \\ & + \pi^2 t(s+t)^2 (2s^6 + 12s^5t + 21s^4t^2 + 20s^3t^3 + 15s^2t^4 + 6st^5 + 2t^6) - 4s^2t^3(s+t)^4 \\ & + r_{is} (-48l_m^2 s^2 t^3 (s+t)^4 + l_{st} (-12l_m s^2 t^2 (3s-t)(s+t)^4 + 12l_t s^2 t^2 (3s^2 + 2st + 2t^2)(s+t)^3 \\ & + 12s^2 t^2 (s+t)^5) + l_t (12l_m s^2 t^3 (s+t)^3 (4s+t) + 12s^2 t^4 (s+t)^3) - 24l_m s^2 t^3 (s+t)^4 \\ & - 12l_{st}^2 s^2 t^2 (s+t)^5 - 12l_t^2 s^2 t^4 (s+t)^3 - 12\pi^2 s^4 t^2 (s+t)^3 + 24s^2 t^3 (s+t)^4) \\ & + r_{is}^2 (-72l_m^2 s^2 t^2 (3s^2 + st + t^2)(s+t)^3 + l_{st} (-12l_m s^2 t (s+t)^3 (5s^3 - 7s^2t + 3st^2 - 3t^3) \\ & + 12l_t s^4 t (s+t)^2 (5s^2 - 2st - 2t^2) - 6s^2 t (s+t)^3 (9s^3 - 13s^2t + 21st^2 - 7t^3)) \\ & + l_t (12l_m s^2 t^2 (18s^3 + 22s^2t + 12st^2 + 3t^3)(s+t)^2 + 6s^2 t^2 (50s^3 + 76s^2t + 42st^2 + 7t^3)(s+t)^2) \\ & - 312l_m s^2 t^2 (2s^2 + st + t^2)(s+t)^3 + 36\pi^2 s^2 t^2 (3s^2 + st + t^2)(s+t)^3 + 12s^2 t^2 (38s^2 + 11st \\ & + 11t^2)(s+t)^3) + r_{is} r_z (-2l_{st}^2 st (2s^2 + st + 2t^2)(s+t)^5 + l_{st} (4l_t st^3 (3s+2t)(s+t)^4 \\ & + 8s^2 t^2 (s+t)^5) - 2l_t^2 st^3 (6s^4 + 15s^3t + 12s^2t^2 + 9st^3 + 2t^4)(s+t) - 4l_t s^2 t^3 (3s^2 + 9st \\ & + 2t^2)(s+t)^2 - 2\pi^2 st (2s^6 + 9s^5t + 21s^4t^2 + 26s^3t^3 + 15s^2t^4 + 9st^5 + 2t^6)(s+t) \\ & - 8s^2 t^3 (8s+9t)(s+t)^3) + r_{is}^2 r_z (24l_m^2 s^2 t^2 (s+t)^3 (4s^2 - st - t^2) + l_{st} (-48l_m s^3 t^2 (s \\ & - t)(s+t)^3 + 24l_t s^4 t^2 (2s-t)(s+t)^2 - 24s^3 t^2 (3s-t)(s+t)^3) + l_t (-24l_m s^3 t^2 (s \\ & + 3st + 2t^2) - 24s^3 t^2 (s+t)^2 (7s^2 + 6st + t^2)) + 24l_m s^2 t^2 (s+t)^3 (13s^2 + 3st + 4t^2) \end{aligned}$$

2. Z-Boson Pair Production

$$\begin{aligned}
& + 24l_t^2 s^4 t^3 (s+t)^2 - 24\pi^2 s^4 t^2 (s+t)^2 (2s+t) - 24s^3 t^2 (s+t)^3 (3s+t) - 4r_{is} r_z^2 s^2 t^3 (s+t)^4 \\
& + r_{is}^2 r_z^2 (-6l_m^2 s^2 t^2 (s+t)^3 (s^2 + st + t^2) - 6l_m s^2 t^2 (s+t)^3 (7s^2 + 16st + 16t^2) - 2l_{st}^2 s^2 (s \\
& + t)^3 (2s^4 + 5s^3 t - st^3 - t^4) + l_{st} (2s^3 t (s+t)^3 (4s^2 + 5st - 2t^2) - 4l_t s^2 t^3 (s+t)^4) \\
& + 2l_t^2 s^2 t^2 (3s^5 + 3s^4 t - 3s^3 t^2 + 12s^2 t^3 + 4st^4 + t^5) + 2l_t s^3 t^2 (s+t) (15s^3 + 30s^2 t - 7st^2 + 2t^3) \\
& + 2\pi^2 s^2 (-2s^7 - 11s^6 t - 18s^5 t^2 - 14s^4 t^3 - 8s^3 t^4 + 12s^2 t^5 + 4st^6 + t^7) - 4s^2 t^2 (s+t)^2 (7s^3 \\
& + 79s^2 t + 156st^2 + 78t^3) \Big) + \mathcal{O}(r_{is}^3, r_z^3) , \tag{2.98}
\end{aligned}$$

and the axial-vector part

$$\begin{aligned}
\mathfrak{A}_{1,\square,\text{ax}}^{\text{LO,ST}} &= \frac{1}{3s^2 t^3 (s+t)^4} \left(\frac{1}{4} \right)^2 \left(2l_{st}^2 t (s+t)^5 (s^3 + 3s^2 t + t^3) + l_{st} (-2l_t t^3 (3s^2 + 2st + 2t^2) (s+t)^4 \right. \\
& - 4st^2 (s+t)^6) + 2l_t^2 t^4 (s+t)^2 (3s^3 + 6s^2 t + 3st^2 + t^3) + 4l_t st^5 (s+t)^3 + \pi^2 t (s+t)^2 (2s^6 \\
& + 12s^5 t + 21s^4 t^2 + 20s^3 t^3 + 15s^2 t^4 + 6st^5 + 2t^6) - 4s^2 t^3 (s+t)^4 + r_{is} (-24l_m^2 s^2 t^3 (s+t)^4 \\
& + l_{st} (-12l_m s^2 t^2 (s-t) (s+t)^4 + 12l_t s^2 t^2 (s^2 - 2st - 2t^2) (s+t)^3 + 12s^2 t^2 (s+t)^5) \\
& + l_t (12l_m s^2 t^3 (s+t)^3 (2s+t) + 12s^2 t^4 (s+t)^3) - 24l_m s^2 t^3 (s+t)^4 + 12l_{st}^2 s^2 t^2 (s+t)^5 \\
& + 12l_t^2 s^2 t^4 (s+t)^3 + 12\pi^2 s^2 t^2 (s^2 + 2st + 2t^2) (s+t)^3 + 24s^2 t^3 (s+t)^4) \\
& + r_{is}^2 (-72l_m^2 s^2 t^2 (s^2 + st + t^2) (s+t)^3 + l_{st} (-12l_m s^2 t (s+t)^3 (s^3 + 5s^2 t + 7st^2 - 3t^3) \\
& + 12l_t s^4 t (s+t)^2 (s^2 + 6st + 6t^2) - 6s^2 t (s+t)^3 (s^3 - 13s^2 t - 3st^2 - 7t^3)) + l_t (12l_m s^2 t^2 (6s^3 \\
& + 18s^2 t + 16st^2 + 3t^3) (s+t)^2 + 6s^2 t^2 (18s^3 + 28s^2 t + 18st^2 + 7t^3) (s+t)^2) - 24l_m s^2 t^2 (8s^2 \\
& + 9st + 9t^2) (s+t)^3 + 36\pi^2 s^2 t^2 (s^2 + st + t^2) (s+t)^3 + 12s^2 t^2 (14s^2 + 11st + 11t^2) (s+t)^3) \\
& + r_{is} r_z (-2l_{st}^2 st (2s^2 + st + 2t^2) (s+t)^5 + l_{st} (4l_t st^3 (3s+2t) (s+t)^4 + 8s^2 t^2 (s+t)^5) \\
& - 2l_t^2 st^3 (6s^4 + 15s^3 t + 12s^2 t^2 + 9st^3 + 2t^4) (s+t) - 4l_t s^2 t^3 (3s^2 + 9st + 2t^2) (s+t)^2 \\
& - 2\pi^2 st (2s^6 + 9s^5 t + 21s^4 t^2 + 26s^3 t^3 + 15s^2 t^4 + 9st^5 + 2t^6) (s+t) - 8s^2 t^3 (2s+3t) (s+t)^3) \\
& + r_{is}^2 r_z (24l_m^2 s^2 t^2 (s+t)^3 (2s^2 + st + t^2) + l_{st} (48l_m s^3 t^3 (s+t)^3 - 24l_t s^4 t^3 (s+t)^2 \\
& - 24s^3 t^2 (s-t) (s+t)^3) + l_t (-24l_m s^3 t^2 (s+t)^2 (2s^2 + 3st + 2t^2) - 24s^3 t^2 (s+t)^3 (3s+t)) \\
& + 24l_m s^2 t^2 (s+t)^3 (5s^2 + 3st + 4t^2) - 24l_t^2 s^4 t^3 (s+t)^2 - 24\pi^2 s^4 t^2 (s+t)^2 (s+2t) \\
& - 24s^3 t^2 (s+t)^3 (3s+t)) + r_{is}^2 r_z^2 (-6l_m^2 s^2 t^2 (s+t)^3 (s^2 + st + t^2) - 6l_m s^2 t^2 (s+t)^3 (5s^2 + 8st \\
& + 8t^2) - 2l_{st}^2 s^2 (s+t)^3 (2s^4 + 5s^3 t - st^3 - t^4) + l_{st} (2s^3 t (s+t)^3 (4s^2 + 5st - 2t^2) \\
& - 4l_t s^2 t^3 (s+t)^4) + 2l_t^2 s^2 t^2 (3s^5 + 3s^4 t - 3s^3 t^2 + 12s^2 t^3 + 4st^4 + t^5) + 2l_t s^3 t^2 (s+t) (15s^3 \\
& + 30s^2 t - 7st^2 + 2t^3) + 2\pi^2 s^2 (-2s^7 - 11s^6 t - 18s^5 t^2 - 14s^4 t^3 - 8s^3 t^4 + 12s^2 t^5 + 4st^6 + t^7) \\
& - 4s^2 t^2 (s+t)^2 (s+3t) (s^2 + 10st + 6t^2) \Big) + \mathcal{O}(r_{is}^3, r_z^3) . \tag{2.99}
\end{aligned}$$

The remaining form factors are available from the ancillary file [84] to this thesis. The transition to the orthogonal form factors $\mathcal{B}_i^{\text{ST}}$ can be performed by making use of Eq. (2.29). Also for the case of the ST approximation it is instructive to look at the convergence behavior of different expansion depths in m_t . The discussion of the impact of the m_Z expansion will be discussed later in section 2.4.6. At LO, one again has the advantage to be able to compare against the exact result. The idea is to infer from the convergence behaviour of consecutive expansion depths a measure of confidence of how well the

approximation describes the exact result and transfer this later to NLO where no exact result is known.

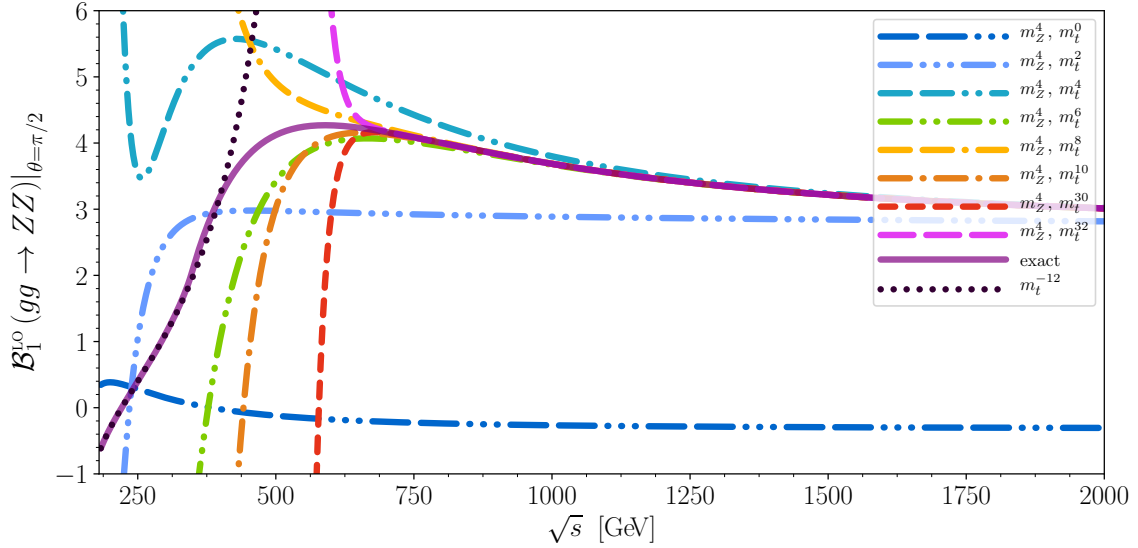


Figure 2.11.: Real part of $\mathcal{B}_1^{\text{LO,ST}}$ for a fixed scattering angle $\theta = \frac{\pi}{2}$ as a function of the centre-of-mass energy \sqrt{s} . The exact result is shown as solid purple line, the ST approximation is drawn for different expansion depths, ranging from m_t^0 (double-dashed and triple-dotted, dark blue) to m_t^{32} (long-dashed, magenta).

Fig. 2.11 shows the real part of the form factor $\mathcal{B}_1^{\text{LO,ST}}$ as a function of \sqrt{s} at a scattering angle of $\theta = \frac{\pi}{2}$. In addition to the exact result drawn as a solid, purple line, the ST expansions are shown as different lines, starting from the 0^{th} order (dark blue, double-dashed, triple-dotted) up to m_t^{32} . In order not to clutter the plot, the expansion depths between m_t^{10} and m_t^{30} are omitted. Note, that in this section all available terms in the m_Z expansion up to m_Z^4 are taken into account.

While in figure 2.11 it is obvious that the first two orders m_t^0 and m_t^2 are and not suited to describe the exact curve as they are far away from the true values, one might ask how to distinguish 'deep enough' expansions that hit the true value from 'too shallow' expansions in the absence of the exact result, as is the situation at NLO. The answer in this case is that as soon as consecutive expansion depths agree with each other, this is a strong indicator that they indeed approximate the exact result. The triple-dotted dark and light blue curves for m_t^0 and m_t^2 show no mutual convergence and are separated by a constant offset even at centre-of-mass energies as high as $\sqrt{s} = 2$ TeV. Starting from m_t^6 , the picture changes and the individual curves merge into a common line that is extended towards lower energies by each additional power in m_t .

This feature gets more distinct when all form factors are combined into the differential partonic cross section which is shown for a scattering angle of $\theta = \frac{\pi}{2}$ in fig. 2.12. Here the benefit of going to higher orders in the m_t expansion is clearly visible in the extended range of agreement with the exact result. Where the m_t^4 term matches the exact result within 5% starting from $\sqrt{s} \gtrsim 3500$ GeV, m_t^6 does this already at centre-of-mass energies

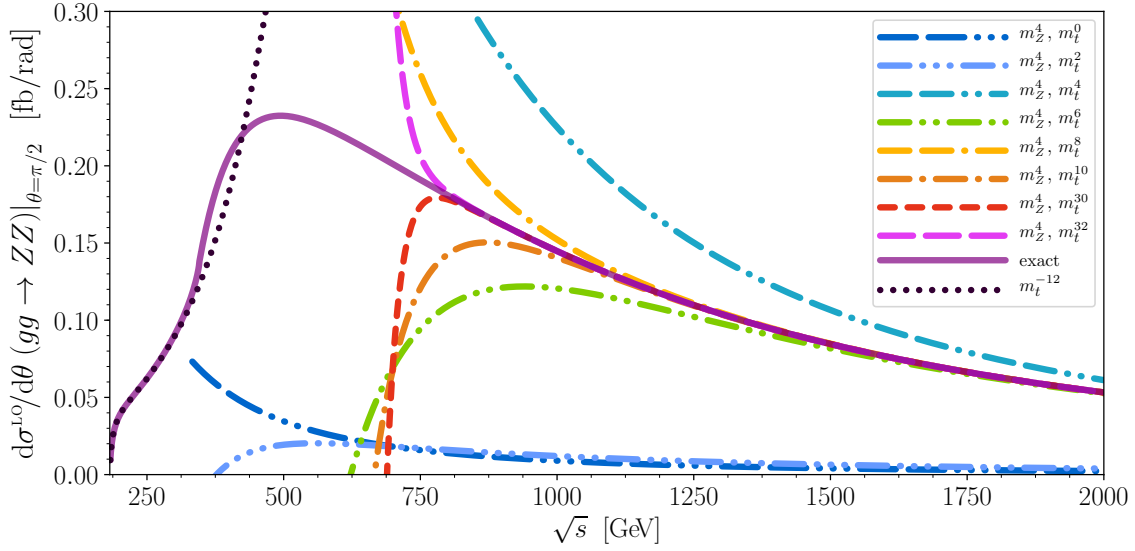


Figure 2.12.: LO differential partonic cross section for $gg \rightarrow ZZ$ for a fixed scattering angle $\theta = \frac{\pi}{2}$. The exact result is shown as solid purple line, the ST approximation is drawn for different expansion depths, ranging from m_t^0 (double-dashed and triple-dotted, dark blue) to m_t^{32} (long-dashed, magenta).

of $\sqrt{s} \gtrsim 1350$ GeV while the m_t^8 terms pushes this to $\sqrt{s} \gtrsim 1000$ GeV. Even though the m_t^{32} term describes the exact result with an high accuracy down to $\sqrt{s} \approx 750$ GeV, it seems very difficult to push past this point and thus unlikely that generating more terms in the m_t expansion after m_t^{32} is the right approach that will yield a good return on investment ratio regarding the expected small penetration into the momentary gap between the LT and ST expansion at their current depths compared to the computational effort of e.g. doubling the number of terms in m_t . Both the question of possible sources for the apparent 'convergence barrier' and a way to nevertheless circumvent it will be addressed in sections 2.4.7 and 2.4.8, respectively.

2.4.5. Comparing LO Exact vs. Expansions

At LO one has the advantage that the majority of the calculations are simple enough that one can test calculational concepts at low computational cost. These concepts can then be used at NLO, where the manipulations required get both more numerous and more complicated but follow the same ideas. This section is intended to compare the exact results against the LT and ST approximation and help to gain confidence in the both the results and the method of their derivation.

Figures 2.13 and 2.14 show the 20 LO form factors $\mathcal{B}_1^{\text{LO}} \dots \mathcal{B}_{20}^{\text{LO}}$ from Eq. (2.69). They are given in a slice of the phase space for a fixed scattering angle $\theta = \frac{\pi}{2}$ as functions of the centre-of-mass energy \sqrt{s} . In each panel, the exact real and imaginary results are shown as solid blue and purple lines. Note that the imaginary part is zero until the centre-of-mass energy reaches the top quark pair production threshold at 346 GeV where also the real part admits a non-differentiable change of its curve shape. The top quark production threshold

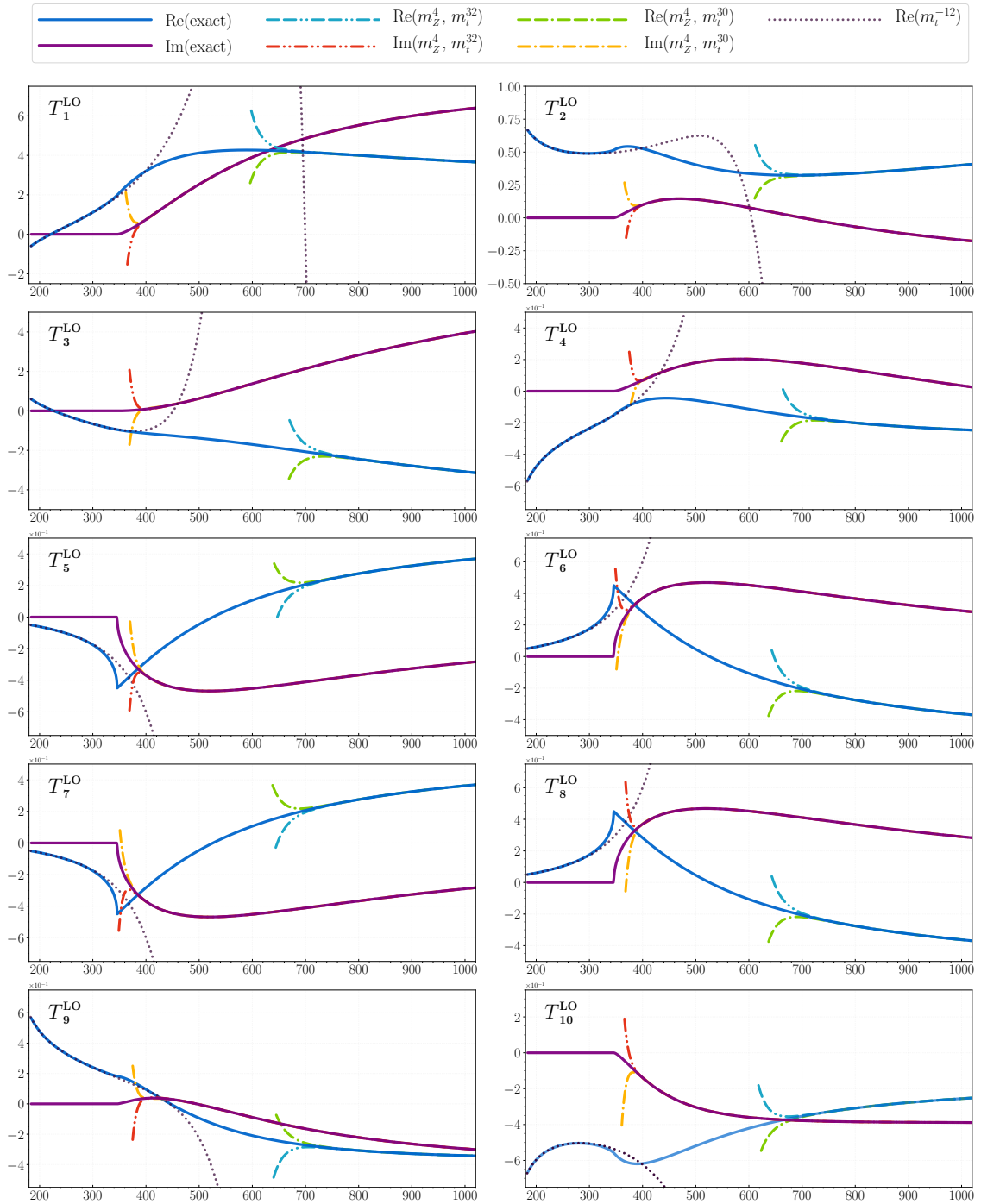


Figure 2.13.: Comparison of the real and imaginary parts of first ten LO form factors $\mathcal{B}_1^{\text{LO}} \dots \mathcal{B}_{10}^{\text{LO}}$ from the exact result (solid lines), large top mass expansion (dotted line) and high energy expansion (dash-dotted lines) at a scattering angle of $\theta = \frac{\pi}{2}$. The x -axis shows the partonic centre-of-mass energy of the process in GeV.

separates also clearly the range of convergence of the large top mass expansion and the high energy expansion. One can observe, that the LT approximation including terms up to

2. Z-Boson Pair Production

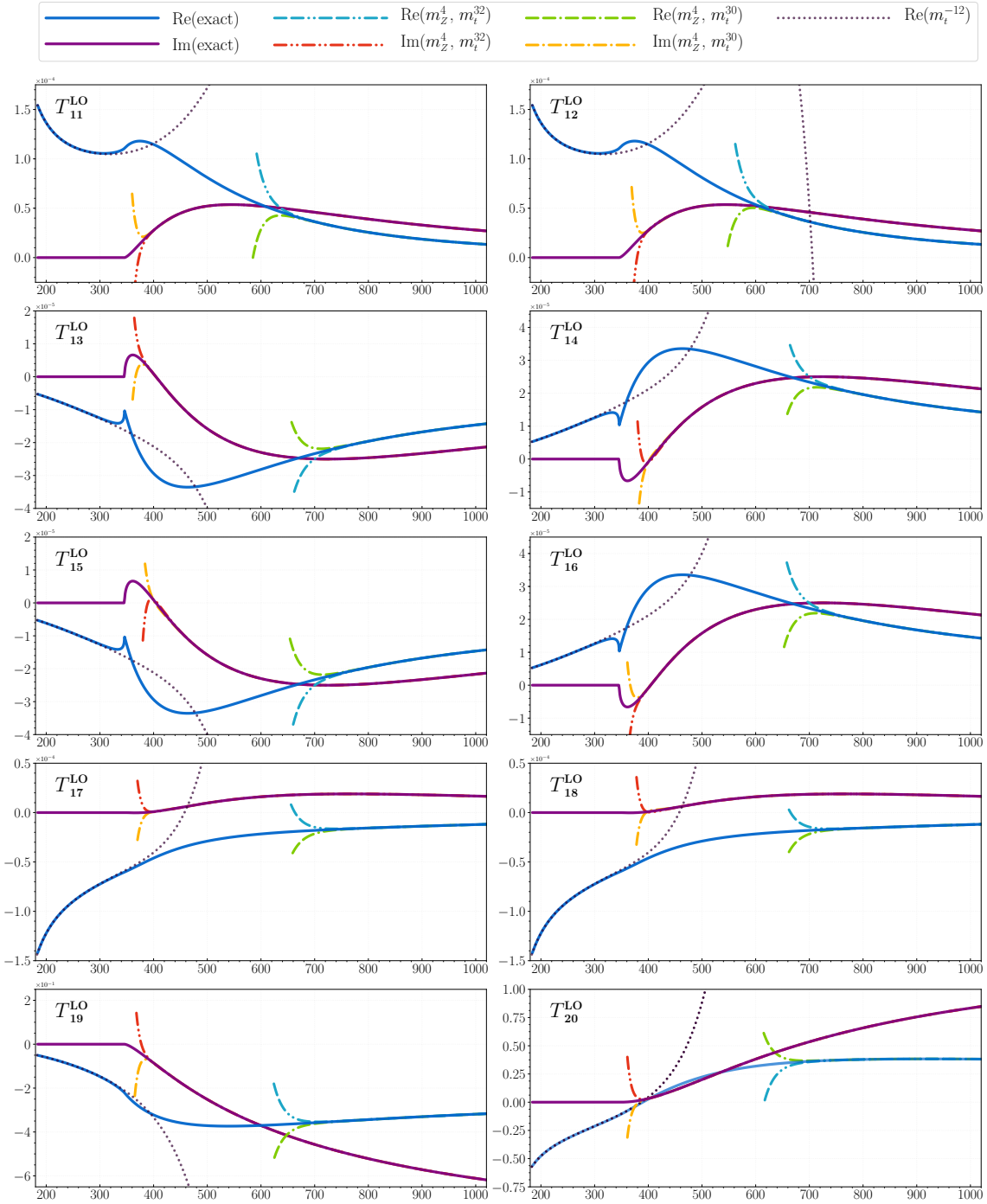


Figure 2.14.: Comparison of the real and imaginary parts of last ten LO form factors $\mathcal{B}_{11}^{LO} \dots \mathcal{B}_{20}^{LO}$ from the exact result (solid lines), large top mass expansion (dotted line) and high energy expansion (dash-dotted lines) at a scattering angle of $\theta = \frac{\pi}{2}$. The x -axis shows the partonic centre-of-mass energy of the process in GeV.

m_t^{-12} (dotted curve) seems to describe the exact result very well up to roughly 340 GeV. For larger values of the centre-of-mass energy \sqrt{s} , the dotted curves starts to deviate slowly

from the exact curve. For values of $\sqrt{s} \geq 346$ GeV the asymptotic expansion series breaks down since $\sqrt{s} \ll m_t^2$ does not hold anymore and the result of the LT approximation cannot be used to describe the process. On this side of the threshold, the high energy expansion ST is better suited to describe the actual shape of the form factors. Starting from infinitely high centre-of-mass energies, the exact result is reproduced very well by the results of the ST approximation including either 32 (double-dotted) or 30 (single-dotted) terms in the m_t expansion and 4 terms in the m_Z expansion. Eventually the convergence breaks down around 750 GeV for the real part (double-dashed) while the imaginary part (single-dashed) stretches nearly to the production threshold and breaks down at only around 400 GeV. Note that the ST curves are truncated for better readability of the plots shortly after they start to diverge from each other.

One important observation one can make from the figures 2.13 and 2.14 is, that as long as two consecutive expansion depths in m_t lie on top of each other, the shape of their curves also agrees with the shape of the exact result. Only when those consecutive orders in the m_t expansion start to diverge from each other, the curves no longer describe the exact result. Recapitulating the exercise of recalculating the LO results suggests that one obtains a reliable approximation of the exact result, as long as consecutive expansion orders in m_t agree. This will be helpful at NLO, where no exact result is known.

Putting everything together, the differential partonic cross section can be computed according to eq (2.78). Splitting the cross section with respect to the individual contributions from Higgs boson mediated 'triangle' contributions (Δ) and continuum 'box' contributions (\square) as in fig 2.7, one gets again three plots, $\Delta \cdot \Delta$ in fig. 2.15, $\Delta \cdot \square$ in fig. 2.16 and $\square \cdot \square$ in fig. 2.17.

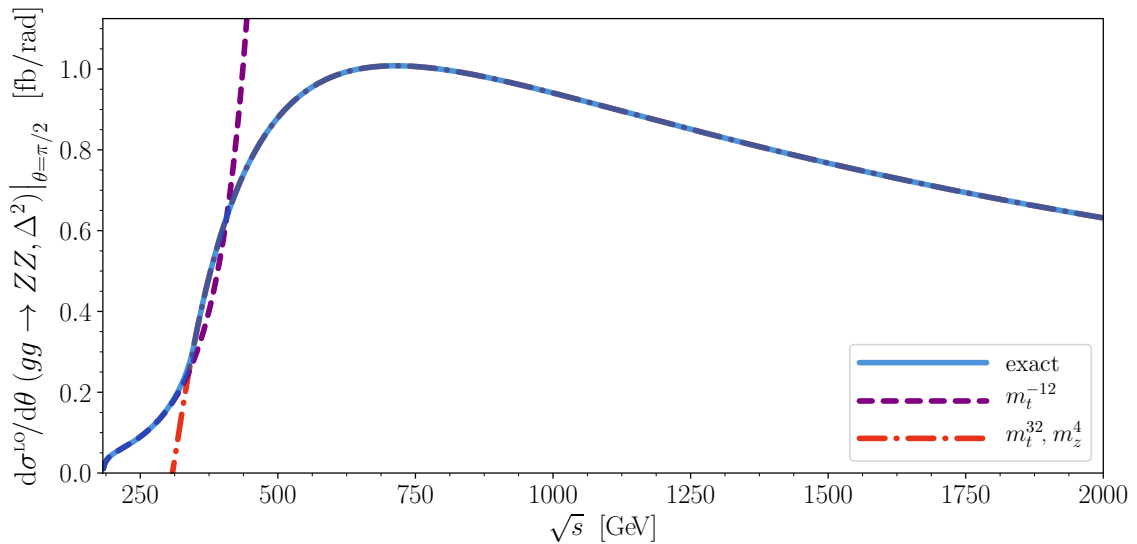


Figure 2.15.: Higgs boson mediated part of the differential partonic cross section at LO for a fixed scattering angle of $\theta = \frac{\pi}{2}$. The exact result is shown as a solid blue curve, the purple, short-dashed curve shows the LT expansion including terms up to m_t^{-12} and the dash-dotted curve shows the ST expansion including m_t^{32}

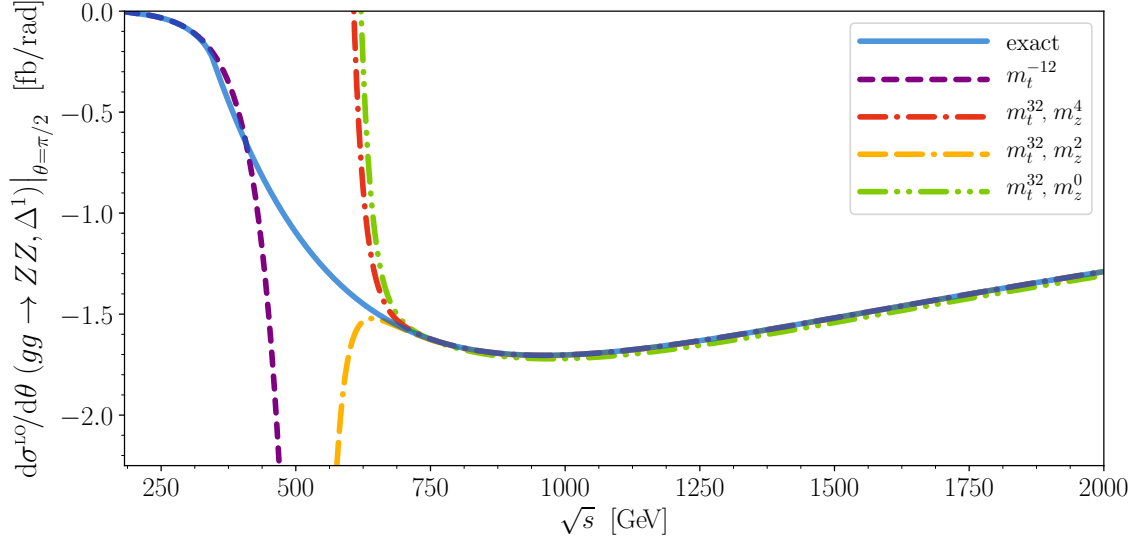


Figure 2.16.: Interference part of the differential partonic cross section at LO for a fixed scattering angle of $\theta = \frac{\pi}{2}$. The exact result is shown as a solid blue curve, the purple, short-dashed curve shows the LT expansion including terms up to m_t^{-12} and the dash-dotted curves show the ST expansion including m_t^{32} and three different expansion depths in m_Z .

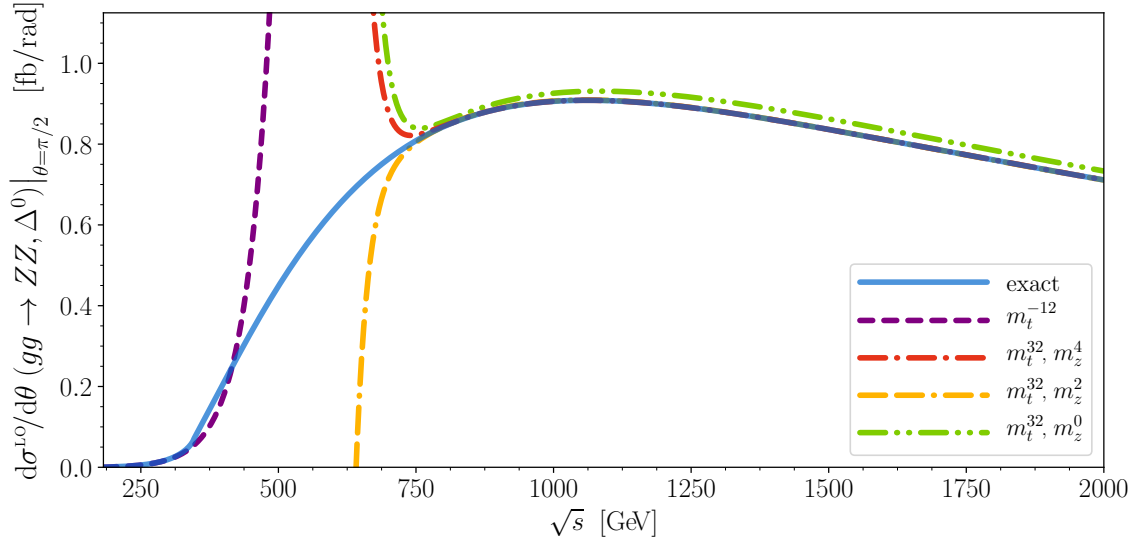


Figure 2.17.: Continuum production part of the differential partonic cross section at LO for a fixed scattering angle of $\theta = \frac{\pi}{2}$. The exact result is shown as a solid blue curve, the purple, short-dashed curve shows the LT expansion including terms up to m_t^{-12} and the dash-dotted curves show the ST expansion including m_t^{32} and three different expansion depths in m_Z .

The purely Higgs boson mediated part of the differential partonic cross section in fig. 2.15 can, at LO and for a scattering angle of $\theta = \frac{\pi}{2}$, be completely reproduced by the

combination of the LT and the ST expansion. Since the dependence on the Z boson mass factorizes in the triangle diagrams, all three expansion depths in m_Z of the ST result are identical and only one curve is shown. In figure 2.16 it becomes clear that the more complicated box diagrams contributing to the interference term are responsible for the break down of the convergence of the ST approximation for energies below $\sqrt{s} \lesssim 750$ GeV. Furthermore, one sees for the first time the effect of incorporating higher terms in the m_Z expansion; the green single-dash, double-dotted line denoting the ST expansion for m_t^{32} and m_Z^0 is clearly not on top of the exact result and follows its shape with a visible offset. The plot in Fig. 2.17 showing the part that originates purely from 'box' diagrams, makes the discrepancy between the exact result and the m_Z^0 term of the ST expansion even more obvious. It seems, that this offset remains for high energies and including at least the first term in the m_Z expansion (yellow curve, double-dashed, single-dotted) is necessary to produce a correct description of the exact result at high energies. Furthermore it seems that there is only a small benefit for going one order higher and computing the m_Z^4 terms. The impact of the Z boson mass expansion will be the topic of the next section. The question of why there seems to be no gain in adding more terms in the m_t expansion will be addressed in section 2.4.7.

2.4.6. Importance of Finite M_Z Corrections

Adding the individual contributions from fig. 2.15 to fig. 2.17 together does not cancel completely the offset the 0^{th} order term in m_Z of the ST approximation has compared to the exact result. As the centre-of-mass energy rises, it even seems to grow stronger and drift further away from the exact result (see fig. 2.18).

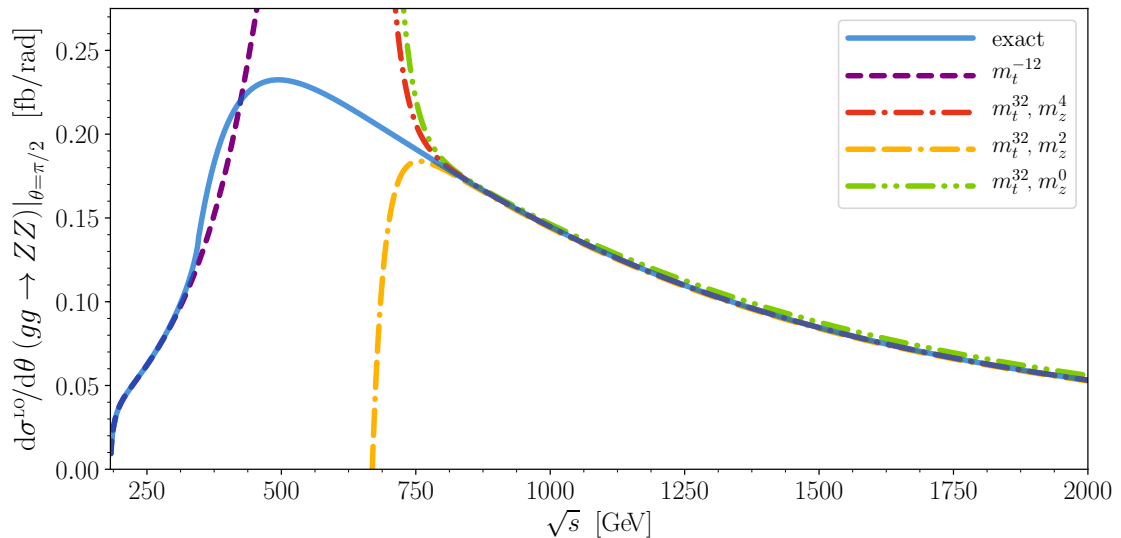


Figure 2.18.: Differential partonic cross section at LO for a fixed scattering angle of $\theta = \frac{\pi}{2}$ for different depths in the Z boson mass expansion.

By normalizing the cross section to the exact result this observation can be confirmed in fig. 2.19, which shows a broader energy range that was enlarged up to 4 TeV.

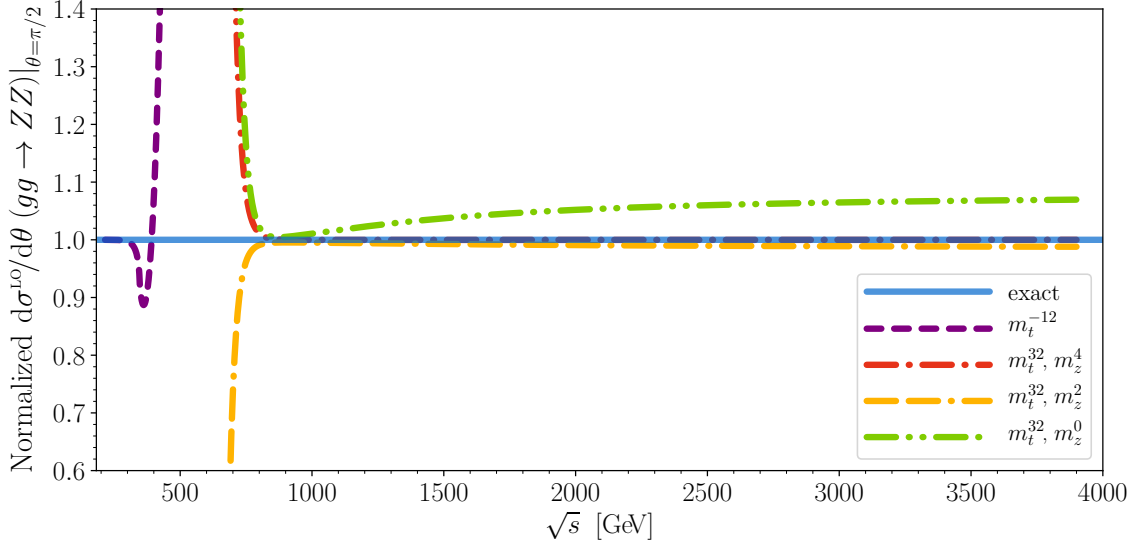


Figure 2.19.: Differential partonic cross section at LO for a fixed scattering angle of $\theta = \frac{\pi}{2}$, normalized to the exact result.

Here, the discrepancy between the exact result and the m_Z^0 term of the ST approximation reaches 7% at $\sqrt{s} = 4$ TeV. This means, the ST approximation describes the exact result in the limit of a vanishing Z boson mass only within a few percent and one needs to include at least the first order in the naïve Taylor expansion in m_Z to match the exact result in the limit of high centre-of-mass energies. Furthermore, it seems that also the second term shows still a visible shift from the exact result.

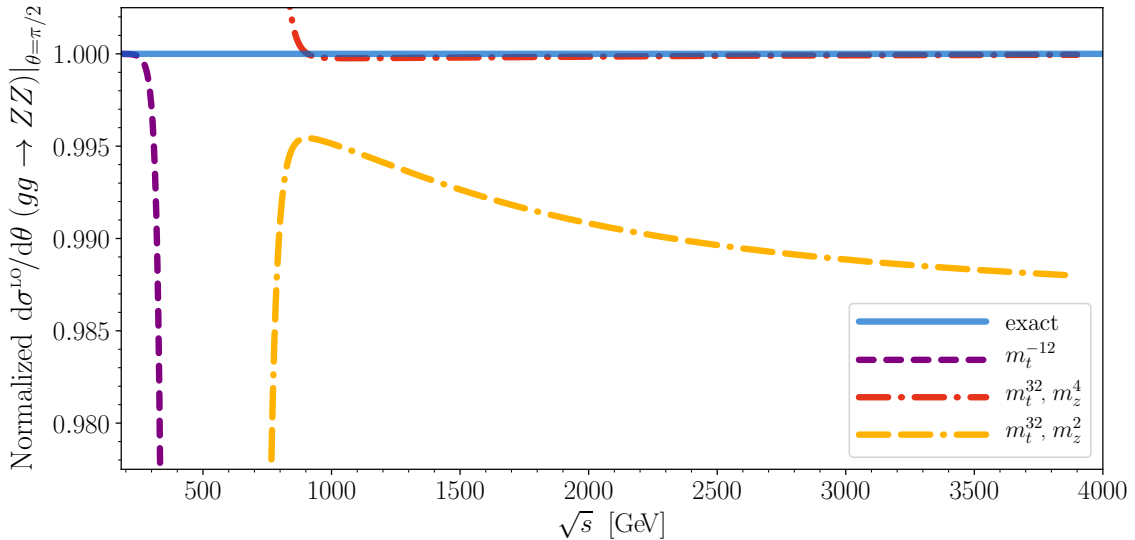


Figure 2.20.: Zoomed version of the differential partonic cross section at LO for a fixed scattering angle of $\theta = \frac{\pi}{2}$, normalized to the exact result.

Fig. 2.20 is a zoomed in version of fig. 2.19. It shows, that also the m_Z^2 term of the ST expansion has a non-vanishing offset from the exact result which at 4 TeV reaches about 1.2%. However, the inclusion of the m_Z^4 term yields finally only a sub permille deviation from the exact result and seems to be well suited to describe the process $gg \rightarrow ZZ$ in the limit of high energies. In summary it should be noted that the ST approximation for $gg \rightarrow ZZ$ shows in the limit $m_Z \rightarrow 0$ a seemingly multiplicative offset that amounts in the case of the differential partonic cross section to several percent. When considering also finite Z mass effects, the exact result can be reproduced at the sub permille level if in the naïve Z mass expansion terms up to m_Z^4 are included.

2.4.7. Radius of Convergence

In the previous sections, the LT and ST approximation were discussed and their convergence on the exact result studied. It is clear that they are separated by the top quark threshold. The phase space region of low energies is described very well by the LT approximation including terms up to m_t^{-12} . Also the region of high energies is neatly reproduced by the ST approximation including terms up to m_t^8 and m_Z^4 . However, there exists a gap which, for a scattering angle of $\theta = \frac{\pi}{2}$, starts slightly below the top quark production threshold around $340 \text{ GeV} \lesssim \sqrt{s}$ and extends up to $\sqrt{s} \lesssim 750 \text{ GeV}$ where the exact result is not being reproduced. Unfortunately, this is where the bulk of the cross section is located and finding a way to close this gap is of major interest.

On the one hand, the LT approximation cannot penetrate this gap since it lies above the top quark production threshold. There, the necessary prerequisite of assuming centre-of-mass energies to be much smaller than the top quark mass is violated and therefore the series in powers of s over m_t^2 will never converge. On the other hand, the ST approximation seems to freeze around $\sqrt{s} \approx 750 \text{ GeV}$ and no matter how many additional terms in m_t or m_Z are added, the series will always diverge for energies below this point.

The reason for this apparent second threshold can be understood by looking at the master integrals which are themselves a series in the ratio $r_{is} = m_t^2/s$. By viewing r_{is} as a real quantity it is not obvious why adding infinitely many terms to the expansion should not reproduce the exact result down to the top quark production threshold. However, if instead one considers the ST solution of the master integrals in the complex r_{is} plane, one does encounter poles away from the real axis. The absolute distance from the origin of the complex r_{is} plane to these poles dictates and reduces artificially the radius of convergence of the ST series approximation of the corresponding master integral.

Since the amplitude and therefore also the form factors and finally the cross section are built from linear combinations of those ST series approximated master integrals, it is clear that once the first integral exceeds its radius of convergence, it acts as the weakest link in the chain and spoils the convergence of the whole linear combination of the different contributions of the single masters that add up to the amplitude.

This can for example be observed in fig 2.11 where for the first few orders in the m_t expansion every new term that is taken into account enlarges the validity range of the ST expansion by several hundred GeV. But starting from m_t^8 , incorporating more terms in the ST expansion does not seem to push the ‘convergence boundary’ lower than 750 GeV.

Here, the problematic integral is $G_3(1, 1, 1, 1)$ ²⁴. Using its original ST series in r_{is} as a basis for building different Padé approximants (see next section 2.4.8) in the same ratio, one can investigate the distribution of poles the different approximants develop in the complex r_{is} plane. While some poles appear at random locations, there is for some distances from the origin a clear clustering of poles. For the integral mentioned above, the closest clustering happens at $|r_{is}| \approx 0.055$ which corresponds to a centre-of-mass energy of $\sqrt{s} \approx 740$ GeV. The second worst integrals are $G_3(1, 1, 0, 1)$, $G_3(0, 1, 0, 1)$, and $G_2(1, 1, 1, 1)$ which all share a pole at the distance $|r_{is}| \approx 0.13$ corresponding to $\sqrt{s} \approx 480$ GeV. Last, the integrals $G_2(1, 0, 1, 0)$, and $G_2(1, 1, 1, 0)$ come with a pole at $|r_{is}| \approx 0.25$ which matches the physical limit at the top quark production threshold at $\sqrt{s} = 346$ GeV. This simple analysis can be used to understand the radius of convergence of the ST expansion.

If it were not for these poles, all it would take to reproduce the exact result would be to include more terms in the m_t series until one reaches the top quark production threshold. Instead, the expressions blow up in the vicinity of the first pole and can afterwards (for lower energies) never convergence on the exact result again. There exists however a way to circumvent this problem and extend the finite radius of convergence by making use of so called *Padé approximants*:

2.4.8. Padé Approximation

Consider a function $f(x)$ that is analytic around $x = 0$. Then $f(x)$ can be expanded into a truncated Taylor series $T_L(x)$ as

$$f(x) = \sum_{l=0}^{\infty} f_l x^l = \sum_{l=0}^L f_l x^l + \mathcal{O}(x^{L+1}) = T_L(x) + \mathcal{O}(x^{L+1}) . \quad (2.100)$$

One can then always find two polynomials $P_n(x)$ and $Q_m(x)$ of the order n and m , respectively, whose ratio $\mathcal{F}_{[n,m]}(x)$ exhibits the same Taylor expansion $T_L(x)$:

$$\mathcal{F}_{[n,m]}(x) = \frac{P_n(x)}{Q_m(x)} = \frac{p_0 + p_1x + p_2x^2 + \dots + p_nx^n}{1 + q_1x + q_2x^2 + \dots + q_mx^m} = T_L(x) + \mathcal{O}(x^{L+1}) , \quad (2.101)$$

where the ratio of the two polynomials is chosen such that the first term q_0 of the polynomial $P_m(x)$ gets normalized to $q_0 = 1$. This ratio $\mathcal{F}_{[n,m]}(x)$ is then called the $[n, m]$ -Padé approximant of the function $f(x)$. Usually, as in this thesis, the function $f(x)$ is not known. Instead, one can start from the power series $T_L(x)$ and construct a $[n, m]$ -Padé approximant by expanding the ansatz (2.101) around $x = 0$ up to and including the order x^L and subsequently comparing the coefficients to the given Taylor expansion $T_L(x)$. It is a well known trait of Padé approximants to develop spurious poles that can appear in principle anywhere in the complex x plane (see e.g. [85] for an extended discussion). Still, the use of rational functions in Padé approximants allows them to incorporate also 'true' poles of the initial function, a feature ordinary Taylor expansions do not have and that can possibly lead to a better description of the unknown function $f(x)$. Since the degree of

²⁴See appendix A.3 for the notation and Ref. [42] for the analytic expression.

the polynomial in the denominator of $\mathcal{F}_{[n,m]}(x)$ is m , the set of relevant poles of the Padé approximant in Eq. (2.101) is given by x_τ with $\tau \in \{1, \dots, m\}$.

In this thesis, all Padé approximations will be calculated locally for a given phase space point (\sqrt{s}, p_T) ²⁵ and start from a power series in m_t like

$$f(x) = f_0 + \sum_{l=1}^L (f_{2n-1} m_t^{2n-1} + f_{2n} m_t^{2n}) x^n + \mathcal{O}(x^{L+1}), \quad (2.102)$$

which is reorganized such that in case there are odd powers of m_t , they are joined into one common coefficient with the next even power of m_t . The Padé approximant $\mathcal{F}_{[n,m]}(x)$ is then derived for numerical values of all variables in $f(x)$ except for x , of course, at $x = 0$, which corresponds to the ST approximation where m_t is assumed to be small. In particular also the prior expansion parameter m_t is set to its physical value $m_t = 173 \text{ GeV}$ ²⁶ since the series is now formed by the variable x . The values of the Padé approximant at the phase space point (\sqrt{s}, p_T) is then given by $\mathcal{F}_{[n,m]}(x = 1)$.

One problem which can occur now is that if one of the poles x_τ mentioned earlier happens to be close to the evaluation point $x = 1$, the value of $\mathcal{F}_{[n,m]}(x = 1)$ might suffer from the proximity to this possibly spurious pole and produce a number that is completely unrelated to the underlying function $f(x)$.

In order to minimize the influence of these spurious poles, the following procedure was developed:

1. Generate a set of Padé approximants:

In this thesis, all high energy ST expansions were calculated up to and including m_t^{32} . That means one can use $L = 16$ in Eq. (2.102) and therefore Padé approximants can be constructed up to $n + m \leq 16$. Note, that not all combinations of n and m lead to good descriptions of the function $f(x)$. It is clear that the smaller the sum of $n + m$, the less information about $f(x)$ can be fed to the Padé approximant. Also an extreme imbalance between the orders of the polynomials $P_n(x)$ and $Q_m(x)$ does usually not lead to good results. Therefore, to maximize both the information transfer from the initial series in the ST approximation and also to stay close to the assumedly best choice of a so called diagonal ($[n, n]$) solution, construct for each phase space point (\sqrt{s}, p_T) five Padé approximants $i = [n, m]$ from the set

$$\mathbb{P} = \{[7/8], [7/9], [8/7], [8/8], [9/7]\} \quad (2.103)$$

that fulfill the conditions

$$16 \geq n + m \geq 15 \quad \text{and} \quad |n - m| \leq 2. \quad (2.104)$$

2. Parametrize their proximity to poles:

In order to make different Padé approximants from the set \mathbb{P} comparable with respect

²⁵With $p_T = \sqrt{p_T^2}$ as defined in Eq. (2.80)

²⁶See eqs. (2.81) and (2.84) for numerical values of the physical constants used in this thesis.

to how possible it is that their value is biased by a nearby pole in the complex plane, compute for each $\mathcal{F}_{[n,m]}(x)$ the zeroes x_τ of the denominator function $Q_m(x)$ and find the one closest to the evaluation point $x = 1$. Then set $x = 1$ and keep for each Padé approximant both its value at $x = 1$ and the distance to its nearest pole:

$$\mathcal{F}_{[n,m]}(x) \rightarrow (\alpha_{[n,m]}, \beta_{[n,m]}) \equiv \left(\mathcal{F}_{[n,m]}(x=1), \min_{\tau=1}^m (|1 - x_\tau|) \right) \quad (2.105)$$

3. Combine them into one Padé based value-error pair:

Each phase space point (\sqrt{s}, p_T) is mapped to a set of five value-distance pairs

$$(\sqrt{s}, p_T) \mapsto (\{\alpha_i\}, \{\beta_i\}) \quad , \quad i \in \mathbb{P} . \quad (2.106)$$

Subsequently, one can take one of the following (non-exhaustive) options:

- Take the results $\{\alpha_i\}$ from all Padé approximants and ignore that some of them stem from evaluations in the proximity of possibly un-physical poles. Then build a mean value with a corresponding standard deviation:

$$\alpha = \frac{1}{|\mathbb{P}|} \sum_{i=1}^{|\mathbb{P}|} \alpha_i \quad , \quad \delta_\alpha = \sqrt{\frac{\sum_{i=1}^{|\mathbb{P}|} (\alpha_i - \alpha)^2}{|\mathbb{P}| - 1}} , \quad (2.107)$$

with the size $|\mathbb{P}| = 5$ of the set of Padé approximants from Eq. (2.103).

- Introduce a cut-off radius ρ and include only results from Padé approximants that are pole-free in the disc $|1 - \rho|$ around their evaluation point $x = 1$. Then proceed as above to generate the mapping $(\sqrt{s}, p_T) \mapsto (\alpha \pm \delta_\alpha)$. Note however, that this option can lead to empty sets \mathbb{P} and that therefore a Padé approximation relying on this method can also yield no result at all for given combinations of phase space points and cut-off radii δ .
- Introduce a re-weighting function, that reduces the impact of values α_i of Padé approximants evaluated in the vicinity of poles, meaning those α_i accompanied by small values β_i . Then generate a value-error pair according to the chosen reweighting function.

Taking the last option allows one to include all values of the Padé approximants from \mathbb{P} , re-weighted by a function depending on the distance to their nearest pole. In this way, no information gets lost and one always produces a result for the Padé approximation that furthermore reflects in both its value and uncertainty estimate the dependence on nearby poles. Choosing a quadratic reweighting function, each value α_i gets assigned the weight

$$\omega_i(\beta_i) = \frac{\beta_i^2}{\sum_j^{|\mathbb{P}|} \beta_j^2} . \quad (2.108)$$

Then, the weighted mean and standard deviation are obtained through

$$\alpha = \sum_{i=1}^{|\mathbb{P}|} \omega_i \alpha_i \quad , \quad \delta_\alpha = \sqrt{\frac{\sum_{i=1}^{|\mathbb{P}|} \omega_i (\alpha_i - \alpha)^2}{1 - \sum_{i=1}^{|\mathbb{P}|} \omega_i^2}} , \quad (2.109)$$

and the phase space point (\sqrt{s}, p_T) is mapped via ‘pole distance reweighted’ (PDR) Padé approximation to the result $(\alpha \pm \delta_\alpha)$.

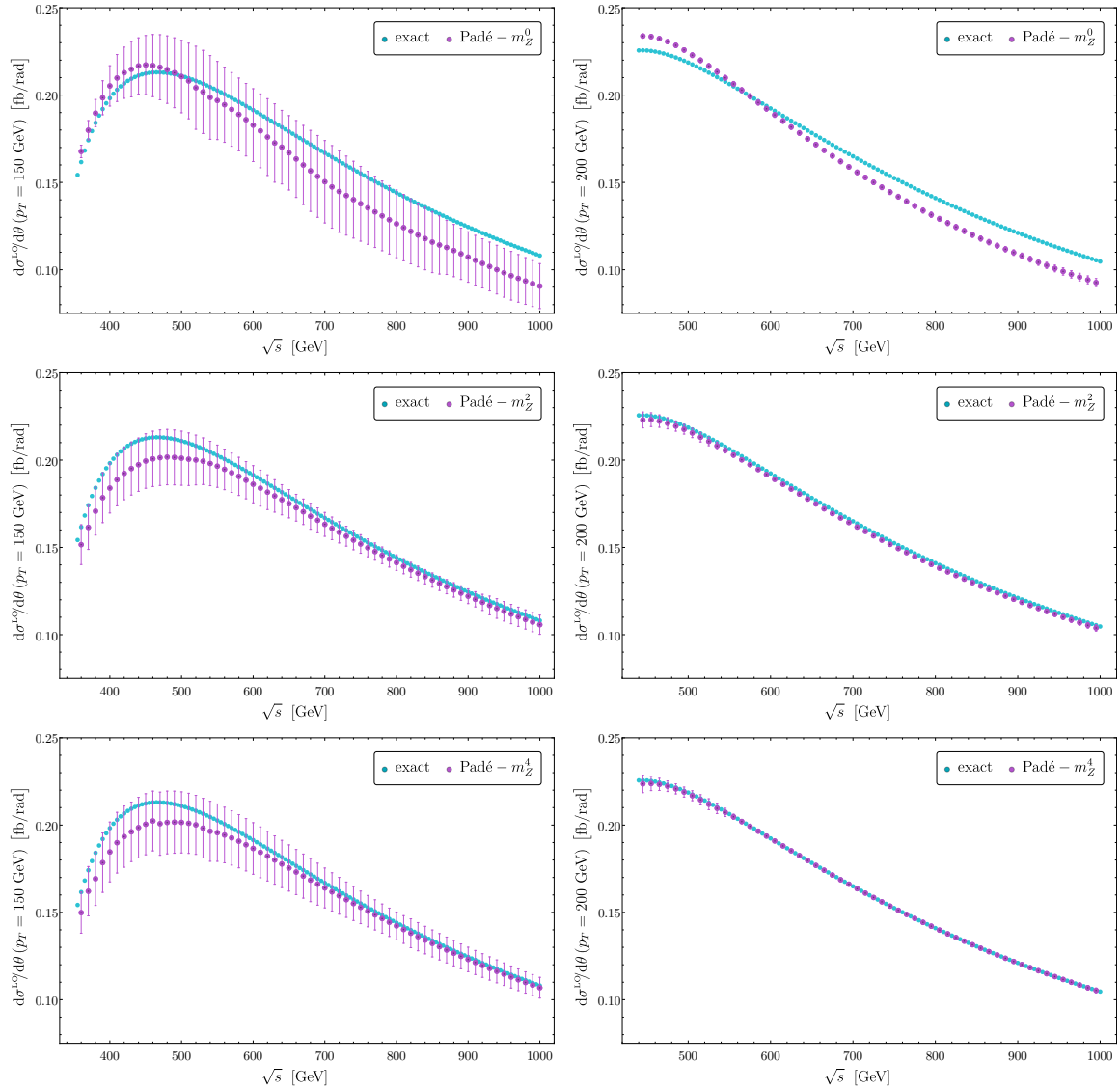


Figure 2.21: Padé approximated differential partonic cross section for fixed transverse momentum of $p_T = 150$ GeV (left panel) and $p_T = 200$ GeV (right panel) for three different expansion depths in m_Z (top to bottom: m_Z^0 , m_Z^2 and m_Z^4). Light blue dots show the exact result, purple dots with error bars show the Padé approximation.

There are of course also different ways to deal with the problem of extending a finite radius of convergence of a given expansion. In Ref. [21] and Ref. [25] for example, the authors first subtract analytic parts of the expression to add them only after the Padé approximation procedure, apply then an variable transformation contorting the complex plane into a unit circle such that branch cuts lie on the perimeter and the function to be approximated is analytic within the circle. Subsequently, Padé approximants tweaked by

an additional ‘noise parameter’ which allows to test the stability of the approximant are constructed and a criterium which Padé approximants with poles within the circle should be removed is formulated.

In this thesis, the somewhat simpler PDR Padé approach introduced above is used as it has the advantage that first it is very easy to apply, second it always returns a prediction and third it allows for a clear interpretation of its associated error.

Fig. 2.21 shows the result of the pole distance reweighted (PDR) Padé approximation of the differential partonic cross section for fixed transverse momenta. One has to stress, that the original data of the ST approximation clearly fails to describe the region of the phase space with centre-of-mass energies of $\sqrt{s} \lesssim 750$ GeV, or below $p_T \lesssim 350$ GeV.

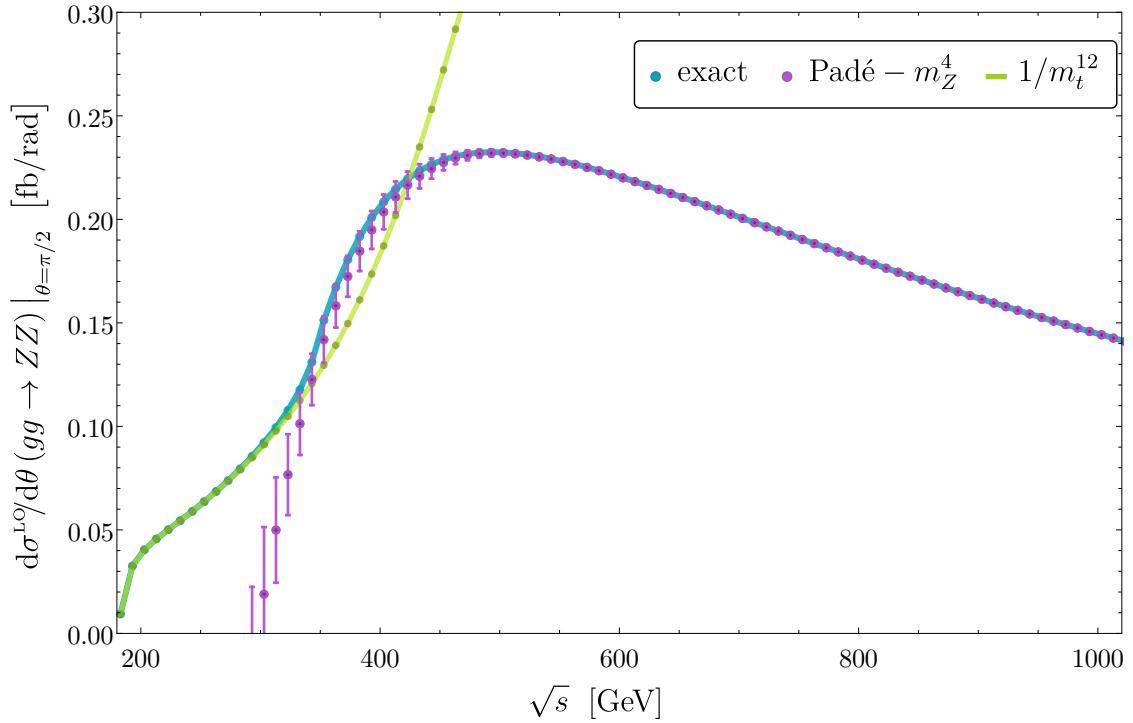


Figure 2.22.: Padé approximated differential partonic cross section for fixed scattering angle of $\theta = \pi/2$. The light blue curve shows the exact result, purple dots with error bars show the Padé approximation including the m_Z^4 corrections and connected green dots give the large top mass expansion up to m_t^{-12} .

One can see from the lower two plots in Fig. 2.21 that the Padé procedure reproduces the exact result very precisely, even for the low value of $p_T = 150$ GeV. Note, that this is a Padé in m_t and not in m_Z . This means, the error estimate of the Padé refers to the function it is supposed to reproduce which is in the case of m_Z^0 , shown in the upper two plots of Fig. 2.21 not the full result with exact dependence on m_Z but rather the top quark dependence of its massless Z boson limit. One learns from this plots, that it is indeed necessary but also sufficient to include the m_Z^4 term in the high energy description of $gg \rightarrow ZZ$ in order to

reproduce the exact result to a reasonable accuracy. The claim, that the m_Z^2 term is not sufficient is emphasized and supported by the two plots in the middle of Fig. 2.21, showing how exactly this contribution fails to land on top of the exact result. Instead, a small, but even though visible negative shift can be observed by eye.

It is impressive to see, that in Fig. 2.22 the exact result is reproduced within the given errors for all values of the centre-of-mass energy \sqrt{s} with the help of the first seven terms of the large top mass expansion and the pole-distance-reweighted Padé-enhanced high energy ST result, including $m_t^{3/2}$ and m_Z^4 corrections. Starting from this success, the same methods tested against the exact calculation at leading order will be employed in the next section for the discussion the NLO results.

2.5. NLO Results

At NLO, the process $gg \rightarrow ZZ$ has contributions from real and virtual corrections. The focus of this thesis lies on the computation of the two-loop virtual corrections. Without the real corrections, this result is incomplete and has poles in ϵ . However, using the Catani subtraction prescription introduced in section 2.3.6, these poles are removed and the NLO virtual contribution is finite. Note, that the finite part depends on the choice of the Catani term in Eq. (2.68). One can then define in analogy to the finite NLO virtual corrections considered for the case of $gg \rightarrow HH$ in Eq. (26) of Ref. [86] the quantity $\widetilde{\mathcal{V}}_{\text{fin}}$ as

$$\widetilde{\mathcal{V}}_{\text{fin}} = \frac{\alpha_s^2(\widetilde{\mu}_R) G_F^2 m_Z^4}{\pi^2 16} \times \sum_{i=1}^{20} c_i \left(\frac{C_A}{2} \left(\pi^2 - \log^2 \left(\frac{\widetilde{\mu}_R^2}{s} \right) \right) |\mathfrak{C}_i^{\text{LO}}|^2 + \left[\mathfrak{C}_i^{\text{LO}} \left(\mathfrak{C}_i^{\text{NLO}} \right)^* + \left(\mathfrak{C}_i^{\text{LO}} \right)^* \mathfrak{C}_i^{\text{NLO}} \right] \right), \quad (2.110)$$

with the definitions

$$\mathfrak{C}_i^{\text{LO}} = \mathcal{B}_i^{\text{LO}} \quad , \quad \mathfrak{C}_i^{\text{NLO}} = \mathcal{B}_i^{\text{NLO}} \Big|_{\mu^2 = -s - i0^+} = \mathcal{B}_i^{\text{NLO}, C_A} + \mathcal{B}_i^{\text{NLO}, C_F} \quad (2.111)$$

which picks out the part of the form factors \mathcal{B}_i that has no contributions proportional to the LO form factors and only the parts proportional to the color factors C_A and C_F remain. Alternatively, one could replace the Catani operator from Eq. (2.68) with \widetilde{C}_{gg} given by

$$\widetilde{C}_{gg} = \left(\frac{\alpha_s}{\pi} \right) \frac{e^{\epsilon \gamma_E}}{\Gamma(1-\epsilon)} \left[\frac{C_A}{2\epsilon^2} \left(\frac{\mu^2}{-s - i0^+} \right)^\epsilon + \frac{\beta_0}{\epsilon} \right], \quad (2.112)$$

in order to directly arrive at the form factors \mathfrak{C}_i from Eq. (2.111). Furthermore, one can restrict Eq. (2.110) to the coefficient of α_s^2 and choose for the renormalization scale $\widetilde{\mu}_R = \sqrt{s}/2$

$$\mathcal{V}_{\text{fin}} \equiv \frac{\widetilde{\mathcal{V}}_{\text{fin}}(\widetilde{\mu}_R)}{\alpha_s^2(\widetilde{\mu}_R)} \quad \text{with} \quad \widetilde{\mu}_R = \frac{\sqrt{s}}{2}. \quad (2.113)$$

Results for \mathcal{V}_{fin} will be shown in section 2.5.2. The next section shows results for the NLO form factors from Eq. (2.111).

2.5.1. NLO Form Factors

The basic pole-distance-reweighted (PDR) Padé procedure described in section 2.4.8 has been shown to work very well. In order to incorporate more information from other Padé approximants than those given in the set in Eq. (2.103) one can introduce further weights that enhances the impact from Padé approximants near the diagonal (where experience shows that diagonal ($n = m$) and close-to-diagonal Padé approximants work best) and suppresses the impact of Padé approximants that contain less information on the underlying power series than others. Starting with the known damping weight for evaluating Padé $[n_i/m_i]$ (see Eq. (2.101)) in the proximity of a pole

$$\text{pd}_i = \min_{j=1}^{m_i} |1 - x_j|_{Q(x_j)=0} \quad \text{with} \quad 0 < \overline{\text{pd}}_i \leq 1, \quad (2.114)$$

with the definition of the quadratic mean

$$\bar{a}_i = \frac{a_i^2}{\sum_j a_j^2} \quad \Rightarrow \quad \sum_i \bar{a}_i = 1, \quad (2.115)$$

one can add an enhancing weight that strengthens the impact of Padé approximants that include a larger number $n_i + m_i$ terms of the underlying power series

$$td_i = n_i + m_i \quad \text{with} \quad 0 < \bar{td}_i \leq 1, \quad (2.116)$$

and add also a weight, that dampens the influence of Padé approximants that stray too far away from the diagonal $[n_i/n_i]$ Padé

$$dd_i = |n_i - m_i| \quad \text{with} \quad 0 < (1 - \bar{dd}_i) \leq 1. \quad (2.117)$$

Combining all weights into one by setting

$$\bar{\omega}_i = \overline{pd_i td_i (1 - dd_i)}, \quad (2.118)$$

one obtains the enhanced version of the PDR, which will for convenience just be called (ePDR). Relaxing the condition in Eq. (2.104) to

$$N_{\text{high}} \geq n + m \geq N_{\text{low}} \quad \text{and} \quad n + m - |n - m| \geq N_{\text{low}}, \quad (2.119)$$

with $N_{\text{high}} = 16$ and $N_{\text{low}} = 10$, one obtains a much larger set of 28 different Padé approximants:

$$\left(\begin{array}{cccccc} [5/5] & [5/6] & [6/5] & [5/7] & [7/5] & [6/6] & [5/8] \\ [8/5] & [6/7] & [7/6] & [5/9] & [9/5] & [6/8] & [8/6] \\ [7/7] & [5/10] & [10/5] & [6/9] & [9/6] & [5/11] & [11/5] \\ [7/8] & [8/7] & [6/10] & [10/6] & [7/9] & [9/7] & [8/8] \end{array} \right). \quad (2.120)$$

The resulting NLO plots for the form factors at fixed scattering angles $\theta = \pi/2$ are shown in Figs. 2.23 and 2.24. Double dashed lines show the real parts of the form factors, single dashed lines show the imaginary part. The LT expansion has triple dots, and the m_i^{30} and m_i^{32} terms of the ST expansion have single and double dots, respectively. The ePDR Padé results from the ST expansions are shown as solid lines. The form factors show all a similar convergence behavior where the imaginary part diverges for centre-of-mass energies below $\sqrt{s} \lesssim 700$ GeV and the real part diverges at about centre-of-mass energies below $\sqrt{s} \lesssim 750$ GeV. The ePDR Padé seems to give a sensible result which remains to be compared against a numerical exact calculation.

2. Z-Boson Pair Production

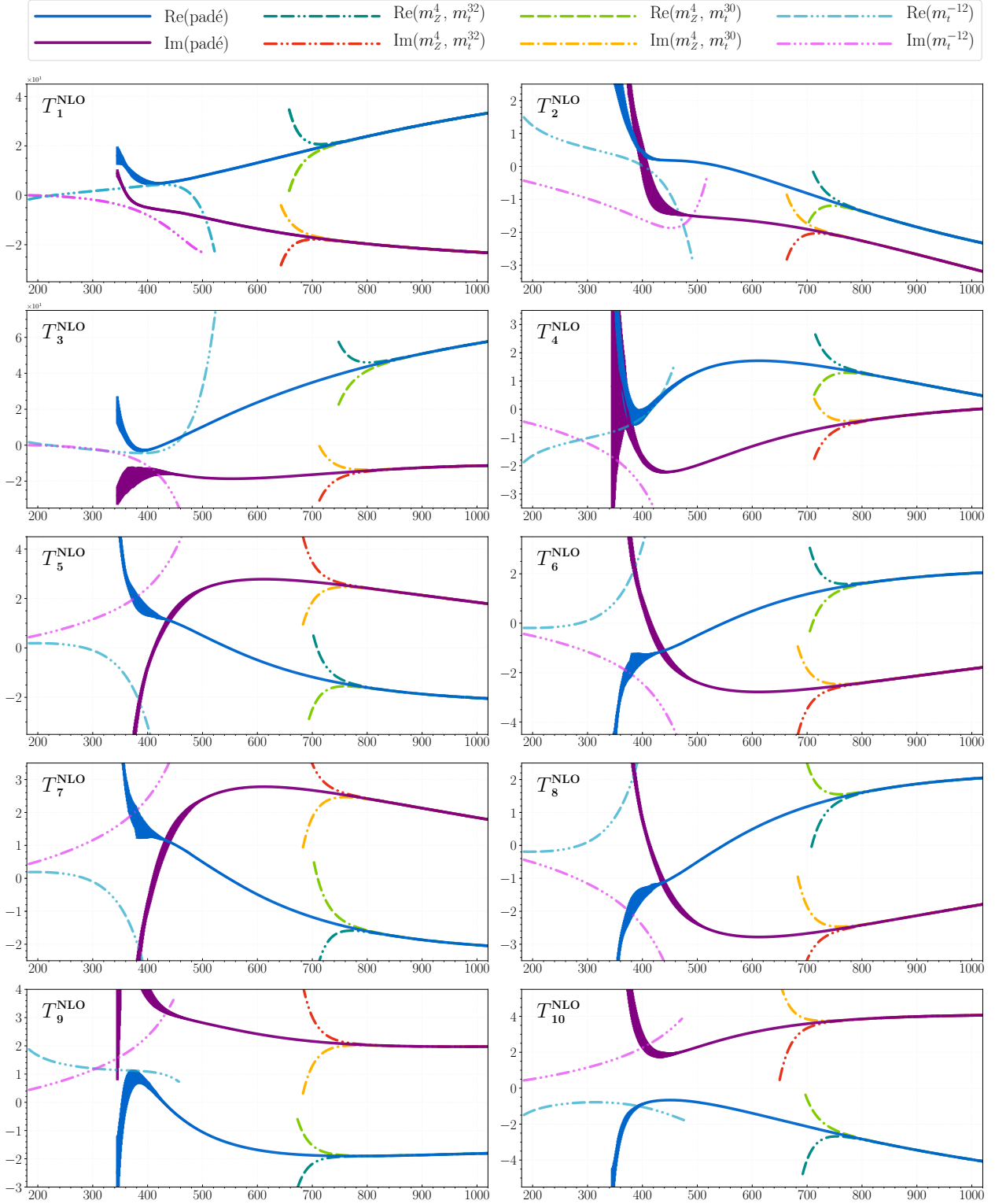


Figure 2.23.: Comparison of the real and imaginary parts of first ten NLO form factors $\mathbb{C}_1^{\text{NLO}} \dots \mathbb{C}_{10}^{\text{NLO}}$ from the extended pole-distance-reweighted Padé result (solid lines with error bars), large top mass expansion (dotted line) and high energy expansion (dash-dotted lines) at a scattering angle of $\theta = \frac{\pi}{2}$. The x -axis shows the partonic centre-of-mass energy of the process in GeV.

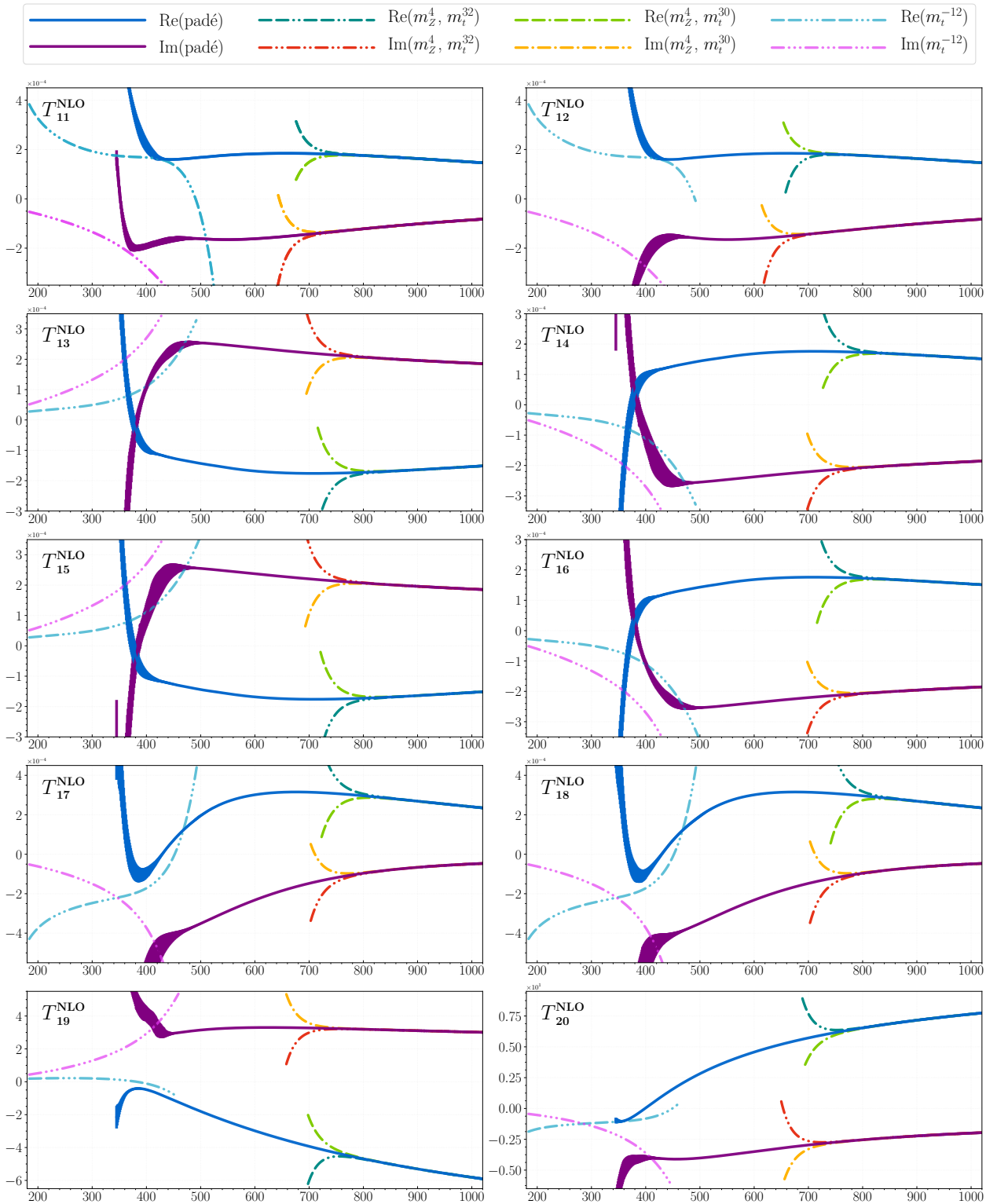


Figure 2.24.: Comparison of the real and imaginary parts of last ten NLO form factors $\mathcal{C}_{11}^{\text{NLO}} \dots \mathcal{C}_{20}^{\text{NLO}}$ from the extended pole-distance-reweighted Padé result (solid lines with error bars), large top mass expansion (dotted line) and high energy expansion (dash-dotted lines) at a scattering angle of $\theta = \frac{\pi}{2}$. The x -axis shows the partonic centre-of-mass energy of the process in GeV.

2.5.2. NLO Virtual Finite XS

The next step is the combination of all results into the finite NLO virtual part of the partonic cross section \mathcal{V}_{fin} as introduced at the beginning of the section.

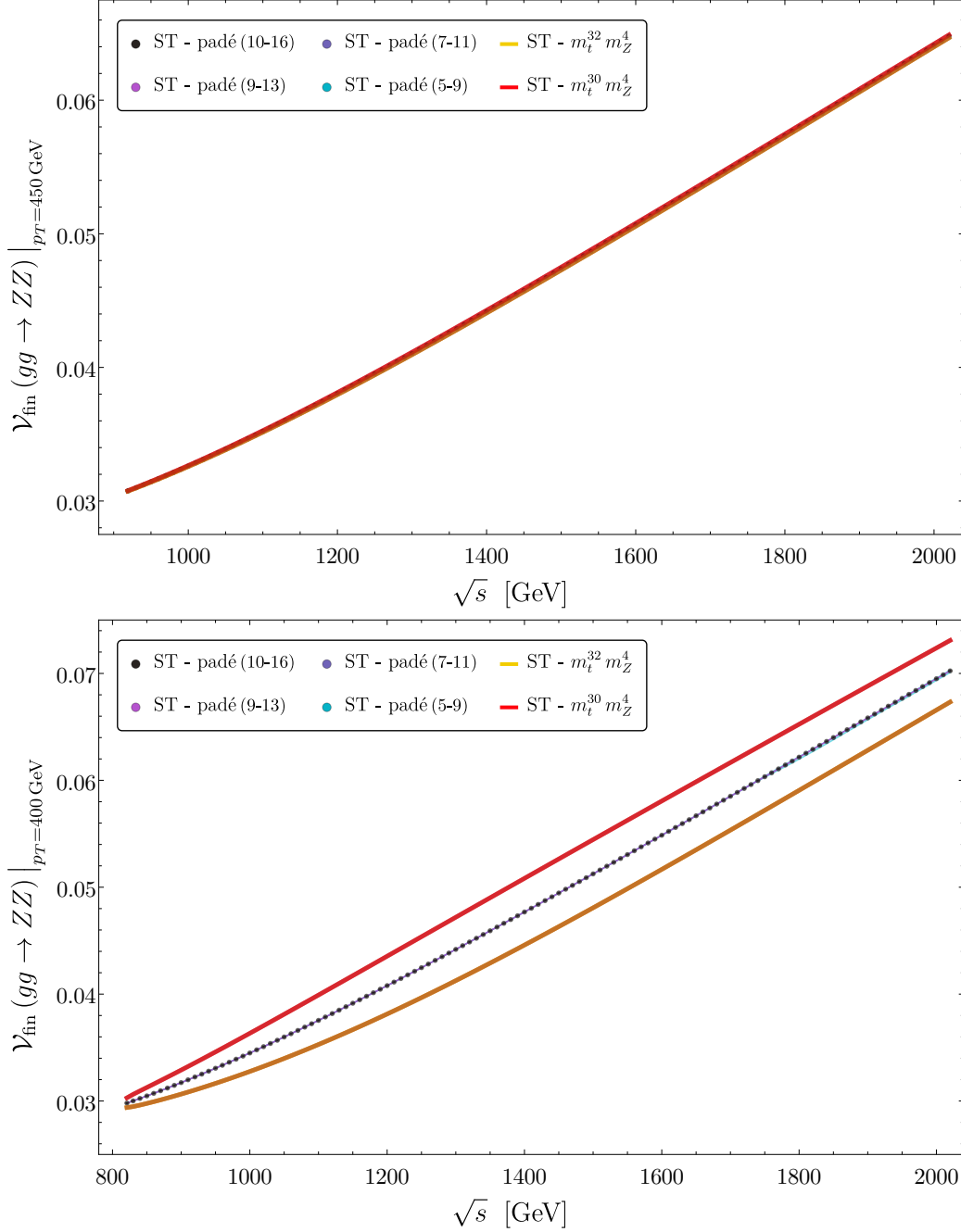


Figure 2.25.: Result for \mathcal{V}_{fin} for fixed transverse momentum of $p_T = 450$ GeV (upper panel) and $p_T = 400$ GeV (lower panel). Black dots with error bars show the result of the ePDR Padé procedure. Colored bands give the error for different choices of Padé sets. Red and yellow lines give in addition the result of the ST expansion up to m_t^{30} and m_t^{32} , respectively.

Fig. 2.25 shows in its upper panel \mathcal{V}_{fin} as a function of \sqrt{s} for a fixed value of $p_T = 450$ GeV. Note, that lowest kinematically allowed value for the centre-of-mass energy \sqrt{s} is given by $\sqrt{s} \geq 2\sqrt{p_T^2 + m_Z^2}$, thus for $p_T = 450$ GeV, the plot starts only from $\sqrt{s} \gtrsim 920$ GeV. At these energies, the high energy expansion works very well and both the m_t^{30} and m_t^{32} result agree on each other. Therefore, all Padé approximants, shown for

$$\{N_{\text{low}}, N_{\text{high}}\} \in \{\{5, 9\}, \{7, 11\}, \{9, 13\}, \{10, 16\}\}, \quad (2.121)$$

in Eq. (2.119), lie just on top of the ST expansion results. For $p_T = 400$ GeV, shown in the lower panel of Fig. 2.25, the two highest expansion depths in m_t drift apart. However, even Padé approximants with $N_{\text{low}} = 5$ and $N_{\text{high}} = 9$ are tightly constrained to a result that lies between the ST curves for m_t^{30} and m_t^{32} .

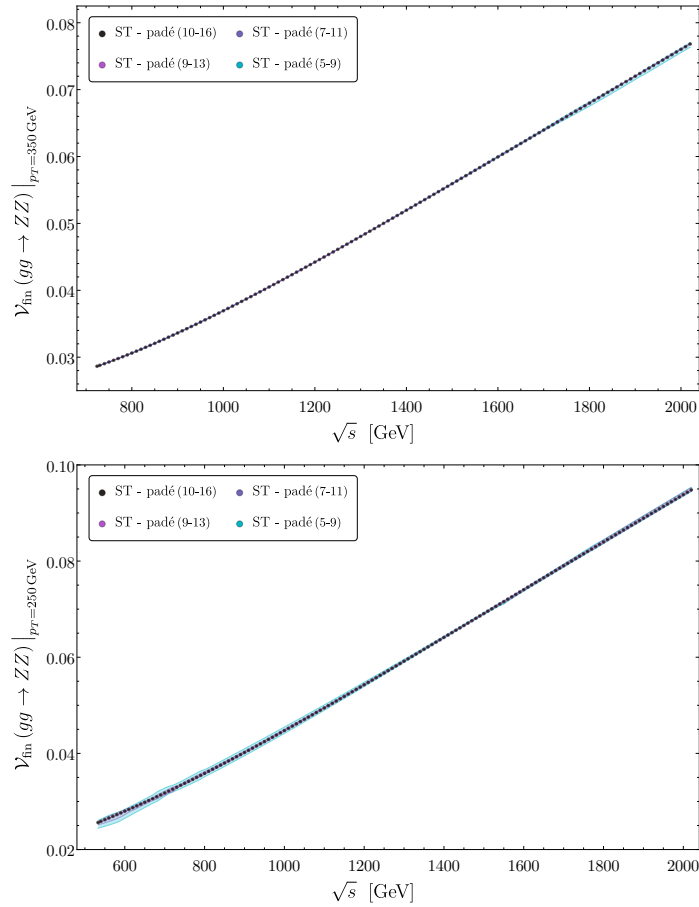


Figure 2.26.: Result for \mathcal{V}_{fin} for fixed transverse momentum of $p_T = 350$ GeV (upper panel) and $p_T = 250$ GeV (lower panel). Black dots with error bars show the result of the ePDR Padé procedure. Colored bands give the error for different choices of Padé sets.

Even though a similarly tight agreement of the results of the ePDR Padé approximants with negligible uncertainty estimates can be observed when going to lower values of p_T (see Fig. 2.26 for $p_T = 350$ GeV (top) and $p_T = 250$ GeV (bottom)) it is clear that starting from $p_T \lesssim 350$ GeV, the ST expansion in its ‘raw’ form cannot be used alone to describe

\mathcal{V}_{fin} as it lies outside of the range shown Fig. 2.26. At $p_T = 200$ GeV one can see for the first time a clear improvement, if higher order terms in the m_t expansion are considered for the construction of the Padé approximants. The light blue band in Fig. 2.27 has the least information on the underlying ST expansion (with $N_{\text{low}} = 5$ and $N_{\text{high}} = 9$ in the condition from Eq. (2.119)), and develops also the broadest uncertainty band which however encloses the much narrower predictions of ePDR Padé results with higher values for N_{low} and N_{high} in violet, purple and black, respectively.

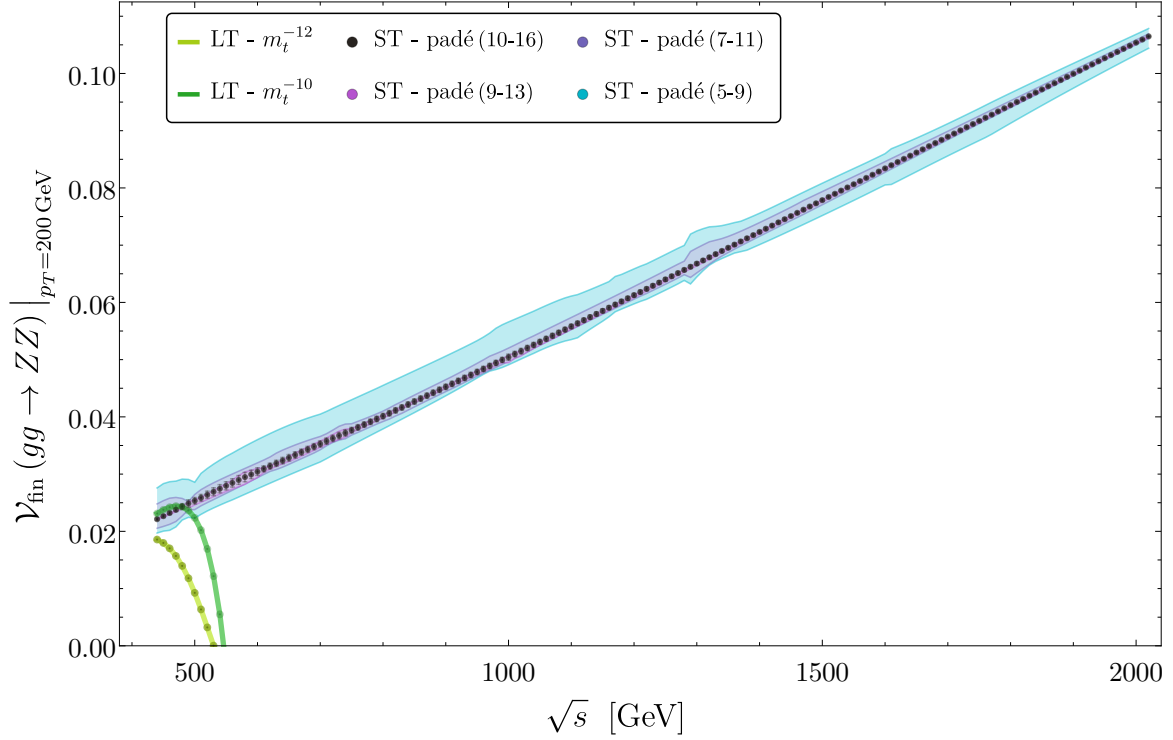


Figure 2.27.: Result for \mathcal{V}_{fin} for fixed transverse momentum of $p_T = 200$ GeV. Black dots with error bars show the result of the ePDR Padé procedure. Colored bands give the error for different choices of Padé sets, light and dark green lines give in addition the result of the LT expansion up to m_t^{-12} and m_t^{-10} , respectively.

Progressing even further towards small transverse momenta of $p_T = 150$ GeV, one observes in the upper panel of Fig. 2.28 a thick error band for the best prediction in form of the black 10-16 ePDR Padé result. Considering less terms in m_t during the construction of the ePDR Padés (purple to violet to light blue) produces less stable predictions and the uncertainty bands get more ‘spiky’. Note that for low centre-of-mass energies \sqrt{s} the order of magnitude from the LT result matches that of the ePDR Padé results. Interpreting this as a sign that the procedure of extending the radius of convergence works well, one can for completeness also compute the $p_T = 100$ GeV plot for \mathcal{V}_{fin} which includes the top quark production threshold at $\sqrt{s} = 346$ GeV, shown as a red line in Fig. 2.28. Very far away from the original region of convergence of the ST expansion, the $p_T = 100$ GeV curve does not give a very trust-inspiring prediction, it matches however the LT expansion in the region where that is valid and comes with a very generous uncertainty estimate.

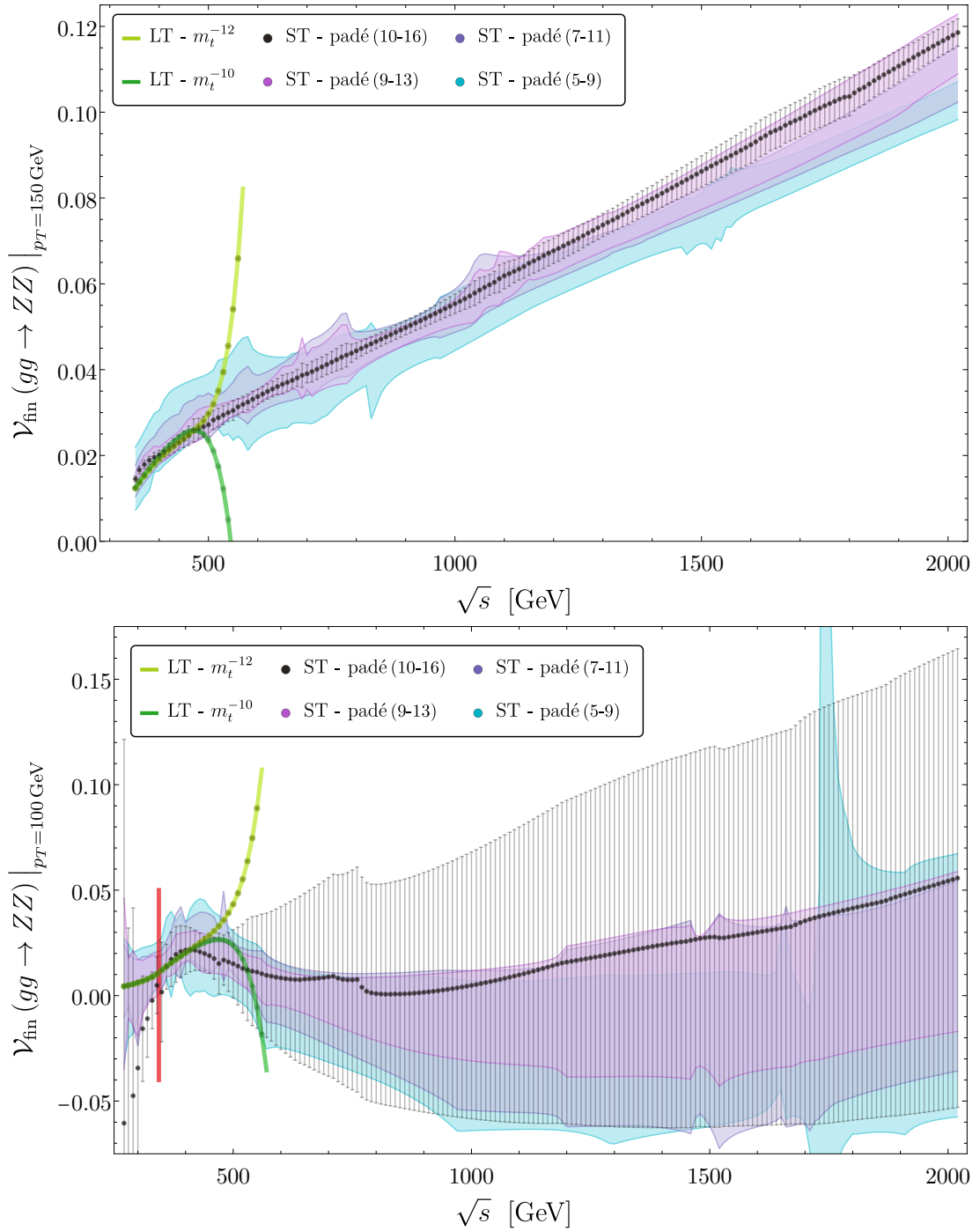


Figure 2.28.: Result for \mathcal{V}_{fin} for fixed transverse momentum of $p_T = 150$ GeV (upper panel) and $p_T = 100$ GeV (lower panel). Black dots with error bars show the result of the ePDR Padé procedure. Colored bands give the error for different choices of Padé sets. Light and dark green lines give in addition the result of the LT expansion up to m_t^{-12} and m_t^{-10} , respectively. The lower plot shows furthermore a red line which marks the production threshold for pairs of top quarks.

One can learn from these plots, that the farther one wants to stretch beyond the initial radius of convergence, the more terms one needs to incorporate in the Padé procedure. With m_t^{32} , one seems to be able to extend the initial radius of convergence which is about $p_T \lesssim 350$ GeV by roughly 200 GeV down to at least a reasonable prediction for $p_T = 150$ GeV. It is interesting to note that, starting from the ST expansion including m_t^{32} , one can indeed produce predictions down to the top quark production threshold, even if the uncertainty estimates for such low values of \sqrt{s} get rather large.

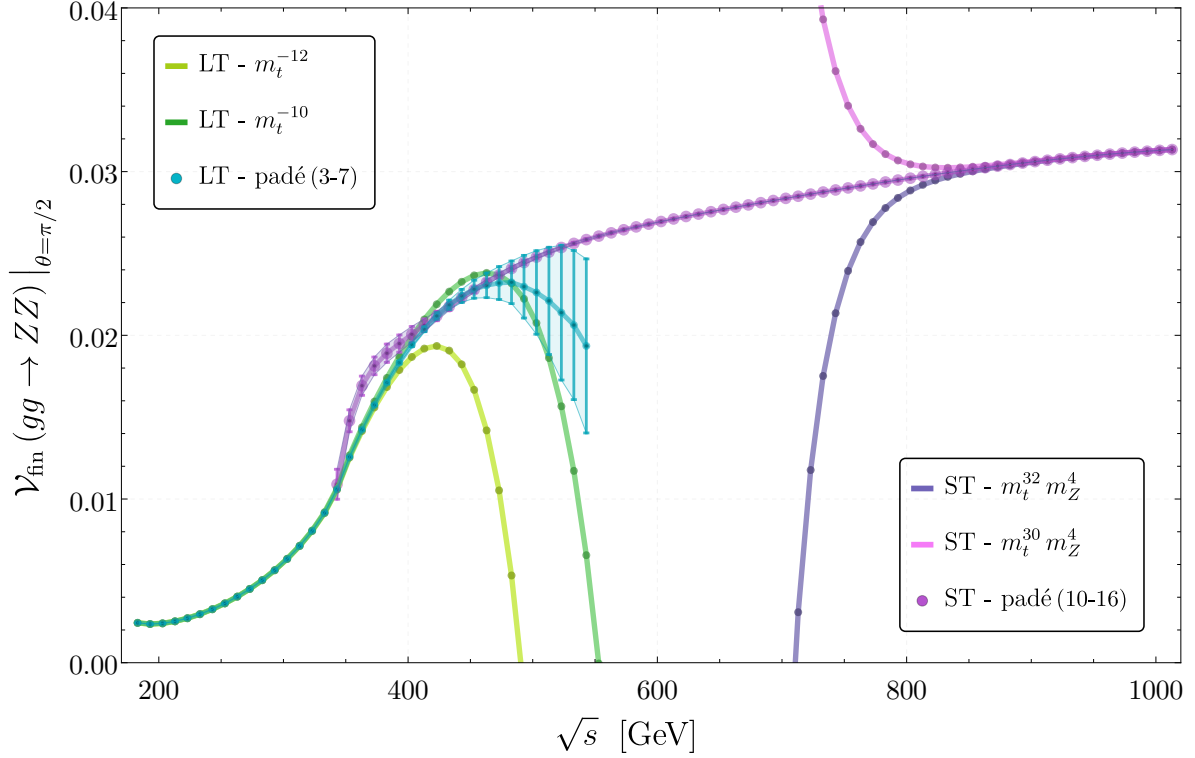


Figure 2.29.: Padé approximated differential partonic cross section for fixed scattering angle of $\theta = \pi/2$. Pink and Dark violet curves show the ST result for m_t^{30} and m_t^{32} , purple gives the ePDR Padé result. The LT result is shown for the curves m_t^{-10} (dark green) and m_t^{-12} (light green). The ePDR Padé result for the LT series is shown in greenish blue.

As a final plot, \mathcal{V}_{fin} is shown in Fig. 2.29 as a function of \sqrt{s} for a fixed scattering angle $\theta = \pi/2$. It seems, that at least for $\theta = \pi/2$ the combination of the ST and LT expansions to the orders calculated in this thesis is sufficient to give a complete description of \mathcal{V}_{fin} for all centre-of-mass energies. It is however also visible, that one would profit most from a threshold expansion or a direct numeric calculation in the region where both Padé approximations overlap. Note again, that \mathcal{V}_{fin} shows only the top quark mass effects and does neither contain contributions from light quarks only nor the interference term between light quarks and the top quark.

2.6. Conclusion and Outlook

In this chapter, the top quark induced corrections to the process $gg \rightarrow ZZ$ were analyzed for both their low- and high-energy NLO behavior. In order to do so, the tensor structure and belonging projectors were derived. Subsequently, the corresponding form factors were calculated at LO exact, and at LO and NLO in the low energy limit of a large top quark mass, including terms up to m_t^{-12} , and in the high energy limit of large centre-of-mass energies and large transverse momenta, as double series in m_Z and m_t up to m_Z^4 and m_t^{32} . The results for both expansions could at LO be compared against the exact calculation. Perfect agreement was found in their supposed region of convergence. Outside of their region of convergence a 'gap' starting shortly below the top quark pair production threshold around 340 GeV and stretching up to 750 GeV could be observed. Furthermore, it could be shown, that using Padé approximations in combination with a newly developed reweighting by pole distance method the region of convergence of the high energy expansion could be extended and for $\theta = \pi/2$ the 'gap' can even be closed and the exact result is reproduced with stable central values and realistic uncertainty estimates.

One observation that could be made was that it is necessary to include the m_Z^4 term in the ST expansion in order to reproduce the exact result below the permille level. Including only m_Z^2 yields an offset of more than 1%.

The analytic NLO result can in ST case be expressed in terms of only a few harmonic polylogarithms with explicit real and imaginary parts. Moreover, it could be observed, that the imaginary part of the amplitude contains at NLO odd powers of m_t . These could be verified against numerical calculations on the master integral level. A finite UV renormalized and IR subtracted result for the virtual corrections to the NLO partonic differential cross section was obtained. Again, the methods that were successfully tested at LO were employed to make predictions on an enhanced region of convergence for the behavior of the form factors and the virtual finite part of the partonic differential cross section.

As a next step it would be interesting to see if the 'gap' near the threshold could be closed by calculations like the 'small p_T expansion' performed in Ref. [87] or with the help of upcoming numerical calculations with full top quark mass dependence, announced in Ref. [88]. It is then also important to include available results from the literature for the light quark contribution to complete the virtual corrections at NLO. Finally, the publication of a C++ program is planned that allows the interpolation of the virtual finite piece of the partonic cross section on the basis of precomputed phase space points and that can be used for fast computations of hadronic cross sections.

3. Higgs-Boson Pair Production

3.1. Introduction

In the Standard Model of particle physics (SM), the Higgs boson is introduced as a scalar doublet field Φ , with the potential

$$V(\Phi) = \mu^2 \Phi^\dagger \Phi + \lambda (\Phi^\dagger \Phi)^2 . \quad (3.1)$$

For $\mu^2 < 0$ and $\lambda > 0$, the potential in Eq. (3.1) has minima at $\Phi = v = \sqrt{\frac{-\mu^2}{\lambda}}$. Choosing one and expanding the fields around it corresponds to spontaneously breaking the electroweak symmetry by which the electroweak gauge bosons acquire their masses as

$$m_W^2 = \frac{g_W^2 v^2}{4} \quad \text{and} \quad m_Z^2 = \frac{g_W^2 v^2}{4 \cos^2(\theta_W)} = \frac{m_W^2}{\cos^2(\theta_W)} . \quad (3.2)$$

The potential takes then the form

$$V(H) = \lambda v^2 H^2 + \lambda v H^3 + \frac{1}{4} \lambda H^4 = \frac{1}{2} m_H^2 H^2 + \lambda v H^3 + \frac{1}{4} \lambda H^4 , \quad (3.3)$$

where the association of the term quadratic in the Higgs field H in Eq. (3.3) with the mass term of the Higgs boson leads to the relation $m_H^2 = 2\lambda v^2$. Measuring the electroweak coupling g_W , the mass of the W boson and the mass of the Higgs boson, one obtains values for both the vacuum expectation value and the parameter λ from the Higgs potential as

$$v = \frac{2m_W}{g_W} = \sqrt{\sqrt{2} G_F} \approx 246 \text{ GeV} \quad \text{and} \quad \lambda = \frac{m_H^2}{2v^2} \approx 0.13 , \quad (3.4)$$

where G_F and m_H are defined in Eqs. (3.29) and (3.31). The cubic and quartic terms in Eq. (3.3) correspond to Higgs boson self interactions. The process of Higgs boson pair production is sensitive to the coupling of three Higgs bosons and gives therefore access to λ . The ratio

$$\kappa_\lambda = \frac{\lambda^{\text{exp}}}{\lambda^{\text{SM}}} , \quad (3.5)$$

give the ‘SM’-likeness of λ^{exp} from collider experiments. Current bounds from CMS [4]

$$-11.8 < \kappa_\lambda < 18.8 \quad (3.6)$$

and ATLAS [5]

$$-5.0 < \kappa_\lambda < 12.0 \quad (3.7)$$

show, that it is a very difficult measurement and that the LHC in its current form will not be able to measure λ with a very high precision. However, with both the upcoming HL-LHC and a possible FCC, it is necessary to provide precise predictions for the Higgs pair production cross section.

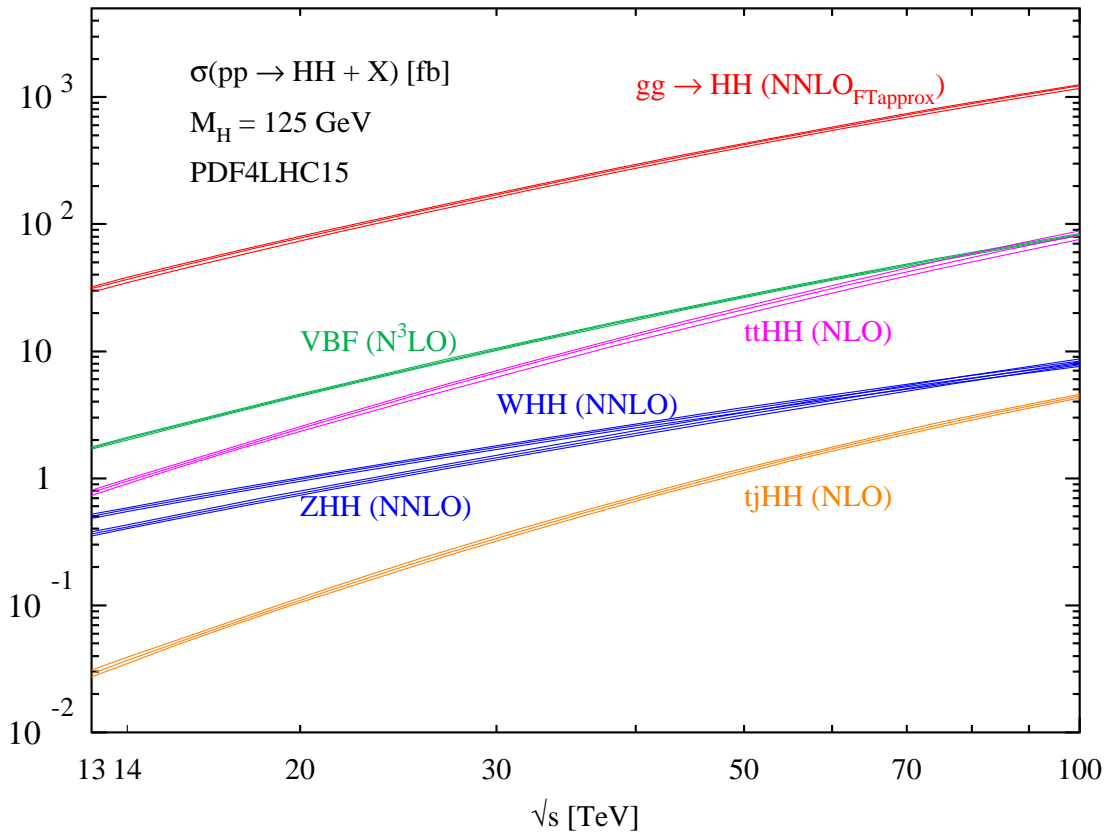


Figure 3.1.: Total hadronic cross sections as a function of the hadronic centre of mass energy \sqrt{s} . The different production channels are shown in blue for Higgs-strahlung, pink for associated production with $t\bar{t}$, green for vector boson fusion and red for gluon fusion. Taken from Ref. [89].

Figure 3.1 shows, that from all channels that participate in the production of two Higgs bosons at proton-proton colliders, the gluon fusion channel (shown in red) has by far the largest cross section since it gets enhanced by the large gluon luminosity at the LHC. Therefore, the process $gg \rightarrow HH$ will be discussed in the rest of this chapter.

The process $gg \rightarrow HH$ has attracted a lot of attention during the last years and only a selection of those many publications will be shown in the following. At LO, the process has been considered in Refs. [90, 91]. Note, that LO refers here to the one-loop computation. At NLO, exact results with the full dependence on all scales are available from numerical calculations in Refs. [92–94]. In Refs. [95, 96] NLO real radiation top quark effects were computed. The limit $m_t \rightarrow \infty$ (Higgs Effective Field Theory) was considered in Ref. [97] at NLO and in Refs. [98–100] at NNLO. A large top mass expansion up to m_t^{12} was done at NLO in Refs. [101, 102]. A combination of a threshold expansion with a large top mass expansion on the base of Padé approximants was performed in Ref. [25]. Soft gluon resummation was considered at NNLL for NLO and NNLO in Refs. [103, 104]. In Ref. [105] NNLO results from the heavy top quark limit were combined with the full top mass dependent NLO results and NNLO real radiation corrections. A small transverse

momentum expansion at NLO was done in Ref. [87]. NNLO real and virtual corrections in the limit of a large top mass were considered in Ref. [106, 107]. See also Ref. [108] for recent developments in the infinite top quark limit.

In this thesis, the top quark induced LO and NLO corrections to the process $gg \rightarrow HH$ are computed in the limit of high energies. Note, that the content of this chapter is based on the publications in Refs. [41, 42, 86, 109].

In section 3.2 the kinematics of the process is discussed and the computational details explained. Subsequently, in section 3.3 the form factors are examined. At LO, they are compared against the exact result. Furthermore is the expansion in the Higgs boson mass and the dependence of the form factors on the scattering angle addressed. Section 3.4 shows the results for the finite virtual NLO piece of the partonic cross section and compares this against numerical results from the literature. Moreover, a combination of the results of the high energy expansion and the numerical calculation is built. Section 3.5 gives predictions for the hadronic cross section. A short conclusion is found in section 3.6.

3.2. $gg \rightarrow HH$

3.2.1. The Process $gg \rightarrow HH$

The process of double Higgs boson production via gluon fusion is a $2 \rightarrow 2$ process with two incoming gluons with momenta p_1 and p_2 and two outgoing¹ Higgs bosons with momenta $-p_3$ and $-p_4$ as depicted in Fig. 3.2.

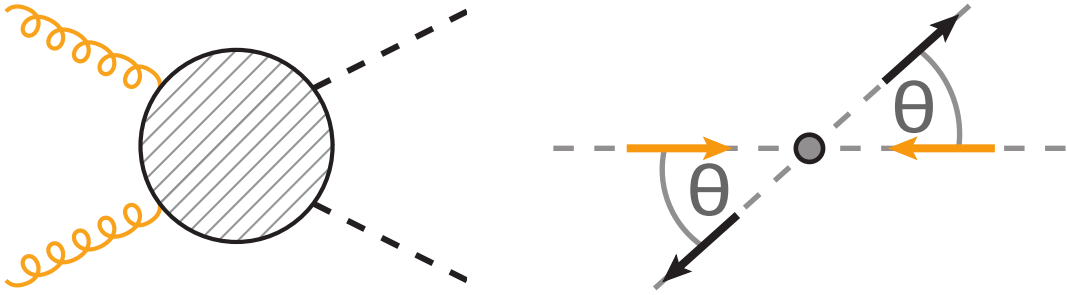


Figure 3.2.: Left: Example graph for the process $gg \rightarrow HH$. Curly lines indicate gluons, dashed lines Higgs bosons. The shaded area in the center of the diagram represents one- and two-loop QCD insertions. Right: Schematic depiction in the center of mass frame of the incoming gluons with momenta p_1 and p_2 along the beam line and the outgoing Higgs bosons with momenta $-p_3$ and $-p_4$, pointing away from the interaction point at an angle θ with respect to the beam line.

Using the centre of mass frame shown in the right panel of Fig. 3.2, with a partonic centre of mass energy \sqrt{s} , the momenta of the two incoming gluons and those of the two outgoing Higgs bosons take the form

$$p_1 = \begin{pmatrix} \sqrt{s}/2 \\ \sqrt{s}/2 \\ 0 \\ 0 \end{pmatrix}, \quad p_2 = \begin{pmatrix} \sqrt{s}/2 \\ -\sqrt{s}/2 \\ 0 \\ 0 \end{pmatrix}, \quad p_3 = \begin{pmatrix} \sqrt{q^2 + m_H^2} \\ q \cos(\theta) \\ q \sin(\theta) \\ 0 \end{pmatrix}, \quad p_4 = \begin{pmatrix} \sqrt{q^2 + m_H^2} \\ -q \cos(\theta) \\ -q \sin(\theta) \\ 0 \end{pmatrix}, \quad (3.8)$$

where the unknown variable q^2 in the momenta of the Higgs bosons is determined by energy-momentum conservation to be $q^2 = \frac{s}{4} - m_H^2$. In this thesis, all external particles are assumed to be on-shell which gives in addition the relations

$$p_1^2 = p_2^2 = 0 \quad \text{and} \quad p_3^2 = p_4^2 = m_H^2. \quad (3.9)$$

¹In this thesis, both the momenta of incoming and outgoing particles are defined as incoming.

3. Higgs-Boson Pair Production

From eqs. (3.8) and (3.9) one can then build the kinematic variables s , t and u

$$s = (p_1 + p_2)^2 = s, \quad (3.10)$$

$$t = (p_1 + p_3)^2 = -\frac{s}{2} \left(1 - 2\frac{m_H^2}{s} - \cos(\theta) \sqrt{1 - 4\frac{m_H^2}{s}} \right), \quad (3.11)$$

$$u = (p_2 + p_3)^2 = -\frac{s}{2} \left(1 - 2\frac{m_H^2}{s} + \cos(\theta) \sqrt{1 - 4\frac{m_H^2}{s}} \right), \quad (3.12)$$

that form the so called Mandelstam variables. They satisfy the equation

$$s + t + u = 2m_H^2. \quad (3.13)$$

So far, the general setup of the process $gg \rightarrow HH$ and its kinematics are very similar to those of Z boson pair production via gluon fusion from chapter 2. The Lorentz structure of the two processes is, however, completely different; by swapping the two Z bosons for two Higgs bosons, one trades two spin 1 particles for two spin 0 particles such that the amplitude for Higgs boson pair production via gluon fusion carries only the Lorentz indices of the incoming gluons:

$$\mathcal{A}_{ggHH} = \sum_{\lambda_1, \lambda_2} \mathcal{E}_\mu^{\lambda_1} \mathcal{E}_\nu^{\lambda_2} \mathcal{A}_{ggHH}^{\mu\nu}, \quad (3.14)$$

where $\mathcal{E}_\mu^{\lambda_1}$ denotes the polarization vector of one of the external gluons with momentum p_1 and polarization λ_1 , as a short hand notation for $\mathcal{E}_\mu(\lambda_1, p_1)$. This means that the corresponding tensor structure is much simpler than the one discussed in section 2.2.2 and can be built from the metric tensor $g^{\mu\nu}$ and combinations of external momenta $p_i^\mu p_j^\nu$ with $i, j \in \{1, 2, 3\}$ alone. Transversality of the polarization vectors to their associated momenta

$$\mathcal{E}_\mu^{\lambda_1} p_1^\mu = 0, \quad \mathcal{E}_\nu^{\lambda_2} p_2^\nu = 0, \quad (3.15)$$

reduces the set of contributing tensors to five, which can further be related to each other by Ward-identities. One finds that the process $gg \rightarrow HH$ has only two independent tensor structures [90]:

$$\begin{aligned} T_1^{\mu\nu} &= g^{\mu\nu} - \frac{1}{(p_1 \cdot p_2)} p_2^\mu p_1^\nu, \\ T_2^{\mu\nu} &= g^{\mu\nu} + \frac{2}{p_T^2} p_3^\mu p_3^\nu + \frac{m_H^2}{p_T^2 (p_1 \cdot p_2)} p_2^\mu p_1^\nu + \frac{2(p_1 \cdot p_3)}{p_T^2 (p_1 \cdot p_2)} p_2^\mu p_3^\nu + \frac{2(p_2 \cdot p_3)}{p_T^2 (p_1 \cdot p_2)} p_3^\mu p_1^\nu, \end{aligned} \quad (3.16)$$

where the transverse momentum squared is given by

$$p_T^2 = \frac{tu - m_H^2}{s} = \frac{s}{2} \sqrt{1 - \frac{4m_H^2}{s}} \sin(\theta). \quad (3.17)$$

The structures in eq. (3.16) are chosen such, that they are orthogonal in the limit $d \rightarrow 4$

$$\sum_{\lambda_1, \lambda_2} \mathcal{E}_\mu^{\lambda_1} \mathcal{E}_\nu^{\lambda_2} T_a^{\mu\nu} \mathcal{E}_{\mu'}^{\lambda_1*} \mathcal{E}_{\nu'}^{\lambda_2*} T_b^{*\mu'\nu'} \stackrel{d \rightarrow 4}{=} c_a \delta_{ab} \quad \text{with} \quad c_a = d - 2, \quad (3.18)$$

where the polarization sums for the external gluons are given by

$$\sum_{\lambda_1} \mathcal{E}_\mu(\lambda_1, p_1) \mathcal{E}_{\mu'}^*(\lambda_1, p_1) = -g_{\mu\mu'} \quad , \quad \sum_{\lambda_2} \mathcal{E}_\nu(\lambda_2, p_2) \mathcal{E}_{\nu'}^*(\lambda_2, p_2) = -g_{\nu\nu'} . \quad (3.19)$$

Note that as in the case of $gg \rightarrow ZZ$, the orthogonality of the tensor structures given in eq. (3.16) holds only in the limit $d \rightarrow 4$. The projectors for the tensor structures $T_1^{\mu\nu}$ and $T_2^{\mu\nu}$ can easily be derived in analogy to section 2.2.3 and are given in appendix B.1.

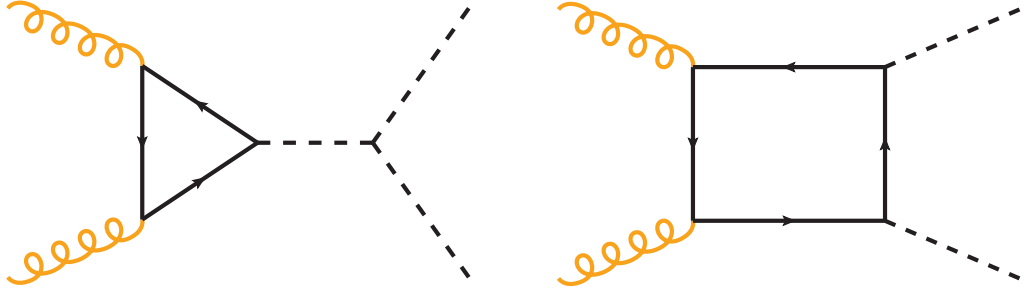


Figure 3.3.: Triangle type (left) and box type (right) diagrams contributing at LO to \mathcal{A}_{ggHH} . Curly lines denote gluons, dashed lines Higgs bosons and solid lines top quarks.

It is interesting to keep contributions that are proportional to the triple Higgs boson coupling separated from the rest. Since they appear always together with a top quark triangle loop as shown in the example diagram on the left hand side of fig. 3.3, these contributions are dubbed ‘triangle’ contributions. The rest of the diagrams fall in a class coming with a top quark box, as shown on the right hand side of fig. 3.3 and are therefore called ‘box’ contributions. Triangle diagrams contribute only to the coefficient of $T_1^{\mu\nu}$, therefore the amplitude from eq. (3.14) can be written

$$\mathcal{A}_{ggHH} = \sum_{\lambda_1, \lambda_2} \mathcal{E}_\mu^{\lambda_1} \mathcal{E}_\nu^{\lambda_2} \delta_{ab} T_F \frac{\alpha_s(\mu)}{\pi} \frac{G_F}{2\sqrt{2}} s [F_1 T_1^{\mu\nu} + F_2 T_2^{\mu\nu}] , \quad (3.20)$$

with the explicit splitting into triangle and box parts according to

$$F_1 = \frac{3m_H^2}{s - m_H^2} F_{\text{tri}} + F_{\text{box1}} \quad \text{and} \quad F_2 = F_{\text{box2}} . \quad (3.21)$$

Here, μ is the renormalization scale, $T_F = \frac{1}{2}$ and δ_{ab} carries the colour indices of the external gluons. It is convenient to extract a factor s from the three form factors F_{tri} , F_{box1} and F_{box2} since this will render them dimensionless and furthermore cancel against powers of s in the flux factor of the cross section. As the right part of the triangle diagram shown in fig. 3.3 always factorizes, one can in addition pull out the Higgs boson propagator from

3. Higgs-Boson Pair Production

F_{tri} and also make the proportionality of the triple Higgs boson coupling to its squared mass m_H^2 explicit. Note that whenever in this thesis an expansion in the Higgs boson mass m_H is performed, the expansion applies only to the three form factors F_{tri} , F_{box1} and F_{box2} . The prefactor in front of F_{tri} in eq. (3.21) is always kept exact. The form factors admit an expansion in the strong coupling constant α_s ,

$$F_i = F_i^{(0)} + \frac{\alpha_s^{(5)}(\mu)}{\pi} F_i^{(1)} + \mathcal{O}\left(\alpha_s^{(5)}(\mu)^2\right). \quad (3.22)$$

The partonic cross section of the process $gg \rightarrow HH$ is then defined as the integral

$$\sigma_{\text{part}}(s_{\text{part}}) = \int_{t(\theta_{\text{min}})}^{t(\theta_{\text{max}})} \frac{d\sigma}{dt} dt = \int_0^\pi \frac{d\sigma}{dt} \frac{dt}{d\theta} d\theta, \quad (3.23)$$

where the integration limits $t(\theta_{\text{min}})$ and $t(\theta_{\text{max}})$ can be obtained from eq. (3.11) at the extreme values of the scattering angle $\theta \in [0, \pi]$

$$t(\theta_{\text{min}} = 0) = -\frac{s}{2} \left(1 - \frac{2m_H^2}{s} - \sqrt{1 - \frac{4m_H^2}{s}} \right) \quad (3.24)$$

$$t(\theta_{\text{max}} = \pi) = -\frac{s}{2} \left(1 - \frac{2m_H^2}{s} + \sqrt{1 - \frac{4m_H^2}{s}} \right). \quad (3.25)$$

and the Jacobian $dt/d\theta$ from the change of variables t to θ is given by

$$\left| \frac{dt}{d\theta} \right| = \frac{s}{2} \sqrt{1 - \frac{4m_H^2}{s}} \sin(\theta). \quad (3.26)$$

Averaging the absolute square of the amplitude over all possible color and polarization states of the incoming gluons yields together with the kinematic flux factor $1/(16\pi s^2)$ for the $2 \rightarrow 2$ decay the differential partonic cross section $d\sigma/dt$

$$\frac{d\sigma}{dt} = \frac{1}{16\pi s^2} \frac{1}{8} \sum_a \frac{1}{8} \sum_b \frac{1}{2} \sum_{\lambda_1} \frac{1}{2} \sum_{\lambda_2} \frac{1}{2} |\mathcal{A}_{\text{ggHH}}|^2 \quad (3.27)$$

$$= \frac{1}{16\pi s^2} \frac{\alpha_s^2}{\pi^2} \frac{G_F^2 T_F^2}{256} s^2 \sum_{i=1}^2 \left(|F_i^{(0)}|^2 + \frac{\alpha_s}{\pi} \left[F_i^{(0)} (F_i^{(1)})^* + (F_i^{(0)})^* F_i^{(1)} \right] \right) + \mathcal{O}\left(\frac{\alpha_s}{\pi}\right)^2, \quad (3.28)$$

where the dependence of the strong coupling constant on the renormalization scale μ is suppressed and a factor $1/2$ is included for the generation of two identical particles in the final state. It cancels for $d = 4$ against the factor $(d - 2)$ from Eq. (3.18). In all following numerical evaluations, the values for the Higgs boson mass and the top quark mass were chosen as

$$m_H = 125 \text{ GeV}, \quad (3.29)$$

$$m_t = 173 \text{ GeV}, \quad (3.30)$$

in order to facilitate the comparison with literature results that have been published prior to the calculations performed in this thesis. Further values used are

$$G_F = 1.1663787 \times 10^{-5} \text{ GeV}^{-2} , \quad (3.31)$$

$$\alpha_s \equiv \alpha_s^{(5)}(m_Z) = 0.1181 \pm 0.0011 . \quad (3.32)$$

3.2.2. Calculation of the Form Factors

The calculation of the form factors from Eq. (3.21) is similar to the approach taken in the case of $gg \rightarrow ZZ$ in the previous chapter. Therefore its description will be kept short in this chapter and the reader is referred to the more detailed descriptions in the corresponding subsections in section 2.3 of chapter 2.

Generation of the amplitude

The calculation starts with the determination of all Feynman diagrams that contribute at leading order (LO) and next-to-leading order (NLO) to the amplitude \mathcal{A}_{ggHH} . This is done with the help of the FORTRAN program `qgraf` [34]. Like in the case of Z boson pair production there are, for di-Higgs boson production via gluon fusion, only 8 Feynman diagrams at LO and 118 Feynman diagrams at NLO. Subsequently, the `qgraf` output is supplemented with the actual Dirac and colour structure using the programs `q2e` and `exp` [38, 39]. In this step, the expressions are also transformed to FORM [29, 30] syntax and all Feynman diagrams are mapped to one of the three 1-loop or 34 2-loop integral families of the problem. The integral families and their graphical representation are explicitly shown in appendix A.3. Next, FORM is used for the projection of the amplitude on the two tensor structures from eq. (3.16) and for performing the Dirac and color [33] algebra of the traces. The resulting expression is a linear combination of scalar Feynman integrals from the 3 LO and 34 NLO integral families. Note, that at this stage of the calculation, the amplitude is exact in both m_t and m_H .

Reduction to master integrals

At this point, one can use the method of Integration By Parts[44, 45] (IBP) to reduce the large number of scalar integrals to a only a small set of master integrals. Since the complexity of IBP reductions grows, in general, rapidly with the number of scales involved, it is very hard to proceed from here and perform the IBP reduction for the $\mathcal{O}(30,000)$ scalar integrals while keeping the expressions exact in d, s, t, m_t and m_H .

The goal of this calculation is to compute the process $gg \rightarrow HH$ in the limit of high energies. It is therefore a natural choice to make the approximation

$$m_H = 0 \tag{3.33}$$

as the Higgs boson mass is the smallest scale in the problem with

$$m_H^2 < m_t^2 \ll s, |t|. \tag{3.34}$$

In order to still obtain finite Higgs boson mass corrections, a naïve Taylor expansion with respect to m_H is performed on the level of the amplitude. Note, that one does not need to do an expansion by regions in m_H , since there is actually only one contributing region² which just corresponds to a simple Taylor expansion (see also the discussion in section 4.1 of Ref. [56]). Note furthermore that Since the Higgs boson couples in this thesis always to

²This can directly be checked for example by using the Mathematica program `asy.m`[110] for expansion by regions of Feynman integrals.

a pair of top quarks, the top quark mass acts as a regulator such that the limit $m_H \rightarrow 0$ is well defined.

The m_H -expansion is performed with the help of the Mathematica[46] program LiteRed [47, 48] up to and including $\mathcal{O}(m_H^4)$ at LO and $\mathcal{O}(m_H^2)$ at NLO. From here on, all dependence on the Higgs boson mass appears explicitly in the amplitude as factors of $(m_H^2)^k$ with $k \in \{0, 1, 2\}$.

$$\mathcal{A}_{ggHH}(s, t, m_t, m_H) = \left(\frac{m_H^2}{4m_t^2}\right)^0 \mathcal{A}_{ggHH}^{(0)}(s, t, m_t) + \left(\frac{m_H^2}{4m_t^2}\right)^2 \mathcal{A}_{ggHH}^{(1)}(s, t, m_t) + \mathcal{O}\left(\frac{m_H^2}{4m_t^2}\right)^4, \quad (3.35)$$

(and in the LO case also m_H^4) in the small expansion parameter $m_H^2/(4m_t^2) \approx 0.13$. This simplifies both the reduction to master integrals and later on their calculation a lot. On the one hand the Taylor expansion increases the number of scalar integrals that need to be reduced to master integrals, by a factor five to $\mathcal{O}(130,000)$. On the other hand however, there is one scale less in the reduction and furthermore all scalar integrals have massless external legs.

For this new, expanded amplitude, the IBP reduction is done separately within each integral family with the help of the C++ program FIRE [50] using additional information on symmetries of the problem generated by the LiteRed package.

Computing the master integrals

The process $gg \rightarrow HH$ can in the limit of high energies be expressed through 10 one-loop master integrals at LO and 161 two-loop master integrals at NLO. Since they are the same as those discussed in the previous chapter for the process $gg \rightarrow ZZ$ their derivation will not be repeated here. Instead, the reader is referred to section 2.3.5 in chapter 2.

Renormalization

The renormalization procedure of the process $gg \rightarrow HH$ is in complete analogy to the renormalization procedure discussed for the case of the process $gg \rightarrow ZZ$ and the reader is referred to the corresponding discussion in section 2.3.6 of chapter 2.

3.3. Form Factors: Analytical and Numerical Results

In section 3.2.1 it was shown, that the amplitude \mathcal{A}_{ggHH} has two tensor structures and can therefore be described by the two corresponding form factors F_1 and F_2 defined in Eq. (3.20). Furthermore, the Higgs boson mediated structure proportional to the triple Higgs boson coupling, can be singled out and split from F_1 according to Eq. (3.21) such that one has effectively the three form factors F_{tri} , F_{box1} and F_{box2} .

Since these admit an expansion in the strong coupling constant given in Eq. (3.22) they will in the following sub-sections first be discussed at leading order (1-loop) and subsequently also at next-to-leading order (2-loop).

3.3.1. Leading Order Results

Starting at leading order has the advantage, that the exact result with the full top quark mass dependence is known. Therefore, all results of the high energy expansion calculation of this thesis will be compared against the exact result to gain confidence in the expressions. The exact result is taken from Ref. [90]. It is furthermore interesting to show also the results of the calculation in the limit of a large top mass. They are available from Ref. [100] up to m_t^{-12} , both for LO and NLO.

The first few terms for the form factors $F_{\text{tri}}^{(0)}$, $F_{\text{box1}}^{(0)}$ and $F_{\text{box2}}^{(0)}$ in the high energy limit read:

$$F_{\text{tri}}^{(0)} = \frac{2m_t^2}{s} \left(4 - l_{ms}^2 \right) + \mathcal{O}(m_t^4), \quad (3.36)$$

$$F_{\text{box1}}^{(0)} = \frac{4m_t^2}{s} \left(2 + \frac{m_H^2}{s} \left((l_{1ts} - l_{ts})^2 + \pi^2 \right) \right) + \mathcal{O}(m_t^4, m_H^4), \quad (3.37)$$

$$\begin{aligned} F_{\text{box2}}^{(0)} &= \frac{2m_t^2}{st(s+t)} \left(-l_{1ts}^2 (s+t)^2 - l_{ts}^2 t^2 - \pi^2 (s^2 + 2st + 2t^2) \right. \\ &\quad \left. + \frac{2m_H^2}{s(s+t)} \left(l_{1ts}^2 s(s+t)^2 + \pi^2 s^3 + 2s^2 t (-2l_{ms} + l_{ts} + \pi^2 - 4) \right. \right. \\ &\quad \left. \left. - st^2 (8l_{ms} + (l_{ts} - 2)l_{ts} + 16) - 4(l_{ms} + 2)t^3 \right) \right) + \mathcal{O}(m_t^4, m_H^4), \quad (3.38) \end{aligned}$$

with the abbreviations

$$l_{ts} = \log\left(-\frac{t}{s}\right) + i\pi, \quad l_{1ts} = \log\left(\frac{s+t}{s}\right) + i\pi, \quad l_{ms} = \log\left(\frac{m_t^2}{s}\right) + i\pi. \quad (3.39)$$

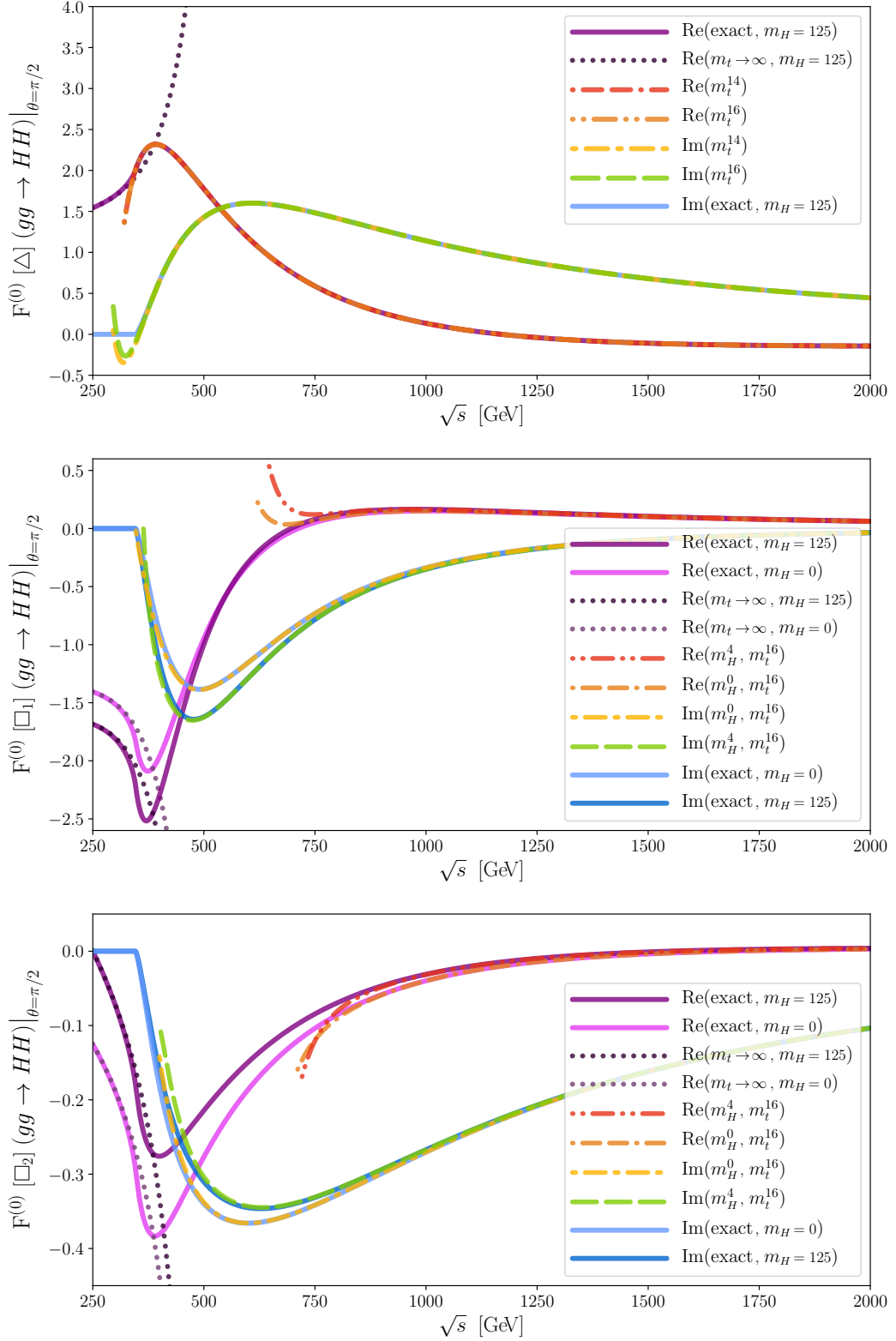


Figure 3.4.: LO form factors $F_{\text{tri}}^{(0)}$, $F_{\text{box1}}^{(0)}$ and $F_{\text{box2}}^{(0)}$ from top to bottom for a fixed scattering angle of $\theta = \pi/2$ as functions of the partonic centre of mass energy \sqrt{s} . Dash-dotted lines show the result of the high energy expansion, dotted lines give the large top mass approximation up to m_t^{-12} , exact results are shown as solid lines. For better readability, the curves are truncated once they start deviating from the exact result.

Fig. 3.4 shows the leading order form factors $F_{\text{tri}}^{(0)}$, $F_{\text{box1}}^{(0)}$ and $F_{\text{box2}}^{(0)}$ for a scattering angle fixed at $\theta = \pi/2$. The topmost plot shows the 'triangle' form factor $F_{\text{tri}}^{(0)}$. The high energy expansion, shown as dash-dotted curves, lie on top of the exact result for the whole range in the centre of mass energy \sqrt{s} shown in this plot, down to the top quark pair production threshold at $\sqrt{s} = 2m_t = 346$ GeV for both real and imaginary part of the form factor. For energies below the top quark pair production threshold, the process develops no imaginary part which is therefore in that range zero. At the same time, the real part is in that range very well reproduced by the large top quark mass expansion, including terms up to $1/m_t^{12}$. Note, that the 'triangle' form factor has no dependence on the Higgs boson mass.

The plots in the middle and at the bottom of Fig. 3.4 give the form factor $F_{\text{box1}}^{(0)}$ and $F_{\text{box2}}^{(0)}$, respectively, again for a fixed scattering angle of $\theta = \pi/2$. Both plots contain each two sets of curves: One, which shows the exact result together with the large top mass expansion and the high energy expansion, where the latter includes all computed terms up to m_H^4 of the Higgs mass expansion. In contrast, for the second set, the limit $m_H \rightarrow 0$ is carefully performed for the exact result and for both the high energy expansion and the large top mass expansion, the Higgs boson mass is explicitly set to zero. One can observe, that – as expected – both the full Higgs boson mass dependent exact result as well as its 'massless-Higgs'-limit are equally well approximated in the high energy region for the real and imaginary parts of the form factors alike. For centre of mass energies smaller than $\sqrt{s} \lesssim 800$ GeV, the high energy expansion diverges from the exact result and cannot be used in that form to describe the form factor in that region of the phase space. A method to nevertheless obtain a good approximation of the form factors for regions below $\sqrt{s} \lesssim 800$ GeV will be discussed in section 3.4. For the imaginary part, the situation is slightly better as it can reproduce the exact result down to centre of mass energies of $\sqrt{s} \approx 500$ GeV before the expansion starts to diverge from the exact result.

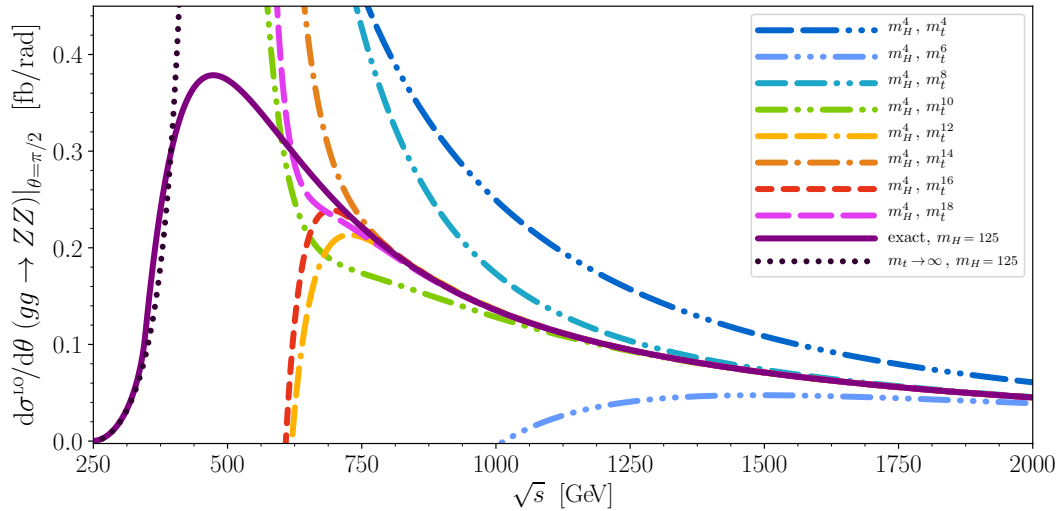


Figure 3.5.: LO differential partonic cross section for $\theta = \pi/2$. The solid curve shows the exact result, the dotted curve gives the large top mass expansion up to $1/m_t^{12}$ and the dash-dotted curves show the high energy expansion for expansion depths up to m_t^{18} .

Figure 3.5 shows the combination of all form factors into the leading order part of the differential partonic cross section according to Eq. (3.27). One observes that, as expected, the higher the energy, the better the description of the high energy approximation is with respect to the exact result. Furthermore, the plot shows that including more powers of the asymptotic expansion in the top quark mass leads to a systematic extension of the energy range in which the high energy expansion reproduces the exact result towards lower centre of mass energies. However, it seems that after including also the m_t^{12} corrections, no significant further improvements can be gained from including higher expansion terms since all following curves start to deviate from the exact result for energies below $\sqrt{s} \lesssim 750$ GeV. On the other hand, it will become clear in section 3.4 that higher terms than m_t^{12} are absolutely necessary for the extension of the convergence radius of the high energy approximation series by means of padé approximants. Using the expansion up to m_t^{32} as an input for those padé approximants allows for a precise description of the exact result to much lower energies than $\sqrt{s} \approx 750$ GeV, nearly covering the whole energy range down to the top pair production threshold.

3.3.2. Finite Higgs Boson Mass Effects

In the high energy expansion, the mass of the Higgs boson is the smallest scale with

$$m_H^2 < m_t^2 \ll s, |t|. \quad (3.40)$$

As long as the right part of the condition in Eq. (3.40) holds, it is a valid approximation to set $m_H = 0$. This can be confirmed in the behavior of the 'box' form factors in the two lower plots of figure 3.4. For large centre of mass energies, the exact result and its limit for $m_H \rightarrow 0$, shown as darker and lighter variants of the purple (real part) and blue (imaginary part) solid lines, respectively, are indistinguishable.

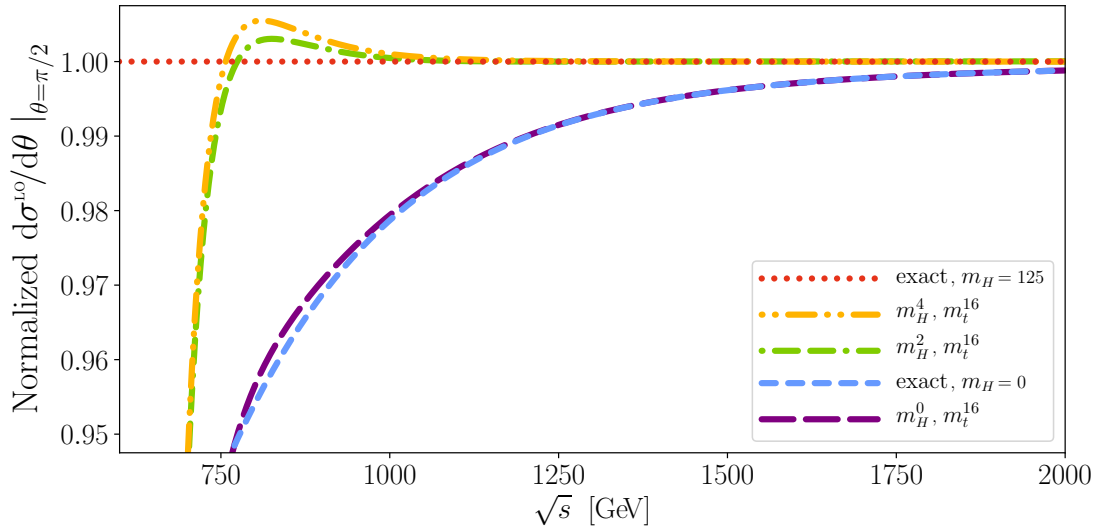


Figure 3.6.: Differential partonic cross section at $\theta = \pi/2$ for different expansion depths in the m_H expansion. The curves are normalized against the exact result with the full Higgs mass dependence (dotted red line). Published in [42].

On the other side, for lower values of \sqrt{s} , the condition (3.40) starts getting violated. As one can see in the imaginary part of the box form factors around $\sqrt{s} \approx 500$ GeV, the exact result in the limit $m_H \rightarrow 0$ is still well reproduced. There is however a clearly visible gap between those curves and the exact result with the full Higgs mass dependence. To point this effect out more generally, Fig. 3.6 shows the differential partonic cross section at $\theta = \pi/2$ for different expansion depths in m_H and a fixed expansion depth in m_t , all normalized against the exact result with full Higgs mass dependence.

The plot shows, in addition to the exact result with its full Higgs boson mass dependence (red, dotted) also the exact result in the limit $m_H \rightarrow 0$ (light blue, dashed) which is well approximated by the m_H^0 terms of the high energy expansion. Where the difference between the exact result and its 'massless limit' starts from a permille deviation at $\sqrt{s} \approx 2000$ GeV, it shows a 2% deviation at $\sqrt{s} \approx 1000$ GeV and reaches slightly more than 5% at $\sqrt{s} \approx 750$ GeV. This means, that one cannot neglect finite Higgs mass effects if one aims for a sub percent approximation of the exact result. The single-dotted, double-dashed green curve yields exactly this precision and deviates less than 0.5% from the exact result down to centre of mass energies of $\sqrt{s} \approx 750$ GeV already by including only the m_H^2 correction term.

In contrast to the di- Z production process, where the inclusion of the m_Z^4 term was necessary to find agreement with the exact result at a sub percent level (see sect. 2.4.6), one observes for $gg \rightarrow HH$ that already the m_H^2 terms leads to a good result and that the inclusion of the m_H^4 term (yellow curve, double-dotted, single-dashed) yields only minor improvements. Gauging on the increase of the complexity for going from m_H^0 to m_H^2 and the experience from calculating the m_Z^4 term in the $gg \rightarrow ZZ$ calculation, the computational effort of including also m_H^4 would probably rise by at least a factor five which would yield a rather small return on investment ratio. Therefore, the NLO form factors were in this thesis only computed up to m_H^2 .

3.3.3. Next-to-Leading Order Results

At next-to-leading order, the process of Higgs boson pair production via gluon fusion has both virtual and real corrections. Both of them are a priori divergent quantities with infrared and ultraviolet divergences. However, if these divergences are regulated with the same, dimensional regularization parameter ϵ , they cancel against each other. The goal of this thesis is determination of the virtual 2-loop corrections and not the computation of the 1-loop, real corrections. One way of still getting a finite result for the virtual contribution without knowing the real corrections is the emulation of the pole structure of the latter via the Catani subtraction procedure given in Eq. (2.67). Note however, that the finite part is not unique since there is some freedom in how to choose the Catani term C_{gg} given in Eq. (2.68). For the choice made in this thesis, the NLO form factors take the form

$$F^{(1)} = F^{(1),C_F} + F^{(1),C_A} + \beta_0 (\log(\mu^2/s) + i\pi) F^{(0)}, \quad (3.41)$$

Since the last part of Eq. (3.41) can simply be reproduced from the leading order result, only the parts of the NLO form factors proportional to the color factors C_A and C_F will be discussed in the following. Again, as at leading order, these split each into a 'triangle' and two 'box' contributions. Where at LO it was possible to compare the high energy

expansion against the exact, analytic result, there exists up to now no such result at NLO – except for the NLO triangle part, which is taken from Ref. [111]. Also at NLO, the high energy expansion is compared against the large top mass expansion, including terms up to m_t^{-12} , taken again from Ref. [100].

To get an impression of how the analytic expressions look like, they are presented in the following for the parts of $F_{\text{tri}}^{(1)}$, $F_{\text{box1}}^{(1)}$ and $F_{\text{box2}}^{(1)}$ that are proportional to C_A or C_F , respectively. For reasons of brevity, only the first term in both the m_t and the m_H expansion is shown. The complete result is given in the ancillary file [84] to this thesis:

$$F_{\text{tri}}^{(1),C_A} = C_A \frac{m_t^2}{180s} \left(2160 - 15l_{ms}^4 - 60(3 + \pi^2)l_{ms}^2 - 2160(l_{ms} + 1)\zeta_3 - 32\pi^4 \right) + \mathcal{O}(m_t^4, m_H^2), \quad (3.42)$$

$$F_{\text{box1}}^{(1),C_A} = C_A \frac{m_t^2}{s^3 t(s+t)} \left(-l_{1ts}^2 (s+t)^2 (s^2 + 3t^2) + 6l_{1ts} t (s+t)^2 (l_{1ts} t + s) - (4l_{1ts}^2 + 6l_{1ts} + 5\pi^2 - 12) s^2 t^2 - 6(l_{1ts}^2 + l_{1ts} + \pi^2) s t^3 - 3(l_{1ts}^2 + \pi^2) t^4 - \pi^2 s^4 - 2(\pi^2 - 6) s^3 t \right) + \mathcal{O}(m_t^4, m_H^2), \quad (3.43)$$

$$F_{\text{box2}}^{(1),C_A} = C_A \frac{m_t^2}{60s^3 t(s+t)} \left(-10i\pi s \left\{ 6H_2(s+t) (s^2(4l_{1ts} + 14l_{1ts} - 7) + st(4l_{1ts} + 14l_{1ts} - 17) - 4t^2) + 48H_{2,1}s(s+t)^2 - 84H_3s^2(s+2t) + 2l_{1ts} (21l_{1ts}^2 + 19\pi^2) s(s+t)^2 + l_{1ts}^2 t ((4l_{1ts} - 27)st - 18s^2 + 12t^2) - \pi^2 (7(2l_{1ts} - 1)s^3 + 2(14l_{1ts} - 3)s^2 t + 2(5l_{1ts} + 3)st^2 - 16t^3) + 12s\zeta_3 (3s^2 + 6st - 4t^2) \right\} - 60H_2s (-14l_{1ts}l_{1ts}s(s+t)^2 + l_{1ts}t (6s^2 + 9st - 4t^2) + \pi^2 s (5s^2 + 10st + 4t^2)) - 60H_{2,1}s(s+t) (s^2(-4l_{1ts} - 14l_{1ts} + 7) + st(-4l_{1ts} - 14l_{1ts} + 17) + 4t^2) + 480H_{2,1,1}s^2(s+t)^2 + 420H_{2,2}s^3(s+2t) - 60H_3s (14l_{1ts}s(s+t)^2 + t(-(4l_{1ts} + 9)st - 6s^2 + 4t^2)) - 480H_4s^2t^2 + 5l_{1ts}^4s^2(s+t)^2 - 40l_{1ts}^3l_{1ts}s^2(s+t)^2 - 10l_{1ts}^2(s+t) (-3((l_{1ts}(7l_{1ts} + 5) + 6)s^3 + (7l_{1ts}(l_{1ts} + 1) + 6)s^2t + (4l_{1ts} + 3)st^2 + 3t^3) - 19\pi^2s^2(s+t)) - 10l_{1ts} (\pi^2s ((18l_{1ts} - 7)s^3 + 36l_{1ts}s^2t + 9(2l_{1ts} + 1)st^2 - 4t^3) + 6t ((l_{1ts}(4l_{1ts} + 3) + 3)s^3 + (l_{1ts}(5l_{1ts} + 6) + 6)s^2t + 3(2l_{1ts} + 1)st^2 + 3l_{1ts}t^3) - 36s^2\zeta_3(s+t)^2) + 5l_{1ts}t^2 ((l_{1ts}^3 + 54l_{1ts} + 36)s^2 + 36(l_{1ts} + 1)st + 18l_{1ts}t^2) - 60st\zeta_3 ((4l_{1ts} + 9)st + 6s^2 - 4t^2) - 10\pi^2 (3(l_{1ts}(7l_{1ts} - 5) - 6)s^4$$

3. Higgs-Boson Pair Production

$$\begin{aligned}
& +(42(l_{ts} - 1)l_{ts} - 23)s^3t + (l_{ts}(23l_{ts} - 42) - 32)s^2t^2 - 2(4l_{ts} + 9)st^3 - 9t^4) \\
& - \pi^4s^2 (195s^2 + 390st + 227t^2) - 210H_2^2s^3(s + 2t) \Big) + \mathcal{O}(m_t^4, m_H^2), \quad (3.44)
\end{aligned}$$

$$\begin{aligned}
F_{\text{tri}}^{(1),CF} &= C_F \frac{m_t^2}{60s} \left(5(l_{ms}^4 - 12l_{ms}^3 + 144l_{ms} + 240) + 240(4l_{ms} - 1)\zeta_3 \right. \\
& \left. + 40\pi^2l_{ms}(l_{ms} + 1) + 12\pi^4 \right) + \mathcal{O}(m_t^4, m_H^2), \quad (3.45)
\end{aligned}$$

$$\begin{aligned}
F_{\text{box1}}^{(1),CF} &= C_F \frac{m_t^2}{s^3t(s+t)} \left(s^2t^2 (12l_{ms} + l_{ts}(7l_{ts} + 12)) + 8\pi^2 + 20 \right) + 2(6l_{ms} + \pi^2 + 10)s^3t \\
& + l_{1ts}^2(s+t)^2(s^2 + 6t^2) - 12l_{1ts}t(s+t)^2(l_{ts}t + s) + 12(l_{ts}^2 + l_{ts} + \pi^2)st^3 \\
& + 6(l_{ts}^2 + \pi^2)t^4 + \pi^2s^4 \Big) + \mathcal{O}(m_t^4, m_H^2), \quad (3.46)
\end{aligned}$$

$$\begin{aligned}
F_{\text{box2}}^{(1),CF} &= C_F \frac{m_t^2}{90s^3t(s+t)} \left(30i\pi s^2 \left\{ 6H_2(s+t)(s(2l_{1ts} + 2l_{ts} - 1) + 2t(l_{1ts} + l_{ts}) + t) \right. \right. \\
& + 24H_{2,1}(s+t)^2 - 12H_3s(s+2t) + 2l_{1ts}(3l_{ts}^2 + 2\pi^2)(s+t)^2 \\
& + l_{ts}^2t((2l_{ts} + 3)t + 6s) + \pi^2((1 - 2l_{ts})s^2 + 2(3 - 2l_{ts})st + 2t^2) \\
& \left. \left. - 12\zeta_3(s^2 + 2st + t^2) \right\} + 60H_2s^2(-6l_{1ts}l_{ts}(s+t)^2 - 3l_{ts}t(2s+t)) \right. \\
& + \pi^2(5s^2 + 10st + 6t^2) - 180H_{2,1}s^2(s+t)(s(2l_{1ts} + 2l_{ts} - 1) \\
& + 2t(l_{1ts} + l_{ts}) + t) - 720H_{2,1,1}s^2(s+t)^2 - 180H_{2,2}s^3(s+2t) \\
& + 180H_3s^2(2l_{1ts}(s+t)^2 + t(-2l_{ts}t + 2s + t)) + 720H_4s^2t^2 \\
& + 90l_{1ts}^2(s+t)^2(s^2(-3l_{ms} - l_{ts}^2 - \pi^2 - 7) - 3t^2) - 30\pi^2(3s^4(3l_{ms} - l_{ts}^2 + 7) \\
& + s^3t(18l_{ms} - 2l_{ts}(3l_{ts} + 1) + 31) + s^2t^2(18l_{ms} - (l_{ts} + 5)(3l_{ts} - 8)) + 18st^3 \\
& + 9t^4) - 30l_{ts}t^2(s^2(l_{ts}(9l_{ms} + (l_{ts} - 6)l_{ts} + 30) + 18) + 18(l_{ts} + 1)st + 9l_{ts}t^2) \\
& - 30l_{1ts}^4s^2(s+t)^2 + 60l_{1ts}^3(l_{ts} + 3)s^2(s+t)^2 + 30l_{1ts}(\pi^2s^2((4l_{ts} + 5)s^2 \\
& + 2(4l_{ts} + 3)st + 4(l_{ts} + 1)t^2) + 3t((6 - 2(l_{ts} - 3)l_{ts})s^3 \\
& + (12 - (l_{ts} - 12)l_{ts})s^2t + 6(2l_{ts} + 1)st^2 + 6l_{ts}t^3) + 12s^2\zeta_3(s+t)^2) \\
& \left. \left. - 180s^2t\zeta_3(-2l_{ts}t + 2s + t) + \pi^4s^2(60s^2 + 120st + 73t^2) + 90H_2^2s^3(s+2t) \right) \right) \\
& + \mathcal{O}(m_t^4, m_H^2), \quad (3.47)
\end{aligned}$$

where the symbols $H_2, H_3, H_4, H_{2,1}, H_{2,2}, H_{2,1,1}$ are abbreviations in obvious notation for the harmonic polylogarithms of the positive argument $-t/s$ (see also Eq. (2.61)).

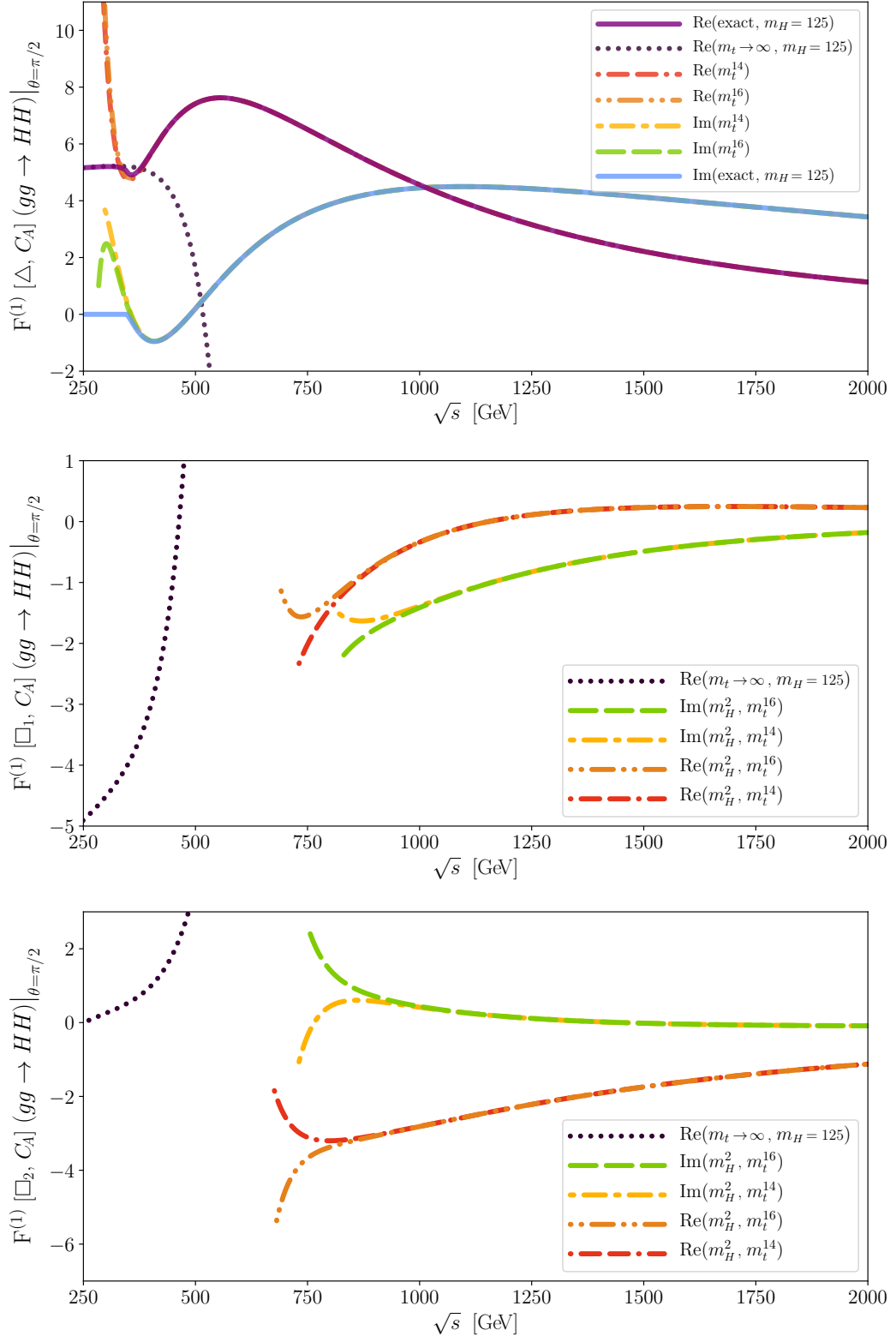


Figure 3.7.: Real and imaginary part of the NLO form factors $F_{\text{tri}}^{(1),CA}$, $F_{\text{box1}}^{(1),CA}$ and $F_{\text{box2}}^{(1),CA}$ from top to bottom for a fixed scattering angle of $\theta = \pi/2$ as functions of the partonic centre of mass energy \sqrt{s} . Dash-dotted lines show the result of the high energy expansion, dotted lines give the large top mass approximation up to m_t^{-12} . In the topmost plot, there are in addition exact results shown as solid lines.

3. Higgs-Boson Pair Production

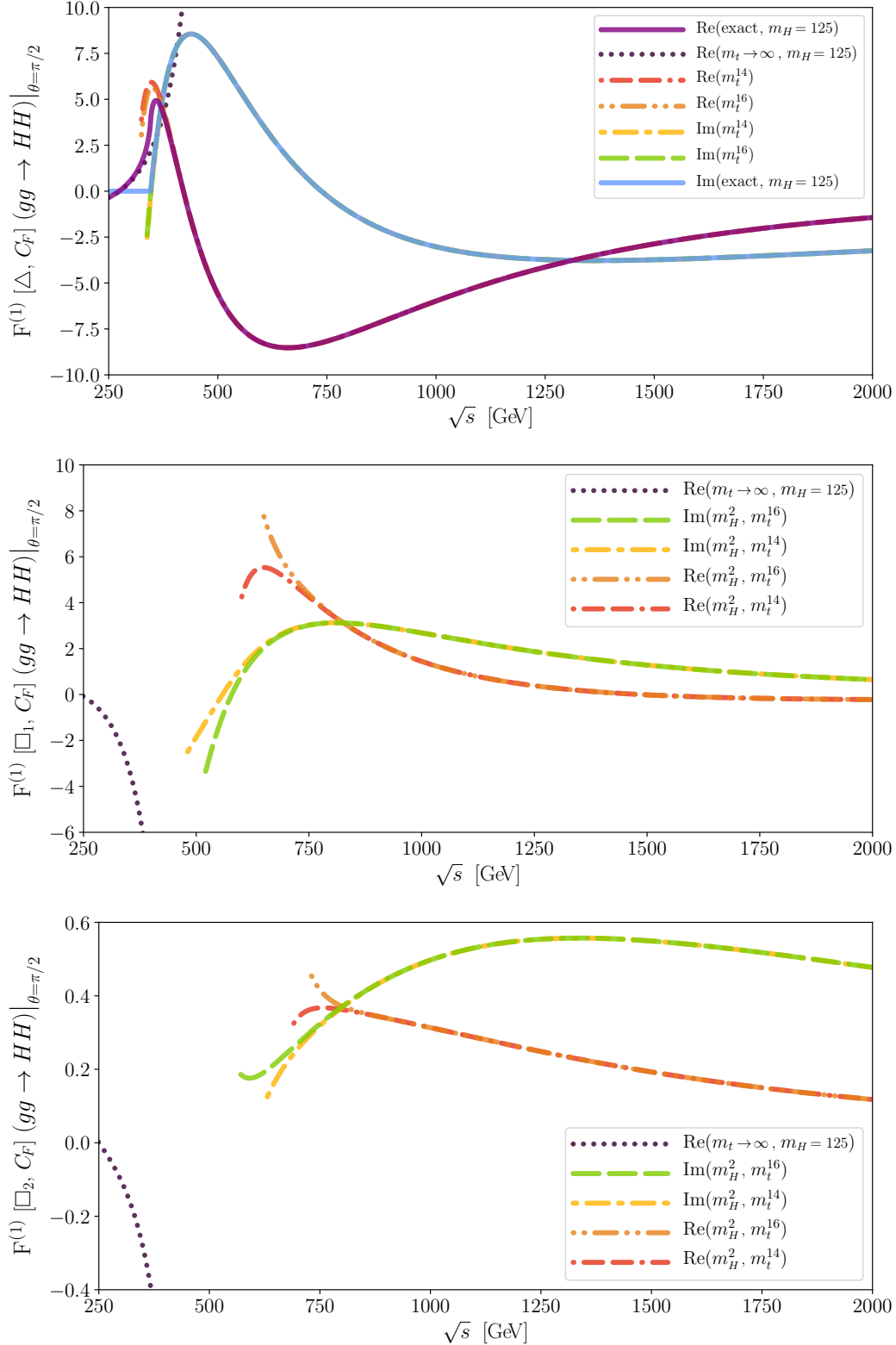


Figure 3.8.: Real and imaginary part of the NLO form factors $F_{\text{tri}}^{(1),CF}$, $F_{\text{box1}}^{(1),CF}$ and $F_{\text{box2}}^{(1),CF}$ from top to bottom for a fixed scattering angle of $\theta = \pi/2$ as functions of the partonic centre of mass energy \sqrt{s} . Dash-dotted lines show the result of the high energy expansion, dotted lines give the large top mass approximation up to m_t^{-12} . In the topmost plot, there are in addition exact results shown as solid lines.

Figures 3.7 and 3.8 show the parts of the form factor $F^{(1)}$ proportional to the color factor C_A and C_F , respectively, for $\theta = \pi/2$. In their topmost panels, the triangle parts $F_{\text{tri}}^{(1),C_A}$ and $F_{\text{tri}}^{(1),C_F}$ are shown. Upon comparing the dashed curves of the high energy expansion of the real and imaginary part, drawn for two different expansion depths m_t^{14} and m_t^{16} , against the corresponding exact results, shown as solid lines, one finds that the high energy expansion lies on top of the exact result and only starts to visibly deviate from it in the close proximity of the top pair production threshold at around $\sqrt{s} \approx 400$ GeV.

The plots in the middle show $F_{\text{box1}}^{(1),C_A}$ and $F_{\text{box1}}^{(1),C_F}$. This time, there is no analytic result available, against which the high energy expansion or the large top mass limit could be compared. However, from looking at the corresponding 'box1' plots at LO one can conclude, that as long as two consecutive expansion depths in m_t agree on each other, they seem to describe the exact result. Following this observation, the high energy expansion gives a precise prediction for the $F_{\text{box1}}^{(1),C_A}$ form factor down to centre of mass energies about $\sqrt{s} \approx 900$ GeV for the imaginary part and $\sqrt{s} \approx 800$ GeV for the real part. For $F_{\text{box1}}^{(1),C_F}$ one finds an inverted convergence behavior since here, the real part of the two expansion starts to deviate earlier from each other at around $\sqrt{s} \approx 750$ GeV and the imaginary part of the high energy expansions agree upon each other much longer down to $\sqrt{s} \approx 600$ GeV. The 'box2' form factors in the bottom tiles of figures 3.7 and 3.8 behave similar to the 'box1' form factors and one can state in general, that the C_F parts of the form factors are slightly better approximated by the high energy expansion than the C_A parts.

The fact, that the large mass expansion shares the same order of magnitude with the high energy expansion gives additional confidence in the correct derivation of the results for the high energy expansion.

3.3.4. Dependence on the Scattering Angle

The high energy expansion works best for maximal $|t|$ or maximal transverse momenta p_t (see definition in Eq. (3.17)), where the scattering angle $\theta = \pi/2$. This becomes clear, when considering, that the master integrals for the high energy expansion are computed under the condition

$$m_t^2 \ll s, |t|. \quad (3.48)$$

In the limit of high energies, $|t|$ is given by

$$|t| \leq \frac{s}{2} (1 - \cos(\theta)). \quad (3.49)$$

Thus, if θ approaches very small or equally very large scattering angles ($\theta \rightarrow 0$ or π), the value of $|t|$ tends to zero and equation (3.48) is violated and the expansion breaks down. This means, that in the high energy limit, one cannot provide good prediction for forward/backward scattering. On the other hand, this does not constitute a major problem since first, the forward/backward scattering are very hard to measure, and second, the biggest part of the cross section comes from the region symmetric top $\theta = \pi/2$.

By reducing the phase space to scattering angles between $\pi/4 \leq \theta \leq 3\pi/4$ one captures still about 70% of the full partonic cross section at a centre of mass energy of $\sqrt{s} = 100$ GeV.

3. Higgs-Boson Pair Production

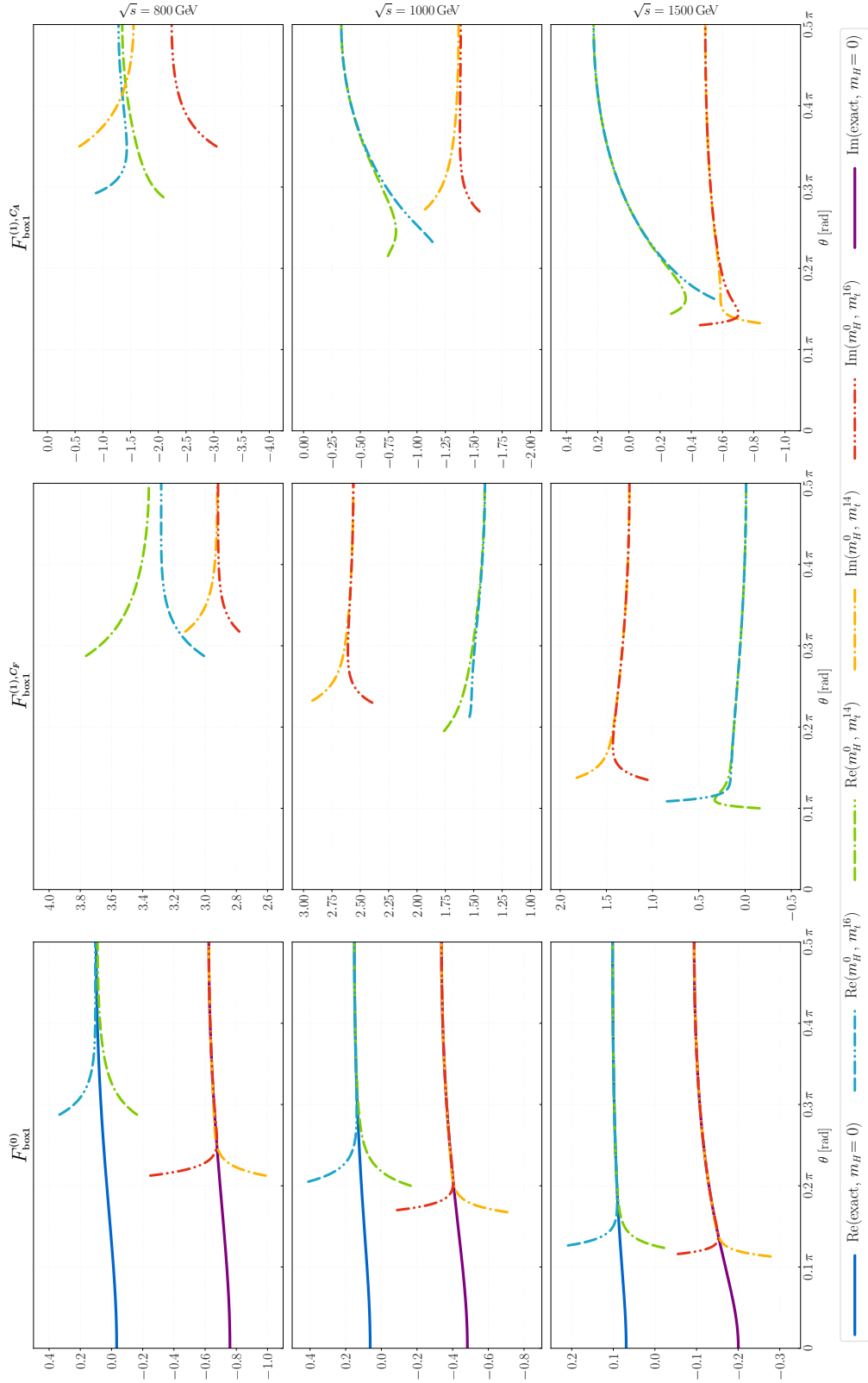


Figure 3.9.: Real and imaginary part of the $F_{\text{box1}}^{(0)}$, $F_{\text{box1}}^{(1),CF}$ and $F_{\text{box1}}^{(1),CA}$ form factors (columns from left to right) as a function of the scattering angle θ for fixed centre of mass energies $\sqrt{s} \in \{800, 1000, 1500\}$ GeV (rows from top to bottom). High energy expansions for m_t^{14} and m_t^{16} are shown as dashed lines, exact results, where available, are shown as solid lines. Published in [42].

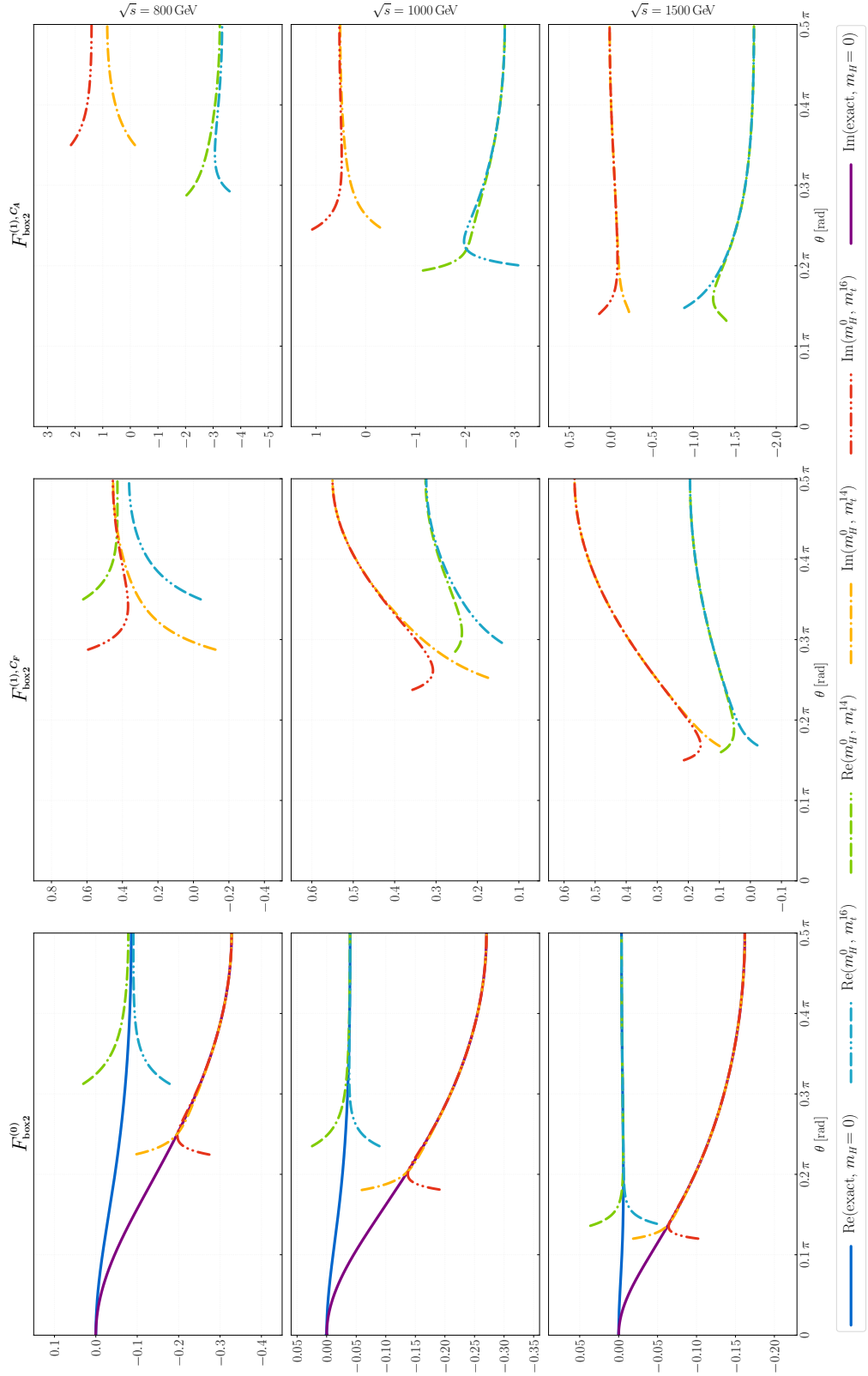


Figure 3.10.: Real and imaginary part of the $F_{\text{box2}}^{(0)}$, $F_{\text{box2}}^{(1),CF}$ and $F_{\text{box2}}^{(1),CA}$ form factors (columns from left to right) as a function of the scattering angle θ for fixed centre of mass energies $\sqrt{s} \in \{800, 1000, 1500\}$ GeV (rows from top to bottom). High energy expansions for m_t^{14} and m_t^{16} are shown as dashed lines, exact results, where available, are shown as solid lines. Published in [42].

Figures 3.9 and 3.10 are intended to point out the behavior of the the high energy expansion form factors F_{box1} and F_{box2} under the variation of θ . Note, that since the F_{tri} form factors has only an s -channel contribution, it does not depend on t and has therefore no θ dependence.

First of all, one can infer from the left most six plots if figures 3.9 and 3.10, showing the leading order form factors $F_{\text{box1}}^{(0)}$ and $F_{\text{box2}}^{(0)}$ for fixed centre of mass energies at $\sqrt{s} \in \{800, 1000, 1500\}$ GeV, that also for a variation in θ the exact result seems to be reproduced as long as two consecutive expansions order in m_t agree on each other. Here, and also for the C_A and C_F parts of $F_{\text{box1}}^{(1)}$ and $F_{\text{box2}}^{(1)}$ one observes – as expected – an extension of the range of convergence towards lower values of θ if one goes to higher centre of mass energies \sqrt{s} . Note, that the same extension happens also towards higher values of θ since the form factors are symmetric with respect to $\theta = \pi/2$ (or, equivalently under the exchange $t \leftrightarrow u$).

Moreover, similar to what could be observed in section 3.3.3, the convergence properties of the high energy expansions with respect to deviations from $\theta = \pi/2$ are better in the case of the C_F form factors than for the corresponding behavior of the C_A form factors. Yet, at $\sqrt{s} = 1500$ GeV, all six form factors span at least a range between $0.2\pi \leq \theta \leq 0.8\pi$ and further improvements to this could be obtained by employing Padé approximants which will be the main point of the following section.

3.4. NLO Virtual Finite

So far, only the triangle part of the NLO result could be compared against the literature since this is the only part which is known in full analytic form. There are however also results from numerical calculations available and the idea of this section is to compare the finite part of the NLO high energy expansion result against the numerical NLO predictions with exact top quark mass dependence from Ref. [92, 93, 112].

3.4.1. Definition: \mathcal{V}_{fin}

As already mentioned in section 3.3.3, the NLO result is incomplete without the real correction, yet one can still obtain a finite result for the NLO virtual part of the cross section by using the Catani subtraction procedure. In Ref. [112], a slightly different version of the Catani term

$$\tilde{C}_{gg} = \left(\frac{\alpha_s}{\pi} \right) \frac{e^{\epsilon\gamma_E}}{\Gamma(1-\epsilon)} \left[\frac{C_A}{2\epsilon^2} \left(\frac{\mu^2}{-s-i0^+} \right)^\epsilon + \frac{\beta_0}{\epsilon} \right], \quad (3.50)$$

was used which – when compared against the definition used in this thesis (see Eq. (2.68)) – leads to NLO form factors that lack the last term in Eq. (3.41) proportional to the LO form factors. Furthermore, in their calculation they consider also contributions from double triangle diagrams as shown in Fig. 3.11:

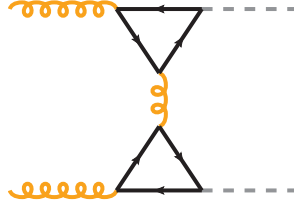


Figure 3.11.: Double triangle Feynman diagram contributing to $gg \rightarrow HH$ at NLO.

To take both changes into account, Eq. (3.21) gets redefined as

$$\mathcal{F}_1^{(0)} \equiv \frac{3m_H^2}{s-m_H^2} F_{\text{tri}}^{(0)} + F_{\text{box1}}^{(0)} \quad \mathcal{F}_2^{(0)} \equiv F_{\text{box2}}^{(0)} \quad (3.51)$$

$$\mathcal{F}_1^{(1)} \equiv \frac{3m_H^2}{s-m_H^2} \hat{F}_{\text{tri}}^{(1)} + \hat{F}_{\text{box1}}^{(1)} + F_{\text{dt1}}^{(1)} \quad \mathcal{F}_2^{(1)} \equiv \hat{F}_{\text{box2}}^{(1)} + F_{\text{dt2}}^{(1)} \quad (3.52)$$

where for the 1-loop form factors $F_{\text{tri}}^{(0)}$, $F_{\text{box1}}^{(0)}$ and $F_{\text{box2}}^{(0)}$ the exact results from Ref. [90] are used and the exact double triangle 2-loop form factor contributions $F_{\text{dt1}}^{(1)}$ and $F_{\text{dt2}}^{(1)}$ – originating from diagrams like that shown in Fig. 3.11 – are taken from Ref. [113].

The 2-loop form factors $\hat{F}_{\text{tri}}^{(1)}$, $\hat{F}_{\text{box1}}^{(1)}$ and $\hat{F}_{\text{box2}}^{(1)}$ are the results of the high energy expansion, including all computed terms in m_t and m_H up to m_t^3 and m_H^2 , evaluated at $\mu^2 = -s - i0^+$. This complies with Eq. (3.50) and corresponds to taking only the C_A and C_F parts of the form factors defined in Eq. (3.41):

$$\hat{F}_i^{(1)} \equiv F_i^{(1)} \Big|_{\mu^2=-s-i0^+} = F_i^{(1),C_A} + F_i^{(1),C_F} \quad \text{for } i \in \{1, 2\}. \quad (3.53)$$

Furthermore, in this thesis, the strong coupling constant α_s is defined in a six flavor scheme. However, in order to compare against the results of Ref. [92, 93, 112] defined in a five flavor scheme, one has to convert both α_s and the gluon wave function G_v from six to five flavors. This is done via the decoupling relations

$$\alpha_s^{(6)}(\mu) = \alpha_s^{(5)}(\mu) \left[1 + \frac{\alpha_s^{(5)}(\mu)}{\pi} \log\left(\frac{\mu^2}{m_i^2}\right) \frac{T_F}{3} + \mathcal{O}\left(\alpha_s^{(5)}(\mu)\right)^2 \right], \quad (3.54)$$

$$G_v^{(6)}(\mu) = G_v^{(5)}(\mu) \left[1 - \frac{\alpha_s^{(5)}(\mu)}{\pi} \log\left(\frac{\mu^2}{m_i^2}\right) \frac{T_F}{3} + \mathcal{O}\left(\alpha_s^{(5)}(\mu)\right)^2 \right]. \quad (3.55)$$

Since for $gg \rightarrow HH$ there are at leading order in α_s the same number of strong couplings as there are external gluon fields, the application of both (3.54) and (3.55) leaves the expressions unchanged except for the replacement $\alpha_s^{(6)}(\mu) \rightarrow \alpha_s^{(5)}(\mu)$. Dropping the superscript (5) from $\alpha_s^{(5)}$, one can then define the quantity $\widetilde{\mathcal{V}}_{\text{fin}}$ in agreement with Eq. (26) of Ref. [25] and the definition used in Ref. [114] as

$$\widetilde{\mathcal{V}}_{\text{fin}} = \frac{\alpha_s^2(\widetilde{\mu}_R)}{\pi^2} \frac{G_F^2 T_F^2}{128} s^2 \sum_{i=1}^2 \left(\frac{C_A}{2} \left(\pi^2 - \log^2\left(\frac{\widetilde{\mu}_R^2}{s}\right) \right) |\mathcal{F}_i^{(0)}|^2 + \left[\mathcal{F}_i^{(0)} \left(\mathcal{F}_i^{(1)} \right)^* + \left(\mathcal{F}_i^{(0)} \right)^* \mathcal{F}_i^{(1)} \right] \right) \quad (3.56)$$

Finally, the renormalization scale is adapted to the choice made in Ref. [114] and set to $\widetilde{\mu}_R = \sqrt{s}/2$ and Eq. (3.56) is divided by α_s^2

$$\mathcal{V}_{\text{fin}} \equiv \frac{\widetilde{\mathcal{V}}_{\text{fin}}(\widetilde{\mu}_R)}{\alpha_s^2(\widetilde{\mu}_R)} \quad \text{with} \quad \widetilde{\mu}_R = \frac{\sqrt{s}}{2}, \quad (3.57)$$

to obtain an expression \mathcal{V}_{fin} which is directly comparable against the numerical results provided in the file `Virt_full_noas.grid` from Ref. [114].

3.4.2. \mathcal{V}_{fin} : Comparison against Literature Results

The file `Virt_full_noas.grid` from Ref. [114] contains a grid of 3398 phase-space points with values for every phase-space point $P_i = (s_i, t_i)$ in the form

$$\left(\beta(s_i), \cos(\theta_i), \mathcal{V}_{\text{fin}}^{\text{grid}}(P_i), \pm\delta_i \right) \quad (3.58)$$

where the parametrization $\beta(s)$ and $\cos(\theta)$ introduced in Ref. [112] can be expressed as

$$\beta(s) = \sqrt{1 - \frac{4m_H^2}{s}} \quad \text{and} \quad \cos(\theta) = \frac{s + 2t - 2m_H^2}{s\beta(s)}. \quad (3.59)$$

It is however in the following convenient, to change to the set of coordinates (\sqrt{s}, p_T) ³.

³See appendix A.4 for in detail instructions on how to perform the change of variables.

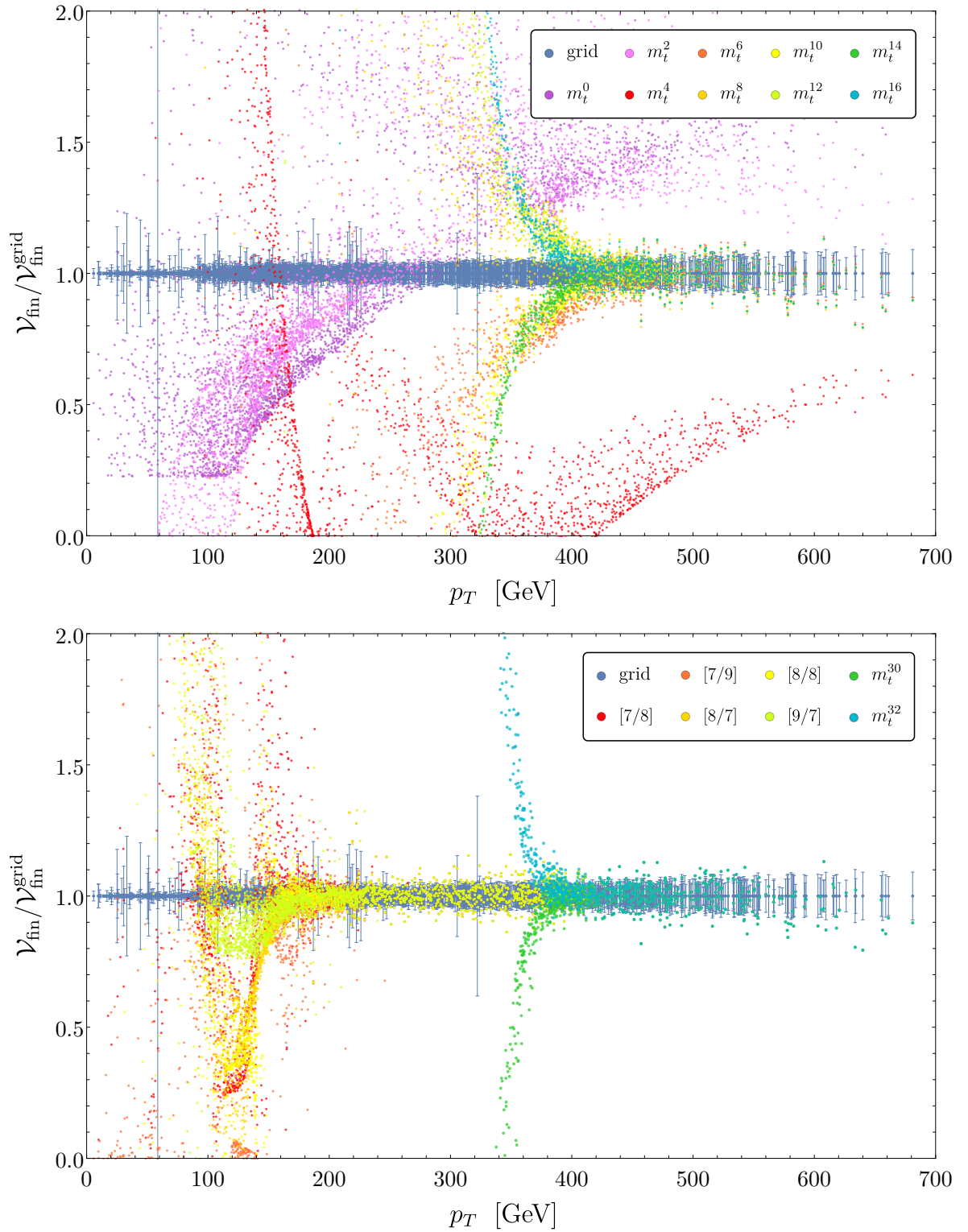


Figure 3.12.: Upper panel: Ratio $\mathcal{V}_{\text{fin}}^N / \mathcal{V}_{\text{fin}}^{\text{grid}}$ for all 3398 points computed in Ref. [114] as a function of p_T . Shown are the numerical results with their uncertainty bars (grid) as well as the results for $\mathcal{V}_{\text{fin}}^N$ including terms from m_t^0 to m_t^{16} . Lower panel: Same plot as above for m_t^{30} and m_t^{32} and five padé approximants $\mathcal{V}_{\text{fin}}^{n,m}$ marked as $[n/m]$. The lower plot is published in [86].

Since the result for \mathcal{V}_{fin} is a mixture of exact results and the high energy expansion it is useful to define

$$\mathcal{V}_{\text{fin}}^N = \sum_{i=0}^N \mathcal{V}_i m_t^i = \mathcal{V}_0 + \sum_{i=2}^N \mathcal{V}_i m_t^i, \quad (3.60)$$

with \mathcal{V}_0 containing all parts, that are exact in m_t and m_H , meaning $F_{\text{tri}}^{(0)}$, $F_{\text{box1}}^{(0)}$, $F_{\text{box2}}^{(0)}$, $F_{\text{dt1}}^{(1)}$ and $F_{\text{dt2}}^{(1)}$ and $\mathcal{V}_{i \neq 0}$ holding the NLO results of the high energy expansion $F_{\text{tri}}^{(1)}$, $F_{\text{box1}}^{(1)}$ and $F_{\text{box2}}^{(1)}$ as coefficients belonging to m_t^i . It should be noted, that the latter includes also the finite Higgs boson mass corrections up to m_H^2 , such that effectively one has

$$\mathcal{V}_i \equiv \mathcal{V}_{i,0} + m_H^2 \mathcal{V}_{i,2} + \mathcal{O}(m_H^4) \quad \text{for} \quad i \geq 2. \quad (3.61)$$

Note, that since the $gg \rightarrow HH$ form factors start from m_t^2 , the high energy expansion contributes only to \mathcal{V}_i with $i \geq 2$ and does in particular not contribute to \mathcal{V}_0 . Using the definition in Eq. (3.60), one can evaluate $\mathcal{V}_{\text{fin}}^N$ for different expansion depths N in m_t at exactly the same phase space points $P_i = (\sqrt{s}, p_T)_i$ as those given in `Virt_full_noas.grid` (in the following referred to as 'the grid') and normalize each value against the corresponding central value $\mathcal{V}_{\text{fin}}^{\text{grid}}(P_i)$ of the grid. Then, the closer the result is to 1, the better it agrees with the grid points from the numerical calculation of the exact result.

The resulting plot is shown as a function of p_T^4 in the upper panel of Fig. 3.12. The grid points themselves are shown as dark blue dots with their associated, normalized uncertainty bars (see Eq. (3.58)). The other colored dots show $\mathcal{V}_{\text{fin}}^N$ for $N \in \{0, 2, \dots, 16\}$. When taking more powers of m_t into account, one observes that starting from m_t^6 (orange dots), the high energy induced results begin to stabilize and converge on a common result which lies for high values of p_T well within a 2σ standard deviation from the grid points. For values of $p_T \lesssim 350$ GeV their values start to diverge and the grid cannot be reproduced. Note, that at $\theta = \pi/2$, $p_T = 350$ GeV corresponds to the centre of mass energy $\sqrt{s} \approx 750$ GeV which is where one observes also the end of convergence for the differential partonic cross section shown in Fig 3.5.

3.4.3. Padé-improved \mathcal{V}_{fin} : Comparison against Literature Results

One way to extend the convergence radius of the high energy expansion beyond $p_T = 350$ is the use of Padé approximations as introduced in section 2.4.8 of chapter 2. Remember, that in the discussion of the odd terms that appear in the master integrals of the high energy expansion it was observed that the combination of any odd term with its following even term in the m_t expansion yields better converging series than splitting those terms up. In the notation used here, Eq. (2.102) has then the form

$$\mathcal{V}_{\text{padé-input}} = \mathcal{V}_0 + \sum_{n=1}^{16} (\mathcal{V}_{2n-1} m_t^{2n-1} + \mathcal{V}_{2n} m_t^{2n}) x^n. \quad (3.62)$$

⁴Note, that in this plot the 2-dimensional phase space $\sqrt{s} - p_T$ is projected on the p_T axis and single values of p_T can be populated by multiple points of the exact calculation with different values of \sqrt{s} .

Using the Mathematica command `PadeApproximant[]` one obtains with

$$\mathcal{V}_{\text{fin}}^{n,m} = \text{PadeApproximant}[\mathcal{V}_{\text{padé-input}}, \{x, 0, \{n, m\}\}] /. x \rightarrow 1, \quad (3.63)$$

any Padé approximant with $n + m \leq 16 = 32/2$. Note, that during the construction of Padé approximants with high values for $n + m$ huge cancellations can occur between the individual terms from $\mathcal{V}_{\text{padé-input}}$ and one needs to assure that the input is known to a sufficiently high precision in order to avoid numerical artifacts. In this thesis, $\mathcal{V}_{\text{padé-input}}$ was always evaluated with a precision of 125 digits. Restricting oneself again to the conditions (2.104) which assure that only those padé approximants are built that first contain the most information on the initial function, i.e. they use in their construction at least terms up to m_t^{30} or higher and second stay close to the diagonal where $n = m$ which usually gives the best results. The five obtained padé approximants $\mathcal{V}_{\text{fin}}^{n,m}$ from the set $[n/m]_i$ given in (2.103) are then again normalized to the central values of the grid and shown together with the m_t^{30} and m_t^{32} results in the lower panel of Fig. 3.12.

One can see that while the results of $\mathcal{V}_{\text{fin}}^{30}$ and $\mathcal{V}_{\text{fin}}^{32}$ approach their convergence barrier at $p_T \lesssim 350$ GeV but show otherwise a similar behavior as $\mathcal{V}_{\text{fin}}^{14}$ and $\mathcal{V}_{\text{fin}}^{16}$ in the upper panel of the same figure, the whole set of padé approximants pushes beyond $p_T = 350$ GeV and stays, except for a few outliers, within 1σ of the numerical exact result in form of the grid points down to $p_T \approx 200$ GeV. For lower values of p_T , the set of padés disperses even though it keeps clustering around the exact result down to $p_T \approx 100$ GeV which encourages further investigations.

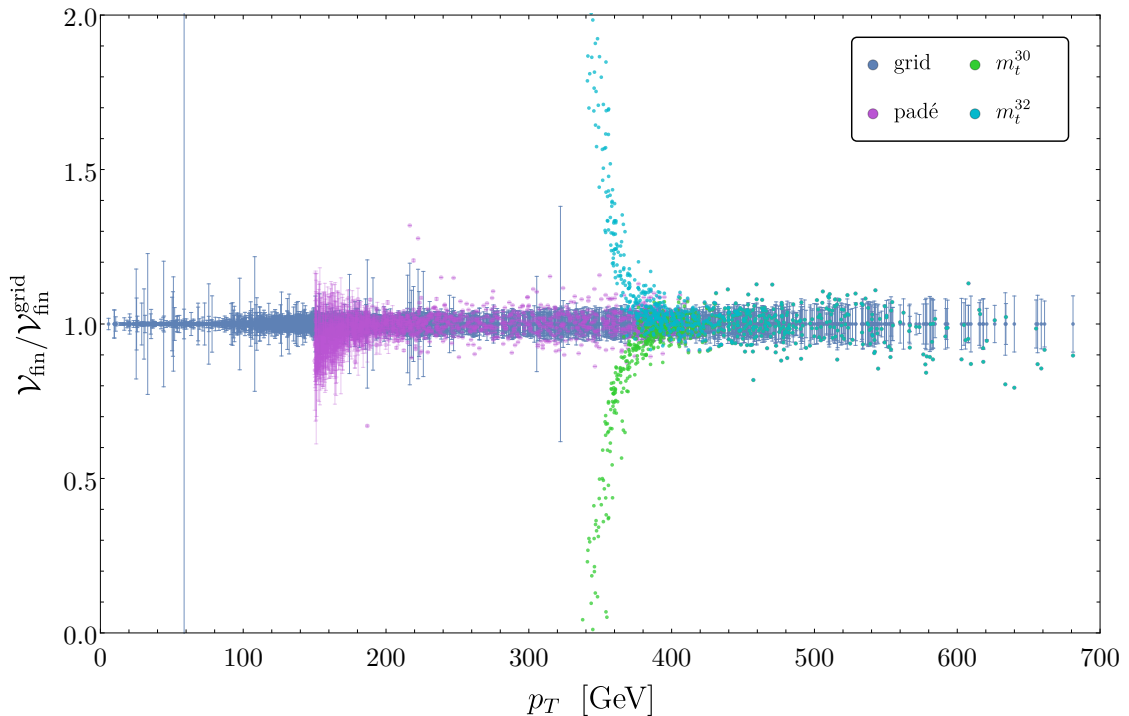


Figure 3.13.: Ratio $\mathcal{V}_{\text{fin}}^N / \mathcal{V}_{\text{fin}}^{\text{grid}}$ for all 3398 points computed in Ref. [114] as a function of p_T . Shown are the numerical results (grid) as well as results for m_t^{30} and m_t^{32} . The purple dots with error bars are the result of the pole-distance-reweighted padé approach.

The idea of this section is to use the extended convergence range achieved through padé approximants with a high level ($n + m$) of information on the exact result which is obtained from a deep expansion in m_t , to create one common prediction for the virtual part of the partonic cross section of the process $gg \rightarrow HH$ that does not only cover a much larger part of the phase space than the initial high energy expansion but comes also with a stable central value and an uncertainty estimate. To do so, the basic pole-distance-reweighted padé approach developed in section 2.4.8 is applied, without any further extensions, on the known set of padé approximants for \mathcal{V}_{fin} given by

$$\mathcal{V}_{\text{fin}}^{n,m} \quad \text{with} \quad [n/m] \in \{[7/8], [7/9], [8/7], [8/8], [9/7]\}. \quad (3.64)$$

The resulting prediction, which in the following will simply be referred to as $\mathcal{V}_{\text{fin}}^{\text{padé}}$, is shown down to values of $p_T = 150$ GeV in Fig. 3.13 as purple dots with uncertainty bars. Comparing this against the single padé approximants in the lower panel of Fig. 3.12 one finds, that the extreme dispersion starting below $p_t \approx 250$ GeV has disappeared for a much cleaner prediction that for values below $p_T \lesssim 200$ GeV centers around the exact result near values of 1 and comes with, for lower values of p_T increasing, uncertainty bands that cover the exact result. One can conclude, that the pole-distance-reweighted padé approach seems to successfully extend the radius of convergence of the high energy expansion and does furthermore seem to lead to reliable and useful predictions.

The direct comparison against the given points of the numerical exact result in Fig. 3.12 and Fig. 3.13 is a good starting point to gain confidence in both the correctness of the high energy expansion results and the usefulness of the simple padé approximations. It is however more interesting to consider \mathcal{V}_{fin} as a function of \sqrt{s} for, e.g., a fixed value of p_T . For this purpose, one can make use of the interpolation procedure `grid_virt[]` provided in Ref. [114] to be able to compare against values of the numerical exact result. Unfortunately, this interpolation routine is built on the limited set of 3398 input points which cannot cover all of the phase space everywhere equally well. As a consequence, the interpolation routine provides in sparsely populated regions of the phase space results that have little to no support by the initial numerical calculation. Since this result comes without any error estimate, it is then difficult to gauge how reliable any output of the interpolation routine is. Therefore, the following procedure was developed to assign an error estimate to an interpolate value $\mathcal{V}_{\text{fin}}^{\text{inter}}$ of the numerical exact calculation at the point $P_0 = \{\sqrt{s_0}, p_{T,0}\}$:

- Define the region $\Delta = \{(\sqrt{s}, p_T) \mid |\sqrt{s_0} - \sqrt{s}| \leq 5 \text{ GeV}, |p_{T,0} - p_T| \leq 10 \text{ GeV}\}$ as the 'neighborhood' of the phase space point P_0 .
- Collect all data points from the original set of 3398 grid points that lie within this area Δ into the set $\mathbb{P} = \{\mathcal{V}_{\text{fin}}^{\text{grid}}(P_1) \pm \delta_1, \mathcal{V}_{\text{fin}}^{\text{grid}}(P_2) \pm \delta_2, \dots, \mathcal{V}_{\text{fin}}^{\text{grid}}(P_n) \pm \delta_n\}$.
- Define for non-empty sets \mathbb{P} : $\sigma_0 = \frac{1}{n} \sum_{i=1}^n |\delta_i|$ as an error estimate for $\mathcal{V}_{\text{fin}}^{\text{inter}}(P_0)$ based on the numerical uncertainty of original data points in the neighborhood of P_0 .
- Mark values $\mathcal{V}_{\text{fin}}^{\text{inter}}(P_0)$ with empty sets \mathbb{P} as 'unsupported by the grid' and assign no error estimate.

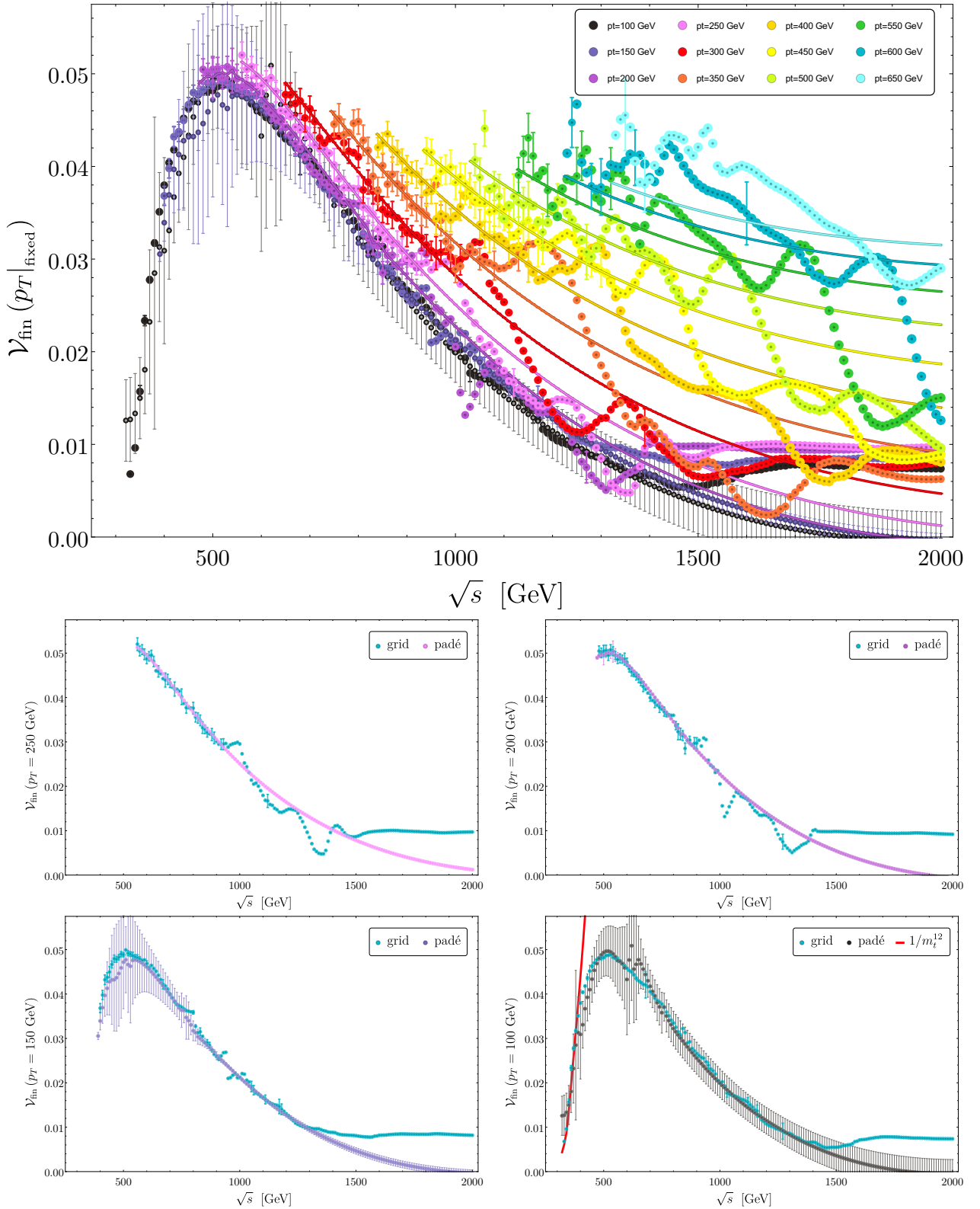


Figure 3.14.: Upper panel: \mathcal{V}_{fin} for different, fixed values of p_T as a function of \sqrt{s} . Points with error bars show the numerical exact result of Ref. [114]. Solid lines show $\mathcal{V}_{\text{fin}}^{\text{padé}}$ with error bars that for large values of p_T become narrower than the linewidth. Published in [86]. Lower panel: Single contributions from the plot above for a better distinction between the individual curves. The lower right plot showing $p_T = 100$ GeV is supplemented with the result of the large top mass expansion in red. Published in [86].

The plots in Fig. 3.14 show $\mathcal{V}_{\text{fin}}^{\text{inter}}$ and $\mathcal{V}_{\text{fin}}^{\text{padé}}$ as a function of \sqrt{s} for fixed values of $p_T = 100, 150, \dots, 650$ GeV in different colors from black to bright blue. One observes, that the result of the interpolation routine from the exact numerical calculations yields an unstable behavior of \mathcal{V}_{fin} for large centre of mass energies where the underlying grid is sparsely populated and yields basically no support. This region can be smoothed out by the solid lines of $\mathcal{V}_{\text{fin}}^{\text{padé}}$ which, once they reach the lower energy regions where the grid is much denser, lie within the uncertainty estimates assigned to $\mathcal{V}_{\text{fin}}^{\text{inter}}$ by the procedure explained above. Note that also $\mathcal{V}_{\text{fin}}^{\text{padé}}$ has an uncertainty estimate which is albeit for the 'high p_T ' curves with $p_T \geq 200$ GeV in general much smaller than the corresponding uncertainties of the the numerical exact result.

The upper two plots of the lower panel of Fig. 3.14 pick out the curves for (from left to right) $p_T = 250$ GeV and $p_T = 200$ GeV. One observes in the region of $\sqrt{s} \lesssim 800$ GeV very good agreement between both $\mathcal{V}_{\text{fin}}^{\text{padé}}$ and $\mathcal{V}_{\text{fin}}^{\text{inter}}$ within their error bounds. At larger centre of mass energies, the interpolated values of the numerical exact calculation loose support on the underlying grid and produce a rather unstable curve. In contrast, the result based on the high energy expansion continues smoothly and yields even for transverse momenta as small as $p_T = 200$ GeV stable results with small uncertainties.

The lower two plots of the lower panel of Fig. 3.14 show on the left the curves for $p_T = 150$ GeV and on the right the curves for $p_T = 100$ GeV. Even though these plots show a region of the phase space which can in the sense of condition (3.40) clearly not be called a high energy region, pole-distance-reweighted padé procedure still captures the exact result within its associated error. For $p_T = 150$ GeV this error-estimate reaches for small values of \sqrt{s} values of up to 20%. Again, the central value smooths out also here leaps in the result of the exact calculation. Most impressive is, that for $p_T = 100$ GeV the high energy induced results for $\mathcal{V}_{\text{fin}}^{\text{padé}}$ coincide within their error estimates with the result of the large top mass expansion, shown in red.

As a concluding remark one can state, that the pole-distance-reweighted padé procedure enhances the predictive power of the high energy expansion far beyond its initial radius of convergence and offers stable central values that come with an uncertainty estimate that reliably includes the exact result.

3.4.4. Application of the NLO Results

As could be seen in the last section, both the results based on the high energy expansion and the numerical exact calculation can profit from each other. The idea is to extend the existing grid of the numerical exact calculations by the results of the pole-distance-reweighted padé procedure in the region where the latter shows small uncertainties. For this purpose, $\mathcal{V}_{\text{fin}}^{\text{padé}}$ was evaluated on an equally spaced grid in the $\beta^5(s) - \cos(\theta)$ plane and the obtained uncertainty predictions normalized to their corresponding central values.

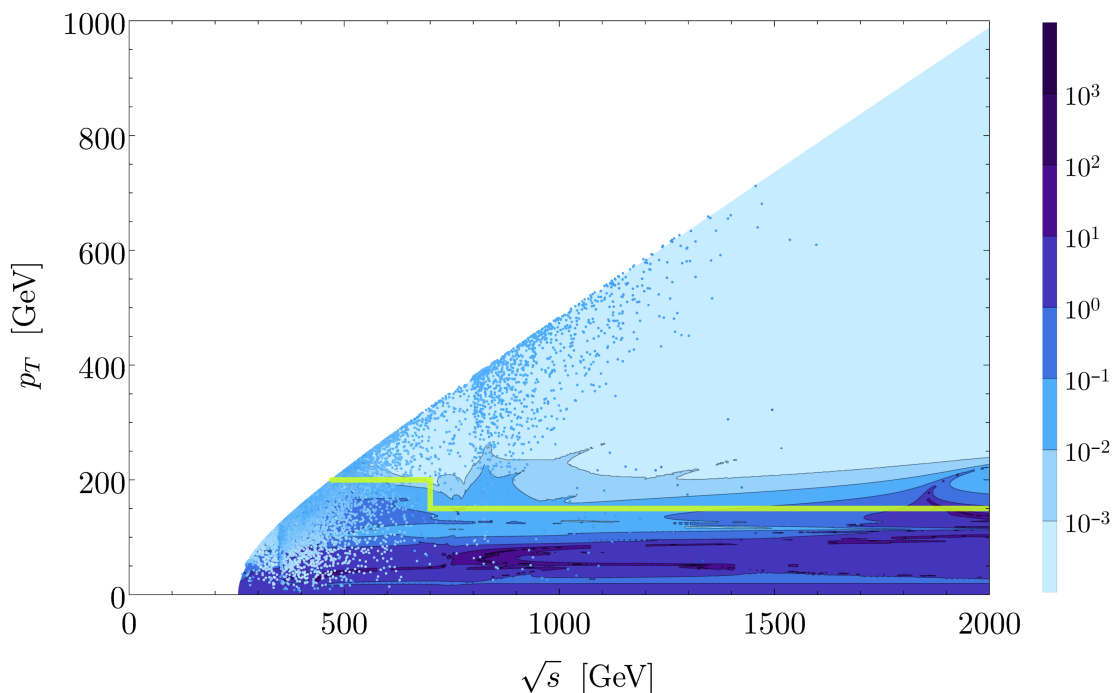


Figure 3.15.: Comparison of the relative error $|\delta^\pm|/|\mathcal{V}_{\text{fin}}^{\text{padé}}|$ of the high energy induced result against the relative error $|\delta^\pm|/|\mathcal{V}_{\text{fin}}^{\text{grid}}|$ of the numerical exact result from Ref. [114]. The value of the relative error is given in percent and color coded from small uncertainties in light blue to large uncertainties in dark violet. Published in [86].

Fig. 3.15 shows the resulting relative uncertainty in percent, color coded from small relative uncertainties in light blue to large relative uncertainties in dark violet. One can infer from areas, where the points of the exact result are brighter than the background whose color is given by relative uncertainty of $\mathcal{V}_{\text{fin}}^{\text{padé}}$ that one should use the exact result there. Equivalently, in areas where the points of the exact result are darker than the background color, the result of $\mathcal{V}_{\text{fin}}^{\text{padé}}$ should be used to describe this region of the phase space. Based on this observation and the plots in Fig. 3.14, the phase space was 'split' by the yellow-green line in Fig. 3.15 between the numerical exact result and the high energy region and one common grid was built and made publicly available in Ref. [86, 115].

Fig. 3.14 shows the same plot as in Fig. 3.16 but with the updated grid from Ref. [115] which includes nearly twice as many numerically evaluated points. One can observe, that the interpolation routine gives now stable results in both the high energy and the low energy region. The 'wiggles' at large values of \sqrt{s} are an artifact of the distribution of input points for the grid. They become very sparse in this region and one could fix that by making the grid more dense.

During this thesis an additional, much denser grid was implemented in a C++ program which uses the interpolation routines from [116]. This grid does not produce the 'wiggles' observed in Fig. 3.16 and provides furthermore error estimates as interpolated uncertainties from surrounding data points. The corresponding results are shown in appendix in Fig. B.4.

3. Higgs-Boson Pair Production

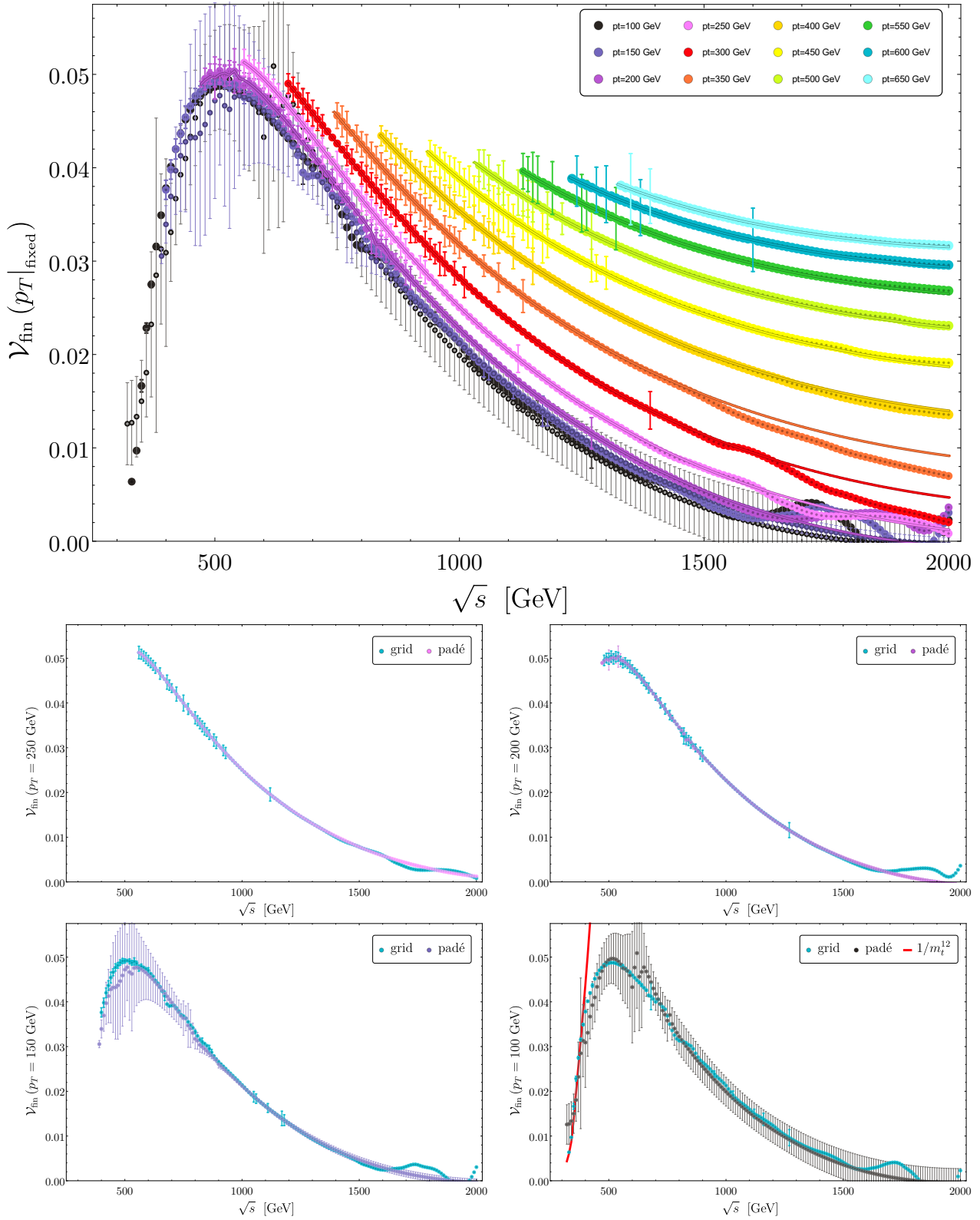


Figure 3.16.: Same plot as in Fig. 3.14 but with the updated grid from Ref. [115]. Published in Ref. [86].

3.5. Hadronic Cross Section

One possible application of the common interpolation routine is the computation of hadronic cross sections. Since in the framework [115], the real radiation corrections are already implemented, one can compare how the full hadronic NLO di-Higgs production cross section is affected by using different implementations for the virtual NLO finite

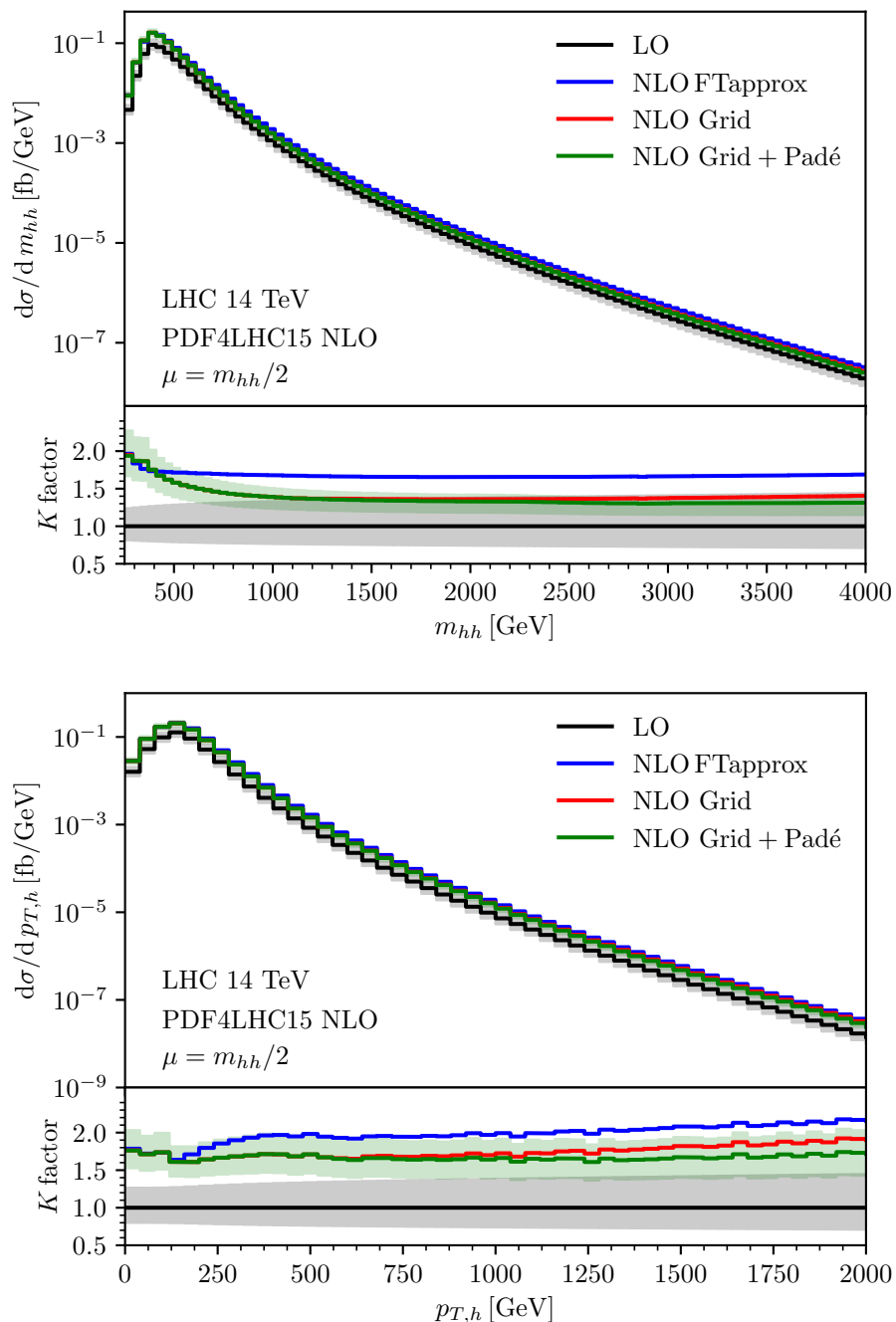


Figure 3.17.: m_{hh} and $p_{T,h}$ distributions for a hadronic centre of mass energy $\sqrt{s_H} = 14$ TeV. Both plots are taken from Ref. [42]

3. Higgs-Boson Pair Production

corrections. Figure 3.17 shows the differential hadronic cross section for a hadronic centre-of-mass energy $\sqrt{s_H} = 14$ TeV as a differential distribution with respect to the invariant mass of the Higgs boson pair (upper panel) or the transverse momentum (lower panel). Black lines show only the LO result, while green lines show the NLO results where the finite NLO part of the virtual corrections from this thesis are used. In addition, the red curve shows the results from the numerical exact calculation without the support of the high energy expansion. As an effect, one can observe that at higher energies, where the support of the underlying grid of the red curve gets sparse, the red curve drifts away from the ‘best prediction’ in green. Note however, that the red curve still is inside of the green uncertainty band which is obtained by a seven point variation of the renormalization and factorization scales. In addition, Fig. 3.17 shows also the result from the large top quark mass limit, rescaled by the exact LO result which is referred to as FTapprox.

Comparing LO with NLO, one can define the K factor which for the shown energy range is close to $K = 1.6$. One can furthermore conclude, that the FTapprox predictions have in general the right shape, but are far to large and should not be used for high energies.

Similar plots for higher hadronic centre-of-mass energies as might for example be achieved at a future circular collider are shown in Fig. 3.18.

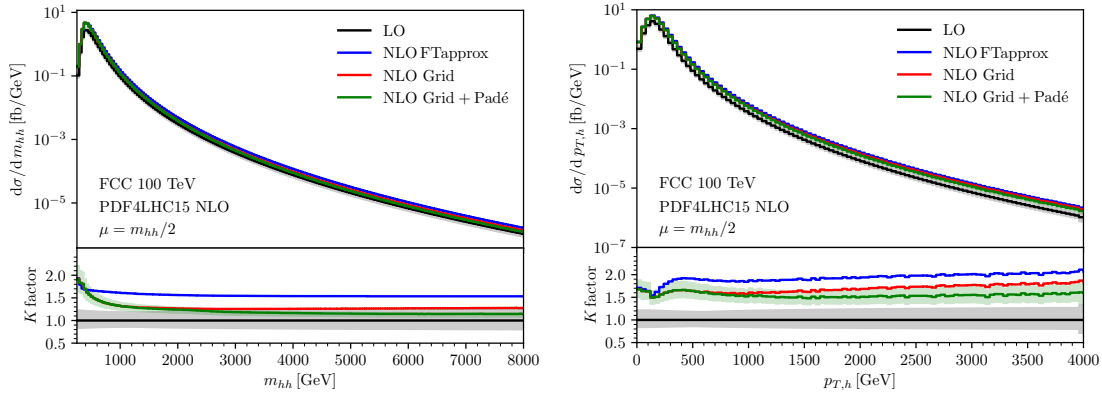


Figure 3.18.: m_{hh} and $p_{T,h}$ distributions for a hadronic centre of mass energy $\sqrt{s_H} = 100$ TeV. Both plots are taken from Ref. [42]

Here, the green curve obtained from the new grid and the red curve, showing the results of the old grid without the results of the high-energy approximation, show a wider separation with the red curve lying at the edge of the error band of the new result. This underlines the lack of high-energy data points in the original data from [114], leading here to unreliable predictions and the need to extend the exact numerical calculation by computing more points in the high-energy region. In conclusion one can say, that in the regions where the results of the numerical calculation from Ref. [114] are densely distributed, the results of the high energy expansion in combination with the PDR Padé approach could be verified and both calculations show mutual agreement. Therefore, instead of calculating more phase space points in the high-energy region, needed for the predictions like the one shown in Fig. 3.18, using the expensive exact numerical approach, one can rely on the analytical expressions derived in this thesis knowing that they reproduce the exact result at a fraction of the computational cost.

3.6. Conclusion and Outlook

In this chapter, the LO and NLO corrections to the process $gg \rightarrow HH$ have been calculated in the high energy expansion up to to order m_t^{32} and m_H^2 . It was shown, that taking the first two terms in the Higgs mass expansion into account is enough to find a good description of the exact result both at LO and at NLO. Results for the form factors could at both LO and NLO be compared against exact calculations. With the help of Padé approximations, the region of convergence of the high energy expansion was significantly enlarged. A combined grid with numerical exact results from [114] and results of the high energy expansion was published in [115] which could be applied to make predictions for the invariant mass of the Higgs boson pair and the Higgs boson transverse momentum distribution at hadronic centre-of-mass energies of $\sqrt{s_H} = 14$ TeV and $\sqrt{s_H} = 100$ TeV. Furthermore it has been shown, that in a large part of the phase space, CPU-intensive exact numerical calculations can be replaced by the evaluation of the analytical results obtained in this thesis.

4. Hadronic Higgs Decay

4.1. Introduction

The high precision measurement of the couplings of the Higgs boson to Standard Model particles is an important research topic in collider physics. In particular, the decay rate of the Higgs boson to bottom quarks and to gluons are interesting in this context, since together they form together nearly 70% of the hadronic Higgs decay. Thus, all other Higgs boson branching ratios depend heavily on them.

The branching ratio into bottom quarks is known exactly in the bottom quark mass m_b both at one loop [117] and at two loop [118–120]. In the limit of vanishing internal bottom quark masses, three [121], four [122, 123] and five-loop corrections [124] were calculated. Exact one-loop electroweak [125, 126] and mixed QCD and electroweak corrections [127] were also computed. The FORTRAN program HDECAY [128] implements a large number of recent theoretical results concerning Standard Model (and beyond) Higgs boson decay widths.

In Ref. [123] it was shown, that at order α_s^3 , the top quark mediated corrections to the hadronic Higgs boson decay are of a similar size compared to the corresponding massless contributions. Since the massless corrections to order α_s^4 are already known [124], this motivates for this thesis the computation of the top quark mediated decay rate into hadrons to order $\mathcal{O}(\alpha_s^4)$. The four-loop process is considered in an effective field theory approach where the top quark is integrated out and effective couplings of the Higgs boson to bottom quarks and gluons remain.

4.2. The Process $H \rightarrow \text{Hadrons}$

This chapter is based on work that has been published in Ref. [129] and Ref. [130] and contributes as a side topic to this thesis. It will therefore be kept rather short since all relevant results have already been presented in the references mentioned above.

The calculation is based on an effective field theory approach where the top quark is integrated out and an effective coupling of the Higgs boson to gluons with fields $G_{\mu\nu}$

$$\begin{array}{c} \text{---} \bullet \begin{array}{l} \nearrow \text{gluon} \\ \searrow \text{gluon} \end{array} \\ \text{---} \bullet \end{array} = C_1 \mathcal{O}_1 \quad \text{with} \quad \mathcal{O}_1 = G_{\mu\nu} G^{\mu\nu}, \quad (4.1)$$

as well as an effective coupling of the Higgs boson to bottom quarks with fields Ψ_b

$$\begin{array}{c} \text{---} \bullet \begin{array}{l} \nearrow \text{quark} \\ \searrow \text{quark} \end{array} \\ \text{---} \bullet \end{array} = C_2 \mathcal{O}_2 \quad \text{with} \quad \mathcal{O}_2 = m_b \bar{\Psi}_b \Psi_b, \quad (4.2)$$

is obtained [131]. Note, that the effective couplings C_1 and C_2 carry all residual dependence on the top quark and are given to five-loop order in Ref. [132–135]. The relevant Lagrangian for the process $H \rightarrow \text{hadrons}$ in this low-energy theory is then given by

$$\mathcal{L}_{\text{eff}} = -\frac{H^0}{v^0} \left(C_1 \mathcal{O}_1^R + C_2 \mathcal{O}_2^R \right) + \mathcal{L}_{\text{QCD}}^{n_f=5} + \mathcal{O}(M_H^2/M_t^2), \quad (4.3)$$

where H^0 and v^0 are the bare Higgs field and its vacuum expectation value and the superscripts R indicate renormalized quantities. Note, that here only QCD corrections to the Higgs boson decay into gluons and bottom quarks are taken into account while contributions from other light quarks or electroweak effects are ignored. See Ref. [123] for a more extensive discussion.

Using the optical theorem, one can obtain the decay width $\Gamma(H \rightarrow \text{hadrons})$ as

$$\Gamma(H \rightarrow \text{hadrons}) = \frac{\sqrt{2}G_F}{16\pi^2 M_H} \sum_{i,j=1}^2 C^i C^j \text{Im}(\Pi_{ij}(q^2 = M_H^2)), \quad (4.4)$$

which allows one to calculate this process via the evaluation of scalar two-point functions defined by the correlators

$$\Pi_{ij}(q^2) = (4\pi)^2 i \int d^d x e^{iqx} \langle 0 | T \left(\mathcal{O}_i^R(x) \mathcal{O}_j^R(0) \right) | 0 \rangle. \quad (4.5)$$

One can then introduce the dimensionless quantities $\widetilde{\Delta}_{ij}$ with

$$\text{Im}(\Pi_{ij}(q^2)) = \kappa_{ij}(q^2) \widetilde{\Delta}_{ij}(\mu^2/q^2), \quad (4.6)$$

such that the top quark mediated hadronic decay width of the Higgs boson in this low-energy effective theory can be written as

$$\Gamma(H \rightarrow \text{hadrons}) = \frac{\sqrt{2}G_F}{16\pi^2 M_H} \sum_{i,j=1}^2 C^i C^j \kappa_{ij} \widetilde{\Delta}_{ij}. \quad (4.7)$$

Setting

$$\frac{1}{\kappa_{11}} = 32\pi M_H^4 \quad \text{and} \quad \frac{1}{\kappa_{12}} = \frac{1}{\kappa_{21}} = \frac{1}{\kappa_{22}} = 6\pi M_H^2 m_b^2, \quad (4.8)$$

yields together with the redefinitions $\Delta_{ii} = \widetilde{\Delta}_{ii}$ and $\Delta_{12} = \widetilde{\Delta}_{12} + \widetilde{\Delta}_{21}$ the decay width

$$\Gamma(H \rightarrow \text{hadrons}) = A_{b\bar{b}} [(C_2)^2 (1 + \Delta_{22}) + C_1 C_2 \Delta_{12}] + A_{gg} (C_1)^2 \Delta_{11}, \quad (4.9)$$

split into a contribution which at leading order has light quarks in the final states and a second contribution which at leading order has purely gluonic final states. The corresponding prefactors read

$$A_{b\bar{b}} = \frac{3M_H m_b^2(\mu)}{8} \frac{\sqrt{2}G_F}{\pi} \quad \text{and} \quad A_{gg} = 2M_H^3 \frac{\sqrt{2}G_F}{\pi}. \quad (4.10)$$

Note however, that starting from NNLO, there are cuts in Δ_{11} which contain also $b\bar{b}$ pairs (see for example the third diagram from the left in the first line of Fig. 4.1. It is therefore not possible to single out the purely gluonic part in the optical theorem framework when higher order corrections are taken into account .

4.3. Calculation of the Correlator Functions

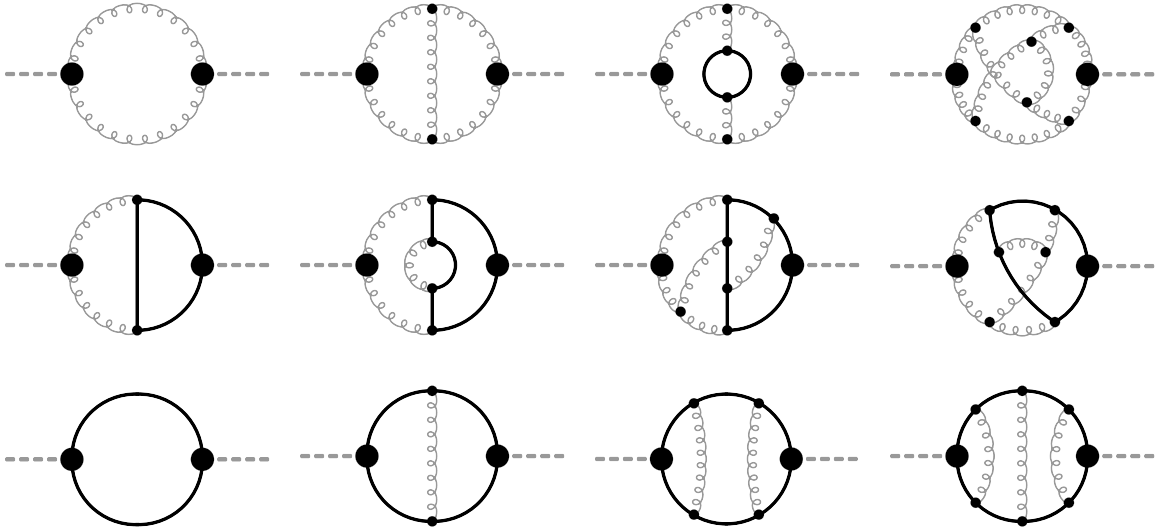


Figure 4.1.: Feynman diagrams contributing to the top quark induced corrections of the hadronic Higgs boson decay. The first, second and third line show contributions to Π_{11} , Π_{12} and Π_{22} , respectively. Big blobs correspond to the effective operators from Eqs. (4.1) and (4.2), small blobs are normal QCD vertices, curly lines denote gluons, solid lines bottom quarks and dashed lines Higgs bosons.

Calculation of the Amplitude

Figure 4.1 shows in three lines example Feynman diagrams of the three types of propagator diagrams, that appear in the context of this chapter, each one coming with two effective couplings to the Higgs boson. They need to be computed for the goal of determining the hadronic Higgs boson decay width at $\mathcal{O}(\alpha_s^4)$. Since the effective couplings C_1 and C_2 are proportional to α_s and 1, respectively (see Eq. (E.1) and (E.2)) and there are only QCD corrections considered here, this means that one needs the individual classes of diagrams contributing to Δ_{11} , Δ_{12} or Δ_{22} at different loop orders:

$$\begin{array}{c} \text{---} \bullet \text{---} \text{---} \bullet \text{---} \\ \text{---} \bullet \text{---} \text{---} \bullet \text{---} \end{array} \quad N\text{-loop diagrams contribute to } C_1^2 \Delta_{11} \text{ at } \mathcal{O}(\alpha_s^{N+1}) \text{ ,} \quad (4.11)$$

$$\begin{array}{c} \text{---} \bullet \text{---} \text{---} \bullet \text{---} \\ \text{---} \bullet \text{---} \text{---} \bullet \text{---} \end{array} \quad N\text{-loop diagrams contribute to } C_1 C_2 \Delta_{12} \text{ at } \mathcal{O}(\alpha_s^N) \text{ ,} \quad (4.12)$$

$$\begin{array}{c} \text{---} \bullet \text{---} \text{---} \bullet \text{---} \\ \text{---} \bullet \text{---} \text{---} \bullet \text{---} \end{array} \quad N\text{-loop diagrams contribute to } C_2^2 \Delta_{22} \text{ at } \mathcal{O}(\alpha_s^{N-1}) \text{ ,} \quad (4.13)$$

The goal of this calculation is the description of the top quark induced QCD corrections at the 4th order in the strong coupling constant α_s . This requires the calculation of 3-loop

diagrams of type (4.11), 4-loop diagrams of type (4.12) and 5-loop diagrams of type (4.13). Since the results for Δ_{11} and Δ_{22} are already available in the literature (see Ref. [136] and Ref. [124], respectively) it is in principle only necessary to extend the $\mathcal{O}(\alpha_s^3)$ result for Δ_{12} from Ref. [123] by one order in α_s to $\mathcal{O}(\alpha_s^4)$. It is however still useful to recompute also parts of the other expressions Δ_{11} and Δ_{22} as an independent cross check which serves also as a validation of the method used to compute the missing Δ_{12} part.

To this end, the established setup introduced in sections 2.3 and 3.2.1 of both chapter 2 and chapter 3 was used and will be briefly described in the following: The amplitude in terms of $\mathcal{O}(15,000)$ Feynman diagrams was generated using qgraf [34]. Subsequently q2e and exp [38, 39] were used to bring the expressions into FORM [29, 30] notation, expand in the bottom mass and map the remaining massless integrals on a set of eleven four-loop families. Using FORM for the Dirac and color algebra [33], the amplitude was written as a linear combination of $\mathcal{O}(1,250,000)$ scalar integrals that were then reduced to pseudo master integrals with the help of 5 GB of reduction tables produced by FIRE 5.1 [52]. Using the FIRE command FindRules [], the set of pseudo master integrals could be reduced to 28 massless four-loop master integrals which are all available in the literature [137–139].

As a cross check, all calculations up to 3-loops were also repeated within the MINCER [140] framework and complete agreement between these calculations to three loops and also with the literature results mentioned above was found.

Renormalization

The renormalization of the strong coupling constant and the mass of the bottom quark is performed in the $\overline{\text{MS}}$ scheme with

$$\alpha_s^0 = Z_{\alpha_s} \alpha_s \quad \text{and} \quad m_b^0 = Z_m m_b, \quad (4.14)$$

where the renormalization constants were taken from Ref. [141]. Care must be taken with the effective operators as they mix under renormalization [123, 142] with

$$\mathcal{O}_1^R = Z_{11} \mathcal{O}_1 + Z_{12} \mathcal{O}_2 \quad \text{and} \quad \mathcal{O}_2^R = \mathcal{O}_2, \quad (4.15)$$

where the renormalization constants Z_{11} and Z_{12} are related to Z_m and Z_{α_s} by

$$Z_{11} = 1 + \alpha_s \frac{\partial}{\partial \alpha_s} \log Z_{\alpha_s} \quad \text{and} \quad Z_{12} = -4\alpha_s \frac{\partial}{\partial \alpha_s} \log Z_m. \quad (4.16)$$

The renormalized quantities Δ_{11} , Δ_{12} and Δ_{22} take then the form

$$\Delta_{11} = (Z_{11})^2 \Delta_{11}^0 + 2Z_{11}Z_{12} \Delta_{12}^0 + (Z_{12})^2 \Delta_{22}^0 \quad (4.17)$$

$$\Delta_{12} = Z_{11} \Delta_{12}^0 + Z_{12} \Delta_{22}^0 \quad (4.18)$$

$$\Delta_{22} = \Delta_{22}^0. \quad (4.19)$$

Note, that due to the proportionality to α_s of Z_{12} , the renormalized α_s^N part of Δ_{11} has only contributions from the $\alpha_s^{(N-1)}$ part of the bare result for Δ_{12}^0 and from the $\alpha_s^{(N-2)}$ part of the bare result for Δ_{22}^0 . Equivalently, the renormalized α_s^N part of Δ_{12} depends only on the bare $\alpha_s^{(N-1)}$ result for Δ_{22}^0 . This means, that in order to obtain the renormalized quantities Δ_{11} , Δ_{12} and Δ_{22} at α_s^4 one needs to compute the bare constituents of Eqs. (4.17), (4.18) and (4.19) at three, four and five-loop order, respectively.

4.4. Results

4.4.1. Δ_{11}

The results for Δ_{11} , corresponding to the evaluation of diagrams like the one given in Eq. (4.11), reads for $C_A = 3$ and $C_F = 4/3$:

$$\begin{aligned} & \frac{m_b^2}{M_H^2} \left(a_s^3 \left(\frac{45L_H^3}{2} + n_l^2 (L_H^2 + 5L_H - 2\zeta_2 + \frac{157}{18}) + 703L_H^2 + n_l \left(-L_H^3 - \frac{319L_H^2}{6} + (6L_H + \frac{319}{3})\zeta_2 - \frac{2770L_H}{9} \right. \right. \right. \\ & + \frac{953\zeta_3}{72} - \frac{40\zeta_5}{9} - \frac{88387}{144} \left. \left. \left. + (-135L_H - 1406)\zeta_2 + (-39L_H - \frac{21977}{24})\zeta_3 + \frac{98009L_H}{24} - \frac{855\zeta_5}{8} + \frac{1162871}{144} \right) \right. \\ & + a_s^2 \left(3L_H^2 + (-3L_H - \frac{15}{2})n_l + \frac{169L_H}{2} - 6\zeta_2 + 6\zeta_3 + \frac{697}{3} \right) + 6a_s \left. \right) + a_s^3 \left(\frac{1331L_H^3}{16} + 1056L_H^2 + n_l^3 \left(-\frac{L_H^3}{54} \right. \right. \\ & - \frac{7L_H^2}{36} + \left(\frac{L_H}{9} + \frac{7}{18} \right) \zeta_2 - \frac{127L_H}{162} + \frac{\zeta_3}{27} - \frac{7127}{5832} \left. \left. \right) + n_l^2 \left(\frac{11L_H^3}{12} + \frac{1609L_H^2}{144} + \left(-\frac{11L_H}{2} - \frac{1609}{72} \right) \zeta_2 + \left(-\frac{5L_H}{6} - \frac{113}{24} \right) \zeta_3 \right. \right. \\ & + \frac{88819L_H}{1728} + \frac{115207}{1296} \left. \left. \right) + n_l \left(-\frac{121L_H^3}{8} - \frac{18761L_H^2}{96} + \left(\frac{363L_H}{4} + \frac{18761}{48} \right) \zeta_2 + \left(55L_H + \frac{11677}{48} \right) \zeta_3 - \frac{544969L_H}{576} - \frac{95\zeta_5}{36} \right. \right. \\ & - \frac{368203}{216} \left. \left. \right) + \left(-\frac{3993L_H}{8} - 2112 \right) \zeta_2 + \left(-\frac{5445L_H}{8} - \frac{44539}{16} \right) \zeta_3 + \frac{965285L_H}{192} + \frac{3465\zeta_5}{8} + \frac{15420961}{1728} \left. \right) + a_s^2 \left(n_l^2 \left(\frac{L_H^2}{12} \right. \right. \\ & + \frac{7L_H}{12} - \frac{\zeta_2}{6} + \frac{127}{108} \left. \left. \right) + n_l \left(-\frac{11L_H^2}{4} - \frac{263L_H}{12} + \frac{11\zeta_2}{2} + \frac{5\zeta_3}{4} - \frac{7189}{144} \right) + \frac{363L_H^2}{16} + \frac{2817L_H}{16} - \frac{363\zeta_2}{8} - \frac{495\zeta_3}{8} + \frac{37631}{96} \right) \\ & + a_s \left(\left(-\frac{L_H}{3} - \frac{7}{6} \right) n_l + \frac{11L_H}{2} + \frac{73}{4} \right) + 1, \end{aligned}$$

where a_s counts the strong couplings $a_s = \alpha_s^{(5)}/\pi$, ζ_i are the Riemann Zeta functions, n_l is the number of light quarks, $L_H = \log(\mu^2/M_H^2)$, m_b is the $\overline{\text{MS}}$ mass of the bottom quark and M_H is the on-shell mass of the Higgs boson. The parts proportional to $m_b^2/M_H^2 a_s^2$ and $m_b^2/M_H^2 a_s^3$ are new. The latter result contributes formally to the order $\mathcal{O}(\alpha_s^5)$. The a_s^3 part without bottom mass dependence was confirmed in Ref. [143].

4.4.2. Δ_{12}

The results for Δ_{12} , corresponding to the evaluation of diagrams like the one given in Eq. (4.12), reads for $C_A = 3$ and $C_F = 4/3$:

$$\begin{aligned} & a_s^3 \left(-\frac{285L_H^3}{2} - 2075L_H^2 + n_l^2 \left(-\frac{2L_H^3}{9} - \frac{28L_H^2}{9} + \left(\frac{4L_H}{3} + \frac{56}{9} \right) \zeta_2 + \left(\frac{8L_H}{3} + \frac{20}{3} \right) \zeta_3 - \frac{407L_H}{27} - \frac{25627}{972} \right) + n_l \left(\frac{34L_H^3}{3} \right. \right. \\ & + \frac{1003L_H^2}{6} + \left(-68L_H - \frac{1003}{3} \right) \zeta_2 + \left(-118L_H - 446 \right) \zeta_3 + \frac{15973L_H}{18} + 10\zeta_4 + \frac{100\zeta_5}{3} + \frac{279451}{162} \left. \left. \right) + (855L_H \right. \\ & + 4150) \zeta_2 + \left(1755L_H + \frac{131389}{18} \right) \zeta_3 - \frac{65267L_H}{6} - 815\zeta_5 - \frac{8957453}{432} \left. \right) + a_s^2 \left(n_l \left(\frac{4L_H^2}{3} + \frac{112L_H}{9} - \frac{8\zeta_2}{3} - \frac{16\zeta_3}{3} \right. \right. \\ & + \frac{283}{9} \left. \left. \right) - 38L_H^2 - \frac{1028L_H}{3} + 76\zeta_2 + 156\zeta_3 - \frac{15073}{18} \right) + a_s \left(-8L_H - \frac{92}{3} \right) \end{aligned}$$

4.4.3. Δ_{22}

The results for Δ_{22} , corresponding to the evaluation of diagrams like the one given in Eq. (4.13), reads for $C_A = 3$ and $C_F = 4/3$:

$$\begin{aligned} & a_s^4 \left(\frac{3895L_H^4}{128} + \frac{51529L_H^3}{96} + \zeta_2 \left(-\frac{11685L_H^2}{32} - \frac{51529L_H}{16} + \frac{23985\zeta_3}{16} - \frac{4548079}{576} \right) + \left(-\frac{23985L_H^2}{32} - \frac{535759L_H}{96} - \frac{3887351}{324} \right) \zeta_3 \right. \\ & + \frac{4548079L_H^2}{1152} + n_l^3 \left(-\frac{L_H^4}{432} - \frac{11L_H^3}{324} + \zeta_2 \left(\frac{L_H^2}{36} + \frac{11L_H}{54} - \frac{\zeta_3}{9} + \frac{275}{648} \right) + \left(\frac{L_H^2}{18} + \frac{5L_H}{27} + \frac{65}{432} \right) \zeta_3 - \frac{275L_H^2}{1296} - \frac{985L_H}{1458} \right. \\ & - \frac{5\zeta_4}{144} + \frac{5\zeta_5}{18} - \frac{520771}{559872} \left. \left. \right) + n_l^2 \left(\frac{143L_H^4}{864} + \frac{3529L_H^3}{1296} + \zeta_2 \left(-\frac{143L_H^2}{72} - \frac{3529L_H}{216} + \frac{259\zeta_3}{36} - \frac{197119}{5184} \right) + \left(-\frac{259L_H^2}{72} - \frac{500L_H}{27} \right. \right. \end{aligned}$$

$$\begin{aligned}
 & -\frac{11875}{432})\zeta_3 + \frac{197119L_H^2}{10368} + \left(\frac{25L_H}{18} - \frac{5015}{432}\right)\zeta_5 + \frac{6209245L_H}{93312} + \frac{5\zeta_3^2}{6} + \frac{311\zeta_4}{96} + \frac{220313525}{2239488} + n_l \left(-\frac{2249L_H^4}{576} - \frac{58843L_H^3}{864}\right. \\
 & + \zeta_2 \left(\frac{2249L_H^2}{48} + \frac{58843L_H}{144} - \frac{2047\zeta_3}{12} + \frac{576623}{576}\right) + \left(\frac{2047L_H^2}{24} + \frac{243511L_H}{432} + \frac{5747185}{5184}\right)\zeta_3 - \frac{576623L_H^2}{1152} + \left(-\frac{5L_H}{3}\right. \\
 & - \frac{49613}{576})\zeta_4 + \left(\frac{41215}{432} - \frac{1115L_H}{24}\right)\zeta_5 - \frac{56935973L_H}{31104} - \frac{955\zeta_3^2}{16} + \frac{2875\zeta_6}{288} + \frac{665\zeta_7}{72} - \frac{1045811915}{373248} + \left(\frac{30115L_H}{48} + \frac{373975}{432}\right)\zeta_5 \\
 & + \frac{49573615L_H}{3456} + \frac{458425\zeta_3^2}{432} + \frac{323975\zeta_4}{576} - \frac{1375\zeta_6}{32} - \frac{178045\zeta_7}{768} + \frac{10811054729}{497664} + a_s^3 \left(\frac{95L_H^3}{8} + \frac{3535L_H^2}{24} + n_l^2 \left(\frac{L_H^3}{54} + \frac{11L_H^2}{54}\right.\right. \\
 & + \left.\left(-\frac{L_H}{9} - \frac{11}{27}\right)\zeta_2 + \left(-\frac{2L_H}{9} - \frac{1}{3}\right)\zeta_3 + \frac{275L_H}{324} + \frac{15511}{11664}\right) + n_l \left(-\frac{17L_H^3}{18} - \frac{277L_H^2}{24} + \left(\frac{17L_H}{3} + \frac{277}{12}\right)\zeta_2 + \left(\frac{59L_H}{6}\right.\right. \\
 & + \left.\frac{262}{9}\right)\zeta_3 - \frac{11651L_H}{216} - \frac{5\zeta_4}{6} - \frac{25\zeta_5}{9} - \frac{46147}{486} + \left(-\frac{285L_H}{4} - \frac{3535}{12}\right)\zeta_2 + \left(-\frac{585L_H}{4} - \frac{109735}{216}\right)\zeta_3 + \frac{49349L_H}{72} \\
 & + \frac{815\zeta_5}{12} + \frac{6163613}{5184} + a_s^2 \left(n_l \left(-\frac{L_H^2}{6} - \frac{11L_H}{9} + \frac{\zeta_2}{3} + \frac{2\zeta_3}{3} - \frac{65}{24}\right) + \frac{19L_H^2}{4} + \frac{106L_H}{3} - \frac{19\zeta_2}{2} - \frac{39\zeta_3}{2} + \frac{10801}{144}\right) + a_s (2L_H \\
 & + \frac{17}{3}) + 1
 \end{aligned}$$

Note that the a_s^4 contribution has been taken from ref. [124]. It is only printed for convenience and completeness here as it corresponds to the evaluation of five loop integrals. All results are given in electronic form in the ancillary file [84] to this thesis.

4.4.4. Numerical Results

In order to separate the top quark induced corrections to $\Gamma(H \rightarrow \text{hadrons})$ from the contribution of light quarks and that of purely gluonic final states one rewrites Eq. (4.9) in the form

$$\Gamma(H \rightarrow \text{hadrons}) = A_{b\bar{b}} (1 + \Delta_{\text{light}} + \Delta_{\text{top}} + \Delta_{gg}), \quad (4.20)$$

with the definitions

$$\Delta_{\text{light}} = \Delta_{22}, \quad (4.21)$$

$$\Delta_{\text{top}} = ((C_2)^2 - 1) (1 + \Delta_{22}) + C_1 C_2 \Delta_{12} + \frac{16M_H^2}{3m_b^2} (C_1)^2 \Delta_{11}^{m_b^2}, \quad (4.22)$$

$$\Delta_{gg} = \frac{16M_H^2}{3m_b^2} (C_1)^2 \Delta_{11}^{m_b=0}, \quad (4.23)$$

where $\Delta_{11}^{m_b=0}$ and $\Delta_{11}^{m_b}$ contain the parts of Δ_{11} proportional to 1 and m_b^2 , respectively. For the numerical evaluation, the following values are chosen: $M_t = 173.21$, $M_H = 125.09$, $\alpha_s^{(5)}(M_Z) = 0.1181$ and $m_b(m_b) = 4.163$. The renormalization scale is then set to $\mu^2 = M_H^2$ and using RunDec [144, 145] with four-loop accuracy one finds $m_b(\mu = M_H) = 2.773$ and $\alpha_s^{(5)}(\mu = M_H) = 0.1127$. One obtains the result for the individual contributions from Eq. (4.20)

$$\Delta_{\text{light}} \approx 0.20331 + 0.03752 + 0.001929 - 0.001368, \quad (4.24)$$

$$\Delta_{\text{top}} \approx 0.00000 + 0.004563 + 0.002562 + 0.000659, \quad (4.25)$$

$$\Delta_{gg} \approx 0.09699 + 0.06235 + 0.01911 + 0.001759, \quad (4.26)$$

where each part is split into the contributions proportional to $\alpha_s^1 \dots \alpha_s^4$. It is curious, that the single contributions Δ_{light} and Δ_{top} show a slow convergence behavior. However, upon building the sum of both contributions

$$1 + \Delta_{\text{light}} + \Delta_{\text{top}} \approx 1 + 0.2033 + 0.04208 + 0.004490 - 0.0007090, \quad (4.27)$$

the convergence is much better, where the α_s^4 term amounts to a 0.057% total correction. This implies, that the top quark induced corrections are indeed necessary to describe the hadronic Higgs boson decay at $\mathcal{O}(\alpha_s^4)$ and cannot be neglected.

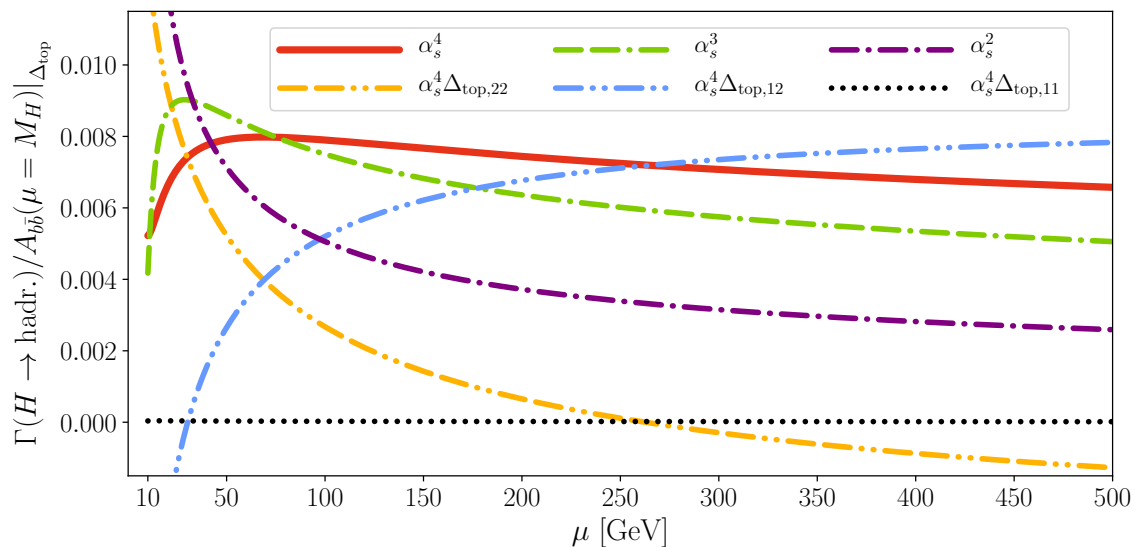


Figure 4.2.: Renormalization scale dependence of the top quark induced corrections Δ_{top} to the decay width $\Gamma(H \rightarrow \text{hadrons})$ normalized to $A_{b\bar{b}}(\mu^2 = M_H^2)$.

Figure 4.2 shows the renormalization scale dependence of the top quark induced corrections to the hadronic Higgs decay from Eq. (4.20) at α_s^4 , split into the contributions from $\Delta_{\text{top},11}$ (dotted, black), $\Delta_{\text{top},12}$ (single dashed, double dotted, blue) and $\Delta_{\text{top},22}$ (double dashed, double dotted, yellow). The combined result is shown as red line. Furthermore, also the top quark induced α_s^2 and α_s^3 corrections are shown as single dotted curves with single dashes in purple and double dashes in green, respectively. First of all, one can observe that with rising order in α_s , the top quark mediated contribution to $\Gamma(H \rightarrow \text{hadrons})/A_{b\bar{b}}(\mu = M_H)$ gets less dependent on the renormalization scale μ . Looking at the individual contributions which are summed up to α_s^4 , one sees that $\Delta_{\text{top},11}$ is two orders of magnitude smaller than $\Delta_{\text{top},12}$ and $\Delta_{\text{top},22}$ and can hardly be distinguished from zero. The reason for this is, that in Δ_{11} , quark loops appear only starting from three loops and are thus strongly suppressed. In contrast, the contributions from $\Delta_{\text{top},12}$ and $\Delta_{\text{top},22}$ are of the same order of magnitude. Their μ dependence nearly cancels against each other, such that the sum of all contributions, shown in red, is very stable with respect to changes in the renormalization scale μ .

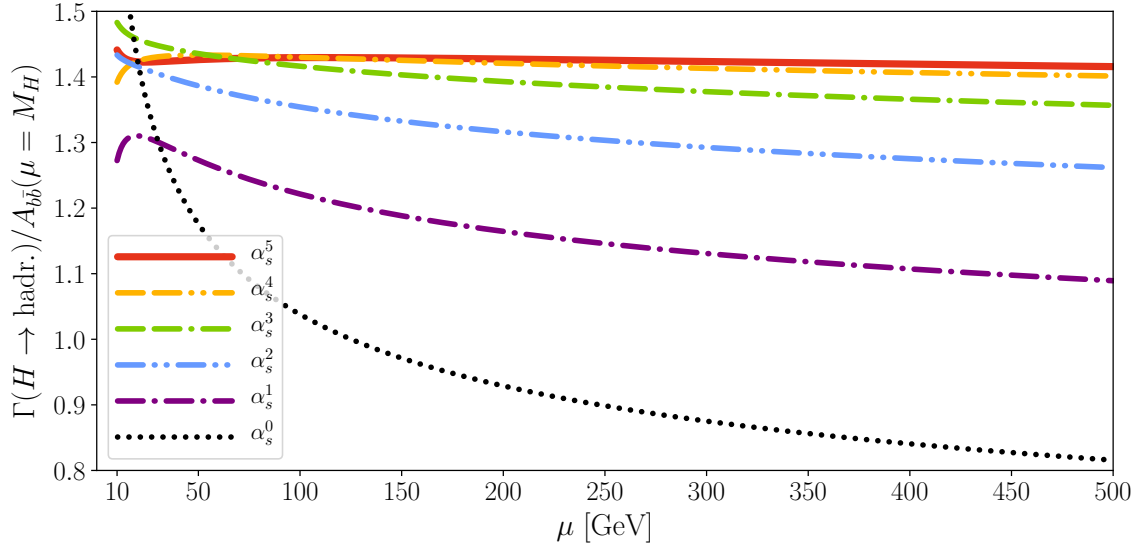


Figure 4.3.: Renormalization scale dependence of the decay width $\Gamma(H \rightarrow \text{hadrons})$ normalized to $A_{b\bar{b}}(\mu^2 = M_H^2)$.

Figure 4.3 shows the renormalization scale dependence of $\Gamma(H \rightarrow \text{hadrons})/A_{b\bar{b}}(\mu = M_H)$. One can observe, that the series in α_s shows good convergence and that the α_s^4 term in yellow shows a much more stable behavior than the green curve which shows the α_s^3 contribution. The α_s^5 result, obtained from the gluonic part only, is nearly μ independent.

4.5. Conclusion

Starting from the observation that at order α_s^3 the top quark induced corrections to the hadronic Higgs boson decay are of the same size as the contribution from massless quarks, in this chapter, the top quark induced corrections of order α_s^4 to the Higgs boson decay into hadrons was calculated. This was done in the framework of an effective field theory where the top quark is integrated out and effective $H\bar{b}b$ and Hgg couplings exist. Using the optical theorem, the necessary quantities to compute are four-loop propagator-type integrals. The computed piece Δ_{12} completes, with the available results from the literature, the QCD corrections to order α_s^4 . It was found, that the previously missing piece is numerically important as it is of the same size but with an opposite sign than the corresponding massless contribution Δ_{22} at the same order in α_s . Only the combination of both results leads to a fast convergence of the perturbative series in α_s . It was furthermore demonstrated that it drastically improves the stability of the decay width with respect to variations of the renormalization scale. To conclude, it is worthwhile mentioning that for the hadronic Higgs decay width five terms in the perturbative expansion are known, which is a very rare fact among most of the physical quantities considered in collider physics.

5. Conclusion and Outlook

The main goal of this thesis was the development of an approximation procedure for virtual gluon fusion NLO two-loop corrections in the limit of high energies. Therefore it was necessary to first identify the inherent tensor structure of the corresponding two-by-two scattering process, define projectors that allow one to write the amplitude in terms of scalar integrals and reduce these integrals to a minimal set of master integrals. Solving these integrals in the limit of high energies with the help of asymptotic expansions and differential equations provided the base for analytic expressions for the form factors and the partonic cross section of the problems. Using a subtraction procedure for IR singularities in two point gluon fusion amplitudes, the renormalized UV and IR finite virtual contribution to the NLO partonic cross section could be computed. The problem of extending the finite radius of convergence of the high energy expansion was addressed by the development of a Padé approximation-based reweighting method that provides both stable predictions and reliable uncertainty estimates. Moreover, all processes were also computed expanding in a large top quark mass.

This procedure was applied in chapter 2 for the examination of top quark mass effects in di- Z boson production via gluon fusion, a process which is greatly enhanced in proton-proton colliders such as the LHC due to the large gluon luminosities. A set of 20 tensor structures was identified and orthogonalized to a smaller set of 18 orthogonal linear combinations. At leading order, the exact result with full dependence on all scales could be computed for the corresponding form factors. The LO results of both expansions could successfully be verified against this exact result. At NLO, seven terms in the large top mass expansion up to $1/m_t^{12}$ were computed. Furthermore, the NLO high energy expansion with $m_Z^2 < m_t^2 \ll s, |t|$ was computed with three terms in the Z boson mass expansion up to m_Z^4 and 32 terms in the top quark mass expansion up to m_t^{32} . This required the reduction of more than 780,000 Feynman integrals and the development of new methods for treating the several ten Terabytes of intermediate analytical expressions.

Interesting findings were, that the imaginary part of some non-planar master integrals features odd powers in m_t that do not vanish in the amplitude. Furthermore it was found, that the m_Z^4 term is necessary for a sub-percent approximation of the exact result in the limit of high energies. Concerning the radius of convergence of the approximations, it was found, that for maximal transverse momenta at a scattering angle of $\theta = \pi/2$, the high energy expansion yields reliable results down to centre-of-mass energies of $\sqrt{s} \gtrsim 750$ GeV. Using the pole-distance-reweighted Padé approximation procedure, the convergence area could be extended down to the close proximity of the top quark pair production threshold around $\sqrt{s} \approx 350$ GeV. On the other hand, the large top mass expansion was shown to yield valid results again up to the close proximity of the top threshold with $\sqrt{s} \lesssim 340$ GeV. Using these techniques, predictions for the NLO form factors and the virtual finite piece of the partonic cross section were made.

Next steps are the inclusion of literature results for massless quarks and the computation of the real radiation. A paper discussing the findings of this thesis is in preparation.

In chapter 3 the process of Higgs pair production via gluon fusion was considered. Since the Higgs boson is a scalar particle, the tensor structure is much simpler and only two form factors are enough to describe the process. Also here, the high energy expansion was calculated at NLO up to m_t^{32} . In contrast to $gg \rightarrow ZZ$ it was however enough to consider only two terms in the m_H expansion up to m_H^2 to get a sub-percent description of the exact result at high energies. The large top mass expansion was only cross checked to low orders and subsequently taken from the literature, at NLO again up to $1/m_t^{12}$. A similar convergence behavior as for $gg \rightarrow ZZ$ could be observed and using the same techniques as before, precise predictions for a large part of the phase space could be made for the virtual finite part of the NLO partonic cross section. These predictions could be verified against a numerical NLO calculation with exact top quark mass dependence. The high energy results were then combined with the results of the numerical exact calculation such that an interpolation routine could be built, that yields precise results for the virtual finite part of the NLO partonic cross section on the whole phase space. The resulting program was made publicly available.

The aim here is, to produce another grid to describe also the results for Z boson pair production.

In addition to the pair production processes above, the hadronic Higgs boson decay was considered at order α_s^4 in chapter 4. Motivated by large top quark mediated contributions at order α_s^3 , the corresponding parts in α_s^4 were computed in an effective field theory with effective Higgs-gluon and Higgs-bottom quark couplings, where the top quark has been integrated out. Using the optical theorem, the problem could be mapped to the evaluation of slightly more than 1,250,000 scalar four-loop propagator-type massless integrals which could all be mapped to known master integrals from the literature. The newly computed top quark mediated piece turned out to be relevant, as it is of the same order of magnitude but opposite signed as the corresponding contribution from light quarks at the same order of α_s .

A.2. Basis Change $T^{\mu\nu\rho\sigma} \rightarrow \mathcal{T}^{\mu\nu\rho\sigma}$

This appendix gives the basis change relations from the simple tensors $\mathcal{T}_i^{\mu\nu\rho\sigma}$ derived in section 2.2.2 of chapter 2 – that are sufficient to write down the amplitude of the process $gg \rightarrow ZZ$ as given in equation (2.24) but lack orthogonality – to a set of orthogonal tensors $T_i^{\mu\nu\rho\sigma}$ derived in section 2.2.4 of the same chapter:

$$T_1^{\mu\nu\rho\sigma} = \mathcal{T}_{17}^{\mu\nu\rho\sigma} \frac{m_Z^2}{p_T^2(p_1 \cdot p_3)(p_2 \cdot p_3)} \quad (\text{A.2})$$

$$T_2^{\mu\nu\rho\sigma} = \mathcal{T}_{17}^{\mu\nu\rho\sigma} \frac{(m_Z^2 - p_T^2)^2}{4p_T^4(p_1 \cdot p_3)(p_2 \cdot p_3)} + \mathcal{T}_{18}^{\mu\nu\rho\sigma} \frac{(m_Z^2 - p_T^2)(p_2 \cdot p_3)}{2p_T^4(p_1 \cdot p_2)(p_1 \cdot p_3)} + \mathcal{T}_{19}^{\mu\nu\rho\sigma} \frac{(m_Z^2 - p_T^2)(p_1 \cdot p_3)}{2p_T^4(p_1 \cdot p_2)(p_2 \cdot p_3)} \\ + \mathcal{T}_{20}^{\mu\nu\rho\sigma} \frac{(p_1 \cdot p_3)(p_2 \cdot p_3)}{p_T^4(p_1 \cdot p_2)^2} \quad (\text{A.3})$$

$$T_3^{\mu\nu\rho\sigma} = \mathcal{T}_9^{\mu\nu\rho\sigma} \frac{m_Z^2}{(p_1 \cdot p_3)(p_2 \cdot p_3)} + \mathcal{T}_{17}^{\mu\nu\rho\sigma} \frac{m_Z^2}{p_T^2(p_1 \cdot p_3)(p_2 \cdot p_3)} \quad (\text{A.4})$$

$$T_4^{\mu\nu\rho\sigma} = \mathcal{T}_9^{\mu\nu\rho\sigma} \frac{(m_Z^2 - p_T^2)^2}{4p_T^2(p_1 \cdot p_3)(p_2 \cdot p_3)} + \mathcal{T}_{10}^{\mu\nu\rho\sigma} \frac{(m_Z^2 - p_T^2)(p_2 \cdot p_3)}{2p_T^2(p_1 \cdot p_2)(p_1 \cdot p_3)} + \mathcal{T}_{11}^{\mu\nu\rho\sigma} \frac{(m_Z^2 - p_T^2)(p_1 \cdot p_3)}{2p_T^2(p_1 \cdot p_2)(p_2 \cdot p_3)} \\ + \mathcal{T}_{12}^{\mu\nu\rho\sigma} \frac{(p_1 \cdot p_3)(p_2 \cdot p_3)}{p_T^2(p_1 \cdot p_2)^2} + \mathcal{T}_{17}^{\mu\nu\rho\sigma} \frac{(m_Z^2 - p_T^2)^2}{4p_T^4(p_1 \cdot p_3)(p_2 \cdot p_3)} + \mathcal{T}_{18}^{\mu\nu\rho\sigma} \frac{(m_Z^2 - p_T^2)(p_2 \cdot p_3)}{2p_T^4(p_1 \cdot p_2)(p_1 \cdot p_3)} \\ + \mathcal{T}_{19}^{\mu\nu\rho\sigma} \frac{(m_Z^2 - p_T^2)(p_1 \cdot p_3)}{2p_T^4(p_1 \cdot p_2)(p_2 \cdot p_3)} + \mathcal{T}_{20}^{\mu\nu\rho\sigma} \frac{(p_1 \cdot p_3)(p_2 \cdot p_3)}{p_T^4(p_1 \cdot p_2)^2} \quad (\text{A.5})$$

$$T_5^{\mu\nu\rho\sigma} = \mathcal{T}_4^{\mu\nu\rho\sigma} \frac{(m_Z^2 - p_T^2)}{2p_T^2(p_1 \cdot p_3)} + \mathcal{T}_5^{\mu\nu\rho\sigma} \frac{(p_1 \cdot p_3)}{p_T^2(p_1 \cdot p_2)} + \mathcal{T}_{17}^{\mu\nu\rho\sigma} \frac{(m_Z^2 - p_T^2)}{2p_T^4(p_1 \cdot p_2)} + \mathcal{T}_{18}^{\mu\nu\rho\sigma} \frac{(m_Z^2 - p_T^2)(p_2 \cdot p_3)}{2p_T^4(p_1 \cdot p_2)(p_1 \cdot p_3)} \\ + \mathcal{T}_{19}^{\mu\nu\rho\sigma} \frac{(p_1 \cdot p_3)^2}{p_T^4(p_1 \cdot p_2)^2} + \mathcal{T}_{20}^{\mu\nu\rho\sigma} \frac{(p_1 \cdot p_3)(p_2 \cdot p_3)}{p_T^4(p_1 \cdot p_2)^2} \quad (\text{A.6})$$

$$T_6^{\mu\nu\rho\sigma} = \mathcal{T}_{13}^{\mu\nu\rho\sigma} \frac{(m_Z^2 - p_T^2)}{2p_T^2(p_2 \cdot p_3)} + \mathcal{T}_{14}^{\mu\nu\rho\sigma} \frac{(p_2 \cdot p_3)}{p_T^2(p_1 \cdot p_2)} - \mathcal{T}_{17}^{\mu\nu\rho\sigma} \frac{(m_Z^2 - p_T^2)}{2p_T^4(p_1 \cdot p_2)} - \mathcal{T}_{18}^{\mu\nu\rho\sigma} \frac{(p_2 \cdot p_3)^2}{p_T^4(p_1 \cdot p_2)^2} \\ - \mathcal{T}_{19}^{\mu\nu\rho\sigma} \frac{(m_Z^2 - p_T^2)(p_1 \cdot p_3)}{2p_T^4(p_1 \cdot p_2)(p_2 \cdot p_3)} - \mathcal{T}_{20}^{\mu\nu\rho\sigma} \frac{(p_1 \cdot p_3)(p_2 \cdot p_3)}{p_T^4(p_1 \cdot p_2)^2} \quad (\text{A.7})$$

$$T_7^{\mu\nu\rho\sigma} = \mathcal{T}_6^{\mu\nu\rho\sigma} \frac{(p_2 \cdot p_3)}{p_T^2(p_1 \cdot p_2)} + \mathcal{T}_7^{\mu\nu\rho\sigma} \frac{(m_Z^2 - p_T^2)}{2p_T^2(p_2 \cdot p_3)} + \mathcal{T}_{17}^{\mu\nu\rho\sigma} \frac{(p_1 \cdot p_3)(p_2 \cdot p_3)}{p_T^4(p_1 \cdot p_2)^2} + \mathcal{T}_{18}^{\mu\nu\rho\sigma} \frac{(p_2 \cdot p_3)^2}{p_T^4(p_1 \cdot p_2)^2} \\ + \mathcal{T}_{19}^{\mu\nu\rho\sigma} \frac{(m_Z^2 - p_T^2)(p_1 \cdot p_3)}{2p_T^4(p_1 \cdot p_2)(p_2 \cdot p_3)} + \mathcal{T}_{20}^{\mu\nu\rho\sigma} \frac{(m_Z^2 - p_T^2)}{2p_T^4(p_1 \cdot p_2)} \quad (\text{A.8})$$

$$T_8^{\mu\nu\rho\sigma} = \mathcal{T}_{15}^{\mu\nu\rho\sigma} \frac{(p_1 \cdot p_3)}{p_T^2(p_1 \cdot p_2)} + \mathcal{T}_{16}^{\mu\nu\rho\sigma} \frac{(m_Z^2 - p_T^2)}{2p_T^2(p_1 \cdot p_3)} + \mathcal{T}_{17}^{\mu\nu\rho\sigma} \frac{(p_1 \cdot p_3)(p_2 \cdot p_3)}{p_T^4(p_1 \cdot p_2)^2} - \mathcal{T}_{18}^{\mu\nu\rho\sigma} \frac{(m_Z^2 - p_T^2)(p_2 \cdot p_3)}{2p_T^4(p_1 \cdot p_2)(p_1 \cdot p_3)} \\ - \mathcal{T}_{19}^{\mu\nu\rho\sigma} \frac{(p_1 \cdot p_3)^2}{p_T^4(p_1 \cdot p_2)^2} - \mathcal{T}_{20}^{\mu\nu\rho\sigma} \frac{(m_Z^2 - p_T^2)}{2p_T^4(p_1 \cdot p_2)} \quad (\text{A.9})$$

$$T_9^{\mu\nu\rho\sigma} = \mathcal{T}_8^{\mu\nu\rho\sigma} \frac{1}{p_T^2} - \mathcal{T}_{17}^{\mu\nu\rho\sigma} \frac{(p_1 \cdot p_3)(p_2 \cdot p_3)}{p_T^4(p_1 \cdot p_2)^2} - \mathcal{T}_{18}^{\mu\nu\rho\sigma} \frac{p_T^2(p_1 \cdot p_2) + (p_2 \cdot p_3)^2}{p_T^4(p_1 \cdot p_2)^2} \quad (\text{A.10})$$

$$- \mathcal{T}_{19}^{\mu\nu\rho\sigma} \frac{p_T^2(p_1 \cdot p_2) + (p_1 \cdot p_3)^2}{p_T^4(p_1 \cdot p_2)^2} - \mathcal{T}_{20}^{\mu\nu\rho\sigma} \frac{(p_1 \cdot p_3)(p_2 \cdot p_3)}{p_T^4(p_1 \cdot p_2)^2}$$

$$T_{10}^{\mu\nu\rho\sigma} = \mathcal{T}_3^{\mu\nu\rho\sigma} - \mathcal{T}_4^{\mu\nu\rho\sigma} \frac{(p_2 \cdot p_3)}{p_T^2(p_1 \cdot p_2)} - \mathcal{T}_5^{\mu\nu\rho\sigma} \frac{(p_1 \cdot p_3)}{p_T^2(p_1 \cdot p_2)} + \mathcal{T}_{15}^{\mu\nu\rho\sigma} \frac{(p_1 \cdot p_3)}{p_T^2(p_1 \cdot p_2)} + \mathcal{T}_{16}^{\mu\nu\rho\sigma} \frac{(p_2 \cdot p_3)}{p_T^2(p_1 \cdot p_2)} \quad (\text{A.11})$$

$$- \mathcal{T}_{17}^{\mu\nu\rho\sigma} \frac{(p_1 \cdot p_3)(p_2 \cdot p_3)}{p_T^4(p_1 \cdot p_2)^2} - \mathcal{T}_{18}^{\mu\nu\rho\sigma} \frac{(p_2 \cdot p_3)^2}{p_T^4(p_1 \cdot p_2)^2} - \mathcal{T}_{19}^{\mu\nu\rho\sigma} \frac{(p_1 \cdot p_3)^2}{p_T^4(p_1 \cdot p_2)^2} - \mathcal{T}_{20}^{\mu\nu\rho\sigma} \frac{(p_1 \cdot p_3)(p_2 \cdot p_3)}{p_T^4(p_1 \cdot p_2)^2}$$

$$T_{11}^{\mu\nu\rho\sigma} = \mathcal{T}_{17}^{\mu\nu\rho\sigma} \frac{m_Z^2(m_Z^2 - p_T^2)}{2p_T^2(p_1 \cdot p_3)(p_2 \cdot p_3)} + \mathcal{T}_{19}^{\mu\nu\rho\sigma} \frac{m_Z^2(p_1 \cdot p_3)}{p_T^2(p_1 \cdot p_2)(p_2 \cdot p_3)} \quad (\text{A.12})$$

$$T_{12}^{\mu\nu\rho\sigma} = \mathcal{T}_{17}^{\mu\nu\rho\sigma} \frac{m_Z^2(m_Z^2 - p_T^2)}{2p_T^2(p_1 \cdot p_3)(p_2 \cdot p_3)} + \mathcal{T}_{18}^{\mu\nu\rho\sigma} \frac{m_Z^2(p_2 \cdot p_3)}{p_T^2(p_1 \cdot p_2)(p_1 \cdot p_3)} \quad (\text{A.13})$$

$$T_{13}^{\mu\nu\rho\sigma} = \mathcal{T}_7^{\mu\nu\rho\sigma} \frac{m_Z^2}{(p_2 \cdot p_3)} + \mathcal{T}_{19}^{\mu\nu\rho\sigma} \frac{m_Z^2(p_1 \cdot p_3)}{p_T^2(p_1 \cdot p_2)(p_2 \cdot p_3)} + \mathcal{T}_{20}^{\mu\nu\rho\sigma} \frac{m_Z^2}{p_T^2(p_1 \cdot p_2)} \quad (\text{A.14})$$

$$T_{14}^{\mu\nu\rho\sigma} = \mathcal{T}_{16}^{\mu\nu\rho\sigma} \frac{m_Z^2}{(p_1 \cdot p_3)} - \mathcal{T}_{18}^{\mu\nu\rho\sigma} - \frac{m_Z^2(p_2 \cdot p_3)}{p_T^2(p_1 \cdot p_2)(p_1 \cdot p_3)} - \mathcal{T}_{20}^{\mu\nu\rho\sigma} \frac{m_Z^2}{p_T^2(p_1 \cdot p_2)} \quad (\text{A.15})$$

$$T_{15}^{\mu\nu\rho\sigma} = + \mathcal{T}_4^{\mu\nu\rho\sigma} \frac{m_Z^2}{(p_1 \cdot p_3)} + \mathcal{T}_{18}^{\mu\nu\rho\sigma} \frac{m_Z^2(p_2 \cdot p_3)}{p_T^2(p_1 \cdot p_2)(p_1 \cdot p_3)} + \mathcal{T}_{17}^{\mu\nu\rho\sigma} \frac{m_Z^2}{p_T^2(p_1 \cdot p_2)} \quad (\text{A.16})$$

$$T_{16}^{\mu\nu\rho\sigma} = \mathcal{T}_{13}^{\mu\nu\rho\sigma} \frac{m_Z^2}{(p_2 \cdot p_3)} - \mathcal{T}_{17}^{\mu\nu\rho\sigma} \frac{m_Z^2}{p_T^2(p_1 \cdot p_2)} - \mathcal{T}_{19}^{\mu\nu\rho\sigma} \frac{m_Z^2(p_1 \cdot p_3)}{p_T^2(p_1 \cdot p_2)(p_2 \cdot p_3)} \quad (\text{A.17})$$

$$T_{17}^{\mu\nu\rho\sigma} = \mathcal{T}_9^{\mu\nu\rho\sigma} \frac{m_Z^2(m_Z^2 - p_T^2)}{2(p_1 \cdot p_3)(p_2 \cdot p_3)} + \mathcal{T}_{11}^{\mu\nu\rho\sigma} \frac{m_Z^2(p_1 \cdot p_3)}{(p_1 \cdot p_2)(p_2 \cdot p_3)} + \mathcal{T}_{17}^{\mu\nu\rho\sigma} \frac{m_Z^2(m_Z^2 - p_T^2)}{2p_T^2(p_1 \cdot p_3)(p_2 \cdot p_3)} \quad (\text{A.18})$$

$$+ \mathcal{T}_{19}^{\mu\nu\rho\sigma} \frac{m_Z^2(p_1 \cdot p_3)}{p_T^2(p_1 \cdot p_2)(p_2 \cdot p_3)}$$

$$T_{18}^{\mu\nu\rho\sigma} = \mathcal{T}_9^{\mu\nu\rho\sigma} \frac{m_Z^2(m_Z^2 - p_T^2)}{2(p_1 \cdot p_3)(p_2 \cdot p_3)} + \mathcal{T}_{10}^{\mu\nu\rho\sigma} \frac{m_Z^2(p_2 \cdot p_3)}{(p_1 \cdot p_2)(p_1 \cdot p_3)} + \mathcal{T}_{17}^{\mu\nu\rho\sigma} \frac{m_Z^2(m_Z^2 - p_T^2)}{2p_T^2(p_1 \cdot p_3)(p_2 \cdot p_3)} \quad (\text{A.19})$$

$$+ \mathcal{T}_{18}^{\mu\nu\rho\sigma} \frac{m_Z^2(p_2 \cdot p_3)}{p_T^2(p_1 \cdot p_2)(p_1 \cdot p_3)}$$

$$T_{19}^{\mu\nu\rho\sigma} = \mathcal{T}_2^{\mu\nu\rho\sigma} - \mathcal{T}_3^{\mu\nu\rho\sigma} + \mathcal{T}_4^{\mu\nu\rho\sigma} \frac{(p_2 \cdot p_3)}{p_T^2(p_1 \cdot p_2)} + \mathcal{T}_5^{\mu\nu\rho\sigma} \frac{(p_1 \cdot p_3)}{p_T^2(p_1 \cdot p_2)} - \mathcal{T}_6^{\mu\nu\rho\sigma} \frac{(p_2 \cdot p_3)}{p_T^2(p_1 \cdot p_2)} \quad (\text{A.20})$$

$$- \mathcal{T}_7^{\mu\nu\rho\sigma} \frac{(p_1 \cdot p_3)}{p_T^2(p_1 \cdot p_2)} + \mathcal{T}_{13}^{\mu\nu\rho\sigma} \frac{(p_1 \cdot p_3)}{p_T^2(p_1 \cdot p_2)} + \mathcal{T}_{14}^{\mu\nu\rho\sigma} \frac{(p_2 \cdot p_3)}{p_T^2(p_1 \cdot p_2)} - \mathcal{T}_{15}^{\mu\nu\rho\sigma} \frac{(p_1 \cdot p_3)}{p_T^2(p_1 \cdot p_2)}$$

$$- \mathcal{T}_{16}^{\mu\nu\rho\sigma} \frac{(p_2 \cdot p_3)}{p_T^2(p_1 \cdot p_2)}$$

$$T_{20}^{\mu\nu\rho\sigma} = \mathcal{T}_1^{\mu\nu\rho\sigma} - \mathcal{T}_3^{\mu\nu\rho\sigma} + \mathcal{T}_4^{\mu\nu\rho\sigma} \frac{(p_2 \cdot p_3)}{p_T^2(p_1 \cdot p_2)} + \mathcal{T}_5^{\mu\nu\rho\sigma} \frac{(p_1 \cdot p_3)}{p_T^2(p_1 \cdot p_2)} + \mathcal{T}_8^{\mu\nu\rho\sigma} \frac{1}{p_T^2} \quad (\text{A.21})$$

$$- \mathcal{T}_9^{\mu\nu\rho\sigma} \frac{(p_1 \cdot p_3)(p_2 \cdot p_3)}{p_T^2(p_1 \cdot p_2)^2} - \mathcal{T}_{10}^{\mu\nu\rho\sigma} \frac{p_T^2(p_1 \cdot p_2) + (p_2 \cdot p_3)^2}{p_T^2(p_1 \cdot p_2)^2} - \mathcal{T}_{11}^{\mu\nu\rho\sigma} \frac{p_T^2(p_1 \cdot p_2) + (p_1 \cdot p_3)^2}{p_T^2(p_1 \cdot p_2)^2}$$

$$- \mathcal{T}_{12}^{\mu\nu\rho\sigma} \frac{(p_1 \cdot p_3)(p_2 \cdot p_3)}{p_T^2(p_1 \cdot p_2)^2} - \mathcal{T}_{15}^{\mu\nu\rho\sigma} \frac{(p_1 \cdot p_3)}{p_T^2(p_1 \cdot p_2)} - \mathcal{T}_{16}^{\mu\nu\rho\sigma} \frac{(p_2 \cdot p_3)}{p_T^2(p_1 \cdot p_2)} - \mathcal{T}_{18}^{\mu\nu\rho\sigma} \frac{1}{p_T^2(p_1 \cdot p_2)}$$

$$- \mathcal{T}_{19}^{\mu\nu\rho\sigma} \frac{1}{p_T^2(p_1 \cdot p_2)}$$

The coefficients γ_{lm} depend only on the masses and momenta of the external particles where p_1 and p_2 are the momenta of the incoming gluons and p_3 and p_4 are the momenta of the outgoing Z bosons and $p_T^2 = 2(p_1 \cdot p_3)(p_2 \cdot p_3)/(p_1 \cdot p_2) - m_Z^2$ is the transverse momentum.

A.3. Integral Families and Master Integrals

The master integrals and the definitions of their propagator structure have already been published in Ref. [41] and Ref. [42]. However, for completeness their definitions shall be repeated in the following. The integration measure is given by

$$\int Dk \equiv e^{\epsilon\gamma_E} \mu^{2\epsilon} \int \frac{d^d k}{i\pi^{d/2}} \quad (\text{A.22})$$

with dimension $d = 4 - 2\epsilon$, dimensional regularization parameter ϵ and renormalization scale μ , the families are defined via their propagators. At one-loop, there are maximally four propagators

$$D_1(p_1, p_2, p_3, p_4) = \{m_t^2 - l_1^2, m_t^2 - (l_1 + p_3)^2, m_t^2 - (l_1 - p_1 - p_2)^2, m_t^2 - (l_1 - p_1)^2\} . \quad (\text{A.23})$$

with the external, incoming momenta p_1, \dots, p_4 , loop momentum l_1 and the top quark mass m_t . In the two-loop case, the families are defined via seven propagators and two irreducible numerators

$$\begin{aligned} D_6(p_1, p_2, p_3, p_4) &= \{m_t^2 - l_1^2, m_t^2 - l_2^2, m_t^2 - (l_2 + p_3)^2, m_t^2 - (l_2 - p_1 - p_2)^2, \\ &\quad m_t^2 - (l_1 - p_1 - p_2)^2, m_t^2 - (l_1 - p_1)^2, -(l_1 - l_2)^2, -(l_1 + p_3)^2, \\ &\quad -(l_2 + p_1)^2\} , \\ D_{20}(p_1, p_2, p_3, p_4) &= \{-l_1^2, m_t^2 - l_2^2, m_t^2 - (l_2 + p_3)^2, m_t^2 - (l_2 - p_1 - p_2)^2, \\ &\quad -(l_1 - p_1 - p_2)^2, -(l_1 - p_1)^2, m_t^2 - (l_1 - l_2)^2, -(l_1 + p_3)^2, -(l_2 + p_1)^2\} , \\ D_{33}(p_1, p_2, p_3, p_4) &= \{-l_1^2, m_t^2 - l_2^2, m_t^2 - (l_2 + p_4)^2, -(l_1 + p_3 + p_4)^2, -(l_1 - p_1)^2, \\ &\quad m_t^2 - (l_1 - l_2 + p_3)^2, m_t^2 - (l_1 - l_2)^2, -(l_1 + p_4)^2, -(l_2 + p_1)^2\} , \\ D_{47}(p_1, p_2, p_3, p_4) &= \{-l_1^2, m_t^2 - l_2^2, m_t^2 - (l_2 + p_4)^2, m_t^2 - (l_2 - p_1 - p_2)^2, \\ &\quad m_t^2 - (l_1 - l_2 + p_2)^2, m_t^2 - (l_1 - l_2)^2, -(l_1 - p_1)^2, -(l_1 + p_4)^2, \\ &\quad -(l_2 + p_1)^2\} , \\ D_{72}(p_1, p_2, p_3, p_4) &= \{m_t^2 - l_1^2, m_t^2 - (l_1 + p_2)^2, m_t^2 - (l_1 + p_1 + p_2)^2, m_t^2 - (l_2 + p_1 + p_2)^2, \\ &\quad m_t^2 - (l_2 - p_3)^2, m_t^2 - (l_1 - p_3)^2, -(l_1 - l_2)^2, -(l_2 + p_2)^2, -(l_2 + p_3)^2\} , \\ D_{75}(p_1, p_2, p_3, p_4) &= \{m_t^2 - l_1^2, m_t^2 - (l_1 + p_4)^2, m_t^2 - (l_1 - p_1 - p_2)^2, -(l_2 - p_1 - p_2)^2, \\ &\quad -(l_2 - p_1)^2, m_t^2 - (l_1 - p_1)^2, m_t^2 - (l_1 - l_2)^2, -(l_2 + p_4)^2, -(l_2 + p_1)^2\} , \\ D_{90}(p_1, p_2, p_3, p_4) &= \{m_t^2 - l_1^2, m_t^2 - (l_1 + p_3)^2, -(l_1 + l_2 - p_1 - p_2)^2, -(l_1 + l_2 - p_1)^2, \\ &\quad m_t^2 - (l_1 - p_1)^2, m_t^2 - (l_2 + p_4)^2, m_t^2 - l_2^2, -(l_2 + p_3)^2, -(l_2 + p_1)^2\} . \end{aligned} \quad (\text{A.24})$$

Here, l_1 and l_2 are the loop momenta. These are the main families since the other families are related to them by permutations of the external momenta. This means, that for one-loop, the families with indices 2 and 3 are obtained from family 1 through

$$D_2(p_1, p_2, p_3, p_4) = D_1(p_1, p_2, p_4, p_3) \quad D_3(p_1, p_2, p_3, p_4) = D_1(p_1, p_4, p_3, p_2) . \quad (\text{A.25})$$

Also at two-loops, the remaining families are related to the ones defined in Eq. (A.24) via

$$\begin{aligned}
 D_4(p_1, p_2, p_3, p_4) &= D_6(p_1, p_4, p_3, p_2) & D_5(p_1, p_2, p_3, p_4) &= D_6(p_1, p_2, p_4, p_3) \\
 D_8(p_1, p_2, p_3, p_4) &= D_6(p_4, p_1, p_3, p_2) & D_{10}(p_1, p_2, p_3, p_4) &= D_6(p_3, p_1, p_4, p_2) \\
 D_{11}(p_1, p_2, p_3, p_4) &= D_6(p_3, p_1, p_2, p_4) & D_{26}(p_1, p_2, p_3, p_4) &= D_{20}(p_4, p_3, p_1, p_2) \\
 D_{51}(p_1, p_2, p_3, p_4) &= D_{47}(p_2, p_1, p_3, p_4) & D_{59}(p_1, p_2, p_3, p_4) &= D_{47}(p_2, p_3, p_1, p_4) \\
 D_{71}(p_1, p_2, p_3, p_4) &= D_{72}(p_1, p_2, p_4, p_3) & D_{73}(p_1, p_2, p_3, p_4) &= D_{72}(p_1, p_4, p_2, p_3) \\
 D_{78}(p_1, p_2, p_3, p_4) &= D_{75}(p_4, p_1, p_2, p_3) & D_{79}(p_1, p_2, p_3, p_4) &= D_{75}(p_2, p_1, p_3, p_4) \\
 D_{84}(p_1, p_2, p_3, p_4) &= D_{75}(p_3, p_2, p_4, p_1) & D_{91}(p_1, p_2, p_3, p_4) &= D_{90}(p_4, p_1, p_2, p_3).
 \end{aligned} \tag{A.26}$$

At one-loop, there are 10 master integrals given by

$$\begin{aligned}
 G_1(1, 1, 1, 1), & \quad G_2(1, 0, 1, 0), & G_2(1, 1, 1, 0), & \quad G_2(1, 1, 1, 1), & G_3(0, 0, 0, 1), \\
 G_3(0, 1, 0, 1), & \quad G_3(1, 0, 1, 0), & G_3(1, 1, 0, 1), & \quad G_3(1, 1, 1, 0), & G_3(1, 1, 1, 1),
 \end{aligned}$$

and at two loops there are 131 planar master integrals

$$\begin{aligned}
 G_4(1, 1, 1, 1, 1, 1, 0, 0), & \quad G_4(1, 1, 1, 1, 1, 2, 0, 0), & G_4(1, 1, 1, 1, 1, 2, 1, 0, 0), & \quad G_5(1, 1, 1, 1, 1, 1, 1, 0, 0), \\
 G_5(1, 1, 1, 1, 1, 1, 2, 0, 0), & \quad G_5(1, 1, 1, 1, 1, 2, 1, 0, 0), & G_6(1, 1, 0, 1, 1, 0, 0, 0, 0), & \quad G_6(1, 1, 0, 1, 1, 1, 0, 0, 0), \\
 G_6(1, 1, 1, 1, 1, 1, 0, 0, 0), & \quad G_6(1, 1, 1, 1, 1, 1, 1, 0, 0), & G_6(1, 1, 1, 1, 1, 1, 2, 0, 0), & \quad G_6(1, 1, 1, 1, 1, 2, 1, 0, 0), \\
 G_8(1, 1, 0, 1, 1, 0, 0, 0, 0), & \quad G_8(1, 1, 0, 1, 1, 1, 0, 0, 0), & G_8(1, 1, 1, 1, 1, 1, 0, 0, 0), & \quad G_8(1, 1, 1, 1, 1, 1, 1, 0, 0), \\
 G_8(1, 1, 1, 1, 1, 1, 2, 0, 0), & \quad G_8(1, 1, 1, 1, 1, 2, 1, 0, 0), & G_{10}(1, 1, 1, 1, 1, 1, 1, 0, 0), & \quad G_{10}(1, 1, 1, 1, 1, 1, 2, 0, 0), \\
 G_{10}(1, 1, 1, 1, 1, 2, 1, 0, 0), & \quad G_{11}(1, 1, 0, 1, 1, 0, 0, 0, 0), & G_{11}(1, 1, 0, 1, 1, 1, 0, 0, 0), & \quad G_{11}(1, 1, 1, 1, 1, 1, 0, 0, 0), \\
 G_{11}(1, 1, 1, 1, 1, 1, 1, 0, 0), & \quad G_{11}(1, 1, 1, 1, 1, 1, 2, 0, 0), & G_{11}(1, 1, 1, 1, 1, 2, 1, 0, 0), & \quad G_{20}(1, 1, 0, 1, 1, 0, 0, 0, 0), \\
 G_{20}(1, 1, 0, 1, 1, 0, 1, 0, 0), & \quad G_{20}(1, 1, 1, 1, 1, 0, 0, 0, 0), & G_{20}(1, 1, 1, 1, 1, 0, 1, 0, 0), & \quad G_{20}(1, 1, 1, 1, 1, 1, 1, 0, 0), \\
 G_{20}(1, 1, 1, 1, 1, 1, 2, 0, 0), & \quad G_{20}(1, 1, 1, 1, 1, 2, 1, 0, 0), & G_{20}(1, 1, 2, 1, 1, 1, 1, 0, 0), & \quad G_{26}(1, 1, 1, 1, 1, 1, 1, 0, 0), \\
 G_{26}(1, 1, 1, 1, 1, 1, 2, 0, 0), & \quad G_{26}(1, 1, 1, 1, 1, 2, 1, 0, 0), & G_{26}(1, 1, 2, 1, 1, 1, 1, 0, 0), & \quad G_{33}(1, 0, 1, 1, 1, 0, 1, 0, 0), \\
 G_{33}(1, 0, 1, 1, 2, 0, 1, 0, 0), & \quad G_{33}(1, 1, 0, 1, 0, 0, 0, 0, 0), & G_{33}(1, 1, 0, 1, 0, 1, 0, 0, 0), & \quad G_{33}(1, 1, 0, 1, 0, 2, 0, 0, 0), \\
 G_{33}(1, 1, 0, 1, 1, 1, 0, 0, 0), & \quad G_{33}(1, 1, 0, 1, 2, 1, 0, 0, 0), & G_{33}(1, 1, 1, 1, 0, 1, 0, 0, 0), & \quad G_{33}(1, 1, 1, 1, 1, 0, 1, 0, 0), \\
 G_{33}(1, 1, 1, 1, 1, 1, 0, 0, 0), & \quad G_{47}(1, 1, 1, 2, 1, 0, 0, 0, 0), & G_{71}(1, 1, 1, 1, 1, 0, 1, 0, 0), & \quad G_{71}(1, 1, 2, 1, 1, 0, 1, 0, 0), \\
 G_{71}(1, 2, 0, 1, 0, 1, 1, 0, 0), & \quad G_{72}(0, 1, 0, 1, 1, 2, 1, 0, 0), & G_{72}(1, 0, 1, 1, 1, 0, 1, 0, 0), & \quad G_{72}(1, 0, 2, 1, 1, 0, 1, 0, 0), \\
 G_{72}(1, 1, 0, 1, 1, 0, 1, 0, 0), & \quad G_{72}(1, 1, 0, 1, 1, 0, 2, 0, 0), & G_{72}(1, 1, 0, 1, 1, 0, 3, 0, 0), & \quad G_{72}(1, 1, 0, 1, 1, 1, 1, 0, 0), \\
 G_{72}(1, 1, 0, 1, 1, 2, 1, 0, 0), & \quad G_{72}(1, 1, 1, 1, 1, 0, 1, 0, 0), & G_{72}(1, 1, 2, 1, 1, 0, 1, 0, 0), & \quad G_{73}(0, 1, 0, 1, 0, 1, 2, 0, 0), \\
 G_{73}(0, 1, 0, 1, 1, 2, 1, 0, 0), & \quad G_{73}(0, 1, 1, 1, 1, 0, 1, 0, 0), & G_{73}(1, 0, 1, 1, 1, 0, 1, 0, 0), & \quad G_{73}(1, 1, 0, 1, 1, 2, 1, 0, 0), \\
 G_{73}(1, 1, 1, 1, 1, 0, 1, 0, 0), & \quad G_{73}(1, 1, 2, 1, 1, 0, 1, 0, 0), & G_{75}(1, 1, 0, 1, 0, 2, 1, 0, 0), & \quad G_{78}(1, 1, 0, 1, 0, 1, 1, 0, 0), \\
 G_{78}(1, 1, 0, 1, 0, 2, 1, 0, 0), & \quad G_{78}(1, 1, 1, 0, 0, 1, 1, 0, 0), & G_{78}(1, 1, 1, 0, 1, 0, 1, 0, 0), & \quad G_{78}(1, 2, 1, 0, 1, 0, 1, 0, 0), \\
 G_{78}(2, 1, 0, 1, 0, 1, 1, 0, 0), & \quad G_{79}(1, 0, 1, 0, 0, 0, 1, 0, 0), & G_{79}(1, 0, 1, 0, 0, 1, 1, 0, 0), & \quad G_{79}(1, 0, 1, 0, 1, 0, 1, 0, 0), \\
 G_{79}(1, 0, 1, 0, 1, 0, 2, 0, 0), & \quad G_{79}(1, 0, 1, 0, 2, 0, 1, 0, 0), & G_{79}(1, 1, 1, 0, 0, 1, 1, 0, 0), & \quad G_{79}(1, 1, 1, 0, 1, 0, 1, 0, 0), \\
 G_{79}(1, 2, 1, 0, 1, 0, 1, 0, 0), & \quad G_{84}(0, 1, 0, 0, 2, 0, 1, 0, 0), & G_{84}(1, 0, 1, 0, 0, 0, 1, 0, 0), & \quad G_{84}(1, 0, 1, 0, 0, 1, 1, 0, 0), \\
 G_{84}(1, 0, 1, 0, 1, 0, 1, 0, 0), & \quad G_{84}(1, 0, 1, 0, 1, 0, 2, 0, 0), & G_{84}(1, 0, 1, 0, 2, 0, 1, 0, 0), & \quad G_{84}(1, 1, 1, 0, 0, 1, 1, 0, 0), \\
 G_{84}(1, 1, 1, 0, 1, 0, 1, 0, 0), & \quad G_{84}(1, 2, 1, 0, 1, 0, 1, 0, 0), & G_{84}(2, 1, 1, 0, 1, 0, 1, 0, 0), & \quad G_{90}(1, 1, 1, 0, 1, 1, 1, 0, 0), \\
 G_{90}(1, 2, 1, 0, 1, 1, 1, 0, 0), & \quad G_{91}(0, 0, 0, 0, 1, 0, 1, 0, 0), & G_{91}(0, 0, 1, 0, 1, 1, 0, 0, 0), & \quad G_{91}(0, 0, 1, 0, 1, 1, 1, 0, 0), \\
 G_{91}(0, 1, 0, 0, 1, 0, 1, 0, 0), & \quad G_{91}(0, 1, 0, 1, 1, 1, 0, 0, 0), & G_{91}(0, 1, 0, 1, 1, 1, 1, 0, 0), & \quad G_{91}(0, 1, 0, 1, 1, 2, 0, 0, 0), \\
 G_{91}(1, 0, 0, 1, 0, 1, 0, 0, 0), & \quad G_{91}(1, 0, 0, 1, 0, 1, 1, 0, 0), & G_{91}(1, 0, 0, 1, 1, 1, 1, 0, 0), & \quad G_{91}(1, 0, 0, 2, 0, 1, 0, 0, 0), \\
 G_{91}(1, 0, 1, 0, 0, 0, 1, 0, 0), & \quad G_{91}(1, 0, 1, 0, 0, 1, 1, 0, 0), & G_{91}(1, 0, 1, 0, 1, 1, 1, 0, 0), & \quad G_{91}(1, 0, 1, 1, 0, 1, 1, 0, 0), \\
 G_{91}(1, 0, 1, 1, 1, 1, 0, 0, 0), & \quad G_{91}(1, 0, 1, 1, 1, 2, 0, 0, 0), & G_{91}(1, 0, 2, 0, 0, 0, 1, 0, 0), & \quad G_{91}(1, 0, 2, 0, 1, 1, 1, 0, 0), \\
 G_{91}(1, 0, 3, 0, 1, 1, 1, 0, 0), & \quad G_{91}(1, 1, 0, 0, 1, 0, 1, 0, 0), & G_{91}(1, 1, 0, 0, 1, 0, 1, 1, 0, 0), & \quad G_{91}(1, 1, 0, 1, 0, 1, 1, 0, 0), \\
 G_{91}(1, 1, 0, 2, 0, 1, 1, 0, 0), & \quad G_{91}(1, 1, 0, 3, 0, 1, 1, 0, 0), & G_{91}(1, 1, 1, 0, 0, 1, 1, 0, 0), & \quad G_{91}(1, 1, 1, 0, 1, 0, 1, 0, 0), \\
 G_{91}(1, 1, 1, 0, 1, 1, 1, 0, 0), & \quad G_{91}(1, 1, 1, 1, 0, 0, 1, 0, 0), & G_{91}(1, 1, 1, 1, 0, 0, 2, 0, 0), & \quad G_{91}(1, 2, 1, 0, 1, 0, 1, 0, 0), \\
 G_{91}(2, 0, 1, 1, 0, 1, 1, 0, 0), & \quad G_{91}(2, 1, 0, 1, 1, 1, 0, 0, 0), & G_{91}(2, 1, 1, 0, 1, 0, 1, 0, 0), &
 \end{aligned} \tag{A.27}$$

and 30 non-planar master integrals

$$\begin{aligned}
 &G_{33}(1, 1, 1, 1, 0, 1, 1, 0, 0), & G_{33}(1, 1, 1, 1, 0, 2, 1, 0, 0), & G_{33}(1, 1, 1, 1, 1, 1, 1, -2, 0), & G_{33}(1, 1, 1, 1, 1, 1, 1, -1, 0), \\
 &G_{33}(1, 1, 1, 1, 1, 1, 1, 0, -2), & G_{33}(1, 1, 1, 1, 1, 1, 1, 0, 0), & G_{59}(1, 0, 1, 1, 1, 1, 1, 0, 0), & G_{59}(1, 1, 0, 1, 1, 1, 1, 0, 0), \\
 &G_{59}(1, 1, 1, 1, 1, 1, 1, -2, 0), & G_{59}(1, 1, 1, 1, 1, 1, 1, -1, 0), & G_{59}(1, 1, 1, 1, 1, 1, 1, 0, -2), & G_{59}(1, 1, 1, 1, 1, 1, 1, 0, -1), \\
 &G_{59}(1, 1, 1, 1, 1, 1, 1, 0, 0), & G_{47}(1, 0, 1, 1, 2, 1, 1, 0, 0), & G_{47}(1, 1, 1, 0, 1, 2, 1, 0, 0), & G_{91}(0, 1, 1, 1, 1, 1, 1, 0, 0), \\
 &G_{91}(1, 0, 1, 1, 1, 1, 1, 0, 0), & G_{91}(1, 0, 1, 1, 1, 1, 2, 0, 0), & G_{91}(1, 1, 1, 1, 0, 1, 1, 0, 0), & G_{91}(1, 1, 1, 1, 1, 1, 1, -2, 0), \\
 &G_{91}(1, 1, 1, 1, 1, 1, 1, -1, 0), & G_{91}(1, 1, 1, 1, 1, 1, 1, 0, -2), & G_{91}(1, 1, 1, 1, 1, 1, 1, 0, -1), & G_{91}(1, 1, 1, 1, 1, 1, 1, 0, 0), \\
 &G_{51}(1, 1, 0, 1, 1, 1, 1, 0, 0), & G_{51}(1, 1, 1, 1, 1, 1, 1, -2, 0), & G_{51}(1, 1, 1, 1, 1, 1, 1, -1, 0), & G_{51}(1, 1, 1, 1, 1, 1, 1, 0, -2), \\
 &G_{51}(1, 1, 1, 1, 1, 1, 1, 0, -1), & G_{51}(1, 1, 1, 1, 1, 1, 1, 0, 0). & &
 \end{aligned} \tag{A.28}$$

A subset of the graphical representations of the planar master integrals is given in Fig. A.1.

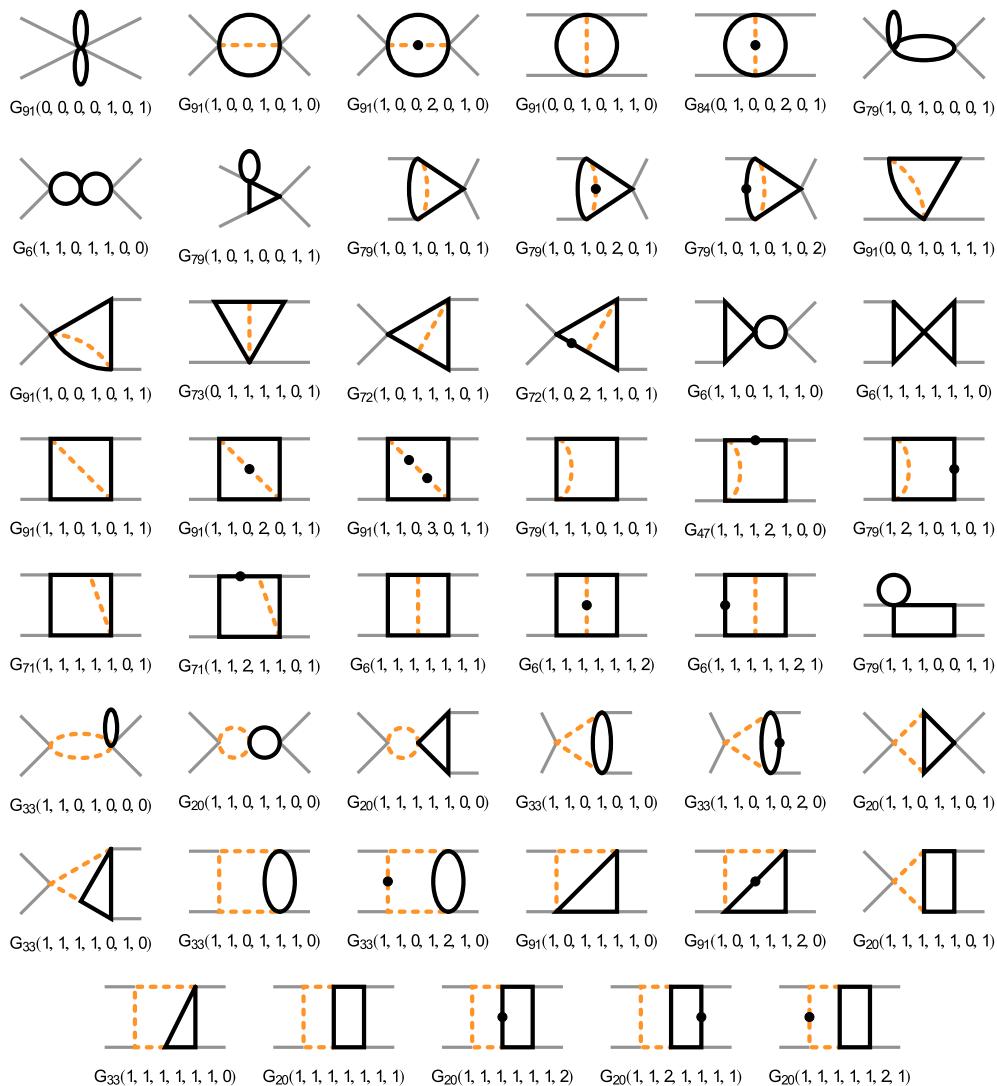


Figure A.1: Graphical representation of a subset of the planar master integrals. Solid grey lines are external legs, dashed orange lines denote massless internal lines and solid black lines denote massive internal lines. One or two dots on one of the lines denotes a squared or cubed propagator, respectively.

Fig. A.2 shows a subset of the non-planar master integrals in their graphical representation.

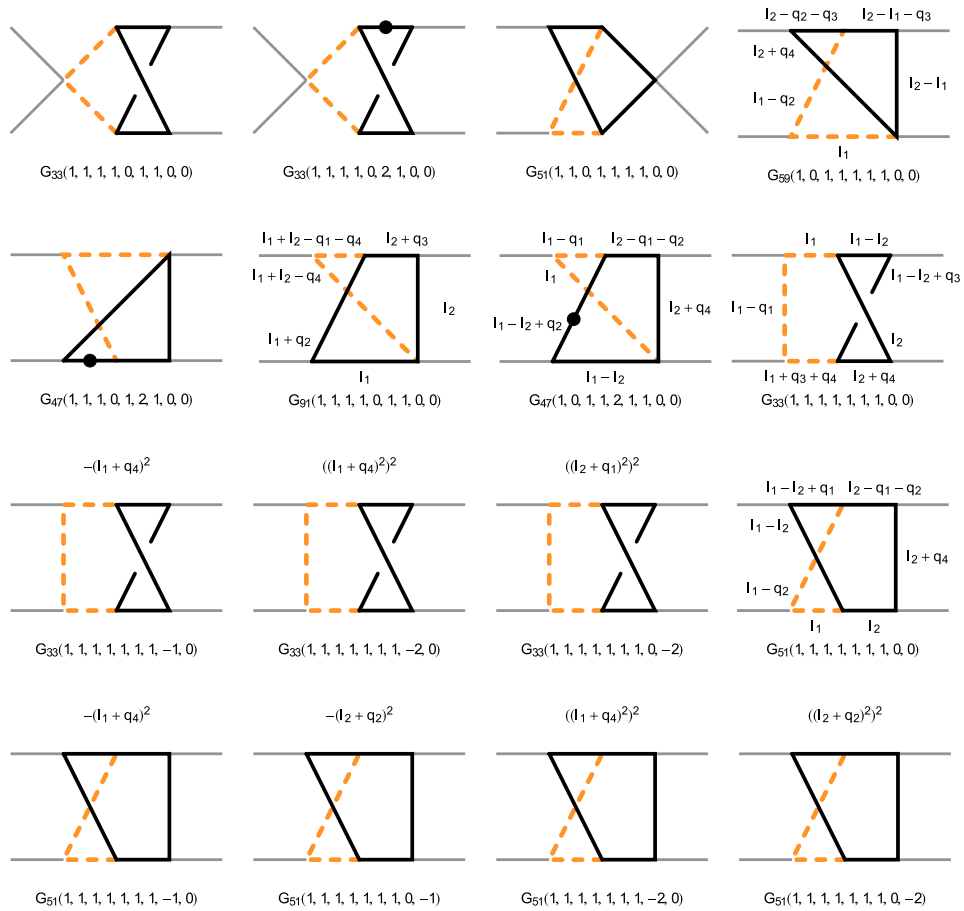


Figure A.2.: Graphical representation of a subset of the non-planar master integrals. Solid grey lines are external legs, dashed orange lines denote massless internal lines and solid black lines denote massive internal lines. One or two dots on one of the lines denotes a squared or cubed propagator, respectively. Negative indices in a master integral denote a numerator. For these cases, the corresponding numerator is given explicitly above the diagram.

The graphical representation of the remaining master integrals can be obtained by permutations of the external legs which is why they are not drawn.

Harmonic Polylogarithms

The master integrals are functions of rational polynomials in s and t , ordinary logarithms and harmonic polylogarithms (see Eq. (2.61)). The latter can be expressed in terms of usual polylogarithms by the following replacements:

$$H_2(x) = \text{Li}_2(x), \quad (\text{A.29})$$

$$H_3(x) = \text{Li}_3(x), \quad (\text{A.30})$$

$$H_4(x) = \text{Li}_4(x), \quad (\text{A.31})$$

$$H_{22}(x) = \frac{\text{Li}_2(x)^2}{2} - 2S_{2,2}(x), \quad (\text{A.32})$$

$$H_{21}(x) = -\text{Li}_3(1-x) + \text{Li}_2(1-x) \log(1-x) + \frac{1}{2} \log(x) \log^2(1-x) + \zeta_3, \quad (\text{A.33})$$

$$H_{211}(x) = -\text{Li}_4(1-x) - \frac{1}{2} \text{Li}_2(1-x) \log^2(1-x) + \text{Li}_3(1-x) \log(1-x) \quad (\text{A.34})$$

$$- \frac{1}{6} \log(x) \log^3(1-x) + \zeta_4, \quad (\text{A.35})$$

A.4. Change of Variables

This appendix shall give a short advice on how to perform a change of variables from t to $\cos(\theta)$ or p_T for the high energy expansion. Given

$$s + t + u = 2m_H^2 \quad \text{and} \quad p_T^2 = \frac{tu - m_H^4}{s}, \quad (\text{A.36})$$

one finds

$$t = m_H^2 - \frac{s}{2} \left(1 - \sqrt{1 - 4 \frac{m_H^2 + p_T^2}{s}} \right) \quad \text{or} \quad t = m_H^2 - \frac{s}{2} \left(1 - \sqrt{1 - 4 \frac{m_H^2}{s} \cos(\theta)} \right). \quad (\text{A.37})$$

To obtain a consistently expanded version of the form factors in m_H , t is to be replaced by either its $\cos(\theta)$ or p_T version from Eq. (A.37) and the rational functions in the form factors are to be expanded in m_H . In addition, the harmonic polylogarithms need to be replaced in the $\cos(\theta)$ case by:

$$\begin{aligned} \text{HPL} \left(\{2\}, -\frac{t}{s} \right) &\rightarrow H_2 + \frac{2m_H^4 l_+}{s^2(x_{p_t} - 1)x_{p_t}^3} - \frac{2m_H^2 l_+}{s x_{p_t}}, \\ \text{HPL} \left(\{3\}, -\frac{t}{s} \right) &\rightarrow -\frac{2m_H^4 H_2}{s^2(x_{p_t} - 1)x_{p_t}^3} + \frac{2m_H^2 H_2}{s x_{p_t}} + H_3, \\ \text{HPL} \left(\{4\}, -\frac{t}{s} \right) &\rightarrow -\frac{2m_H^4 H_3}{s^2(x_{p_t} - 1)x_{p_t}^3} + \frac{2m_H^2 H_3}{s x_{p_t}} + H_4, \\ \text{HPL} \left(\{2, 1\}, -\frac{t}{s} \right) &\rightarrow H_{2,1} - \frac{m_H^4 l_+^2}{s^2(x_{p_t} - 1)x_{p_t}^3} + \frac{m_H^2 l_+^2}{s x_{p_t}}, \\ \text{HPL} \left(\{2, 2\}, -\frac{t}{s} \right) &\rightarrow m_H^4 \left(\frac{4H_{2,1}}{s^2(x_{p_t} - 1)x_{p_t}^3} + \frac{2l_+ H_2}{s^2(x_{p_t} - 1)x_{p_t}^3} \right) + m_H^2 \left(-\frac{4H_{2,1}}{s x_{p_t}} - \frac{2l_+ H_2}{s x_{p_t}} \right) + H_{2,2}, \\ \text{HPL} \left(\{2, 1, 1\}, -\frac{t}{s} \right) &\rightarrow H_{2,1,1} + \frac{m_H^4 l_+^3}{3s^2(x_{p_t} - 1)x_{p_t}^3} - \frac{m_H^2 l_+^3}{3s x_{p_t}}, \\ \log \left(\frac{s+t}{s} \right) &\rightarrow -\frac{2m_H^4 (x_{p_t}^3 - 2x_{p_t}^2 + 2x_{p_t} + 1)}{s^2 x_{p_t}^3 (x_{p_t} + 1)^2} + \frac{2m_H^2 (x_{p_t} - 1)}{s x_{p_t} (x_{p_t} + 1)} + l_+, \\ \log \left(-\frac{t}{s} \right) &\rightarrow -\frac{2m_H^4 (x_{p_t}^2 - x_{p_t} + 1)}{s^2 (x_{p_t} - 1) x_{p_t}^3} + \frac{2m_H^2}{s x_{p_t}} + L_- \end{aligned} \quad (\text{A.38})$$

with $x_{p_T} = \sqrt{1 - \frac{4p_T^2}{s}}$ and

$$H_{i,j,\dots} = \text{HPL} \left(\{i, j, \dots\}, \frac{1 - x_{p_T}}{2} \right), \quad l_+ = \log \left(\frac{1 + x_{p_T}}{2} \right) \quad \text{and} \quad L_- = \log \left(\frac{1 - x_{p_T}}{2} \right). \quad (\text{A.39})$$

For a variable change in favor of p_T , the following replacements apply:

$$\begin{aligned}
\text{HPL} \left(\{2\}, \frac{-t}{s} \right) &\rightarrow H_2 + m_H^4 \left(-\frac{2(2 \cos(\theta) - 1)l_+}{(\cos(\theta) - 1)s^2} - \frac{2(\cos(\theta) - 1)}{(\cos(\theta) + 1)s^2} \right) - \frac{2l_+ m_H^2}{s}, \\
\text{HPL} \left(\{3\}, \frac{-t}{s} \right) &\rightarrow m_H^4 \left(\frac{2l_+}{s^2} - \frac{2(2 \cos(\theta) - 1)H_2}{(\cos(\theta) - 1)s^2} \right) - \frac{2m_H^2 H_2}{s} + H_3, \\
\text{HPL} \left(\{4\}, \frac{-t}{s} \right) &\rightarrow m_H^4 \left(\frac{2H_2}{s^2} - \frac{2(2 \cos(\theta) - 1)H_3}{(\cos(\theta) - 1)s^2} \right) - \frac{2m_H^2 H_3}{s} + H_4, \\
\text{HPL} \left(\{2, 1\}, \frac{-t}{s} \right) &\rightarrow H_{2,1} + m_H^4 \left(-\frac{(2 \cos(\theta) - 1)l_+^2}{(\cos(\theta) - 1)s^2} - \frac{2(\cos(\theta) - 1)l_+}{(\cos(\theta) + 1)s^2} \right) - \frac{l_+^2 m_H^2}{s}, \\
\text{HPL} \left(\{2, 2\}, \frac{-t}{s} \right) &\rightarrow m_H^4 \left(-\frac{2(2 \cos(\theta) - 1)l_+ H_2}{(\cos(\theta) - 1)s^2} - \frac{2(\cos(\theta) - 1)H_2}{(\cos(\theta) + 1)s^2} + \frac{4(2 \cos(\theta) - 1)H_{2,1}}{(\cos(\theta) - 1)s^2} \right) \\
&\quad + m_H^2 \left(\frac{4H_{2,1}}{s} - \frac{2l_+ H_2}{s} \right) + H_{2,2}, \\
\text{HPL} \left(\{2, 1, 1\}, \frac{-t}{s} \right) &\rightarrow H_{2,1,1} + m_H^4 \left(-\frac{(2 \cos(\theta) - 1)l_+^3}{3(\cos(\theta) - 1)s^2} - \frac{(\cos(\theta) - 1)l_+^2}{(\cos(\theta) + 1)s^2} \right) - \frac{l_+^3 m_H^2}{3s}, \\
\log \left(\frac{s+t}{s} \right) &\rightarrow -\frac{2(2 \cos(\theta)^2 - \cos(\theta) + 1) m_H^4}{(\cos(\theta) + 1)^2 s^2} - \frac{2(\cos(\theta) - 1)m_H^2}{(\cos(\theta) + 1)s} + l_+, \\
\log \left(\frac{-t}{s} \right) &\rightarrow -\frac{2(2 \cos(\theta) - 1)m_H^4}{(\cos(\theta) - 1)s^2} - \frac{2m_H^2}{s} + l_-
\end{aligned} \tag{A.40}$$

with the abbreviations

$$H_{i,j,\dots} = \text{HPL} \left(\{i, j, \dots\}, \frac{1 - \cos(\theta)}{2} \right), \quad l_+ = \log \left(\frac{1 + \cos(\theta)}{2} \right) \quad \text{and} \quad l_- = \log \left(\frac{1 - \cos(\theta)}{2} \right). \tag{A.41}$$

After replacing of the harmonic polylogarithms in the amplitude (or the form factors, respectively) with the rules above, one needs to truncate the amplitude at m_H^4 . In this thesis, the variable change to p_T is made.

B. Appendix $gg \rightarrow HH$

B.1. Projectors

In order to project out from the amplitude the form factors F_1 and F_2 from Eq. (3.20) with

$$F_i = P_{i,\mu\nu} \mathcal{A}_{ggHH}^{\mu\nu}, \quad (\text{B.1})$$

one needs the projectors $P_{1,\mu\nu}$ and $P_{2,\mu\nu}$ defined by (see for example [54, 93])

$$\begin{aligned} P_{1,\mu\nu} &= -\frac{p_{1,v}p_{2,\mu}p_{33}}{4p_{12}p_T^2} - \frac{p_{1,v}p_{2,\mu}}{4p_{12}} + \frac{p_{1,v}p_{3,\mu}p_{23}}{2p_{12}p_T^2} + \frac{p_{2,\mu}p_{3,v}p_{13}}{2p_{12}p_T^2} - \frac{p_{3,\mu}p_{3,v}}{2p_T^2} \\ &+ \frac{1}{(2-4\epsilon)} \left[\frac{p_{1,v}p_{2,\mu}p_{33}}{2p_{12}p_T^2} - \frac{p_{1,v}p_{2,\mu}}{2p_{12}} - \frac{p_{1,v}p_{3,\mu}p_{23}}{p_{12}p_T^2} - \frac{p_{2,\mu}p_{3,v}p_{13}}{p_{12}p_T^2} + \frac{p_{3,\mu}p_{3,v}}{p_T^2} + g_{\mu\nu} \right], \\ P_{2,\mu\nu} &= \frac{p_{1,v}p_{2,\mu}p_{33}}{4p_{12}p_T^2} + \frac{p_{1,v}p_{2,\mu}}{4p_{12}} - \frac{p_{1,v}p_{3,\mu}p_{23}}{2p_{12}p_T^2} - \frac{p_{2,\mu}p_{3,v}p_{13}}{2p_{12}p_T^2} + \frac{p_{3,\mu}p_{3,v}}{2p_T^2} \\ &+ \frac{1}{(2-4\epsilon)} \left[\frac{p_{1,v}p_{2,\mu}p_{33}}{2p_{12}p_T^2} - \frac{p_{1,v}p_{2,\mu}}{2p_{12}} - \frac{p_{1,v}p_{3,\mu}p_{23}}{p_{12}p_T^2} - \frac{p_{2,\mu}p_{3,v}p_{13}}{p_{12}p_T^2} + \frac{p_{3,\mu}p_{3,v}}{p_T^2} + g_{\mu\nu} \right], \end{aligned} \quad (\text{B.2})$$

where p_T is given in Eq. (3.17) and $p_{12} = p_1 \cdot p_2$.

B.2. Additional Plots

In this appendix, some additional plots are presented that served as cross checks. Figures B.1, B.2 and B.3 show in a more detailed way how the PDR Padé approach from section 2.5.1 works for the example of \mathcal{V}_{fin} of the process $gg \rightarrow HH$. While the pink dots show the individual Padé approximants, the light blue dots with error bars give the result of the pole-distance-reweighted Padé procedure. In Fig. B.1 one can see in the region between $\sqrt{s} \gtrsim 500$ GeV and $\sqrt{s} \lesssim 800$ GeV results of one of the Padé approximants, that are ignored by the PDR Padé approach as the points are heavily influenced by a nearby pole. A direct comparison to the result of the extended PDR Padé approach introduced in section 2.4.8 is given in Fig. B.2. Here, many more Padé approximants contribute, some of which completely miss the exact result shown as violet points. However, the ePDR Padé approach filters out the reliable points and its prediction shown as light blue dots with error bars is even more refined and closer to the exact result than the PDR Padé result from Fig. B.1.

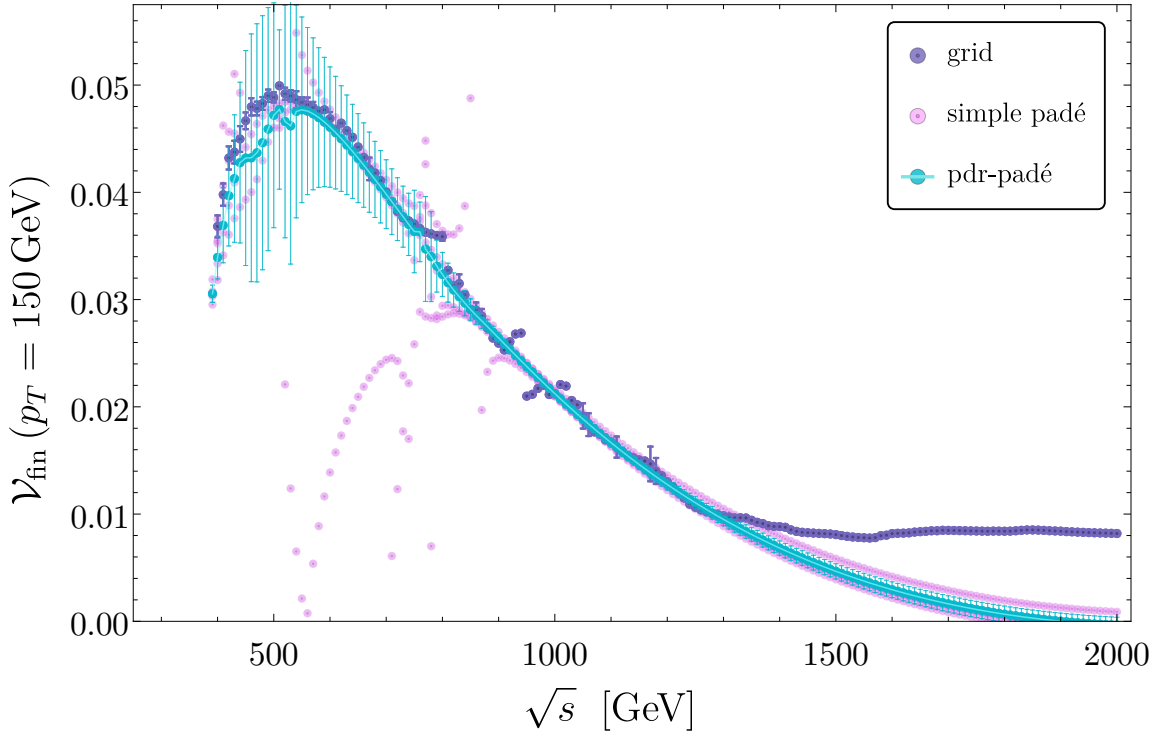


Figure B.1: NLO virtual finite part of the process $gg \rightarrow HH$ for fixed $p_T = 150$ GeV as a function of \sqrt{s} . Plum colored points with uncertainty bars correspond to the numerical exact result with solid support from nearby points. Plum colored points without errorbars are obtained from the numerical exact result via interpolation in a region that is not well covered by the underlying grid. Light pink dots are obtained by computing the simple padé approximants $\mathcal{V}_{\text{fin}}^{n,m}$ with $[n/m] \in \{[7/8], [7/9], [8/7], [8/8], [9/7]\}$. Light blue points are obtained by applying the pole-distance-reweighting procedure to the set of simple Padés. The corresponding error bars give an indicator for the reliability of the central value prediction.

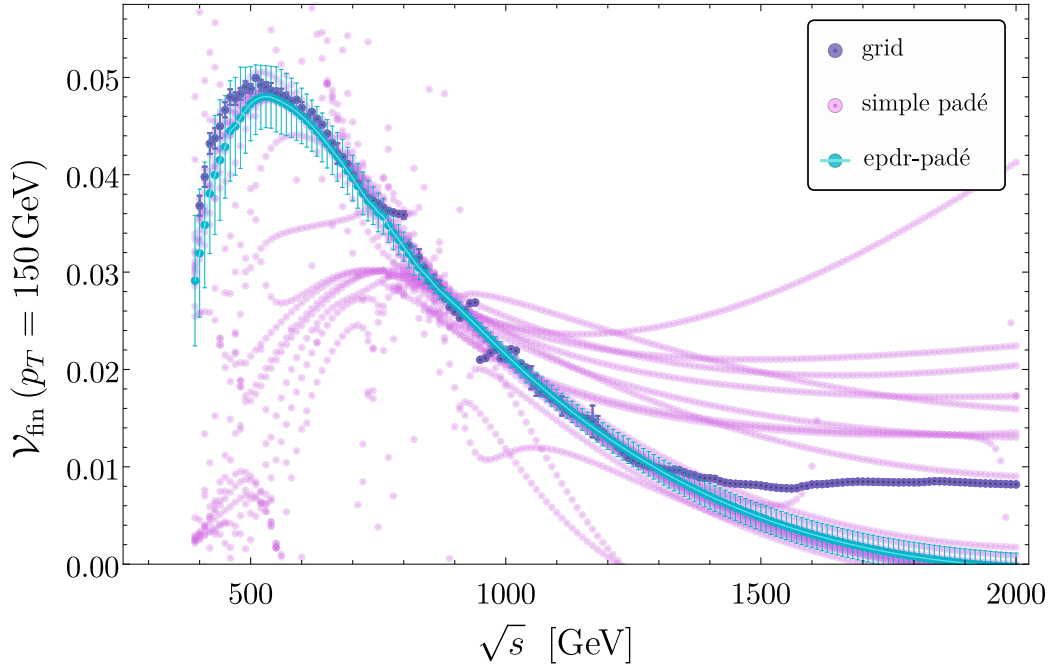


Figure B.2.: Same plot as above with the extended reweighting procedure favoring Padés with higher $n + m$ and which are closer to the diagonal where $n = m$. 28 Padés obeying the conditions $16 \geq n + m \geq 10$ and $n + m - |n - m| \geq 10$ contribute to the light pink dots.

Figure B.3 shows, that the ePDR Padé approach yields also good results if ‘lower quality’ Padés are used that have less information on the underlying series.

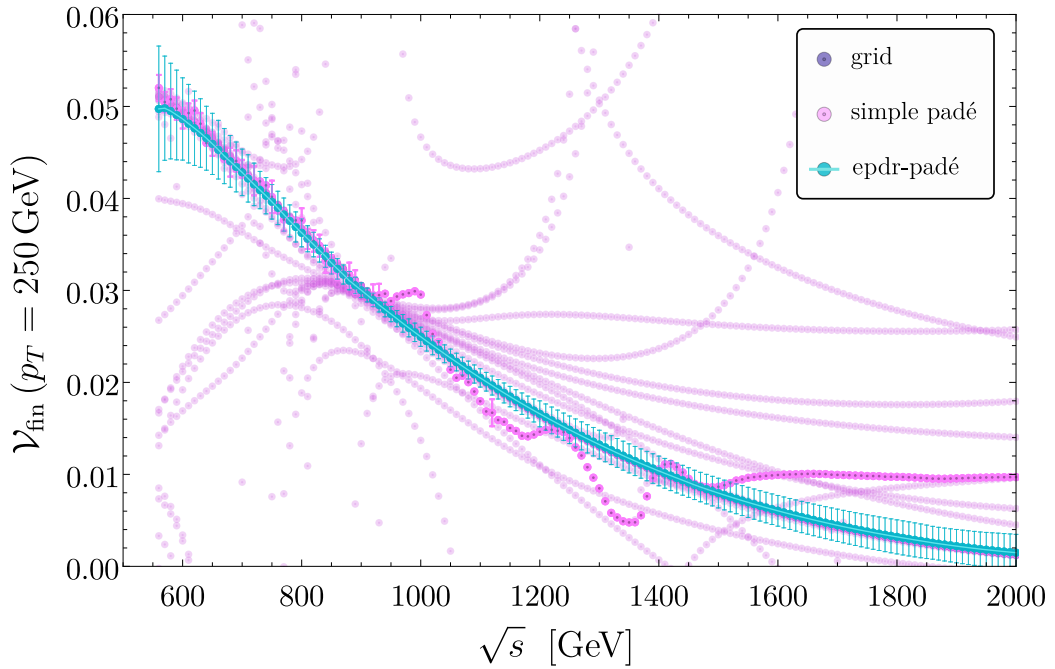


Figure B.3.: Extended reweighting procedure applied on NLO v_{fin} for $p_T = 250$ GeV for 28 Padés obeying the conditions $12 \geq n + m \geq 6$ and $n + m - |n - m| \geq 6$.

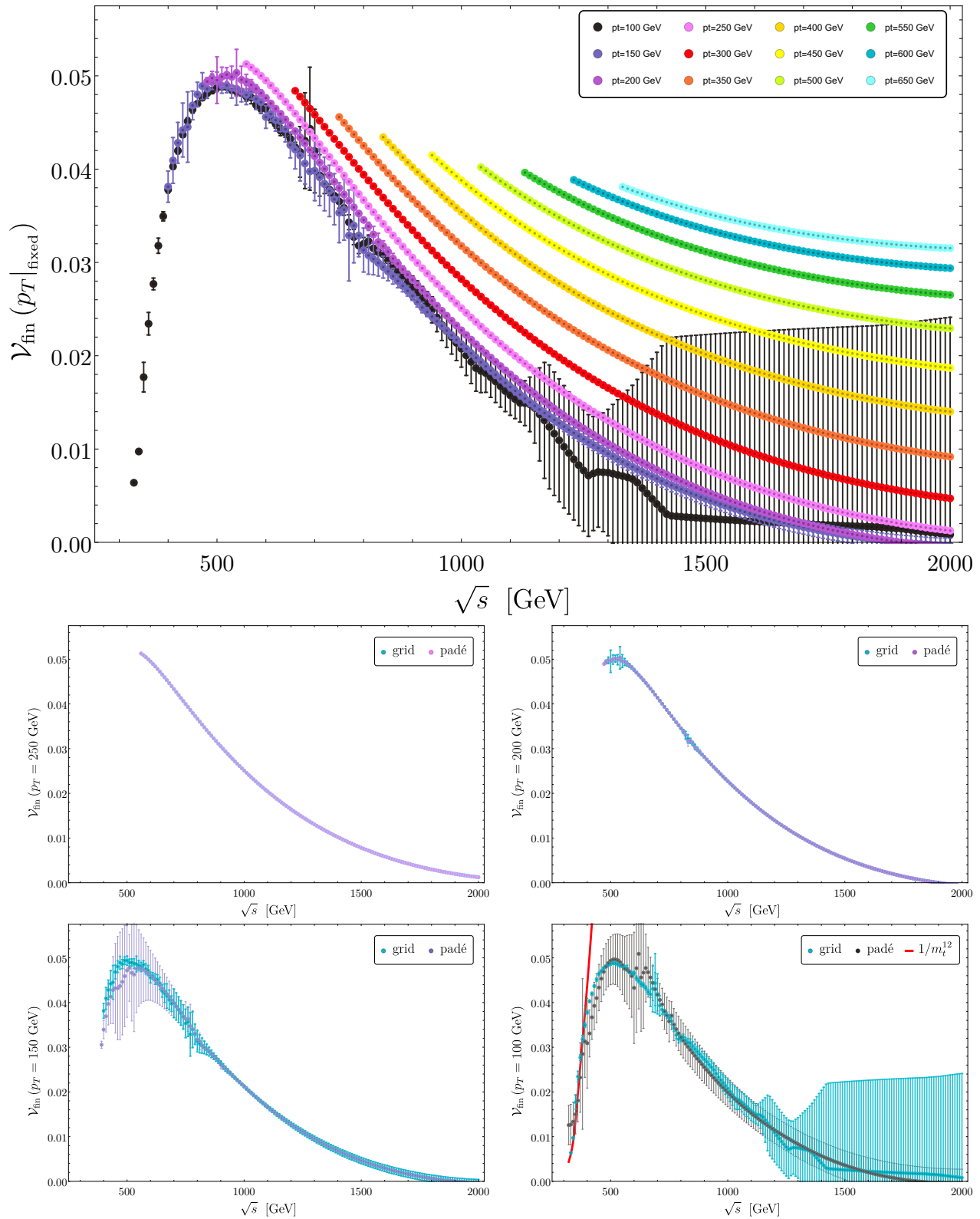


Figure B.4.: Same plot as in Fig. 3.14 but with unpublished dense C++ interpolation.

Figure B.4 shows the results of a different C++ implementation of the \mathcal{V}_{fin} grid for $gg \rightarrow HH$ that is much denser and provides in addition also an error estimate. In short, the interpolator does the following:

1. Use the original grid points $\mathcal{V}_{\text{grid}}$ from Ref. [114] as input for the Mathematica function Interpolation.
2. Evaluate this function on a dense grid of 50,000 points which is rectangular in the coordinates of $\beta^5(s)$ and $\cos(\theta)$.
3. Artificially force extreme values for $\{\beta^5(s), \cos(\theta)\} \in \{0, 1\}$ to zero and assign a large error in order to avoid misleading extrapolation effects.
4. Repeat the procedure for the numerical errors $\delta(\mathcal{V}_{\text{grid}})$.
5. Evaluate also the PDR Padé result gained from the high-energy expansion directly on the same grid. Save the central value $\mathcal{V}_{\text{padé}}$ and the error grid $\delta(\mathcal{V}_{\text{padé}})$.
6. The c++ interpolator can now work on the four grids $\mathcal{V}_{\text{padé}}$, $\delta(\mathcal{V}_{\text{padé}})$, $\mathcal{V}_{\text{grid}}$ and $\delta(\mathcal{V}_{\text{grid}})$. For any given phase-space point, it returns an value-error pair based on the grid that is supposed to yield the best result in that region (see the separation of the phase space by the yellow-green line in Fig. 3.15).

Steps 1-5 are of course only executed once to produce the four grids $\mathcal{V}_{\text{padé}}$, $\delta(\mathcal{V}_{\text{padé}})$, $\mathcal{V}_{\text{grid}}$ and $\delta(\mathcal{V}_{\text{grid}})$. Note, that this are only preliminary results and the program is yet to be published.

One can observe two things from comparing Fig. 3.14 with Fig. B.4. First, the wiggles at high centre-of-mass energies \sqrt{s} disappear in the C++ version, since the grid is just much more dense in this region. Second, the $p_T = 100$ GeV curve shown in black develops large errors for centre-of-mass energies $\sqrt{s} \gtrsim 1100$ GeV. The reason for these is, that for $p_T = 100$ GeV, the interpolator takes only the data of $\mathcal{V}_{\text{grid}}$ into account which has only little support in the region $\sqrt{s} \gtrsim 1100$ GeV and no support at all for $\sqrt{s} \gtrsim 1400$ GeV. This means step 3 takes effect, the central value is extrapolated to zero and the error grows fast and the loss of support from the underlying data becomes visible.

C. Appendix $gg \rightarrow \gamma\gamma$

C.1. Tensor Structure

One can use the setup developed for the calculations done in this thesis to also consider the process of di-photon production via gluon fusion $gg \rightarrow \gamma\gamma$. Note, that this and the following chapter are not intended to be complete but they should rather be seen as a possible starting point for a similar calculation as the ones performed in this thesis. While most of the setup remains unchanged, the tensor structure of the new process is however different. Following the idea of Ref. [146], one can derive in analogy to Section 2.2.2 a set of tensor structures requiring first transversality between the polarization vectors of the external gluons and photons to their corresponding momenta

$$\mathcal{E}_\mu^{\lambda_1} p_1^\mu = 0, \quad \mathcal{E}_\nu^{\lambda_2} p_2^\nu = 0, \quad \mathcal{E}_\rho^{\lambda_3} p_3^\rho = 0, \quad \mathcal{E}_\sigma^{\lambda_4} p_4^\sigma = 0,$$

and choosing then a gauge configuration that minimizes the complexity of the tensor structure

$$\mathcal{E}_\mu^{\lambda_1} p_2^\mu = 0, \quad \mathcal{E}_\nu^{\lambda_2} p_1^\nu = 0, \quad \mathcal{E}_\rho^{\lambda_3} p_4^\rho = 0, \quad \mathcal{E}_\sigma^{\lambda_4} p_3^\sigma = 0.$$

This yields an amplitude that can be constructed from only 10 tensor structures:

$$\begin{aligned} \mathcal{A}_{gg\gamma\gamma} = & \sum_{\lambda_1, \lambda_2, \lambda_3, \lambda_4} \mathcal{E}_\mu^{\lambda_1} \mathcal{E}_\nu^{\lambda_2} \mathcal{E}_\rho^{\lambda_3} \mathcal{E}_\sigma^{\lambda_4} \left(a_1 g^{\mu\nu} g^{\rho\sigma} + a_2 g^{\mu\rho} g^{\nu\sigma} + a_3 g^{\mu\sigma} g^{\nu\rho} \right. \\ & + (a_9 - a_{10} - a_{11} + a_{12}) g^{\mu\nu} p_1^\rho p_1^\sigma + (a_6 - a_7) g^{\nu\sigma} p_1^\rho p_3^\mu - a_{14} g^{\nu\rho} p_1^\sigma p_3^\mu \\ & + (a_4 - a_5) g^{\mu\sigma} p_1^\rho p_3^\nu + a_{13} g^{\mu\rho} p_1^\sigma p_3^\nu + a_8 g^{\rho\sigma} p_3^\mu p_3^\nu \\ & \left. + (a_{17} - a_{18} - a_{19} + a_{20}) p_1^\rho p_1^\sigma p_3^\mu p_3^\nu \right), \end{aligned} \quad (\text{C.1})$$

where a_1, \dots, a_{20} are the form factors belonging to the simple tensors from Eq. (A.1). Computing the 10 form factor combinations from Eq. (C.1), one can reuse the results of the simple form factors of the $gg \rightarrow ZZ$ calculation, where m_Z and the axial coupling to a Z boson is set to zero and the vector coupling to a Z boson is replaced by the corresponding coupling a photon. However, this is not the topic of this thesis.

D. Appendix $gg \rightarrow Z\gamma$

D.1. Tensor Structure

For completeness, one can also compute the process of $gg \rightarrow Z\gamma$, which can be decomposed into 14 tensor structures with the same methods as in the last chapter C.1. Transversality between the polarization vectors of the external particles and their corresponding momenta

$$\mathcal{E}_\mu^{\lambda_1} p_1^\mu = 0, \quad \mathcal{E}_\nu^{\lambda_2} p_2^\nu = 0, \quad \mathcal{E}_\rho^{\lambda_3} p_3^\rho = 0, \quad \mathcal{E}_\sigma^{\lambda_4} p_4^\sigma = 0,$$

together with choosing a gauge configuration similar to what was done in Ref. [146] and minimizing thereby the complexity of the tensor structure

$$\mathcal{E}_\mu^{\lambda_1} p_2^\mu = 0, \quad \mathcal{E}_\nu^{\lambda_2} p_3^\nu = 0, \quad \mathcal{E}_\rho^{\lambda_3} p_1^\rho = 0,$$

yields an amplitude that can be constructed from 14 tensor structures:

$$\begin{aligned} \mathcal{A}_{ggZ\gamma} = & \sum_{\lambda_1, \lambda_2, \lambda_3, \lambda_4} \mathcal{E}_\mu^{\lambda_1} \mathcal{E}_\nu^{\lambda_2} \mathcal{E}_\rho^{\lambda_3} \mathcal{E}_\sigma^{\lambda_4} \left(a_1 g^{\mu\nu} g^{\rho\sigma} + a_2 g^{\mu\rho} g^{\nu\sigma} + a_3 g^{\mu\sigma} g^{\nu\rho} \right. \\ & + (a_{31} - a_{110}) g^{\mu\rho} p_1^\nu p_1^\sigma + a_{44} g^{\mu\sigma} p_1^\nu p_2^\rho + (a_{11} - a_{22}) g^{\mu\nu} p_1^\sigma p_2^\rho \\ & + (a_{52} - a_{110}) g^{\mu\rho} p_1^\nu p_2^\sigma + (a_{12} - a_{22}) g^{\mu\nu} p_2^\rho p_2^\sigma + a_{63} g^{\rho\sigma} p_1^\nu p_3^\mu \\ & + (a_{15} - a_{24}) g^{\nu\rho} p_1^\sigma p_3^\mu + a_7 g^{\nu\sigma} p_2^\rho p_3^\mu + (a_{67} - a_{123}) p_1^\nu p_1^\sigma p_2^\rho p_3^\mu \\ & \left. + (a_{16} - a_{24}) g^{\nu\rho} p_2^\sigma p_3^\mu + (a_{71} - a_{123}) p_1^\nu p_2^\rho p_2^\sigma p_3^\mu \right). \end{aligned} \quad (\text{D.1})$$

The a_i in Eq. (D.1) are the form factors of the simple tensors from Eq. (A.1). Note, that this choice of a tensor decomposition is not unique

E. Appendix $H \rightarrow$ Hadrons

E.1. Effective Couplings

For convenience, the effective couplings C_1 and C_2 were taken from the literature [132–135] and reproduced here up to the relevant order in $a_s = \alpha_s^{(5)}(\mu)/\pi$ with $L_t = \log(\mu^2/M_t^2)$, the Riemann Zeta function ζ_n and the Polylogarithm function $\text{Li}_n(z)$:

$$\begin{aligned}
 C_1 = & -a_s \frac{1}{12} - a_s^2 \frac{11}{48} - a_s^3 \left[\frac{2777}{3456} + \frac{19}{192} L_t - n_l \left(\frac{67}{1152} - \frac{1}{36} L_t \right) \right] \\
 & + a_s^4 \left[\frac{2761331}{497664} - \frac{897943}{110592} \zeta_3 - \frac{2417}{3456} L_t - \frac{209}{768} L_t^2 \right. \\
 & \quad - n_l \left(\frac{58723}{248832} - \frac{110779}{165888} \zeta_3 + \frac{91}{648} L_t + \frac{23}{384} L_t^2 \right) \\
 & \quad \left. + n_l^2 \left(\frac{6865}{373248} - \frac{77}{20736} L_t + \frac{1}{216} L_t^2 \right) \right] + \mathcal{O}(a_s^5), \tag{E.1}
 \end{aligned}$$

$$\begin{aligned}
 C_2 = & 1 + a_s^2 \left[\frac{5}{18} - \frac{1}{3} L_t \right] + a_s^3 \left[-\frac{841}{1296} + \frac{5}{3} \zeta_3 - \frac{79}{36} L_t - \frac{11}{12} L_t^2 + n_l \left(\frac{53}{216} + \frac{1}{18} L_t \right) \right] \\
 & + a_s^4 \left[\frac{609215}{186624} - \frac{4}{3} \zeta_2 + \frac{374797}{13824} \zeta_3 - \frac{4123}{144} \zeta_4 - \frac{575}{36} \zeta_5 + \frac{62}{9} \text{Li}_4 \left(\frac{1}{2} \right) - \frac{4}{9} \ln 2 \zeta_2 \right. \\
 & \quad - \frac{31}{18} (\ln 2)^2 \zeta_2 + \frac{31}{108} (\ln 2)^4 - \left[\frac{4645}{144} - \frac{55}{4} \zeta_3 \right] L_t - \frac{91}{8} L_t^2 - \frac{121}{48} L_t^3 \\
 & \quad + n_l \left(-\frac{11557}{15552} + \frac{2}{9} \zeta_2 - \frac{221}{288} \zeta_3 + \frac{163}{72} \zeta_4 - \frac{4}{9} \text{Li}_4 \left(\frac{1}{2} \right) + \frac{1}{9} (\ln 2)^2 \zeta_2 \right. \\
 & \quad \left. - \frac{1}{54} (\ln 2)^4 + \frac{9535}{2592} L_t + \frac{109}{144} L_t^2 + \frac{11}{36} L_t^3 \right) \\
 & \quad \left. + n_l^2 \left(\frac{3401}{23328} - \frac{7}{54} \zeta_3 - \frac{31}{324} L_t - \frac{1}{108} L_t^3 \right) \right] + \mathcal{O}(a_s^5). \tag{E.2}
 \end{aligned}$$

Acknowledgements

First of all I want to thank Prof. Dr. Matthias Steinhauser for supervising my PhD thesis, for his continuous support, advice, helpful discussions and the marvelous team he put together. I also want to thank Prof. Dr. Kirill Melnikov for agreeing to be the second reviewer of this thesis and his helpful insights and comments towards the end of my writing period. I am especially thankful for the invaluable help of Go and Josh throughout the last three years. It has been a great pleasure to work with you.

I want to thank Tobias, Josh, Go and Conny for proofreading parts of this thesis and Mustafa, Flo, Matthias, Marvin, Aliaksei and so many more for delightful discussions on physics and beyond. I want to thank the people at the Institute for Theoretical Particle Physics who made the last years a lot of fun. I hope you will soon be rewarded with a new building!

A huge thank you goes to my admin colleagues, Konstantin, Mustafa and Martin. We spent quite some time together on improving the technical heart of the institute and I am glad you were part of this team.

Finally, I want to thank my family for their never-ending support and for giving me the possibility to study physics and thereby finding my wonderful wife and love, Conny.

Thank you, Conny, you are simply the best.

Auf zu neuen Ufern.

Bibliography

- [1] Georges Aad et al. “Observation of a new particle in the search for the Standard Model Higgs boson with the ATLAS detector at the LHC”. In: *Phys. Lett.* B716 (2012), pp. 1–29. DOI: [10.1016/j.physletb.2012.08.020](https://doi.org/10.1016/j.physletb.2012.08.020). arXiv: [1207.7214 \[hep-ex\]](https://arxiv.org/abs/1207.7214) (cit. on p. 1).
- [2] Serguei Chatrchyan et al. “Observation of a New Boson at a Mass of 125 GeV with the CMS Experiment at the LHC”. In: *Phys. Lett.* B716 (2012), pp. 30–61. DOI: [10.1016/j.physletb.2012.08.021](https://doi.org/10.1016/j.physletb.2012.08.021). arXiv: [1207.7235 \[hep-ex\]](https://arxiv.org/abs/1207.7235) (cit. on p. 1).
- [3] M. Tanabashi et al. “Review of Particle Physics”. In: *Phys. Rev. D* 98 (3 Aug. 2018), p. 030001. DOI: [10.1103/PhysRevD.98.030001](https://doi.org/10.1103/PhysRevD.98.030001). URL: <https://link.aps.org/doi/10.1103/PhysRevD.98.030001> (cit. on pp. 1, 32).
- [4] Albert M Sirunyan et al. “Combination of searches for Higgs boson pair production in proton-proton collisions at $\sqrt{s} = 13$ TeV”. In: *Phys. Rev. Lett.* 122.12 (2019), p. 121803. DOI: [10.1103/PhysRevLett.122.121803](https://doi.org/10.1103/PhysRevLett.122.121803). arXiv: [1811.09689 \[hep-ex\]](https://arxiv.org/abs/1811.09689) (cit. on pp. 1, 68).
- [5] Georges Aad et al. “Combination of searches for Higgs boson pairs in pp collisions at $\sqrt{s} = 13$ TeV with the ATLAS detector”. In: *Phys. Lett.* B800 (2020), p. 135103. DOI: [10.1016/j.physletb.2019.135103](https://doi.org/10.1016/j.physletb.2019.135103). arXiv: [1906.02025 \[hep-ex\]](https://arxiv.org/abs/1906.02025) (cit. on pp. 1, 68).
- [6] D. de Florian et al. “Handbook of LHC Higgs Cross Sections: 4. Deciphering the Nature of the Higgs Sector”. In: (2016). DOI: [10.2172/1345634](https://doi.org/10.2172/1345634), [10.23731/CYRM-2017-002](https://doi.org/10.23731/CYRM-2017-002). arXiv: [1610.07922 \[hep-ph\]](https://arxiv.org/abs/1610.07922) (cit. on p. 6).
- [7] Albert M Sirunyan et al. “Measurements of properties of the Higgs boson decaying into the four-lepton final state in pp collisions at $\sqrt{s} = 13$ TeV”. In: *JHEP* 11 (2017), p. 047. DOI: [10.1007/JHEP11\(2017\)047](https://doi.org/10.1007/JHEP11(2017)047). arXiv: [1706.09936 \[hep-ex\]](https://arxiv.org/abs/1706.09936) (cit. on p. 6).
- [8] Nikolas Kauer and Giampiero Passarino. “Inadequacy of zero-width approximation for a light Higgs boson signal”. In: *JHEP* 08 (2012), p. 116. DOI: [10.1007/JHEP08\(2012\)116](https://doi.org/10.1007/JHEP08(2012)116). arXiv: [1206.4803 \[hep-ph\]](https://arxiv.org/abs/1206.4803) (cit. on p. 6).
- [9] Fabrizio Caola and Kirill Melnikov. “Constraining the Higgs boson width with ZZ production at the LHC”. In: *Phys. Rev. D* 88 (2013), p. 054024. DOI: [10.1103/PhysRevD.88.054024](https://doi.org/10.1103/PhysRevD.88.054024). arXiv: [1307.4935 \[hep-ph\]](https://arxiv.org/abs/1307.4935) (cit. on p. 6).
- [10] John M. Campbell, R. Keith Ellis, and Ciaran Williams. “Bounding the Higgs Width at the LHC Using Full Analytic Results for $gg \rightarrow e^- e^+ \mu^- \mu^+$ ”. In: *JHEP* 04 (2014), p. 060. DOI: [10.1007/JHEP04\(2014\)060](https://doi.org/10.1007/JHEP04(2014)060). arXiv: [1311.3589 \[hep-ph\]](https://arxiv.org/abs/1311.3589) (cit. on p. 6).
- [11] E. W. Nigel Glover and J. J. van der Bij. “Z BOSON PAIR PRODUCTION VIA GLUON FUSION”. In: *Nucl. Phys.* B321 (1989), pp. 561–590. DOI: [10.1016/0550-3213\(89\)90262-9](https://doi.org/10.1016/0550-3213(89)90262-9) (cit. on pp. 6, 32, 39).

- [12] T. Matsuura and J. J. van der Bij. “Characteristics of leptonic signals for Z boson pairs at hadron colliders”. In: *Z. Phys.* C51 (1991), pp. 259–266. DOI: [10.1007/BF01475793](https://doi.org/10.1007/BF01475793) (cit. on p. 6).
- [13] C. Zecher, T. Matsuura, and J. J. van der Bij. “Leptonic signals from off-shell Z boson pairs at hadron colliders”. In: *Z. Phys.* C64 (1994), pp. 219–226. DOI: [10.1007/BF01557393](https://doi.org/10.1007/BF01557393). arXiv: [hep-ph/9404295](https://arxiv.org/abs/hep-ph/9404295) [hep-ph] (cit. on p. 6).
- [14] T. Binoth, N. Kauer, and P. Mertsch. “Gluon-induced QCD corrections to $pp \rightarrow ZZ \rightarrow l \text{ anti-}l l\text{-prime anti-}l\text{-prime}$ ”. In: *Proceedings, 16th International Workshop on Deep Inelastic Scattering and Related Subjects (DIS 2008): London, UK, April 7-11, 2008*. 2008, p. 142. DOI: [10.3360/dis.2008.142](https://doi.org/10.3360/dis.2008.142). arXiv: [0807.0024](https://arxiv.org/abs/0807.0024) [hep-ph] (cit. on p. 6).
- [15] Andreas von Manteuffel and Lorenzo Tancredi. “The two-loop helicity amplitudes for $gg \rightarrow V_1 V_2 \rightarrow 4 \text{ leptons}$ ”. In: *JHEP* 06 (2015), p. 197. DOI: [10.1007/JHEP06\(2015\)197](https://doi.org/10.1007/JHEP06(2015)197). arXiv: [1503.08835](https://arxiv.org/abs/1503.08835) [hep-ph] (cit. on pp. 6, 11).
- [16] Fabrizio Caola, Johannes M. Henn, Kirill Melnikov, Alexander V. Smirnov, and Vladimir A. Smirnov. “Two-loop helicity amplitudes for the production of two off-shell electroweak bosons in gluon fusion”. In: *JHEP* 06 (2015), p. 129. DOI: [10.1007/JHEP06\(2015\)129](https://doi.org/10.1007/JHEP06(2015)129). arXiv: [1503.08759](https://arxiv.org/abs/1503.08759) [hep-ph] (cit. on p. 6).
- [17] Simone Alioli, Fabrizio Caola, Gionata Luisoni, and Raul Röntsch. “ZZ production in gluon fusion at NLO matched to parton-shower”. In: *Phys. Rev. D* 95.3 (2017), p. 034042. DOI: [10.1103/PhysRevD.95.034042](https://doi.org/10.1103/PhysRevD.95.034042). arXiv: [1609.09719](https://arxiv.org/abs/1609.09719) [hep-ph] (cit. on p. 6).
- [18] Kirill Melnikov and Matthew Dowling. “Production of two Z-bosons in gluon fusion in the heavy top quark approximation”. In: *Phys. Lett.* B744 (2015), pp. 43–47. DOI: [10.1016/j.physletb.2015.03.030](https://doi.org/10.1016/j.physletb.2015.03.030). arXiv: [1503.01274](https://arxiv.org/abs/1503.01274) [hep-ph] (cit. on pp. 6, 35).
- [19] Fabrizio Caola, Matthew Dowling, Kirill Melnikov, Raoul Röntsch, and Lorenzo Tancredi. “QCD corrections to vector boson pair production in gluon fusion including interference effects with off-shell Higgs at the LHC”. In: *JHEP* 07 (2016), p. 087. DOI: [10.1007/JHEP07\(2016\)087](https://doi.org/10.1007/JHEP07(2016)087). arXiv: [1605.04610](https://arxiv.org/abs/1605.04610) [hep-ph] (cit. on p. 6).
- [20] John M. Campbell, R. Keith Ellis, Michal Czakon, and Sebastian Kirchner. “Two loop correction to interference in $gg \rightarrow ZZ$ ”. In: *JHEP* 08 (2016), p. 011. DOI: [10.1007/JHEP08\(2016\)011](https://doi.org/10.1007/JHEP08(2016)011). arXiv: [1605.01380](https://arxiv.org/abs/1605.01380) [hep-ph] (cit. on pp. 6, 8, 35).
- [21] Ramona Gröber, Andreas Maier, and Thomas Rauh. “Top quark mass effects in $gg \rightarrow ZZ$ at two loops and off-shell Higgs interference”. In: (2019). arXiv: [1908.04061](https://arxiv.org/abs/1908.04061) [hep-ph] (cit. on pp. 6, 53).
- [22] P. A. Baikov and David J. Broadhurst. “Three loop QED vacuum polarization and the four loop muon anomalous magnetic moment”. In: *Artificial intelligence in high-energy and nuclear physics '95. Proceedings, 4th International Workshop On Software Engineering, Artificial Intelligence, and Expert Systems, Pisa, Italy, April 3-8, 1995*. 1995, pp. 0167–172. arXiv: [hep-ph/9504398](https://arxiv.org/abs/hep-ph/9504398) [hep-ph] (cit. on p. 6).

- [23] David J. Broadhurst, J. Fleischer, and O. V. Tarasov. “Two loop two point functions with masses: Asymptotic expansions and Taylor series, in any dimension”. In: *Z. Phys. C60* (1993), pp. 287–302. DOI: [10.1007/BF01474625](https://doi.org/10.1007/BF01474625). arXiv: [hep-ph/9304303](https://arxiv.org/abs/hep-ph/9304303) [hep-ph] (cit. on p. 6).
- [24] J. Fleischer and O. V. Tarasov. “Calculation of Feynman diagrams from their small momentum expansion”. In: *Z. Phys. C64* (1994), pp. 413–426. DOI: [10.1007/BF01560102](https://doi.org/10.1007/BF01560102). arXiv: [hep-ph/9403230](https://arxiv.org/abs/hep-ph/9403230) [hep-ph] (cit. on p. 6).
- [25] Ramona Gröber, Andreas Maier, and Thomas Rauh. “Reconstruction of top-quark mass effects in Higgs pair production and other gluon-fusion processes”. In: *JHEP* 03 (2018), p. 020. DOI: [10.1007/JHEP03\(2018\)020](https://doi.org/10.1007/JHEP03(2018)020). arXiv: [1709.07799](https://arxiv.org/abs/1709.07799) [hep-ph] (cit. on pp. 6, 53, 69, 92).
- [26] Joshua Davies, Ramona Gröber, Andreas Maier, Thomas Rauh, and Matthias Steinhauser. “Padé approach to top-quark mass effects in gluon fusion amplitudes”. In: *14th International Symposium on Radiative Corrections: Application of Quantum Field Theory to Phenomenology (RADCOR 2019) Avignon, France, September 8-13, 2019*. 2019. arXiv: [1912.04097](https://arxiv.org/abs/1912.04097) [hep-ph] (cit. on p. 6).
- [27] Bernd A. Kniehl and Johann H. Kuhn. “QCD Corrections to the Z Decay Rate”. In: *Nucl. Phys. B329* (1990), pp. 547–573. DOI: [10.1016/0550-3213\(90\)90070-T](https://doi.org/10.1016/0550-3213(90)90070-T) (cit. on pp. 8, 18).
- [28] John M. Campbell, R. Keith Ellis, and Giulia Zanderighi. “Next-to-leading order predictions for $WW + 1$ jet distributions at the LHC”. In: *JHEP* 12 (2007), p. 056. DOI: [10.1088/1126-6708/2007/12/056](https://doi.org/10.1088/1126-6708/2007/12/056). arXiv: [0710.1832](https://arxiv.org/abs/0710.1832) [hep-ph] (cit. on pp. 8, 18).
- [29] J. A. M. Vermaseren. “New features of FORM”. In: (2000). arXiv: [math-ph/0010025](https://arxiv.org/abs/math-ph/0010025) [math-ph] (cit. on pp. 16, 76, 110).
- [30] M. Tentyukov and J. A. M. Vermaseren. “The Multithreaded version of FORM”. In: *Comput. Phys. Commun.* 181 (2010), pp. 1419–1427. DOI: [10.1016/j.cpc.2010.04.009](https://doi.org/10.1016/j.cpc.2010.04.009). arXiv: [hep-ph/0702279](https://arxiv.org/abs/hep-ph/0702279) [hep-ph] (cit. on pp. 16, 76, 110).
- [31] Joshua Davies. *Issue #270*. <https://github.com/vermaseren/form/issues/270>. 2019 (cit. on p. 16).
- [32] Joshua Davies. *Issue #336*. <https://github.com/vermaseren/form/issues/336>. 2019 (cit. on p. 16).
- [33] T. van Ritbergen, A. N. Schellekens, and J. A. M. Vermaseren. “Group theory factors for Feynman diagrams”. In: *Int. J. Mod. Phys. A14* (1999), pp. 41–96. DOI: [10.1142/S0217751X99000038](https://doi.org/10.1142/S0217751X99000038). arXiv: [hep-ph/9802376](https://arxiv.org/abs/hep-ph/9802376) [hep-ph] (cit. on pp. 16, 76, 110).
- [34] Paulo Nogueira. “Automatic Feynman graph generation”. In: *J. Comput. Phys.* 105 (1993), pp. 279–289. DOI: [10.1006/jcph.1993.1074](https://doi.org/10.1006/jcph.1993.1074) (cit. on pp. 17, 76, 110).
- [35] V. A. Smirnov. “Renormalization and asymptotic expansions”. In: *Prog. Phys.(Birkhauser)* 14 (1991), pp. 1–380 (cit. on p. 19).

- [36] Vladimir A. Smirnov. “Asymptotic expansions in momenta and masses and calculation of Feynman diagrams”. In: *Mod. Phys. Lett.* A10 (1995), pp. 1485–1500. DOI: [10.1142/S0217732395001617](https://doi.org/10.1142/S0217732395001617). arXiv: [hep-th/9412063 \[hep-th\]](https://arxiv.org/abs/hep-th/9412063) (cit. on p. 19).
- [37] Vladimir A. Smirnov. “Applied asymptotic expansions in momenta and masses”. In: *Springer Tracts Mod. Phys.* 177 (2002), pp. 1–262 (cit. on pp. 19, 24).
- [38] T. Seidensticker. “Automatic application of successive asymptotic expansions of Feynman diagrams”. In: *6th International Workshop on New Computing Techniques in Physics Research: Software Engineering, Artificial Intelligence Neural Nets, Genetic Algorithms, Symbolic Algebra, Automatic Calculation (AIHENP 99) Heraklion, Crete, Greece, April 12-16, 1999*. 1999. arXiv: [hep-ph/9905298 \[hep-ph\]](https://arxiv.org/abs/hep-ph/9905298) (cit. on pp. 19, 76, 110).
- [39] R. Harlander, T. Seidensticker, and M. Steinhauser. “Complete corrections of Order α_s^2 to the decay of the Z boson into bottom quarks”. In: *Phys. Lett.* B426 (1998), pp. 125–132. DOI: [10.1016/S0370-2693\(98\)00220-2](https://doi.org/10.1016/S0370-2693(98)00220-2). arXiv: [hep-ph/9712228 \[hep-ph\]](https://arxiv.org/abs/hep-ph/9712228) (cit. on pp. 19, 76, 110).
- [40] Matthias Steinhauser. “MATAD: A Program package for the computation of Massive TADpoles”. In: *Comput. Phys. Commun.* 134 (2001), pp. 335–364. DOI: [10.1016/S0010-4655\(00\)00204-6](https://doi.org/10.1016/S0010-4655(00)00204-6). arXiv: [hep-ph/0009029 \[hep-ph\]](https://arxiv.org/abs/hep-ph/0009029) (cit. on pp. 19, 24).
- [41] Joshua Davies, Go Mishima, Matthias Steinhauser, and David Wellmann. “Double-Higgs boson production in the high-energy limit: planar master integrals”. In: *JHEP* 03 (2018), p. 048. DOI: [10.1007/JHEP03\(2018\)048](https://doi.org/10.1007/JHEP03(2018)048). arXiv: [1801.09696 \[hep-ph\]](https://arxiv.org/abs/1801.09696) (cit. on pp. 20, 22, 24, 70, 124).
- [42] Joshua Davies, Go Mishima, Matthias Steinhauser, and David Wellmann. “Double Higgs boson production at NLO in the high-energy limit: complete analytic results”. In: *JHEP* 01 (2019), p. 176. DOI: [10.1007/JHEP01\(2019\)176](https://doi.org/10.1007/JHEP01(2019)176). arXiv: [1811.05489 \[hep-ph\]](https://arxiv.org/abs/1811.05489) (cit. on pp. 20, 23, 24, 26, 50, 70, 81, 88, 89, 101, 102, 124).
- [43] S. Laporta. “High precision calculation of multiloop Feynman integrals by difference equations”. In: *Int. J. Mod. Phys.* A15 (2000), pp. 5087–5159. DOI: [10.1016/S0217-751X\(00\)00215-7](https://doi.org/10.1016/S0217-751X(00)00215-7). arXiv: [hep-ph/0102033 \[hep-ph\]](https://arxiv.org/abs/hep-ph/0102033) (cit. on p. 21).
- [44] K. G. Chetyrkin and F. V. Tkachov. “Integration by Parts: The Algorithm to Calculate beta Functions in 4 Loops”. In: *Nucl. Phys.* B192 (1981), pp. 159–204. DOI: [10.1016/0550-3213\(81\)90199-1](https://doi.org/10.1016/0550-3213(81)90199-1) (cit. on pp. 21, 76).
- [45] F. V. Tkachov. “A Theorem on Analytical Calculability of Four Loop Renormalization Group Functions”. In: *Phys. Lett.* 100B (1981), pp. 65–68. DOI: [10.1016/0370-2693\(81\)90288-4](https://doi.org/10.1016/0370-2693(81)90288-4) (cit. on pp. 21, 76).
- [46] Wolfram Research, Inc. *Mathematica, Version 12.0*. Champaign, IL, 2019. URL: <https://www.wolfram.com/mathematica> (cit. on pp. 21, 77).
- [47] R. N. Lee. “Presenting LiteRed: a tool for the Loop InTEgrals REDuction”. In: (2012). arXiv: [1212.2685 \[hep-ph\]](https://arxiv.org/abs/1212.2685) (cit. on pp. 21, 77).

- [48] Roman N. Lee. “LiteRed 1.4: a powerful tool for reduction of multiloop integrals”. In: *J. Phys. Conf. Ser.* 523 (2014), p. 012059. DOI: [10.1088/1742-6596/523/1/012059](https://doi.org/10.1088/1742-6596/523/1/012059). arXiv: [1310.1145 \[hep-ph\]](https://arxiv.org/abs/1310.1145) (cit. on pp. 21, 77).
- [49] A. V. Smirnov and F. S. Chuharev. “FIRE6: Feynman Integral REduction with Modular Arithmetic”. In: (2019). arXiv: [1901.07808 \[hep-ph\]](https://arxiv.org/abs/1901.07808) (cit. on pp. 21, 22).
- [50] A. V. Smirnov. “Algorithm FIRE – Feynman Integral REduction”. In: *JHEP* 10 (2008), p. 107. DOI: [10.1088/1126-6708/2008/10/107](https://doi.org/10.1088/1126-6708/2008/10/107). arXiv: [0807.3243 \[hep-ph\]](https://arxiv.org/abs/0807.3243) (cit. on pp. 21, 77).
- [51] A. V. Smirnov and V. A. Smirnov. “FIRE4, LiteRed and accompanying tools to solve integration by parts relations”. In: *Comput. Phys. Commun.* 184 (2013), pp. 2820–2827. DOI: [10.1016/j.cpc.2013.06.016](https://doi.org/10.1016/j.cpc.2013.06.016). arXiv: [1302.5885 \[hep-ph\]](https://arxiv.org/abs/1302.5885) (cit. on p. 21).
- [52] Alexander V. Smirnov. “FIRE5: a C++ implementation of Feynman Integral REduction”. In: *Comput. Phys. Commun.* 189 (2015), pp. 182–191. DOI: [10.1016/j.cpc.2014.11.024](https://doi.org/10.1016/j.cpc.2014.11.024). arXiv: [1408.2372 \[hep-ph\]](https://arxiv.org/abs/1408.2372) (cit. on pp. 21, 110).
- [53] J. A. M. Vermaseren. “Tuning FORM with large calculations”. In: *Nucl. Phys. Proc. Suppl.* 116 (2003). [343(2002)], pp. 343–347. DOI: [10.1016/S0920-5632\(03\)80196-2](https://doi.org/10.1016/S0920-5632(03)80196-2). arXiv: [hep-ph/0211297 \[hep-ph\]](https://arxiv.org/abs/hep-ph/0211297) (cit. on p. 23).
- [54] Jonathan Grigo. “Korrekturen höherer Ordnung zur Produktion von Higgs-Boson-Paaren”. German. PhD thesis. 2015. DOI: [10.5445/IR/1000048688](https://doi.org/10.5445/IR/1000048688) (cit. on pp. 23, 131).
- [55] V. A. Smirnov. *Feynman integral calculus*. 2006 (cit. on pp. 24, 25).
- [56] Go Mishima. “High-Energy Expansion of Two-Loop Massive Four-Point Diagrams”. In: *JHEP* 02 (2019), p. 080. DOI: [10.1007/JHEP02\(2019\)080](https://doi.org/10.1007/JHEP02(2019)080). arXiv: [1812.04373 \[hep-ph\]](https://arxiv.org/abs/1812.04373) (cit. on pp. 24, 25, 76).
- [57] Roberto Bonciani, Vittorio Del Duca, Hjalte Frellesvig, Johannes M. Henn, Francesco Moriello, and Vladimir A. Smirnov. “Two-loop planar master integrals for Higgs→3 partons with full heavy-quark mass dependence”. In: *JHEP* 12 (2016), p. 096. DOI: [10.1007/JHEP12\(2016\)096](https://doi.org/10.1007/JHEP12(2016)096). arXiv: [1609.06685 \[hep-ph\]](https://arxiv.org/abs/1609.06685) (cit. on p. 24).
- [58] Matteo Becchetti and Roberto Bonciani. “Two-Loop Master Integrals for the Planar QCD Massive Corrections to Di-photon and Di-jet Hadro-production”. In: *JHEP* 01 (2018), p. 048. DOI: [10.1007/JHEP01\(2018\)048](https://doi.org/10.1007/JHEP01(2018)048). arXiv: [1712.02537 \[hep-ph\]](https://arxiv.org/abs/1712.02537) (cit. on p. 24).
- [59] Luise Adams, Ekta Chaubey, and Stefan Weinzierl. “Analytic results for the planar double box integral relevant to top-pair production with a closed top loop”. In: *JHEP* 10 (2018), p. 206. DOI: [10.1007/JHEP10\(2018\)206](https://doi.org/10.1007/JHEP10(2018)206). arXiv: [1806.04981 \[hep-ph\]](https://arxiv.org/abs/1806.04981) (cit. on p. 24).
- [60] Stefano Di Vita, Stefano Laporta, Pierpaolo Mastrolia, Amedeo Primo, and Ulrich Schubert. “Master integrals for the NNLO virtual corrections to μe scattering in QED: the non-planar graphs”. In: *JHEP* 09 (2018), p. 016. DOI: [10.1007/JHEP09\(2018\)016](https://doi.org/10.1007/JHEP09(2018)016). arXiv: [1806.08241 \[hep-ph\]](https://arxiv.org/abs/1806.08241) (cit. on p. 24).

- [61] M. Beneke and Vladimir A. Smirnov. “Asymptotic expansion of Feynman integrals near threshold”. In: *Nucl. Phys.* B522 (1998), pp. 321–344. DOI: [10.1016/S0550-3213\(98\)00138-2](https://doi.org/10.1016/S0550-3213(98)00138-2). arXiv: [hep-ph/9711391](https://arxiv.org/abs/hep-ph/9711391) [[hep-ph](#)] (cit. on pp. 24, 25).
- [62] A. V. Kotikov. “Differential equations method: New technique for massive Feynman diagrams calculation”. In: *Phys. Lett.* B254 (1991), pp. 158–164. DOI: [10.1016/0370-2693\(91\)90413-K](https://doi.org/10.1016/0370-2693(91)90413-K) (cit. on p. 24).
- [63] T. Gehrmann and E. Remiddi. “Differential equations for two loop four point functions”. In: *Nucl. Phys.* B580 (2000), pp. 485–518. DOI: [10.1016/S0550-3213\(00\)00223-6](https://doi.org/10.1016/S0550-3213(00)00223-6). arXiv: [hep-ph/9912329](https://arxiv.org/abs/hep-ph/9912329) [[hep-ph](#)] (cit. on p. 24).
- [64] E. Remiddi and J. A. M. Vermaseren. “Harmonic polylogarithms”. In: *Int. J. Mod. Phys.* A15 (2000), pp. 725–754. DOI: [10.1142/S0217751X00000367](https://doi.org/10.1142/S0217751X00000367). arXiv: [hep-ph/9905237](https://arxiv.org/abs/hep-ph/9905237) [[hep-ph](#)] (cit. on p. 25).
- [65] Vladimir A. Smirnov. “Analytic tools for Feynman integrals”. In: *Springer Tracts Mod. Phys.* 250 (2012), pp. 1–296. DOI: [10.1007/978-3-642-34886-0](https://doi.org/10.1007/978-3-642-34886-0) (cit. on p. 25).
- [66] M. Czakon. “Automatized analytic continuation of Mellin-Barnes integrals”. In: *Comput. Phys. Commun.* 175 (2006), pp. 559–571. DOI: [10.1016/j.cpc.2006.07.002](https://doi.org/10.1016/j.cpc.2006.07.002). arXiv: [hep-ph/0511200](https://arxiv.org/abs/hep-ph/0511200) [[hep-ph](#)] (cit. on p. 25).
- [67] A. V. Smirnov and V. A. Smirnov. “On the Resolution of Singularities of Multiple Mellin-Barnes Integrals”. In: *Eur. Phys. J.* C62 (2009), pp. 445–449. DOI: [10.1140/epjc/s10052-009-1039-6](https://doi.org/10.1140/epjc/s10052-009-1039-6). arXiv: [0901.0386](https://arxiv.org/abs/0901.0386) [[hep-ph](#)] (cit. on p. 25).
- [68] Helaman R. P. Ferguson, David H. Bailey, and Steve Arno. “Analysis of PSLQ, An Integer Relation Finding Algorithm”. In: *Mathematics of Computation* 68.225 (1999), pp. 351–369. ISSN: 00255718, 10886842. URL: <http://www.jstor.org/stable/2585116> (cit. on p. 25).
- [69] D Maitre. “HPL, a mathematica implementation of the harmonic polylogarithms”. In: *Comput. Phys. Commun.* 174 (2006), pp. 222–240. DOI: [10.1016/j.cpc.2005.10.008](https://doi.org/10.1016/j.cpc.2005.10.008). arXiv: [hep-ph/0507152](https://arxiv.org/abs/hep-ph/0507152) [[hep-ph](#)] (cit. on p. 26).
- [70] Daniel Maitre. “Extension of HPL to complex arguments”. In: *Comput. Phys. Commun.* 183 (2012), p. 846. DOI: [10.1016/j.cpc.2011.11.015](https://doi.org/10.1016/j.cpc.2011.11.015). arXiv: [hep-ph/0703052](https://arxiv.org/abs/hep-ph/0703052) [[hep-ph](#)] (cit. on p. 26).
- [71] Kirill Kudashkin, Kirill Melnikov, and Christopher Wever. “Two-loop amplitudes for processes $gg \rightarrow Hg$, $qg \rightarrow Hq$ and $q\bar{q} \rightarrow Hg$ at large Higgs transverse momentum”. In: *JHEP* 02 (2018), p. 135. DOI: [10.1007/JHEP02\(2018\)135](https://doi.org/10.1007/JHEP02(2018)135). arXiv: [1712.06549](https://arxiv.org/abs/1712.06549) [[hep-ph](#)] (cit. on p. 26).
- [72] Alexander V. Smirnov. “FIESTA4: Optimized Feynman integral calculations with GPU support”. In: *Comput. Phys. Commun.* 204 (2016), pp. 189–199. DOI: [10.1016/j.cpc.2016.03.013](https://doi.org/10.1016/j.cpc.2016.03.013). arXiv: [1511.03614](https://arxiv.org/abs/1511.03614) [[hep-ph](#)] (cit. on p. 26).
- [73] S. Borowka, G. Heinrich, S. Jahn, S. P. Jones, M. Kerner, J. Schlenk, and T. Zirke. “pySecDec: a toolbox for the numerical evaluation of multi-scale integrals”. In: *Comput. Phys. Commun.* 222 (2018), pp. 313–326. DOI: [10.1016/j.cpc.2017.09.015](https://doi.org/10.1016/j.cpc.2017.09.015). arXiv: [1703.09692](https://arxiv.org/abs/1703.09692) [[hep-ph](#)] (cit. on p. 26).

- [74] John C. Collins. *Renormalization*. Vol. 26. Cambridge Monographs on Mathematical Physics. Cambridge: Cambridge University Press, 1986. ISBN: 9780521311779, 9780511867392. DOI: [10.1017/CB09780511622656](https://doi.org/10.1017/CB09780511622656). URL: <http://www-spires.fnal.gov/spires/find/books/www?cl=QC174.17.R46C65::1985> (cit. on p. 28).
- [75] Stefano Catani. “The Singular behavior of QCD amplitudes at two loop order”. In: *Phys. Lett. B* 427 (1998), pp. 161–171. DOI: [10.1016/S0370-2693\(98\)00332-3](https://doi.org/10.1016/S0370-2693(98)00332-3). arXiv: [hep-ph/9802439](https://arxiv.org/abs/hep-ph/9802439) [hep-ph] (cit. on pp. 28, 29).
- [76] Daniel de Florian and Javier Mazzitelli. “A next-to-next-to-leading order calculation of soft-virtual cross sections”. In: *JHEP* 12 (2012), p. 088. DOI: [10.1007/JHEP12\(2012\)088](https://doi.org/10.1007/JHEP12(2012)088), [10.1007/JHEP12\(2012\)088](https://doi.org/10.1007/JHEP12(2012)088). arXiv: [1209.0673](https://arxiv.org/abs/1209.0673) [hep-ph] (cit. on p. 29).
- [77] R. Mertig, M. Bohm, and Ansgar Denner. “FEYN CALC: Computer algebraic calculation of Feynman amplitudes”. In: *Comput. Phys. Commun.* 64 (1991), pp. 345–359. DOI: [10.1016/0010-4655\(91\)90130-D](https://doi.org/10.1016/0010-4655(91)90130-D) (cit. on p. 32).
- [78] Vladyslav Shtabovenko, Rolf Mertig, and Frederik Orellana. “New Developments in FeynCalc 9.0”. In: *Comput. Phys. Commun.* 207 (2016), pp. 432–444. DOI: [10.1016/j.cpc.2016.06.008](https://doi.org/10.1016/j.cpc.2016.06.008). arXiv: [1601.01167](https://arxiv.org/abs/1601.01167) [hep-ph] (cit. on p. 32).
- [79] T. Hahn and M. Perez-Victoria. “Automatized one loop calculations in four-dimensions and D-dimensions”. In: *Comput. Phys. Commun.* 118 (1999), pp. 153–165. DOI: [10.1016/S0010-4655\(98\)00173-8](https://doi.org/10.1016/S0010-4655(98)00173-8). arXiv: [hep-ph/9807565](https://arxiv.org/abs/hep-ph/9807565) [hep-ph] (cit. on p. 32).
- [80] Thomas Hahn, Sebastian Paßehr, and Christian Schappacher. “FormCalc 9 and Extensions”. In: *PoS LL2016* (2016). [J. Phys. Conf. Ser. 762, no. 1, 012065 (2016)], p. 068. DOI: [10.22323/1.260.0068](https://doi.org/10.22323/1.260.0068), [10.1088/1742-6596/762/1/012065](https://doi.org/10.1088/1742-6596/762/1/012065). arXiv: [1604.04611](https://arxiv.org/abs/1604.04611) [hep-ph] (cit. on p. 32).
- [81] G. J. van Oldenborgh and J. A. M. Vermaseren. “New algorithms for one-loop integrals”. In: *Zeitschrift für Physik C Particles and Fields* 46.3 (Sept. 1990), pp. 425–437. ISSN: 1431-5858. DOI: [10.1007/BF01621031](https://doi.org/10.1007/BF01621031). URL: <https://doi.org/10.1007/BF01621031> (cit. on p. 32).
- [82] Hiren H. Patel. “Package-X: A Mathematica package for the analytic calculation of one-loop integrals”. In: *Comput. Phys. Commun.* 197 (2015), pp. 276–290. DOI: [10.1016/j.cpc.2015.08.017](https://doi.org/10.1016/j.cpc.2015.08.017). arXiv: [1503.01469](https://arxiv.org/abs/1503.01469) [hep-ph] (cit. on p. 32).
- [83] Hiren H. Patel. “Package-X 2.0: A Mathematica package for the analytic calculation of one-loop integrals”. In: *Comput. Phys. Commun.* 218 (2017), pp. 66–70. DOI: [10.1016/j.cpc.2017.04.015](https://doi.org/10.1016/j.cpc.2017.04.015). arXiv: [1612.00009](https://arxiv.org/abs/1612.00009) [hep-ph] (cit. on p. 32).
- [84] David Wellmann. *PhD Thesis - ancillary files*. Institute for Theoretical Particle Physics, Karlsruhe Institute of Technology. URL: <https://www.ttp.kit.edu/preprints/2019/ttp20-001> (cit. on pp. 33, 34, 36, 40, 83, 112).
- [85] Herbert Stahl. “Spurious Poles in Padé Approximation”. In: *J. Comput. Appl. Math.* 99.1-2 (Nov. 1998), pp. 511–527. ISSN: 0377-0427. DOI: [10.1016/S0377-0427\(98\)00180-0](https://doi.org/10.1016/S0377-0427(98)00180-0). URL: [http://dx.doi.org/10.1016/S0377-0427\(98\)00180-0](http://dx.doi.org/10.1016/S0377-0427(98)00180-0) (cit. on p. 50).

- [86] Joshua Davies, Gudrun Heinrich, Stephen P. Jones, Matthias Kerner, Go Mishima, Matthias Steinhauser, and David Wellmann. “Double Higgs boson production at NLO: combining the exact numerical result and high-energy expansion”. In: *JHEP* 11 (2019), p. 024. DOI: [10.1007/JHEP11\(2019\)024](https://doi.org/10.1007/JHEP11(2019)024). arXiv: [1907.06408 \[hep-ph\]](https://arxiv.org/abs/1907.06408) (cit. on pp. 56, 70, 93, 97, 99, 100).
- [87] Roberto Bonciani, Giuseppe Degrossi, Pier Paolo Giardino, and Ramona Gröber. “Analytical Method for Next-to-Leading-Order QCD Corrections to Double-Higgs Production”. In: *Phys. Rev. Lett.* 121.16 (2018), p. 162003. DOI: [10.1103/PhysRevLett.121.162003](https://doi.org/10.1103/PhysRevLett.121.162003). arXiv: [1806.11564 \[hep-ph\]](https://arxiv.org/abs/1806.11564) (cit. on pp. 65, 70).
- [88] Bakul Agarwal and Andreas von Manteuffel. “On the two-loop amplitude for $gg \rightarrow ZZ$ production with full top-mass dependence”. In: 2019. arXiv: [1912.08794 \[hep-ph\]](https://arxiv.org/abs/1912.08794) (cit. on p. 65).
- [89] J. Alison et al. “Higgs Boson Pair Production at Colliders: Status and Perspectives”. In: *Double Higgs Production at Colliders Batavia, IL, USA, September 4, 2018-9, 2019*. Ed. by B. Di Micco, M. Gouzevitch, J. Mazzitelli, and C. Vernieri. 2019. arXiv: [1910.00012 \[hep-ph\]](https://arxiv.org/abs/1910.00012). URL: <https://lss.fnal.gov/archive/2019/conf/fermilab-conf-19-468-e-t.pdf> (cit. on p. 69).
- [90] E. W. Nigel Glover and J. J. van der Bij. “HIGGS BOSON PAIR PRODUCTION VIA GLUON FUSION”. In: *Nucl. Phys.* B309 (1988), pp. 282–294. DOI: [10.1016/0550-3213\(88\)90083-1](https://doi.org/10.1016/0550-3213(88)90083-1) (cit. on pp. 69, 72, 78, 91).
- [91] T. Plehn, M. Spira, and P. M. Zerwas. “Pair production of neutral Higgs particles in gluon-gluon collisions”. In: *Nucl. Phys.* B479 (1996). [Erratum: *Nucl. Phys.* B531,655(1998)], pp. 46–64. DOI: [10.1016/0550-3213\(96\)00418-X](https://doi.org/10.1016/0550-3213(96)00418-X), [10.1016/S0550-3213\(98\)00406-4](https://doi.org/10.1016/S0550-3213(98)00406-4). arXiv: [hep-ph/9603205 \[hep-ph\]](https://arxiv.org/abs/hep-ph/9603205) (cit. on p. 69).
- [92] S. Borowka, N. Greiner, G. Heinrich, S. P. Jones, M. Kerner, J. Schlenk, U. Schubert, and T. Zirke. “Higgs Boson Pair Production in Gluon Fusion at Next-to-Leading Order with Full Top-Quark Mass Dependence”. In: *Phys. Rev. Lett.* 117.1 (2016). [Erratum: *Phys. Rev. Lett.* 117,no.7,079901(2016)], p. 012001. DOI: [10.1103/PhysRevLett.117.079901](https://doi.org/10.1103/PhysRevLett.117.079901), [10.1103/PhysRevLett.117.012001](https://doi.org/10.1103/PhysRevLett.117.012001). arXiv: [1604.06447 \[hep-ph\]](https://arxiv.org/abs/1604.06447) (cit. on pp. 69, 91, 92).
- [93] S. Borowka, N. Greiner, G. Heinrich, S. P. Jones, M. Kerner, J. Schlenk, and T. Zirke. “Full top quark mass dependence in Higgs boson pair production at NLO”. In: *JHEP* 10 (2016), p. 107. DOI: [10.1007/JHEP10\(2016\)107](https://doi.org/10.1007/JHEP10(2016)107). arXiv: [1608.04798 \[hep-ph\]](https://arxiv.org/abs/1608.04798) (cit. on pp. 69, 91, 92, 131).
- [94] Julien Baglio, Francisco Campanario, Seraina Glaus, Margarete Mühlleitner, Michael Spira, and Juraj Streicher. “Gluon fusion into Higgs pairs at NLO QCD and the top mass scheme”. In: *Eur. Phys. J.* C79.6 (2019), p. 459. DOI: [10.1140/epjc/s10052-019-6973-3](https://doi.org/10.1140/epjc/s10052-019-6973-3). arXiv: [1811.05692 \[hep-ph\]](https://arxiv.org/abs/1811.05692) (cit. on p. 69).
- [95] R. Frederix, S. Frixione, V. Hirschi, F. Maltoni, O. Mattelaer, P. Torrielli, E. Vryonidou, and M. Zaro. “Higgs pair production at the LHC with NLO and parton-shower effects”. In: *Phys. Lett.* B732 (2014), pp. 142–149. DOI: [10.1016/j.physletb.2014.03.026](https://doi.org/10.1016/j.physletb.2014.03.026). arXiv: [1401.7340 \[hep-ph\]](https://arxiv.org/abs/1401.7340) (cit. on p. 69).

- [96] F. Maltoni, E. Vryonidou, and M. Zaro. “Top-quark mass effects in double and triple Higgs production in gluon-gluon fusion at NLO”. In: *JHEP* 11 (2014), p. 079. DOI: [10.1007/JHEP11\(2014\)079](https://doi.org/10.1007/JHEP11(2014)079). arXiv: [1408.6542 \[hep-ph\]](https://arxiv.org/abs/1408.6542) (cit. on p. 69).
- [97] S. Dawson, S. Dittmaier, and M. Spira. “Neutral Higgs boson pair production at hadron colliders: QCD corrections”. In: *Phys. Rev. D* 58 (1998), p. 115012. DOI: [10.1103/PhysRevD.58.115012](https://doi.org/10.1103/PhysRevD.58.115012). arXiv: [hep-ph/9805244 \[hep-ph\]](https://arxiv.org/abs/hep-ph/9805244) (cit. on p. 69).
- [98] Daniel de Florian and Javier Mazzitelli. “Two-loop virtual corrections to Higgs pair production”. In: *Phys. Lett. B* 724 (2013), pp. 306–309. DOI: [10.1016/j.physletb.2013.06.046](https://doi.org/10.1016/j.physletb.2013.06.046). arXiv: [1305.5206 \[hep-ph\]](https://arxiv.org/abs/1305.5206) (cit. on p. 69).
- [99] Daniel de Florian and Javier Mazzitelli. “Higgs Boson Pair Production at Next-to-Next-to-Leading Order in QCD”. In: *Phys. Rev. Lett.* 111 (2013), p. 201801. DOI: [10.1103/PhysRevLett.111.201801](https://doi.org/10.1103/PhysRevLett.111.201801). arXiv: [1309.6594 \[hep-ph\]](https://arxiv.org/abs/1309.6594) (cit. on p. 69).
- [100] Jonathan Grigo, Kirill Melnikov, and Matthias Steinhauser. “Virtual corrections to Higgs boson pair production in the large top quark mass limit”. In: *Nucl. Phys. B* 888 (2014), pp. 17–29. DOI: [10.1016/j.nuclphysb.2014.09.003](https://doi.org/10.1016/j.nuclphysb.2014.09.003). arXiv: [1408.2422 \[hep-ph\]](https://arxiv.org/abs/1408.2422) (cit. on pp. 69, 78, 83).
- [101] Jonathan Grigo, Jens Hoff, Kirill Melnikov, and Matthias Steinhauser. “On the Higgs boson pair production at the LHC”. In: *Nucl. Phys. B* 875 (2013), pp. 1–17. DOI: [10.1016/j.nuclphysb.2013.06.024](https://doi.org/10.1016/j.nuclphysb.2013.06.024). arXiv: [1305.7340 \[hep-ph\]](https://arxiv.org/abs/1305.7340) (cit. on p. 69).
- [102] Jonathan Grigo, Jens Hoff, and Matthias Steinhauser. “Higgs boson pair production: top quark mass effects at NLO and NNLO”. In: *Nucl. Phys. B* 900 (2015), pp. 412–430. DOI: [10.1016/j.nuclphysb.2015.09.012](https://doi.org/10.1016/j.nuclphysb.2015.09.012). arXiv: [1508.00909 \[hep-ph\]](https://arxiv.org/abs/1508.00909) (cit. on p. 69).
- [103] Ding Yu Shao, Chong Sheng Li, Hai Tao Li, and Jian Wang. “Threshold resummation effects in Higgs boson pair production at the LHC”. In: *JHEP* 07 (2013), p. 169. DOI: [10.1007/JHEP07\(2013\)169](https://doi.org/10.1007/JHEP07(2013)169). arXiv: [1301.1245 \[hep-ph\]](https://arxiv.org/abs/1301.1245) (cit. on p. 69).
- [104] Daniel de Florian and Javier Mazzitelli. “Higgs pair production at next-to-next-to-leading logarithmic accuracy at the LHC”. In: *JHEP* 09 (2015), p. 053. DOI: [10.1007/JHEP09\(2015\)053](https://doi.org/10.1007/JHEP09(2015)053). arXiv: [1505.07122 \[hep-ph\]](https://arxiv.org/abs/1505.07122) (cit. on p. 69).
- [105] Massimiliano Grazzini, Gudrun Heinrich, Stephen Jones, Stefan Kallweit, Matthias Kerner, Jonas M. Lindert, and Javier Mazzitelli. “Higgs boson pair production at NNLO with top quark mass effects”. In: *JHEP* 05 (2018), p. 059. DOI: [10.1007/JHEP05\(2018\)059](https://doi.org/10.1007/JHEP05(2018)059). arXiv: [1803.02463 \[hep-ph\]](https://arxiv.org/abs/1803.02463) (cit. on p. 69).
- [106] Joshua Davies, Florian Herren, Go Mishima, and Matthias Steinhauser. “NNLO real corrections to $gg \rightarrow HH$ in the large- m_t limit”. In: *14th International Symposium on Radiative Corrections: Application of Quantum Field Theory to Phenomenology (RADCOR 2019) Avignon, France, September 8-13, 2019*. 2019. arXiv: [1912.01646 \[hep-ph\]](https://arxiv.org/abs/1912.01646) (cit. on p. 70).
- [107] Joshua Davies and Matthias Steinhauser. “Three-loop form factors for Higgs boson pair production in the large top mass limit”. In: *JHEP* 10 (2019), p. 166. DOI: [10.1007/JHEP10\(2019\)166](https://doi.org/10.1007/JHEP10(2019)166). arXiv: [1909.01361 \[hep-ph\]](https://arxiv.org/abs/1909.01361) (cit. on p. 70).

- [108] Long-Bin Chen, Hai Tao Li, Hua-Sheng Shao, and Jian Wang. “The gluon-fusion production of Higgs boson pair: N³LO QCD corrections and top-quark mass effects”. In: (2019). arXiv: [1912.13001 \[hep-ph\]](https://arxiv.org/abs/1912.13001) (cit. on p. 70).
- [109] Joshua Davies, Go Mishima, Matthias Steinhauser, and David Wellmann. “Double Higgs Production in the High Energy Limit”. In: *PoS LL2018* (2018), p. 022. DOI: [10.22323/1.303.0022](https://doi.org/10.22323/1.303.0022) (cit. on p. 70).
- [110] Bernd Jantzen, Alexander V. Smirnov, and Vladimir A. Smirnov. “Expansion by regions: revealing potential and Glauber regions automatically”. In: *Eur. Phys. J. C72* (2012), p. 2139. DOI: [10.1140/epjc/s10052-012-2139-2](https://doi.org/10.1140/epjc/s10052-012-2139-2). arXiv: [1206.0546 \[hep-ph\]](https://arxiv.org/abs/1206.0546) (cit. on p. 76).
- [111] Robert Harlander and Philipp Kant. “Higgs production and decay: Analytic results at next-to-leading order QCD”. In: *JHEP* 12 (2005), p. 015. DOI: [10.1088/1126-6708/2005/12/015](https://doi.org/10.1088/1126-6708/2005/12/015). arXiv: [hep-ph/0509189 \[hep-ph\]](https://arxiv.org/abs/hep-ph/0509189) (cit. on p. 83).
- [112] G. Heinrich, S. P. Jones, M. Kerner, G. Luisoni, and E. Vryonidou. “NLO predictions for Higgs boson pair production with full top quark mass dependence matched to parton showers”. In: *JHEP* 08 (2017), p. 088. DOI: [10.1007/JHEP08\(2017\)088](https://doi.org/10.1007/JHEP08(2017)088). arXiv: [1703.09252 \[hep-ph\]](https://arxiv.org/abs/1703.09252) (cit. on pp. 91, 92).
- [113] Giuseppe Degrossi, Pier Paolo Giardino, and Ramona Gröber. “On the two-loop virtual QCD corrections to Higgs boson pair production in the Standard Model”. In: *Eur. Phys. J. C76.7* (2016), p. 411. DOI: [10.1140/epjc/s10052-016-4256-9](https://doi.org/10.1140/epjc/s10052-016-4256-9). arXiv: [1603.00385 \[hep-ph\]](https://arxiv.org/abs/1603.00385) (cit. on p. 91).
- [114] G. Heinrich, S. P. Jones, M. Kerner, G. Luisoni, and E. Vryonidou. *hhgrid*. <https://github.com/mppmu/hhgrid>. 2017 (cit. on pp. 92, 93, 95–97, 99, 102, 103, 135).
- [115] Joshua Davies, Gudrun Heinrich, Stephen P. Jones, Matthias Kerner, Go Mishima, Matthias Steinhauser, and David Wellmann. *hhgrid*. <https://github.com/mppmu/hhgrid>. 2019 (cit. on pp. 99–101, 103).
- [116] M. Galassi et al. *GNU Scientific Library Reference Manual - Third Edition*. Network Theory Ltd., 2009. ISBN: 0954612078. URL: <http://www.gnu.org/software/gsl/> (cit. on p. 99).
- [117] E. Braaten and J. P. Leveille. “Higgs Boson Decay and the Running Mass”. In: *Phys. Rev. D* 22 (1980), p. 715. DOI: [10.1103/PhysRevD.22.715](https://doi.org/10.1103/PhysRevD.22.715) (cit. on p. 106).
- [118] K. G. Chetyrkin, Johann H. Kuhn, and M. Steinhauser. “Heavy quark current correlators to O(α_s^2)”. In: *Nucl. Phys. B* 505 (1997), pp. 40–64. DOI: [10.1016/S0550-3213\(97\)00481-1](https://doi.org/10.1016/S0550-3213(97)00481-1). arXiv: [hep-ph/9705254 \[hep-ph\]](https://arxiv.org/abs/hep-ph/9705254) (cit. on p. 106).
- [119] R. Harlander and M. Steinhauser. “Higgs decay to top quarks at O(α_s^2)”. In: *Phys. Rev. D* 56 (1997), pp. 3980–3990. DOI: [10.1103/PhysRevD.56.3980](https://doi.org/10.1103/PhysRevD.56.3980). arXiv: [hep-ph/9704436 \[hep-ph\]](https://arxiv.org/abs/hep-ph/9704436) (cit. on p. 106).
- [120] K. G. Chetyrkin, R. Harlander, and M. Steinhauser. “Singlet polarization functions at O(α_s^2)”. In: *Phys. Rev. D* 58 (1998), p. 014012. DOI: [10.1103/PhysRevD.58.014012](https://doi.org/10.1103/PhysRevD.58.014012). arXiv: [hep-ph/9801432 \[hep-ph\]](https://arxiv.org/abs/hep-ph/9801432) (cit. on p. 106).

- [121] S. G. Gorishnii, A. L. Kataev, S. A. Larin, and L. R. Surguladze. “Corrected Three Loop QCD Correction to the Correlator of the Quark Scalar Currents and γ (Tot) ($H^0 \rightarrow$ Hadrons)”. In: *Mod. Phys. Lett. A*5 (1990), pp. 2703–2712. DOI: [10.1142/S0217732390003152](https://doi.org/10.1142/S0217732390003152) (cit. on p. 106).
- [122] K. G. Chetyrkin. “Correlator of the quark scalar currents and Gamma(tot) ($H \rightarrow$ hadrons) at $O(\alpha_s^3)$ in pQCD”. In: *Phys. Lett. B*390 (1997), pp. 309–317. DOI: [10.1016/S0370-2693\(96\)01368-8](https://doi.org/10.1016/S0370-2693(96)01368-8). arXiv: [hep-ph/9608318](https://arxiv.org/abs/hep-ph/9608318) [[hep-ph](#)] (cit. on p. 106).
- [123] K. G. Chetyrkin and M. Steinhauser. “Complete QCD corrections of order $O(\alpha_s^3)$ to the hadronic Higgs decay”. In: *Phys. Lett. B*408 (1997), pp. 320–324. DOI: [10.1016/S0370-2693\(97\)00779-X](https://doi.org/10.1016/S0370-2693(97)00779-X). arXiv: [hep-ph/9706462](https://arxiv.org/abs/hep-ph/9706462) [[hep-ph](#)] (cit. on pp. 106, 107, 110).
- [124] P. A. Baikov, K. G. Chetyrkin, and Johann H. Kuhn. “Scalar correlator at $O(\alpha_s^4)$, Higgs decay into b-quarks and bounds on the light quark masses”. In: *Phys. Rev. Lett.* 96 (2006), p. 012003. DOI: [10.1103/PhysRevLett.96.012003](https://doi.org/10.1103/PhysRevLett.96.012003). arXiv: [hep-ph/0511063](https://arxiv.org/abs/hep-ph/0511063) [[hep-ph](#)] (cit. on pp. 106, 110, 112).
- [125] Bernd A. Kniehl. “Radiative corrections for $H \rightarrow f \text{ anti-}f (\gamma)$ in the standard model”. In: *Nucl. Phys. B*376 (1992), pp. 3–28. DOI: [10.1016/0550-3213\(92\)90065-J](https://doi.org/10.1016/0550-3213(92)90065-J) (cit. on p. 106).
- [126] A. Dabelstein and W. Hollik. “Electroweak corrections to the fermionic decay width of the standard Higgs boson”. In: *Z. Phys. C*53 (1992), pp. 507–516. DOI: [10.1007/BF01625912](https://doi.org/10.1007/BF01625912) (cit. on p. 106).
- [127] Luminita Mihaila, Barbara Schmidt, and Matthias Steinhauser. “ $\Gamma(H \rightarrow b\bar{b})$ to order α_s^3 ”. In: *Phys. Lett. B*751 (2015), pp. 442–447. DOI: [10.1016/j.physletb.2015.10.078](https://doi.org/10.1016/j.physletb.2015.10.078). arXiv: [1509.02294](https://arxiv.org/abs/1509.02294) [[hep-ph](#)] (cit. on p. 106).
- [128] A. Djouadi, J. Kalinowski, and M. Spira. “HDECAY: A Program for Higgs boson decays in the standard model and its supersymmetric extension”. In: *Comput. Phys. Commun.* 108 (1998), pp. 56–74. DOI: [10.1016/S0010-4655\(97\)00123-9](https://doi.org/10.1016/S0010-4655(97)00123-9). arXiv: [hep-ph/9704448](https://arxiv.org/abs/hep-ph/9704448) [[hep-ph](#)] (cit. on p. 106).
- [129] Joshua Davies, Matthias Steinhauser, and David Wellmann. “Completing the hadronic Higgs boson decay at order α_s^4 ”. In: *Nucl. Phys. B*920 (2017), pp. 20–31. DOI: [10.1016/j.nuclphysb.2017.04.012](https://doi.org/10.1016/j.nuclphysb.2017.04.012). arXiv: [1703.02988](https://arxiv.org/abs/1703.02988) [[hep-ph](#)] (cit. on p. 107).
- [130] Joshua Davies, Matthias Steinhauser, and David Wellmann. “Hadronic Higgs boson decay at order α_s^4 and α_s^5 ”. In: *PoS DIS2017* (2018), p. 295. DOI: [10.22323/1.297.0295](https://doi.org/10.22323/1.297.0295). arXiv: [1706.00624](https://arxiv.org/abs/1706.00624) [[hep-ph](#)] (cit. on p. 107).
- [131] Takeo Inami, Takahiro Kubota, and Yasuhiro Okada. “Effective Gauge Theory and the Effect of Heavy Quarks in Higgs Boson Decays”. In: *Z. Phys. C*18 (1983), pp. 69–80. DOI: [10.1007/BF01571710](https://doi.org/10.1007/BF01571710) (cit. on p. 107).
- [132] Y. Schroder and M. Steinhauser. “Four-loop decoupling relations for the strong coupling”. In: *JHEP* 01 (2006), p. 051. DOI: [10.1088/1126-6708/2006/01/051](https://doi.org/10.1088/1126-6708/2006/01/051). arXiv: [hep-ph/0512058](https://arxiv.org/abs/hep-ph/0512058) [[hep-ph](#)] (cit. on pp. 107, 141).

- [133] K. G. Chetyrkin, Johann H. Kuhn, and Christian Sturm. “QCD decoupling at four loops”. In: *Nucl. Phys.* B744 (2006), pp. 121–135. DOI: [10.1016/j.nuclphysb.2006.03.020](https://doi.org/10.1016/j.nuclphysb.2006.03.020). arXiv: [hep-ph/0512060](https://arxiv.org/abs/hep-ph/0512060) [[hep-ph](#)] (cit. on pp. 107, 141).
- [134] Tao Liu and Matthias Steinhauser. “Decoupling of heavy quarks at four loops and effective Higgs-fermion coupling”. In: *Phys. Lett.* B746 (2015), pp. 330–334. DOI: [10.1016/j.physletb.2015.05.023](https://doi.org/10.1016/j.physletb.2015.05.023). arXiv: [1502.04719](https://arxiv.org/abs/1502.04719) [[hep-ph](#)] (cit. on pp. 107, 141).
- [135] Marvin Gerlach, Florian Herren, and Matthias Steinhauser. “Wilson coefficients for Higgs boson production and decoupling relations to $\mathcal{O}(\alpha_s^4)$ ”. In: *JHEP* 11 (2018), p. 141. DOI: [10.1007/JHEP11\(2018\)141](https://doi.org/10.1007/JHEP11(2018)141). arXiv: [1809.06787](https://arxiv.org/abs/1809.06787) [[hep-ph](#)] (cit. on pp. 107, 141).
- [136] P. A. Baikov and K. G. Chetyrkin. “Top Quark Mediated Higgs Boson Decay into Hadrons to Order α_s^5 ”. In: *Phys. Rev. Lett.* 97 (2006), p. 061803. DOI: [10.1103/PhysRevLett.97.061803](https://doi.org/10.1103/PhysRevLett.97.061803). arXiv: [hep-ph/0604194](https://arxiv.org/abs/hep-ph/0604194) [[hep-ph](#)] (cit. on p. 110).
- [137] P. A. Baikov and K. G. Chetyrkin. “Four Loop Massless Propagators: An Algebraic Evaluation of All Master Integrals”. In: *Nucl. Phys.* B837 (2010), pp. 186–220. DOI: [10.1016/j.nuclphysb.2010.05.004](https://doi.org/10.1016/j.nuclphysb.2010.05.004). arXiv: [1004.1153](https://arxiv.org/abs/1004.1153) [[hep-ph](#)] (cit. on p. 110).
- [138] A. V. Smirnov and M. Tentyukov. “Four Loop Massless Propagators: a Numerical Evaluation of All Master Integrals”. In: *Nucl. Phys.* B837 (2010), pp. 40–49. DOI: [10.1016/j.nuclphysb.2010.04.020](https://doi.org/10.1016/j.nuclphysb.2010.04.020). arXiv: [1004.1149](https://arxiv.org/abs/1004.1149) [[hep-ph](#)] (cit. on p. 110).
- [139] R. N. Lee, A. V. Smirnov, and V. A. Smirnov. “Master Integrals for Four-Loop Massless Propagators up to Transcendentality Weight Twelve”. In: *Nucl. Phys.* B856 (2012), pp. 95–110. DOI: [10.1016/j.nuclphysb.2011.11.005](https://doi.org/10.1016/j.nuclphysb.2011.11.005). arXiv: [1108.0732](https://arxiv.org/abs/1108.0732) [[hep-th](#)] (cit. on p. 110).
- [140] S. A. Larin, F. V. Tkachov, and J. A. M. Vermaseren. “The FORM version of MINCER”. In: (1991) (cit. on p. 110).
- [141] K. G. Chetyrkin. “Four-loop renormalization of QCD: Full set of renormalization constants and anomalous dimensions”. In: *Nucl. Phys.* B710 (2005), pp. 499–510. DOI: [10.1016/j.nuclphysb.2005.01.011](https://doi.org/10.1016/j.nuclphysb.2005.01.011). arXiv: [hep-ph/0405193](https://arxiv.org/abs/hep-ph/0405193) [[hep-ph](#)] (cit. on p. 110).
- [142] V. P. Spiridonov. “Anomalous Dimension of $G_{\mu\nu}^2$ and β Function”. In: (1984) (cit. on p. 110).
- [143] F. Herzog, B. Ruijl, T. Ueda, J. A. M. Vermaseren, and A. Vogt. “On Higgs decays to hadrons and the R-ratio at N⁴LO”. In: *JHEP* 08 (2017), p. 113. DOI: [10.1007/JHEP08\(2017\)113](https://doi.org/10.1007/JHEP08(2017)113). arXiv: [1707.01044](https://arxiv.org/abs/1707.01044) [[hep-ph](#)] (cit. on p. 111).
- [144] K. G. Chetyrkin, Johann H. Kuhn, and M. Steinhauser. “RunDec: A Mathematica package for running and decoupling of the strong coupling and quark masses”. In: *Comput. Phys. Commun.* 133 (2000), pp. 43–65. DOI: [10.1016/S0010-4655\(00\)00155-7](https://doi.org/10.1016/S0010-4655(00)00155-7). arXiv: [hep-ph/0004189](https://arxiv.org/abs/hep-ph/0004189) [[hep-ph](#)] (cit. on p. 112).

- [145] Barbara Schmidt and Matthias Steinhauser. “CRunDec: a C++ package for running and decoupling of the strong coupling and quark masses”. In: *Comput. Phys. Commun.* 183 (2012), pp. 1845–1848. DOI: [10.1016/j.cpc.2012.03.023](https://doi.org/10.1016/j.cpc.2012.03.023). arXiv: [1201.6149](https://arxiv.org/abs/1201.6149) [hep-ph] (cit. on p. 112).
- [146] Thomas Gehrmann, Lorenzo Tancredi, and Erich Weihs. “Two-loop QCD helicity amplitudes for $g g \rightarrow Z g$ and $g g \rightarrow Z \gamma$ ”. In: *JHEP* 04 (2013), p. 101. DOI: [10.1007/JHEP04\(2013\)101](https://doi.org/10.1007/JHEP04(2013)101). arXiv: [1302.2630](https://arxiv.org/abs/1302.2630) [hep-ph] (cit. on pp. 137, 139).